

Study of $\pi^+ \rightarrow e^+ \nu_e$ decay

by

Chloé Malbrunot

Dipl.-Ing., Technische Universität Wien (Vienna University of Technology), 2007
M.Sc., Ecole Centrale Marseille, 2007

A THESIS SUBMITTED IN PARTIAL FULFILLMENT OF
THE REQUIREMENTS FOR THE DEGREE OF

DOCTOR OF PHILOSOPHY

in

The Faculty of Graduate Studies

(Physics)

THE UNIVERSITY OF BRITISH COLUMBIA

(Vancouver)

April 2012

© Chloé Malbrunot 2012

Abstract

The pion branching ratio ($R^\pi = \frac{\Gamma(\pi^+ \rightarrow e^+ \nu_e + \pi^+ \rightarrow e^+ \nu_e \gamma)}{\Gamma(\pi^+ \rightarrow \mu^+ \nu_\mu + \pi^+ \rightarrow \mu^+ \nu_\mu \gamma)}$) is an auspicious observable for a test of the standard model of particle physics (SM). R^π has been calculated within this framework with high precision because the strong interaction dynamics cancel out in the ratio and the structure dependence only appears through electroweak corrections. Since the discovery of the electronic pion decay in 1958, R^π was measured with increasing precision and confirmed the SM value of $R_{SM}^\pi = 1.2352(2) \times 10^{-4}$. However, the current experimental precision is 20 times worse than the theoretical one leaving a large window for potential new physics at “high-mass” scales (up to ~ 1000 TeV).

The PIENU experiment aims at measuring R^π with an improved precision by a factor larger than 5 over the previous experiment at TRIUMF ($R_{exp}^\pi = (1.2265 \pm 0.0056) \times 10^{-4}$) in order to confront the theoretical prediction at the 0.1% level. The result presented in this thesis focuses on a fraction of the data taken since the beginning of physics data taking in 2009. A blind analysis has been implemented in order to avoid a human bias. With this set of data, the procedure is established for the final analysis. An improvement by a factor 1.17, dominated by statistical uncertainty, has been reached in the branching ratio precision. If added to the current Particle Data Group value, the result of this analysis reduces the uncertainty on the branching ratio by $\sim 25\%$.

Le rapport de branchement du pion ($R^\pi = \frac{\Gamma(\pi^+ \rightarrow e^+ \nu_e + \pi^+ \rightarrow e^+ \nu_e \gamma)}{\Gamma(\pi^+ \rightarrow \mu^+ \nu_\mu + \pi^+ \rightarrow \mu^+ \nu_\mu \gamma)}$) est une observable privilégiée pour un test du modèle standard de la physique des particules. R^π a été calculé dans ce cadre avec une haute précision parce que les dynamiques de l’interaction forte s’annulent en prenant le rapport et les effets hadroniques n’apparaissent qu’à travers les corrections électro-faibles. Depuis la découverte en 1958 de la désintégration du pion en positron, R^π a été mesuré avec une précision croissante. Toutefois, la

Abstract

précision expérimentale actuelle est de 20 fois inférieure à la précision théorique ce qui laisse le champ libre pour l'apparition de phénomènes non-standard dont les énergies pourraient atteindre jusqu'à ~ 1000 TeV.

L'expérience PIENU vise à mesurer R^π avec une précision 5 fois supérieure à celle obtenue par la précédente expérience à TRIUMF ($R^\pi = (1.2265 \pm 0.0056) \times 10^{-4}$). Le résultat présenté dans cette thèse se concentre sur une fraction des données prises depuis 2009 pour lesquelles une analyse en aveugle a été développée. L'analyse qui sera utilisée pour l'obtention du résultat final est basée sur le travail détaillé dans ce document. Malgré une statistique limitée, la précision dans la mesure de R^π a été améliorée par un facteur 1.17 ce qui représente une amélioration de $\sim 25\%$ de la valeur actuelle listée par le "Particle Data Group".

Preface

The PIENU collaboration has about 25 members from 11 different institutions. I joined the experiment in September 2007 before the construction of the beamline extension and assembly of the detector. I actively participated in the tests on the beamline for which I prepared the trigger and tested the NaI(Tl) crystal with the help of A. A. Aguilar-Arevalo. I subsequently analyzed the data taken and reported the results in a technical note. The result of those tests were published in [1]. The description of the beamline is made in chapter 3.

I designed and built the PIENU trigger. The description of the trigger is made in chapter 3 and Appendix A. I was responsible for the tests of the wire chambers and the implementation of a large part of the slow controls. Together with Chris Pearson, I adapted the TIGC module (which is an important part of the digital trigger system) to the specific needs of the PIENU experiment. I was extensively involved in the 2009 engineering runs during which the first high statistics measurement with the NaI(Tl) were made and photo-nuclear reactions in the crystal observed. Those data were analyzed by Luca Doria and Toshio Numao and published in [2].

I participated in all physics data taking runs in 2009, 2010 and 2011. The extensive number of shifts required the remote participation of “off-site” collaborators. For this purpose, a comprehensive documentation of all online monitoring devices and associated troubleshooting instructions had to be written. I was fully responsible for this task. Over the years of data taking, I took over 200 shifts and was a run coordinator for several months.

The physics runs taken in 2009 were analyzed by Kaoru Yamada and Toshio Numao. I also participated in the analysis for which the results were published in [3]. A brief description of this analysis is presented in chapter 8.

I was the first PhD student working on the branching ratio analysis and was the principal contributor to this work. Together with Masaharu Aoki, I

Preface

took the lead in developing the blind analysis strategy adopted for this analysis. The blind analysis technique is described in chapter 1. I performed the data selection for 2010 data and actively participated in the development of the “first-stage” data decoding. I was the major participant in all parts of the analysis presented in chapter 4 and chapter 5. The analysis of the lineshape data was done with the help of Tristan Sullivan.

Beside the work of research, I was one of the administrators of the desktop and cluster computers of the PIENU collaboration and was responsible for maintaining the PIENU website.

Table of Contents

Abstract	ii
Preface	iv
Table of Contents	vi
List of Tables	x
List of Figures	xi
Glossary	xvi
Acknowledgements	xx
Dedication	xxii
1 Introduction	1
1.1 Overview of the PIENU experiment	1
1.1.1 Brief discussion on the branching ratio	1
1.1.2 Overview of the experimental technique	1
1.2 Previous experimental measurements	4
1.2.1 Some history	4
1.2.2 Details and lessons from the E248 experiment	5
1.3 Blind analysis technique	8
1.4 Outline of the thesis	10
2 Theoretical Background	11
2.1 The standard model of particle physics	11
2.1.1 A brief introduction	11
2.1.2 Symmetries in the SM	13
2.1.3 Successes and flaws of the SM	14
2.2 V-A theory	17
2.2.1 Pion decay rate	18

Table of Contents

2.2.2	Helicity suppression	20
2.2.3	Lepton universality	20
2.2.4	Review of pion and muon decay modes	24
2.3	Radiative corrections	25
2.4	Beyond the standard model	30
2.4.1	Neutrinos	31
2.4.2	New pseudo-scalar interactions	33
2.4.3	New scalar interactions	37
2.4.4	Conclusions	37
3	Description of the Experiment	38
3.1	The M13 beamline	38
3.1.1	Beamline momentum calibration	41
3.1.2	Particle and magnetic background	42
3.2	The detector	43
3.2.1	Overview	43
3.2.2	Plastic scintillators	45
3.2.3	Wire chambers	46
3.2.4	Silicon detectors	47
3.2.5	NaI calorimeter	50
3.2.6	CsI calorimeter	51
3.2.7	Detector assembly and performance	52
3.3	The trigger	62
3.4	The data acquisition system	65
3.4.1	The electronics	65
3.4.2	The slow controls	69
3.4.3	MIDAS	69
3.5	History and future of the experiment	70
4	Time Spectrum Analysis	71
4.1	Overview	71
4.2	Variable extraction	71
4.2.1	From VT48	71
4.2.2	From COPPER waveform	72
4.2.3	From VF48 waveform	72
4.3	Calibration	74
4.3.1	ADC and pedestal calibration	74
4.3.2	Gain stabilization	76
4.3.3	Energy calibration	77
4.4	Event selection	80

Table of Contents

4.4.1	Quality of data	81
4.4.2	Pion selection	83
4.4.3	Decay positron selection	84
4.4.4	Background rejection	85
4.4.5	Acceptance cut	88
4.4.6	Summary of all selection cuts	89
4.5	Timing fit: extraction of the raw branching ratio	90
4.5.1	Pulse shape fitting	90
4.5.2	Construction of the time spectra	93
4.5.3	The fit	93
4.6	Systematics checks	103
4.7	Linearity	106
4.8	Effects of trigger inefficiencies	107
4.9	Muon decay-in-flight correction	108
4.10	Energy dependence of t_0	110
5	Corrections and Systematics	112
5.1	Tail correction	112
5.1.1	Suppressed spectrum	112
5.1.2	Lower limit estimation	118
5.1.3	Lineshape measurement	121
5.1.4	Upper limit estimation from Monte Carlo	126
5.1.5	Corrections to the tail fraction	141
5.1.6	Tail estimation from Monte Carlo	146
5.2	Acceptance correction	146
5.2.1	Monte Carlo studies	148
5.2.2	Result	152
5.2.3	Test of the Monte Carlo	153
5.3	Other systematics	155
5.3.1	Effect of tracking detector inefficiencies in the acceptance definition	155
5.3.2	Effect of multiple hits in WC3	156
6	Simulation	160
6.1	Beam and tracking	160
6.1.1	Beam	160
6.1.2	Tracking performance	162
6.2	Detector geometry	162
6.2.1	Plastic scintillators	164
6.2.2	Silicon	164

Table of Contents

6.2.3	Wire chambers	164
6.2.4	CsI	164
6.3	Radiative decays in $\pi^+ \rightarrow e^+\nu_e$	167
6.4	Energy loss processes	167
6.5	Muon decay-in-flight	169
7	Results	170
7.1	Corrections	170
7.2	Systematic checks	170
8	Neutrino Analysis	172
8.1	Brief introduction to the theory	172
8.2	Brief description of the analysis	173
8.2.1	Selection cuts	173
8.2.2	Fitting procedure	175
8.3	Results	175
9	Conclusions	179
9.1	Results	179
9.2	Comments on the results	179
9.3	Foreseen improvements	181
9.3.1	Statistical uncertainty	181
9.3.2	Time analysis	181
9.3.3	Tail analysis	182
9.3.4	Acceptance correction	182
9.3.5	Massive neutrino analysis	182
	Bibliography	183
 Appendices		
A	Full Trigger Diagram	198
B	X and Y Position of Tracking Detectors	199
C	Muon Runs	200

List of Tables

2.1	Matter particle content of the standard model	12
2.2	Gauge bosons	12
2.3	Experimental results on lepton universality tests	22
2.4	Pion decay modes	25
2.5	Muon decay modes	25
2.6	Summary of the electroweak corrections to R_0^π	30
3.1	Sizes of all PIENU detectors	45
3.2	Readout scheme of the plastic scintillators PMTs	46
3.3	Approximate proportions of decays in flight events to decay-at-rest events from Monte Carlo calculations	60
3.4	Rate of each trigger	65
3.5	Summarized list of slow controls	69
3.6	History and future of the PIENU experiment	70
4.1	Result of the time spectrum fit	100
4.2	List of systematic checks on the time spectrum fit	104
5.1	Summary of the suppressed spectrum cuts	119
5.2	List of special positron runs taken in 2009	123
5.3	List of the low energy tail components based on lineshape obtained with MC and data	137
5.4	MC estimation of the proportion of a few energy dependent processes for $\pi^+ \rightarrow e^+ \nu_e$ and $\pi^+ \rightarrow \mu^+ \rightarrow e^+$ events	148
5.5	Estimation of the level of uncertainty in the detector positions	150
5.6	List of systematics studies on the acceptance	151
7.1	List of corrections to the branching ratio	170
C.1	List of muon runs taken in 2010	200

List of Figures

1.1	Schematic illustration of the two pionic decays in the PIENU target	2
1.2	Energy deposited in the target for $\pi^+ \rightarrow e^+\nu_e$ and $\pi^+ \rightarrow \mu^+ \rightarrow e^+$ events	3
1.3	Time and Energy spectra of $\pi^+ \rightarrow e^+\nu_e$ and $\pi^+ \rightarrow \mu^+ \rightarrow e^+$ events from simulation	3
1.4	History of the pion branching ratio experimental results . . .	6
1.5	Experimental setup of the E248 experiment at TRIUMF . . .	7
1.6	Suppressed Spectrum obtained by the E248 experiment . . .	8
1.7	Evolution in time of the neutron's lifetime experimental result	9
1.8	Blinding technique for the PIENU experiment	10
2.1	Standard model and point-like representation of pion decay .	18
2.2	Schematic illustration of the helicity suppressed $\pi^+ \rightarrow e^+\nu_e$ decay	20
2.3	Experimental bounds as of 2008 on g_e and g_μ deviation from universality	23
2.4	Feynman diagrams of radiative contributions to the branching ratio	26
2.5	Additional Feynman diagrams which contribute to the leading order QED correction to the branching ratio	28
2.6	Constraints on RPV parameters from R_π	36
3.1	The M13 beam channel	39
3.2	Picture of the setup tests prior to the beamline extension construction	40
3.3	Picture of the M13 area after the beamline extension installation	40
3.4	Particle separation at $F\mathcal{B}$	41
3.5	G4beamline simulation of the M13 beamline	42
3.6	Schematic diagram of the experimental apparatus	44
3.7	Schematic of a wire chamber plane	47
3.8	Picture of a beam wire chamber plane before assembly	48

List of Figures

3.9	Picture of the WC1 and WC2 assembly	48
3.10	Picture of the WC3 detector	49
3.11	Picture of S1 and S2 assembly mounted on their support structure	49
3.12	Schematic drawing of the silicon readout scheme	50
3.13	Picture of the NaI crystal	51
3.14	Picture of the NaI crystal in the CsI enclosure	51
3.15	Picture of one of the CsI crystal	53
3.16	Technical design of the PIENU apparatus and picture of the detector setup	54
3.17	Picture of the detector inside the temperature-controlled enclosure	55
3.18	Temperature variation in the detector area	55
3.19	Schematic drawing of the detector setup for special positron runs	56
3.20	Beam positron spectrum in the NaI	57
3.21	Beam positron energy in the NaI crystal. Comparison between data and Monte Carlo	58
3.22	Schematic drawing of the tracking devices and the different decay-in-flight backgrounds	61
3.23	Simulation of the kink angle θ for different pion decay modes	62
3.24	Schematic drawing of a simplified trigger diagram	64
3.25	A waveform digitized by COPPER	66
4.1	Schematic drawing of the variables extraction from a waveform readout by COPPER	73
4.2	Charge deposited in the left “high-strip” versus the right “high-strip” of the silicon detectors	75
4.3	Comparison of the amount of charge deposited in each CsI crystal of the inner upstream part between data and MC	78
4.4	Variation of the cosmic peak energy with the CsI crystal position as obtained with the CRY cosmic simulation package	79
4.5	Sum of the energy deposited in the downstream material from MC	81
4.6	Data stability	82
4.7	Energy deposited in B1 versus the Time of flight and energy deposited in B2	83
4.8	Beam profile at the centre of WC1	84

List of Figures

4.9	Scatter plot of the minimum energy deposited in the downstream counters as a function of the energy deposited in the NaI	86
4.10	Radial distribution of events in WC3	89
4.11	Summary of the fraction of events removed by each cut	90
4.12	Comparison of all events with energies larger than 50 MeV in the calorimeters with late muon decay events	91
4.13	Histograms of COPPER templates	92
4.14	Fit of a COPPER 500 MHz waveform	92
4.15	“High-energy” and “low-energy” time spectra	93
4.16	Time spectra of “old-muon” background from simulation	98
4.17	Time spectrum of $\pi^+ \rightarrow \mu^+ \nu_\mu \gamma$ background from simulation	99
4.18	Time spectra for $t > 0$ with residuals of the fit	101
4.19	Time spectra for $t < 0$ with residuals of the fit	102
4.20	Time distribution of beam positrons	105
4.21	Time spectrum for muon runs fitted with an exponential function	107
4.22	T2 inefficiency as a function of time	108
4.23	Decay time of MDIF events	109
4.24	Positron spectra from muon decay at rest and muon decay in flight (MC)	109
4.25	Variation of t_0 as a function of the energy deposited in the NaI111	111
5.1	Total Energy cut	113
5.2	Kink angle for $\pi^+ \rightarrow e^+ \nu_e$ and $\pi^+ \rightarrow \mu^+ \rightarrow e^+$ events	115
5.3	S3 Energy cut	117
5.4	Comparison of 3-pulse fit and 2-pulse fit on an early $\pi^+ \rightarrow \mu^+ \rightarrow e^+$ event in the target	118
5.5	Contour plot of the Total Energy as a function of $\Delta\chi^2$ for $\pi^+ \rightarrow e^+ \nu_e$ and $\pi^+ \rightarrow \mu^+ \rightarrow e^+$ events	119
5.6	NaI energy after suppressed spectrum cuts	120
5.7	Illustration of the lower limit estimation technique using the suppressed spectrum	122
5.8	Illustration of the matching procedure for the lineshape	125
5.9	Lineshape obtained with data compared to the suppressed spectrum	127
5.10	Comparison of the data and MC lineshapes with beam positrons hitting the center of the crystal at five different angles	130
5.11	Photo-nuclear events and traversed length in the NaI	131

List of Figures

5.12	MC simulation of the increase of the tail fraction as a function of the beam positron angle hitting the center of the NaI crystal with or without photo-nuclear reactions	132
5.13	MC lineshape compared with data lineshape	134
5.14	Comparison of the lineshape measurements with a MC simulation of beam positrons	135
5.15	Tail fraction estimated from MC and data lineshapes	136
5.16	Upper and Lower limits on the tail	140
5.17	Total Energy for MDIF	142
5.18	Fit of the suppressed spectrum	143
5.19	Energy deposited in the target and the calorimeters by Bhabha-scattered events	144
5.20	Comparison of the $\pi^+ \rightarrow e^+\nu_e$ energy spectrum in the calorimeters for data and MC	145
5.21	Summary of the evolution of the tail fraction with corrections	147
5.22	Effect on the acceptance of different pion stopping point along the beam axis	152
5.23	Effect on the acceptance of a shift of the tracking detectors along the beam axis	152
5.24	Effect on the acceptance of a shift of the tracking detectors along the x axis	153
5.25	Effect on the acceptance of a shift of the tracking detectors along the y axis	153
5.26	Effect on the acceptance of a change in the downstream plastic scintillators thicknesses	154
5.27	Effect on the acceptance of an increase in the threshold energy of the downstream trigger detectors	154
5.28	Acceptance change with WC3 inefficiencies	156
5.29	S3 inefficiency curves	157
5.30	Distribution on the surface of WC3 of the events missed by S3_Y	158
5.31	Acceptance change with S3 inefficiencies	159
5.32	Acceptance change with multiple hits in WC3	159
6.1	Comparison between data and MC of the pion beam distribution in the target	161
6.2	Z vertex reconstruction and “real” pion stop distribution in the target from MC	162
6.3	Difference between reconstructed and true position in S1_Y .	163

List of Figures

6.4	Stability of the difference between reconstructed and true position in WC3_3	163
6.5	NaI and CsI front geometry in the MC	165
6.6	Comparison of the energy deposited in CsI for MC and data .	166
6.7	Angle between e^+ and γ for radiative events	168
6.8	Energy of photon versus positron for $\pi^+ \rightarrow e^+\nu_e \gamma$ events in MC	168
6.9	Acceptance as a function of WC3 radius for two different energy thresholds on electromagnetic processes in the MC . . .	169
7.1	Effect of the acceptance cut on the branching ratio	171
7.2	Effect of the cut-off energy on the branching ratio	171
8.1	Energy spectra in the NaI for $\pi^+ \rightarrow e^+\nu_e$ decays and beam positrons	174
8.2	Normalized amplitude of the potential peaks in the $\pi^+ \rightarrow e^+\nu_e$ spectrum	176
8.3	Combined 90% C.L. upper limits	177
9.1	Summary of uncertainties and comparison with the E248 experiment	180
A.1	The complete PIENU trigger diagram	198
B.1	Distribution of the difference between reconstructed tracks from WC1-2 detectors and hit position in all other tracking detectors using beam muons	199

Glossary

Each entry is followed by (G) if it refers to a general term widely used in the physicist's community or by (E) if it is a term specific to the PIENU experiment.

- ADC** (G) Analog to Digital Converter.
- ATLAS** (G) The acronym stands for "A Toroidal Lhc ApparatuS". It is an experiment taking place at the LHC, CERN. The ATLAS experiment uses a general-purpose detector to investigate a wide range of physics, including the search for the Higgs.
- B1** (E) B1 and B2 are the two beam scintillator counters in the PIENU assembly. *B1*, *B2*, *B3* also denote the three dipole magnets in the M13 beamline.
- BGO** (G) Abbreviation for "Bismuth germanium oxide" which is an inorganic chemical compound used in experimental physics for its scintillation properties.
- BNL** (G) Brookhaven National Laboratory, Upton, NY, USA.
- BSM** (G) It stands for "Beyond the Standard Model" and usually refers to theories including models of new physics phenomena.
- CAD** (G) Computer-aided design.
- CERN** (G) European Organization for Nuclear Research (Organisation européenne pour la recherche nucléaire). It is the world's largest particle physics laboratory. It is located in Geneva on the Franco-Swiss border.
- CF₄** (G) Carbon tetrafluoride, a quench gas commonly used in wire chambers.

GLOSSARY

- CMS** (G) The acronym stands for “Compact Muon Solenoid”. It is an experiment taking place at the LHC, CERN. It has similar physics goals to the ATLAS experiment.
- COPPER** (E) COPPER stands for : COmmon Pipelined Platform for Electronics Readout. It is a data acquisition system developed at KEK and used in the PIENU experiment.
- CP** (G) CP-symmetry is the combination of C-symmetry (charge conjugation symmetry) and P-symmetry (parity symmetry).
- CsI** (G) Cesium Iodide.
- DAQ** (G) Data Acquisition System.
- E248** (E) Pion decay experiment at TRIUMF performed in the 1980’s.
- E949/E787** (G) Rare kaon decay experiments at BNL.
- EPICS** (G) EPICS is a set of Open Source software tools, libraries and applications developed collaboratively and used worldwide to create distributed soft real-time control systems for scientific instruments such as particle accelerators.
- G4beamline** (G) G4beamline is a single-particle tracking program based on the Geant4 simulation toolkit. It is specifically designed for the simulation of beamlines.
- Geant4** (G) Toolkit written in C++ for the simulation of the passage of particles through matter.
- KEK** (G) High Energy Accelerator Research Organization, in Tokyo’s area, Japan.
- LHC** (G) The acronym stands for “Large Hadron Collider”. It is the world’s largest and highest-energy particle accelerator. It was built by the European Organization for Nuclear Research (CERN) and was designed to reach a total collision energy of 14 TeV.
- M13** (E) Pion beam channel in TRIUMF’s meson hall.
- MC** (G) Monte Carlo. Denotes a class of computational algorithms that relies on repeated random sampling and is used for simulating physical processes. The Geant4 software uses Monte Carlo methods.

GLOSSARY

MDAR	(E) Muon decay-at-rest.
MDIF	(E) Muon decay-in-flight.
MIDAS	(E) Data acquisition system which is used in particle and nuclear experiments.
NaI	(G) Sodium Iodide.
NIM	(G) The Nuclear Instrumentation Module (NIM) standard defines mechanical and electrical specifications for electronics modules used in experimental physics.
NMR	(G) An NMR probe (there is one for each dipole magnet in the M13 beamline) is an instrument used to measure the magnetic field.
PDAR	(E) Pion decay-at-rest.
PDG	(G) The “Particle Data Group” is an international collaboration that reviews particle physics and related areas of astrophysics, and compiles/analyzes data on particle properties.
PDIF	(E) Pion decay-in-flight.
PEN	(G) An experiment taking place at PSI which measures $\pi \rightarrow e + \nu(\gamma)$ decay branching ratio.
PMT	(G) Photo-Multiplier Tube.
PSI	(G) Paul Scherrer Institute. Research centre for natural and engineering sciences in Villigen, Switzerland.
R-parity	(G) It is a symmetry which prevents the appearance of terms in supersymmetric extension of the Standard Model that would violate lepton and baryon number conservation. The symmetry is defined as $P_R = (-1)^{2s+3B+L}$ where s stands for spin, B for baryon number and L for lepton number.
SLAC	(G) Stanford Linear Accelerator Center in Menlo Park, CA, USA.
SM	(G) Standard Model of Particle physics.
SUSY	(G) Abbreviation for “supersymmetry” which is a possible extension to the Standard Model.

GLOSSARY

- T1** (E) T1 and T2 are the two telescope scintillator counters in the PIENU assembly.
- TDC** (G) Time to Digital Converter.
- TIGC** (E) VME-based module used in the PIENU experiment. It generates a trigger based on the weighted amplitude sum information it receives from ADC modules.
- TRIUMF** (G) Canada's National Laboratory for Nuclear and Particle Physics, Vancouver.
- V-A** (G) Refers to the theory of weak interaction.
- V1** (E) V1, V2 and V3 are the three veto scintillator counters in the PIENU assembly.
- VF48** (E) ADC module based on VME standard.
- VT48** (E) TDC module based on VME standard.
- WC** (G) Wire Chamber.

Acknowledgements

First of all, I would like to express my gratitude to my supervisor, Doug Bryman who offered support and guidance throughout this PhD.

I am indebted to Toshio Numao for the many discussions and for the scrutiny of his comments on the analysis and the thesis. I am grateful to the PIENU Postdocs: Luca Doria, Aleksey Sher and Dmitry Vavilov for their important participation to the detector construction and to the development of the simulation and analysis codes. My particular thanks go to Luca Doria and Dmitry Vavilov for their quick and efficient proof-reading of this document's final draft. I would like to acknowledge the important contribution of Peter Gumplinger in the development of the GEANT4 code for PIENU. I am thankful to Tristan Sullivan for his participation in the tail analysis. Special thanks to Kaoru Yamada with whom I spend innumerable hours in the counting room during the beamline testing and engineering runs. He gave me great insights into the experiment and I am very pleased to have him as a friend.

I would like to acknowledge the important insights of Richard Mischke during the writing of the thesis. As an “external reviewer” he provided me with very useful critiques on the analysis. I am also grateful to the “off-site” PIENU group, in particular to Masaharu Aoki, Marvin Blecher and Alexis Aguilar-Arevalo for their insights and contributions to the analysis. I would also like to acknowledge the help of the many other members of the PIENU group who contributed to the experiment and the shift taking effort including David Britton, Chaomin Chen, Joseph Comfort, Ahmed Hussein, Youichi Igarashi, Steve Ketell, Leonid Kurchaninov, Laurence Littenberg, Philip Lu and Makoto Yoshida.

A word of thanks is also due to the TRIUMF DAQ group and especially to Renée Poutissou and Konstantin Olchanski for setting up the PIENU DAQ as well as to Chris Pearson for the many hours spent debugging TIGC in an enjoyable mood! I am also thankful to Grant Sheffer for his help dur-

Acknowledgements

ing the tests of the wire chambers.

I would also like to thank all the Master, Summer and Co-op students who contributed to the analysis as well as the shift-taking effort: Mingming Ding, Katharina Gill, Kevin Hildebrand, Cameron Hurst, Naosuke Ito, Shintaro Ito, Haotian Pang, Eric Thewalt and Ben Walker.

Thanks also to the many visitors, friends and family, who brought fresh air and a bit of the old continent's flair during those years of expatriation. I would also like to greatly thank the "Vancouverian" friends and most especially the BCDIJLMMMPR group for the great times spent together!!

My last and biggest thank goes to Stephan. Thank you for your support and for the decisions and compromises that we were able to make together along the past years. And thank you in advance for all those that we will make in the future!

À ma famille.

Chapter 1

Introduction

1.1 Overview of the PIENU experiment

1.1.1 Brief discussion on the branching ratio

The PIENU experiment aims at precisely measuring the rate of pion decay including the radiative components:

$$R^\pi = \frac{\Gamma\left((\pi^+ \rightarrow e^+\nu_e) + (\pi^+ \rightarrow e^+\nu_e\gamma)\right)}{\Gamma\left((\pi^+ \rightarrow \mu^+\nu_\mu) + (\pi^+ \rightarrow \mu^+\nu_\mu\gamma)\right)} \quad (1.1)$$

This branching ratio has been very precisely calculated within the framework of the standard model (SM). The current experimental value is 20 times less precise than the theoretical calculation, which leaves a large window in which non-standard physics can appear. Non-standard physics could include new interactions or exotic particles. Alternatively if the SM value is confirmed, tighter constraints on new physics scenarios can be set. Chapter 2 will present a detailed description of the sensitivity of the pion branching ratio measurement to new physics.

1.1.2 Overview of the experimental technique

The PIENU experiment is being carried out in the M13 area at TRIUMF, Canada's National Laboratory for Nuclear and Particle Physics, which is located on the University of British Columbia's campus in Vancouver, Canada. The pion beam, produced by the accelerated proton beam hitting a fixed Beryllium target, is directed to the M13 area where the PIENU experiment is located. The mono-energetic ($E_k \sim 18.9$ MeV) pions stop in a target schematically represented in Fig.1.1. The pion decays most of the time to a neutrino and a muon, which subsequently decays in the target into a positron and associated neutrinos (a decay which in the rest of the thesis will be referred as: $\pi^+ \rightarrow \mu^+ \rightarrow e^+$). Alternatively the pion directly decays into a positron and a neutrino (which will be referred as a $\pi^+ \rightarrow e^+\nu_e$ decay). These two decays have different time and energy characteristics that

1.1. Overview of the PIENU experiment

can be precisely measured and used to extract the branching ratio.

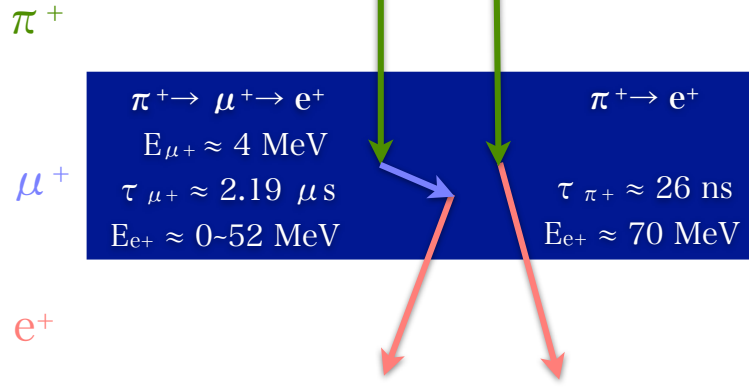


Figure 1.1: Schematic illustration of the two pionic decays in the PIENU target.

First, in the target, the range of the muon from a $\pi^+ \rightarrow \mu^+ \rightarrow e^+$ decay is about 1 mm which is well within the thickness of the PIENU target. Therefore, the entire muon kinetic energy of 4.12 MeV is deposited in the target while a $\pi^+ \rightarrow e^+ \nu_e$ decay has no additional energy (other than a small energy loss contribution from the positron) deposited in the target as shown in Fig.1.2. The decay positrons of both decays have different energy spectra. The positron from the 3-body muon decay ($\mu^+ \rightarrow e^+ \nu_e \bar{\nu}_\mu$) has a broad range of energy with an endpoint at 52.8 MeV, while the positron of the 2-body $\pi^+ \rightarrow e^+ \nu_e$ decay has a well defined energy of 69.8 MeV. And finally, the pion and muon decay constants are different by almost two orders of magnitude leading to significantly different time spectra. In Fig.1.3, the time and energy spectra of $\pi^+ \rightarrow e^+ \nu_e$ and $\pi^+ \rightarrow \mu^+ \rightarrow e^+$ events are superimposed. The analysis strategy takes advantage of these differences. An energy cut shown as a dashed black line in Fig.1.3 separates the bulk of $\pi^+ \rightarrow e^+ \nu_e$ and $\pi^+ \rightarrow \mu^+ \rightarrow e^+$ events. The time spectra of those two distributions are fitted simultaneously with functions taking into account the backgrounds in both distributions. The result of this fit gives access to the “raw branching ratio” to which a number of corrections have to be applied. The fitting procedure and the corrections will be explained in detail in chapter 4 and chapter 5 respectively.

1.1. Overview of the PIENU experiment

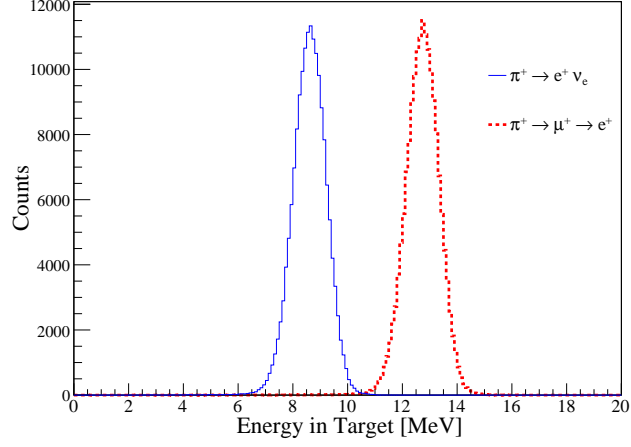


Figure 1.2: Energy deposited in the target for $\pi^+ \rightarrow e^+ \nu_e$ (blue/thin line) and $\pi^+ \rightarrow \mu^+ \rightarrow e^+$ (red/dashed line) events (MC).

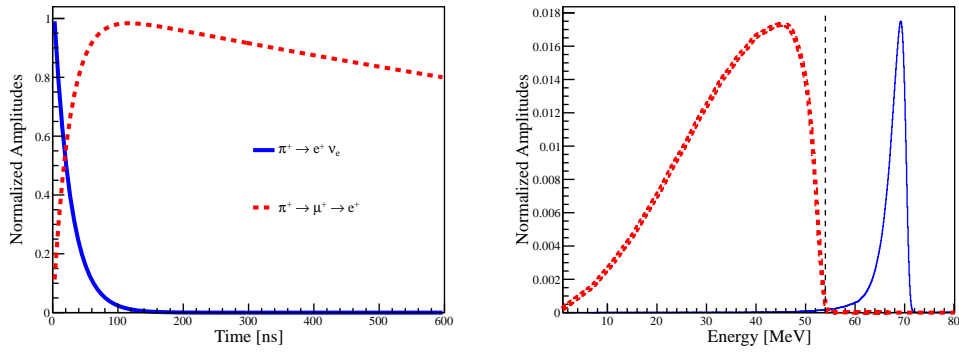


Figure 1.3: Time spectra (left) and energy spectra in the calorimeters (right) of $\pi^+ \rightarrow e^+ \nu_e$ and $\pi^+ \rightarrow \mu^+ \rightarrow e^+$ decays obtained from simulation. The spectra are normalized to the same amplitude.

1.2 Previous experimental measurements

1.2.1 Some history

The pion was discovered in 1947 in cosmic ray showers by Cecil Powell and collaborators [4]. For this discovery, C. Powell and H. Yukawa, who had predicted the existence of mesons, were awarded respectively the 1950 and 1949 Nobel Prizes [5]. The pion was the first “real”¹ meson to be discovered and gave the start to the “particle-rush”. Over the following years, a variety of particles were discovered that stimulated the construction of giant high-energy accelerators of which the LHC is the current epitome.

The muon had been discovered ten years earlier and was first believed to be the particle that Yukawa had predicted to be the carrier of a strong and short range force. But the muon did not appear to interact strongly with matter and was soon viewed as a mere heavy electron.

The charged pion being the lightest (139.6 MeV) of the charged meson particles can only decay into lighter leptons, namely to a muon or to an electron. The muon mass (105.7 MeV) is 34 MeV below the pion mass while the electron is about 280 times lighter than the pion, so, from pure phase-space consideration, the electronic decay should be greatly favored over the muonic decay. But for more than 10 years, only the pion decay into a muon was observed which was a great puzzle and triggered an experimental search for the electronic decay.

In 1957, an experiment carried out at the Enrico Fermi Institute [6] did not identify any $\pi^+ \rightarrow e^+\nu_e$ decays and set a limit for the branching ratio around $R_{1957} = 10^{-6}$ confirming a previous result by Lokanathan and Steinberger [7]. These results contradicted the theory that the decay of a pion should go through an axial-vector interaction yielding a branching ratio of the order of 10^{-4} . The so-called V-A theory had been proposed the same year by Sudarshan and Marshak [8] (and “publicized”² by Feynman and Gell-Mann [10] among others) as a theory of weak interaction in which parity was violated. Hints of parity violation in the weak decay of Kaons had indeed been noticed by T. Lee and C. Yang [11] in 1956 and confirmed the same year in the beta decay of cobalt-60 by the team of C. S. Wu [12] and other independent measurements. With the exception of the $\pi^+ \rightarrow e^+\nu_e$ decay the validity of a universal Fermi interaction was holding. Further attempts were therefore made to measure the branching ratio. In 1958, the $\pi^+ \rightarrow e^+\nu_e$ decay was discovered at CERN [13] and Columbia University

¹The muon which was discovered before the pion used to be called the “mu meson”.

²according to Feynman’s own words [9].

1.2. Previous experimental measurements

[14]. The first precise measurement of the branching ratio was done by the team of H. L. Anderson³ using a magnetic spectrometer [15]. With the addition of radiative corrections of 2.5%, the measured branching ratio was $R_{1960} = (1.27 \pm 0.07) \times 10^{-4}$, providing a measurement precision close to 5% and entirely in agreement with the hypothesis of a universal axial vector interaction. Several other experiments followed to confirm and improve this result. The experiment by Di Capua *et al.* [16] used a 23 cm diameter \times 24 cm long NaI(Tl) detector that could also detect photons from the radiative decays. Their measurement therefore included most of the inner-bremsstrahlung effect. With a collection of more than 10^4 $\pi^+ \rightarrow e^+ \nu_e$ events, they obtained a branching ratio of $R_{1964} = (1.247 \pm 0.028) \times 10^{-4}$ improving the measurement precision by a factor of 3. This result was later revised to $R_{1964,r} = (1.274 \pm 0.024) \times 10^{-4}$ [17] to account for a change in the pion lifetime. Almost 20 years later, another experiment with a larger and better NaI(Tl) crystal was carried out at TRIUMF by Bryman *et al.* [18]. Their result was $R_{1986} = (1.218 \pm 0.014) \times 10^{-4}$ from a sample of 3×10^4 $\pi^+ \rightarrow e^+ \nu_e$ events. Two subsequent experiments were carried out at TRIUMF [19] (E248 experiment) and PSI [20] few years later. The TRIUMF experiment carried on with a NaI(Tl) crystal as the main calorimeter detector while the PSI team used a 4π BGO calorimeter surrounding the target. Both experiments achieved comparable levels of statistical and systematic uncertainties. The weighted average of these two experiments $R_{1994_{av}} = 1.231 \pm 0.004 \times 10^{-4}$ was in agreement with the prediction of the Standard Model (SM) of particle physics which, by that time, predicted a branching ratio with the inclusion of radiative corrections and assuming universality⁴ of $R_{th} = (1.2350 \pm 0.0005) \times 10^{-4}$ [21].

Fig.1.4 shows the summary of these experimental results. The current PDG average using R_{1986} and the last PSI and TRIUMF results gives $R_{PDG_{av}} = 1.230 \pm 0.004 \times 10^{-4}$ [22].

1.2.2 Details and lessons from the E248 experiment at TRIUMF

The schematic of the E248 experimental setup is shown in Fig.1.5 and described in detail in [23]. Pions were stopped in a scintillator target. The main detector was a cylindrical NaI(Tl) crystal whose axis was oriented at 90° with respect to the beam so as not to get direct contamination from

³who was also an author of the negative result published 3 years earlier [6].

⁴more on this in §2.2.3.

1.2. Previous experimental measurements

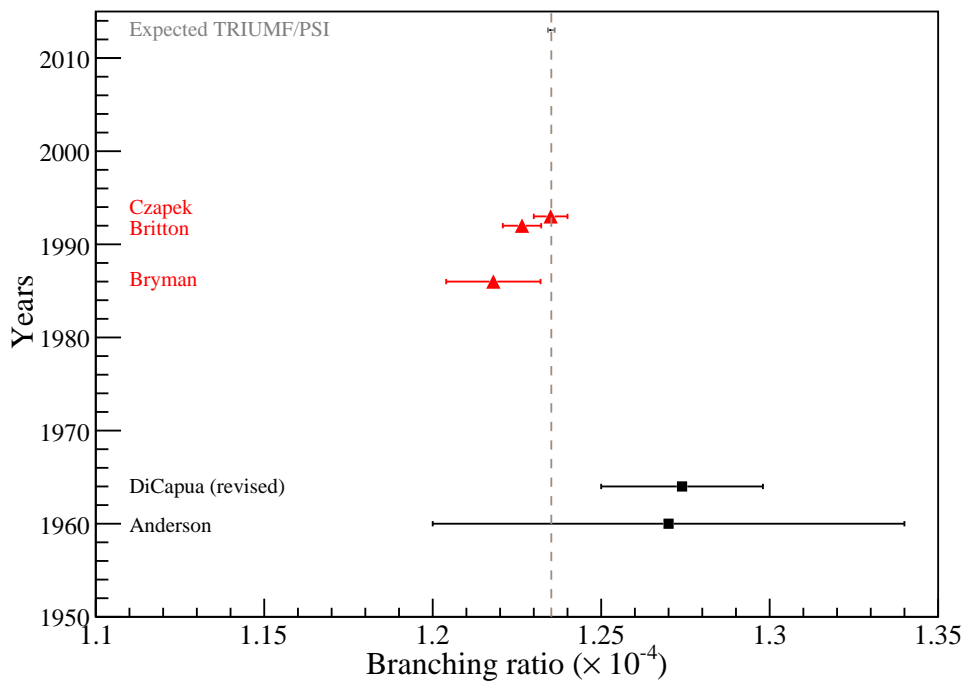


Figure 1.4: History of the pion branching ratio experimental results. The values indicated by red triangles are used by the current PDG average. The hatched line indicates the SM value and the last point shows, for comparison, the expected uncertainty from the new PSI and TRIUMF experiment assuming the SM value.

1.2. Previous experimental measurements

beam particles. The solid angle was only 2% of 4π steradians.

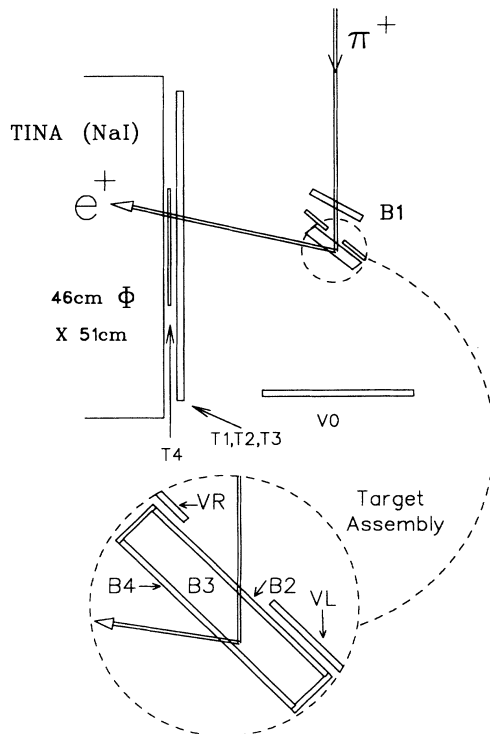


Figure 1.5: Experimental setup of the E248 experiment at TRIUMF.

The experiment took data for a month and collected about 10^5 $\pi^+ \rightarrow e^+ \nu_e$ events. The branching ratio result was $R_{1992} = 1.2265 \pm 0.0034(\text{stat}) \pm 0.0044(\text{sys}) \times 10^{-4}$ [19, 23]. Systematic and statistical errors were of the same order. The main systematic uncertainty came from the estimation of the $\pi^+ \rightarrow e^+ \nu_e$ low energy tail buried under the $\pi^+ \rightarrow \mu^+ \rightarrow e^+$ spectrum. To obtain this tail, they formed a so-call “suppressed spectrum” by suppressing the events identified as $\pi^+ \rightarrow \mu^+ \rightarrow e^+$ events. The result is shown in Fig.1.6. One can clearly see that there remains in this spectrum a component from $\pi^+ \rightarrow \mu^+ \rightarrow e^+$ decay. These are mostly events in which the pion decayed-in-flight before the target (in the rest of the thesis, these events will be called PDIF) and deposited a smaller amount of energy in the target than the pions which decayed at rest (PDAR). For these $\pi^+ \rightarrow \mu^+ \rightarrow e^+$ events

1.3. Blind analysis technique

remaining in the suppressed spectrum, the sum of the energy deposited in the target looked like a $\pi^+ \rightarrow e^+ \nu_e$ event. They could therefore not be removed by a target energy cut. The experiment had no tracking capability upstream of the target and could therefore only reject PDIF based on the energy deposited in the target. The fraction of the events below 52 MeV over the total number of $\pi^+ \rightarrow e^+ \nu_e$ events was about 20% and was dominated by these PDIF events. The estimation of the tail was also limited by the size of the data sample.

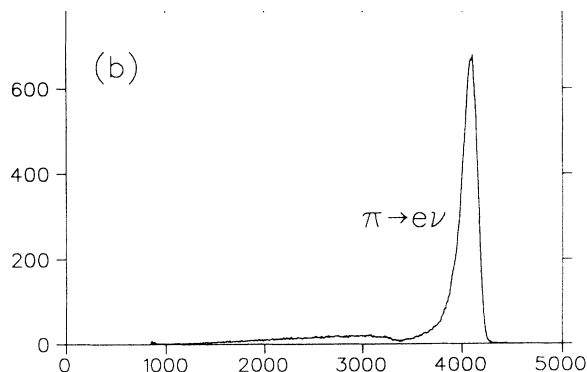


Figure 1.6: Suppressed spectrum obtained by the E248 experiment at TRIUMF. Most of the low energy background was due to PDIF.

The PIENU experiment is based on a similar detector concept but in which the “weak points” of the previous experiment have been taken into account to have a better control on the sources of systematics. For example, sets of tracking detectors have been added to enable suppression of PDIF events. Much larger data samples will be accumulated with a larger solid angle and longer running time. The detector has also been placed facing the beam to reduce the variation of traversed material along the positron path. The performance of the PIENU detector in terms of those improvements is described in §3.2.7.

1.3 Blind analysis technique

Although, none of the previous experiments measuring the $\pi^+ \rightarrow e^+ \nu_e$ branching ratio have, so far, used a blind analysis technique to extract their result, it is widely recognized to be an important tool to reduce possible

human biases. Especially, in the field of high precision experiments, where corrections have to be well controlled and systematics thoroughly scrutinized, the impact of human conscious or unconscious bias cannot be neglected. A famous example that illustrates the need for blind analysis is the PDG’s history plot [22] like the one shown in Fig.1.7. This particular plot shows the history of the experimental results on the neutron lifetime. The strikingly good agreement of the central value for sets of subsequent experimental results might point to the existence of a bias. The motivations for

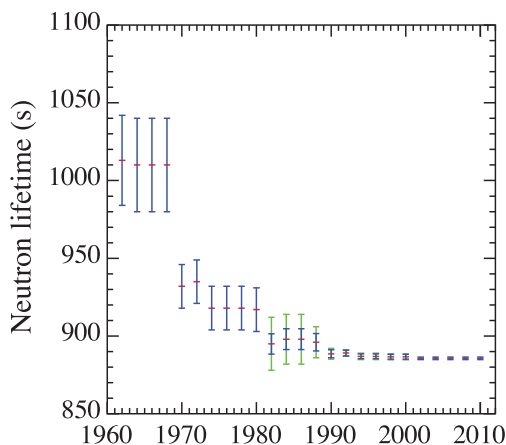


Figure 1.7: Evolution in time (years) of the neutron’s lifetime experimental result. Each data point represents an experimental result.

blind analysis in the particle physics field in general have been exposted in many papers (e.g: [24], [25], [26]). However, the blinding technique is fully dependent on the experiment and can be sometimes difficult to implement. For the PIENU experiment it was key that the blinding procedure should not artificially hide or create new systematic effects which would handicap the analysis. The orthogonality (at least at first order) of the energy deposited in the target and the time of individual decays was used to blind the value of the “raw branching ratio” [27]. A smooth and unknown inefficiency function with an average level different for the $\pi^+ \rightarrow e^+\nu_e$ and $\pi^+ \rightarrow \mu^+ \rightarrow e^+$ side of the target energy was used to randomly reject events as schematically illustrated in Fig.1.8 . The number of $\pi^+ \rightarrow \mu^+ \rightarrow e^+$ and $\pi^+ \rightarrow e^+\nu_e$ events rejected being different, the branching ratio was changed without distorting the time spectrum on which the fitting was performed.

The blinding was not applied to the data used for corrections, since as long as the value of the “raw branching ratio” is blinded, corrections can be studied on the unblinded sets of data.

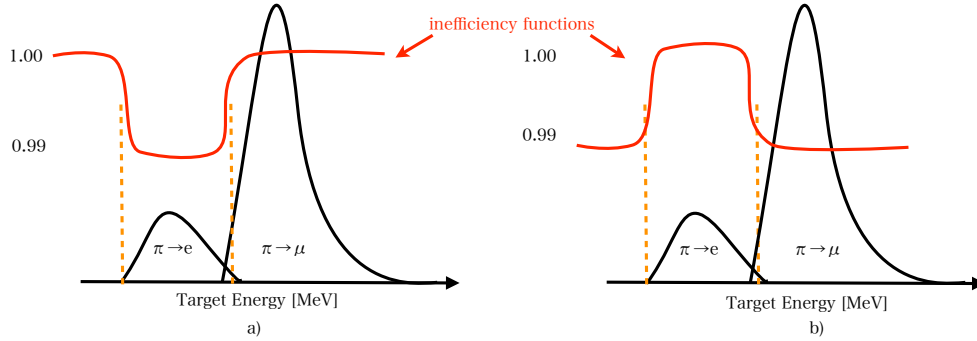


Figure 1.8: Blinding technique for the PIENU experiment. A smooth inefficiency function removes events based on their energy deposited in the target. Depending on the levels of the function (unknown to the experimenters), this procedure lowers -case a)- or raises -case b)- the branching ratio.

1.4 Outline of the thesis

Recently, important progress has been achieved in theoretical calculations of the $\pi^+ \rightarrow e^+ \nu_e$ branching ratio which has called for even more precise measurements. Two experiments at PSI and TRIUMF have been working for the last few years on measuring the pion branching ratio with the final goal of improving the measurement by almost a factor 10.

This thesis will detail the work done over the past four years at the detector and analysis level for the PIENU experiment and will present the preliminary results obtained with a partial set of the available data. Chapter 2 will develop the theoretical background. The following chapters will describe the experimental apparatus (chapter 3), present the analysis strategy (chapter 4 and 5) and Monte Carlo simulations (chapter 6) and finally expose the preliminary and intermediary results on the branching ratio (chapter 7) and on the massive neutrino search (chapter 8) based on data taken in 2010 and 2009 respectively. The author’s personal contributions to the experiment are detailed in the Preface.

Chapter 2

Theoretical Background

There is a theory which states that if ever anyone discovers exactly what the Universe is for and why it is here, it will instantly disappear and be replaced by something even more bizarre and inexplicable. There is another theory which states that this has already happened.

Douglas Adams

In the first section of this chapter, a brief overview of the current status of the standard model (SM) of particle physics will be made. A brief discussion on the general structure of the theory will be followed by a short description of the highlights and flaws of the current model. This first section is therefore intended as a general introduction to the field of particle physics. The following sections will specifically deal with theoretical backgrounds of direct interest to the PIENU experiment.

2.1 The standard model of particle physics

2.1.1 A brief introduction

The current formulation of the standard model of elementary particle physics dates back to the 1960s. The experimental observation of “partons” at SLAC [28, 29] which were later associated with the predicted quarks [30, 31] was quickly followed by the “November revolution” of 1974 with the simultaneous discovery of the charm quark at SLAC and BNL. The third generation of leptons and quarks was discovered in the following years.

The SM describes matter as built on twelve fundamental fermions (six leptons and six quarks⁵) arranged in three generations as shown in Table 2.1.

⁵Quarks carry a colour quantum number. Each quark can “appear” in one of the three colour charges: {r,b,g}. If colour is taken into account, we should number 6 quarks per generation and therefore a total of 24 fundamental fermions.

2.1. The standard model of particle physics

Table 2.1: Matter particle content of the standard model.

Particles	Generation	Charge ($Q/ e $)
Leptons	e μ τ	-1
	ν_e ν_μ ν_τ	0
Quarks	u c t	+2/3
	d s b	-1/3

The interactions between the particles are mediated by so-called gauge bosons and the strength of the interaction is given by the gauge couplings associated with each field. These couplings are part of the 19 free parameters in the SM, including masses, mixing angles, etc., which have to be⁶ determined experimentally.

Table 2.2 shows the interactions described by the SM together with their mediators and their respective strengths. Although gravity is not described by the SM it has been added to the interaction table for completeness.

Table 2.2: The four fundamental interactions

	Theories	Interactions	Mediators	Strength ⁷
SM	QCD $SU(3)_C$	Strong	gluon, g	$g^2 \approx 1$
	Electroweak	Electromagnetic	photon, γ	$\alpha \approx 10^{-2}$
	$SU(2)_L^W \times U(1)^W$	Weak	W^\pm, Z^0	$G_{\text{Fermi}} \approx 10^{-5}$
		Gravity		$G_{\text{Newton}} \approx 10^{-39}$

The SM is based on invariance under local gauge transformations; a requirement that ensures the “renormalizability” of the theory. Renormalization refers to the process in which logarithmically divergent terms arising from the interaction involving virtual particles that contribute to the physically measured quantities (like charge or mass) are absorbed in the definition of those physical quantities. In practice, one can introduce a cut-off energy which ensures the convergence of the integrals. If the cut-off energy is well

⁶Two parameters which remain to be experimentally determined are associated with the Higgs field.

⁷For gravity and the weak force, a mass must be introduced to give a dimensionless quantity for the strength of the force. In this table, the proton mass is used.

chosen and the underlying theory is renormalizable, the divergences inherent to the perturbation expansion have no physical consequences [32].

The underlying symmetry of the strong interaction is described by the non-Abelian $SU(3)_C$ group which is the transformation group of the quarks. The standard electroweak model based on $SU(2)_L^W \times U(1)^W$ symmetry is a unification of the electromagnetic ($U(1)$ symmetry) and the weak interaction ($SU(2)$ symmetry). Unlike the massless photon of QED, the mediators of the weak interaction have a mass. The introduction of the weak mediators' mass into the SM is done by the Higgs mechanism which spontaneously breaks the $SU(2)_L^W \times U(1)^W$ symmetry leading to three massive vector bosons (W^\pm , Z^0) and one massive scalar boson (the Higgs) while keeping $U(1)$ symmetry intact and therefore retaining the “masslessness” of the photon. In the SM, all fundamental fermions acquire a mass through coupling with the Higgs boson. These masses are the product of the Higgs vacuum expectation value ($v = (\sqrt{2}G_{Fermi})^{-1/2} \approx 246$ GeV) and the Yukawa coupling constants associated with each fermion.

2.1.2 Symmetries in the SM

As has become clear from the previous paragraph, our understanding and description of physical phenomena is governed by symmetries described by mathematical groups. Through Noether's theorem, every continuous symmetry is associated with a conserved quantity. There also exist discrete symmetries like Parity (P), Charge conjugation (C) and Time reversal (T). Some interactions conserve those symmetries or combinations of those symmetries and others break them partially or maximally. However, the combination of those three discrete symmetries (called CPT symmetry) must be conserved. This is a cornerstone of our current understanding of physics. Lorentz invariance which describes continuous space-time symmetry and CPT symmetry are connected via the CPT theorem [33–35] which proves that any quantum field theory is symmetric under the CPT transformation if it respects Lorentz invariance, locality and unitarity (i.e. conservation of probability). To complete our short description of symmetries, we should note that there exist in the SM so-called “accidental symmetries”. Those are symmetries arising in the model because the dimension of the terms which would break them is too high to appear in the Lagrangian. Baryon and lepton numbers as well as lepton flavour are examples of such accidental symmetries in the SM.

Quark flavour is not conserved in the SM. Indeed, the weak interaction is responsible for an intergenerational mixing in the quark sector which is

2.1. The standard model of particle physics

characterized by the Cabbibo-Kobayashi-Maskawa (CKM) matrix, V_{CKM} , named after the initials of the physicists whose work led to the establishment of this phenomenon [36, 37]. In particular, Kobayashi and Maskawa were awarded the Nobel Prize in 2008 for this discovery.

The CKM matrix is defined as follows:

$$\begin{pmatrix} d' \\ s' \\ b' \end{pmatrix} = V_{CKM} \begin{pmatrix} d \\ s \\ b \end{pmatrix} = \begin{pmatrix} V_{ud} & V_{us} & V_{ub} \\ V_{cd} & V_{cs} & V_{cb} \\ V_{td} & V_{ts} & V_{tb} \end{pmatrix} \begin{pmatrix} d \\ s \\ b \end{pmatrix} \quad (2.1)$$

where (d', s', b') are the quark weak eigenstates and (d, s, b) their mass eigenstates. Each of the components of the V_{CKM} have been determined experimentally. The latest results give the following absolute values of the CKM matrix parameters [22]:

$$V_{CKM} = \begin{pmatrix} 0.97425 \pm 0.00022 & 0.2252 \pm 0.0009 & 0.00389 \pm 0.00044 \\ 0.230 \pm 0.011 & 1.023 \pm 0.036 & 0.0406 \pm 0.0013 \\ 0.0084 \pm 0.0006 & 0.0387 \pm 0.0021 & 0.88 \pm 0.07 \end{pmatrix} \quad (2.2)$$

Those values are consistent with an unitary matrix in conformity with the SM.

Detailed description of the theoretical structure of the SM can be found in many references, for example [38]. Examples of more introductory text books are [39–41].

2.1.3 Successes and flaws of the SM

The SM has proved to be very successful in explaining and predicting nature's behaviour. A particular milestone of its success was the correct prediction of the W and Z boson's mass 10 years before their direct observation in 1983 at the CERN $p\bar{p}$ collider. Since then, the SM's predictive power has been tested to great precision and no clear indications of discrepancies between the data and the model have been observed so far [42]. However an important fundament of the theory, namely the Higgs field that provides mass to fermions and massive gauge particles has not been fully validated yet. The Higgs particle remains to be observed at colliders, but the phase space available for its discovery has shrunk considerably over the last few years. The lower limit on the SM Higgs mass is $m_H > 114.4$ GeV from direct searches at LEP-2 [43]. An upper limit can be extracted from precision measurements of electroweak observables. If a top quark mass of 173.1 ± 1.3 GeV [44] and a W^\pm boson mass of 80.399 ± 0.023 GeV [45] is used

2.1. The standard model of particle physics

together with the lower bound from LEP, an upper limit of $m_H < 186$ GeV at 95% confidence level (C.L.) is obtained [46, 47]. New direct results are also available from the Tevatron. The latest combined $D\bar{O}$ and CDF result excluded the region $158 < m_H < 173$ GeV/ c^2 at the 95% C.L. [48]. New direct limits from the ATLAS and CMS experiments at the LHC exclude the regions $127 < m_H < 600$ GeV/ c^2 at the 95 % confidence level [49, 50]. Those results leave only small mass windows for the SM Higgs and the LHC will soon have covered them. But even if the Higgs boson is found at the LHC, there are intrinsic problems arising from the fact that the Higgs is a scalar particle. Indeed, loop corrections to the Higgs mass squared are quadratic in the cut-off scale Λ (scale at which the SM breaks down) which leads to huge corrections to the Higgs mass [51]. Explaining a light Higgs would either require fine-tuned cancellations to these corrections or a Λ around the TeV scale. The last option would imply new physics at energies very close to those probed until now but with seemingly no effect on the processes taking place at those energies which is sometimes referred to as the “LEP Paradox” [52].

Beyond the Higgs sector, there are a number of open questions in particle physics that are left unanswered by the SM. We cite some of them here:

- Although there are clear indications from oscillation experiments that neutrinos have mass, the mass generation mechanism is currently not included in the SM. Several mass generation mechanisms are possible. A more detailed discussion on neutrinos in the SM and its extensions is in §2.4.1.
- The 12 elementary particles of the SM are not the constituents of dark matter which, according to astronomical observations, accounts for almost 1/4 of the universe’s content. In comparison, the amount of known matter in the universe (the matter described by the SM) is less than 5% [53].
- According to the CPT theorem mentioned previously, matter and antimatter have exactly the same or opposite properties. This implies that matter and anti-matter should have been created (and be present) in the same proportions. From observations however, there is so far no evidence for large concentrations of antimatter anywhere in the Universe. Sakharov has pointed out in 1967 [54] that an asymmetry could be generated under the three following conditions: baryon number violation, C and CP symmetry violation and interactions outside of thermal equilibrium. These conditions provide an explanation in

2.1. The standard model of particle physics

principle for the observed asymmetry, but it is unclear if they can be related to anything measurable. For example, the current level of CP violation in the SM is too small to account for the observed asymmetry. Not only does this show the limitation of our understanding of matter genesis, but it also highlights the apparent “unnatural” suppression of CP violation in the SM. It is indeed puzzling to see that CP phases in all sectors of the SM are always largely suppressed. In the weak sector, the amplitudes of CP violating effects parametrized in the CKM are relatively small while the neutrinos θ_{13} angle which would characterize the amplitude of CP violation in the leptonic sector has not been measured yet to be different from zero⁸. In the strong sector, the experimental upper bound on the electric-dipole moment of the neutron implies that the QCD CP violating parameter is very small, if not zero⁹.

All in all, the SM has been a very successful way of describing nature, but it is certainly incomplete as have been shown by the experimental facts mentioned above.

From a phenomenological point of view, the current arrangement of particles and forces is also rather unsatisfactory. Why are there four forces with notably different strengths (see Table 2.2)? Why should there be so many free parameters in the model? What underlies the arrangement in three generations? Those questions suggest the existence of deeper symmetries. Indeed, the fact that leptons and quarks are point-like particles which can both be arranged in three generations, are indistinguishable under the electroweak force and that the charge of the quarks are an exact divider of the leptons’s charge, point to the fact that QCD and the Electroweak theories could be unified (in the same manner that QED and the weak force are unified under the Electroweak theory) under a larger symmetry which would contain $SU(2) \times SU(1)$ and $SU(3)_C$ as sub-groups. This is the idea behind grand-unified-theories (also known under the acronym GUT). The natural next step would be the inclusion of a quantum mechanical model of gravity into an “universal” quantum field theory which could be the first step to a “Theory Of Everything”.

In this section, we have briefly summarized the current theoretical status of the Standard Model of Particle Physics and some of the questions which re-

⁸The current best experimental limit is from the double-CHOOZ reactor experiment [55]: $\sin^2(2\theta_{13}) < 0.16$ at the 90% confidence level (C.L.). However, the combined T2K [56] and double-CHOOZ result excludes $\sin^2(2\theta_{13}) = 0$ at the 3σ C.L.

⁹The smallness of θ_{QCD} constitutes a puzzle known as “the strong CP problem.”

main unanswered. We will discuss in §2.4, how the measurement of the pion branching ratio can bring some insights to part of those questions by setting limits on “New Physics” scenarios or revealing new types of interactions not accounted for in the SM.

2.2 V-A theory

After the brief excursion into the SM, this section will focus on the weak interaction which is of direct interest to the study of pion decay. For this purpose we will go back in the historical development of the theory at the time when Sudarshan and Marshak proposed the V-A theory of weak interaction.

The development of the V-A theory started with Fermi’s model of β -decay based on the analogy with electromagnetism. The matrix element for the weak process was written as the product of a baryonic and a leptonic current, where the currents were products of the particles’ wavefunctions (Ψ) with 4-vector operators (\mathcal{O}).

$$\mathcal{M} = G\mathcal{J}_{baryon}\mathcal{J}_{lepton} = G(\bar{\Psi}_b\mathcal{O}\Psi_b)(\bar{\Psi}_l\mathcal{O}\Psi_l) \quad (2.3)$$

From relativistic invariance, the operator can in principle be vector (V), axial-vector (A), scalar (S), pseudoscalar (P) or tensor (T). After the discovery of parity violation, it became clear that there must be two types of operators with opposite parity at play. It was also observed that leptons and anti-leptons in weak decays had opposite helicity states which discarded the S, P and T operators. The general form of the weak operator was therefore reduced down to:

$$\mathcal{O} = \frac{1}{2}\gamma_\mu(C_V + \gamma_5 C_A) \quad (2.4)$$

where the γ matrices are the 4×4 Dirac matrices and C_A and C_V are constant coefficients. The additional observation that neutrinos are produced in pure helicity states leads to $C_A = -C_V$ and therefore to the so-called universal weak operator:

$$\mathcal{O} = \frac{1}{2}\gamma_\mu(1 - \gamma_5) \quad (2.5)$$

The vector and axial-vector components of the operator have the same magnitude but are opposite in sign which leads to maximal parity violation in weak decays and is the reason for the “V-A” naming of the theory.

2.2.1 Pion decay rate

The pion is the lightest hadron¹⁰ so it can only decay weakly to lighter leptons: the muon or the electron (with their associated neutrinos).

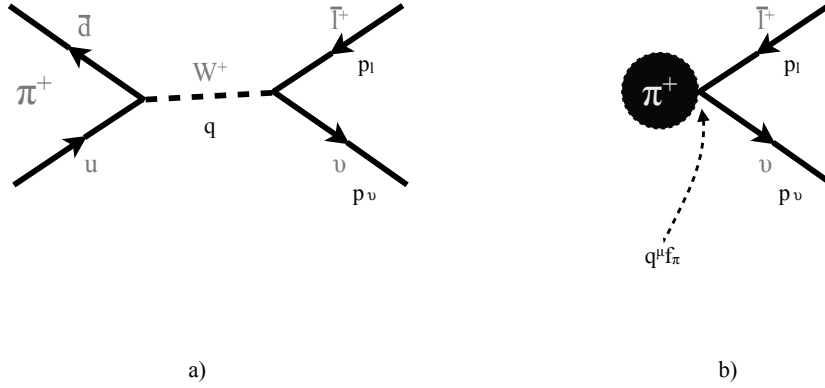


Figure 2.1: a) Standard model description of pion decay. b) Point-like interpretation of the same decay.

The differential decay rate for $\pi^+ \rightarrow l^+ \nu_l$ (where $l = e$ or μ) can be written as:

$$d\Gamma = \frac{1}{2m_\pi} |\mathcal{M}|^2 \frac{1}{E_l E_\nu} \frac{d^3 p_l}{(2\pi)^3} \frac{d^3 p_\nu}{(2\pi)^3} (2\pi)^4 \delta^4(q - p_l - p_\nu) \quad (2.6)$$

where m_π is the mass of pion and q , p_l and p_ν are the four-momenta indicated in Fig.2.1. The matrix element \mathcal{M} is the product of the propagator and the leptonic and hadronic currents.

$$\mathcal{M} = \frac{ig^{\mu\nu}}{M_W^2 - q^2} \mathcal{J}_{\mu\pi} \mathcal{J}_{l\nu} \quad (2.7)$$

However, in our case, the momentum transfer is small compared to the mass of the W boson so that the momentum transfer q in the propagator's

¹⁰The neutral pion is slightly lighter than the charged pions so the decay $\pi^\pm \rightarrow \pi^0 e^\pm \nu$ is allowed but has a branching ratio of 10^{-8} , see Table 2.4 .

2.2. V-A theory

denominator can be neglected leading to eq.2.8. Doing this is equivalent to assuming a Fermi point-like interaction as shown in Fig.2.1 b).

$$\mathcal{M} = \frac{iG}{\sqrt{2}} \mathcal{J}_\pi \mathcal{J}_l = \frac{iG}{\sqrt{2}} \langle 0 | V - A | \pi \rangle \bar{u}(p_l) \gamma_\mu (1 - \gamma_5) v(p_\nu) \quad (2.8)$$

where G is the Fermi coupling constant mentioned in Table 2.2. It is related to the W-lepton coupling constants g_l by:

$$\frac{G}{\sqrt{2}} = \frac{g_l^2}{8M_W^2} \quad (2.9)$$

Since the first part of the matrix element in eq.2.8 connects the pseudoscalar pion to the scalar vacuum, the vector part of the weak operator vanishes to give:

$$\mathcal{M} = \frac{iG}{\sqrt{2}} \langle 0 | A | \pi \rangle \bar{u}(p_l) \gamma_\mu (1 - \gamma_5) v(p_\nu) \quad (2.10)$$

The term $\langle 0 | A | \pi \rangle$ cannot be described in terms of quark currents since the quarks are bound inside the pion by the strong force. We know however that this term should be a Lorentz 4-vector and the only 4-vector available is the momentum transfer q . We therefore write:

$$\langle 0 | A | \pi \rangle = i f_\pi q^\mu \quad (2.11)$$

$$\mathcal{M} = \frac{iG}{\sqrt{2}} f_\pi q^\mu \bar{u}(p_l) \gamma_\mu (1 - \gamma_5) v(p_\nu) \quad (2.12)$$

where f_π is a constant which parametrizes the hadronic interaction.

After squaring of the matrix element and summation over the final spin states (the detection of the decay lepton is insensitive to the spin state), we get:

$$|\mathcal{M}|^2 = 4G^2 f_\pi^2 m_l^2 p_l p_\nu \quad (2.13)$$

This last expression can then be incorporated in Eq.2.6. After integration over the energy, we get an expression for the decay rate

$$\Gamma_{\pi \rightarrow l + \nu_l} = G^2 \frac{m_\pi f_\pi^2 m_l^2}{8\pi} \left(1 - \frac{m_l^2}{m_\pi^2}\right)^2 \quad (2.14)$$

This decay rate is a function of the pion's form factor f_π which is theoretically not well-known. However, if one measures the ratio of pion decay into muon and positron, this term cancels out at the first order to give:

$$R_0^\pi = \frac{\Gamma_{\pi \rightarrow e + \nu_e}}{\Gamma_{\pi \rightarrow \mu + \nu_\mu}} = \frac{m_e^2}{m_\mu^2} \left(\frac{m_\pi^2 - m_e^2}{m_\pi^2 - m_\mu^2} \right)^2 \quad (2.15)$$

which is simply a ratio of masses.

2.2.2 Helicity suppression

If we substitute the masses in eq.2.15 with their latest PDG values, we get [57]:

$$R_0^\pi = 1.28336(2) \times 10^{-4} \quad (2.16)$$

where the error reflects the uncertainty on the masses. R_0^π is a small number because of the muon's larger mass in the factorized term m_e^2/m_μ^2 in eq.2.15. However, at first sight it is a surprising result since from phase-space considerations the electronic decay should be favoured over the muonic one. This result is in fact a direct consequence of the $\frac{1}{2}(1 - \gamma_5)$ term discussed at the beginning of this section (see eq.2.5). This term selects the left-handed component of massless particles and right-handed components of massless anti-particles. In the case of $\pi^+ \rightarrow e^+\nu_e$ decay, the electronic neutrino ν_e (assumed to be massless) must be left-handed which means that the direction of its momentum and spin must be anti-parallel. Since the pion has spin 0, from angular-momentum conservation, the positron must be left-handed as well, as illustrated in Fig.2.2. Since the positron is not exactly massless the decay is allowed but is "helicity suppressed" by a factor inversely proportional to its mass. For the muon, the same argument applies but since its mass is 200 times larger than the positron mass, the suppression is much smaller and therefore the $\pi^+ \rightarrow \mu^+\nu_\mu$ decay is favoured over the $\pi^+ \rightarrow e^+\nu_e$ decay.



Figure 2.2: Schematic illustration of the helicity suppressed $\pi^+ \rightarrow e^+\nu_e$ decay.

2.2.3 Lepton universality

It is important here to comment on the step between eq.2.8 and eq.2.10. There we have assumed a point-like Fermi interaction and included the W-lepton coupling inside the Fermi coupling constant. This is valid until eq.2.14

2.2. V-A theory

but as soon as the branching ratio is calculated another assumption has to be made to write eq.2.15. Namely, that the electron and muon couplings to the W^+ boson are the same. This assumption is actually embedded in the SM under the name “lepton universality”. This property of the SM states that the coupling between leptons and gauge bosons is the same for all charged leptons. It is a strong cornerstone of the theory since a “genuine” deviation from universality would require new interactions in order to generate new coupling constants for each charged lepton. Also, these couplings would have to be “tuned” to agree with the experimentally measured ratio of couplings which is to-date consistent with 1. However, new physics could also reveal itself through an “apparent” deviation from universality if the branching ratio is considered as

$$R_{exp}^{\pi} = \left(\frac{g_e}{g_{\mu}}\right)^2 R_{SM}^{\pi} \quad (2.17)$$

where g_e and g_{μ} are respectively the coupling of the W^+ boson to the electron and muon. We will discuss the effect of “New Physics” on the branching ratio in more detail in §2.4.

The universality of the charged lepton’s couplings to the W bosons has been tested in many decays. Table 2.3 presents the current experimental status.

Despite the much larger uncertainty in the τ mass compared to the μ and π masses, the BABAR experiment at SLAC has improved the precision of $\mu - e$ universality test through the measurement of the $\tau^- \rightarrow \mu^- \bar{\nu}_{\mu} \nu_{\tau} / \tau^- \rightarrow e^- \bar{\nu}_e \nu_{\tau}$ branching ratio. However, it is followed closely by the average of the last pion branching ratio experiments which should be improved by at least a factor 5 when the final results from both PIENU and PEN experiments become available.

It also worth mentioning that the τ and π decay experiments are testing different parts of the weak interaction. Indeed, we discussed previously that the pion being a pseudoscalar particle, its decay is only sensitive to the axial part of the V-A interaction while the tau is sensitive to both vector and axial parts. Therefore the two experiments are complementary for a comprehensive test of lepton universality.

To quantify the current bounds, the couplings to the W boson can be assumed to be flavour dependent with ϵ quantifying the deviation from the universal coupling constant [62].

$$\mathcal{L} = \sum_{l=e,\mu,\tau} \frac{g_l}{\sqrt{2}} W_{\mu}^{+} \bar{\nu}_l \gamma^{\mu} \left(\frac{1 - \gamma_5}{2}\right) l^{-} + h.c. \quad (2.18)$$

2.2. V-A theory

Table 2.3: Experimental results on lepton universality tests (unless otherwise stated, numbers are taken from [58]).

Decay mode	$(g_\mu/g_e)^2$
$\mathcal{B}_{\tau \rightarrow \mu}/\mathcal{B}_{\tau \rightarrow e}$	1.0018 ± 0.0014^a [59]
$\mathcal{B}_{\pi \rightarrow \mu}/\mathcal{B}_{\pi \rightarrow e}$	1.0021 ± 0.0016^b
$\mathcal{B}_{K \rightarrow \mu}/\mathcal{B}_{K \rightarrow e}$	0.996 ± 0.005^c [60]
$\mathcal{B}_{K \rightarrow \pi \mu}/\mathcal{B}_{K \rightarrow \pi e}$	1.002 ± 0.002
$\mathcal{B}_{W \rightarrow \mu}/\mathcal{B}_{W \rightarrow e}$	0.997 ± 0.010
	$(g_\tau/g_\mu)^2$
$\mathcal{B}_{\tau \rightarrow e} \tau_\mu/\tau_\tau$	1.0006 ± 0.0022
$\Gamma_{\tau \rightarrow \pi}/\Gamma_{\pi \rightarrow \mu}$	0.9909 ± 0.0038^a
$\Gamma_{\tau \rightarrow K}/\Gamma_{K \rightarrow \mu}$	0.9813 ± 0.0095^a
$\mathcal{B}_{W \rightarrow \tau}/\mathcal{B}_{W \rightarrow \mu}$	1.039 ± 0.013
	$(g_\tau/g_e)^2$
$\mathcal{B}_{\tau \rightarrow \mu} \tau_\mu/\tau_\tau$	1.0005 ± 0.0023
$\mathcal{B}_{W \rightarrow \tau}/\mathcal{B}_{W \rightarrow e}$	1.036 ± 0.014

^a includes last results from BABAR: respectively $(g_\mu/g_e)^2 = 1.0036 \pm 00020$, $(g_\tau/g_\mu)_{\tau \rightarrow \pi}^2 = 0.9859 \pm 0057$, $(g_\tau/g_\mu)_{\tau \rightarrow K}^2 = 0.9836 \pm 0087$ [61].

^b This is based on the average of the three last pion branching ratio measurements.

^c This is based on the last NA62 result [60].

$$g_l = g(1 - \frac{\epsilon_l}{2}) \quad (2.19)$$

A global fit on available data can then be performed to extract the constraint on ϵ . The result of the fit is shown in Fig.2.3. The results from the PIENU and PEN experiments are expected to greatly improve those bounds.

Neutral current lepton universality has also been tested in the measurements of the partial decay width of the Z boson to pairs of leptons in experiments at LEP and SLAC. In this case, the neutral current is:

$$\mathcal{J}_{NC}^\mu = -\frac{ig}{\cos \theta_W} \bar{l} \gamma^\mu \left(\frac{v_l - a_l \gamma^5}{2} \right) l \quad (2.20)$$

where l denotes decay leptons. Universality in the neutral sector is tested by extracting v_l and a_l for each lepton generation.

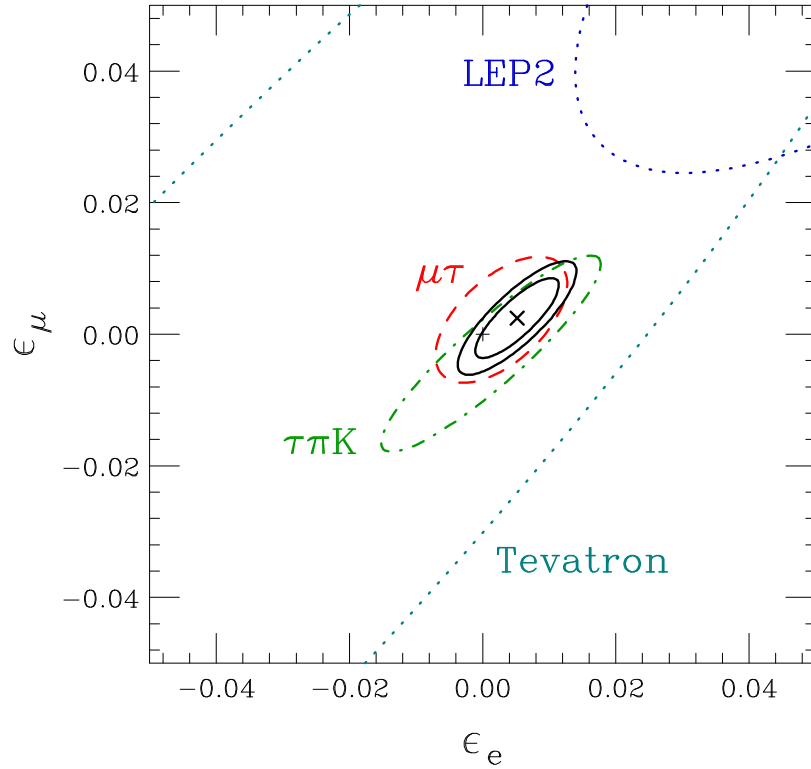


Figure 2.3: Experimental bounds as of 2008 on g_e and g_μ deviation from universality [62]. The green dotted and dashed line shows the constraint from the measurement of τ , K and π branching ratio. The red dashed line indicates the constraints from τ and μ lifetime measurements. The Tevatron (based on partial results from CDF and $D\bar{O}$ experiments) and LEP2 bounds show constraints from W decay measurements.

2.2. V-A theory

A very complete (but slightly outdated in terms of experimental results) theoretical review of lepton universality in the neutral and charged weak interaction can be found in [63].

To conclude this section, it should be noted that due to the difference in the mass and weak eigenstates in the quark sector, the physical coupling of quarks to the W boson is modified by the CKM parameters mentioned in §2.1.2. Therefore a V_{ud} term must enter in the pion decay rate formula. In eq.2.14 it is absorbed in the definition of f_π . The definition can be changed to extract the CKM term:

$$\Gamma_{\pi \rightarrow l + \nu_l} = G^2 \frac{m_\pi f_\pi^2 |V_{ud}|^2 m_l^2}{8\pi} \left(1 - \frac{m_l^2}{m_\pi^2}\right)^2 \quad (2.21)$$

However this term vanishes in the ratio R_0^π which is the reason why the pion branching ratio is one of the few electroweak observables that involve hadrons and yet is precisely calculable. Indeed, the QCD effects like f_π or lepton flavor independent QCD radiative corrections that could bring large theoretical uncertainties cancel in the ratio. We will discuss in detail in §2.3 the corrections which contribute to the theoretical uncertainties at higher orders.

2.2.4 Review of pion and muon decay modes

The pion has a lifetime of 26.033 ± 0.005 ns [22] and decays most often into a muon and a neutrino. The decay to a positron and a neutrino has a similar branching ratio as the pion's radiative decay to muon as shown in Table 2.4. The muon decays with a lifetime of 2.197034 ± 0.000021 μ s [22] into three modes listed in Table 2.5.

Every decay whose branching ratio is smaller than 10^{-7} can be ignored at our level of precision. This is the case of the three last decays listed in Table 2.4¹¹. However, the PIENU calorimeter is sensitive to photons and from Table 2.4 and 2.5, it can be seen that radiative processes in both muon and pion decays have a relatively large branching ratio and must therefore be taken into account in the calculation of the branching ratio. A detailed discussion of the radiative corrections to R_0^π follows in the next section.

¹¹The decay $\pi^+ \rightarrow e^+ \nu_e \bar{\nu} \nu$ has a SM branching ratio of 10^{-16} which is totally negligible at our level of precision.

2.3. Radiative corrections

Table 2.4: Measured pion decay modes [22].

Decay mode	Fraction (Γ_i/Γ)
$\pi^+ \rightarrow \mu^+ \nu_\mu$	$(99.98770 \pm 0.00004)\%$
$\pi^+ \rightarrow \mu^+ \nu_\mu \gamma^a$	$(2.00 \pm 0.25) \times 10^{-4}$
$\pi^+ \rightarrow e^+ \nu_e$	$(1.230 \pm 0.004) \times 10^{-4}$
$\pi^+ \rightarrow e^+ \nu_e \gamma^b$	$(7.39 \pm 0.05) \times 10^{-7}$
$\pi^+ \rightarrow e^+ \nu_e \pi^0$	$(1.036 \pm 0.006) \times 10^{-8}$
$\pi^+ \rightarrow e^+ \nu_e e^+ e^-$	$(3.2 \pm 0.5) \times 10^{-9}$
$\pi^+ \rightarrow e^+ \nu_e \nu \bar{\nu}$	$< 5 \times 10^{-6}$

^a with a γ cut-off energy: $E_\gamma > 1$ MeV

^b $E_\gamma > 10$ MeV

Table 2.5: Measured Muon decay modes [22].

Decay mode	Fraction (Γ_i/Γ)
$\mu^+ \rightarrow e^+ \nu_e \bar{\nu}_\mu$	$\approx 100\%$
$\mu^+ \rightarrow e^+ \nu_e \bar{\nu}_\mu \gamma^a$	$(1.4 \pm 0.4)\%$
$\mu^+ \rightarrow e^+ \nu_e \bar{\nu}_\mu e^+ e^-$	$(3.4 \pm 0.4) \times 10^{-5}$

^a with a γ cut-off energy: $E_\gamma > 10$ MeV

2.3 Radiative corrections

The observed branching ratio includes the effect of physical and virtual photons and therefore the knowledge of radiative corrections to the branching ratio is essential to being able to compare precisely the theoretical and experimental branching ratio.

The Feynman diagrams of the radiative corrections due to the emission of real photons are shown in Fig.2.4 a), those are referred as Inner Bremsstrahlung photons (IB γ). Another contribution comes from the emission and reabsorption of photons (ER γ) pictured in Fig.2.4 b). The contribution of IB γ and ER γ to the branching ratio has been calculated by Kinoshita [64] and Berman [65] assuming a point-like pion. They found that the rate was dependent on an infra-red cut-off for photons of very low energy which are emitted near the maximum electron energy. However, the amplitudes of

2.3. Radiative corrections

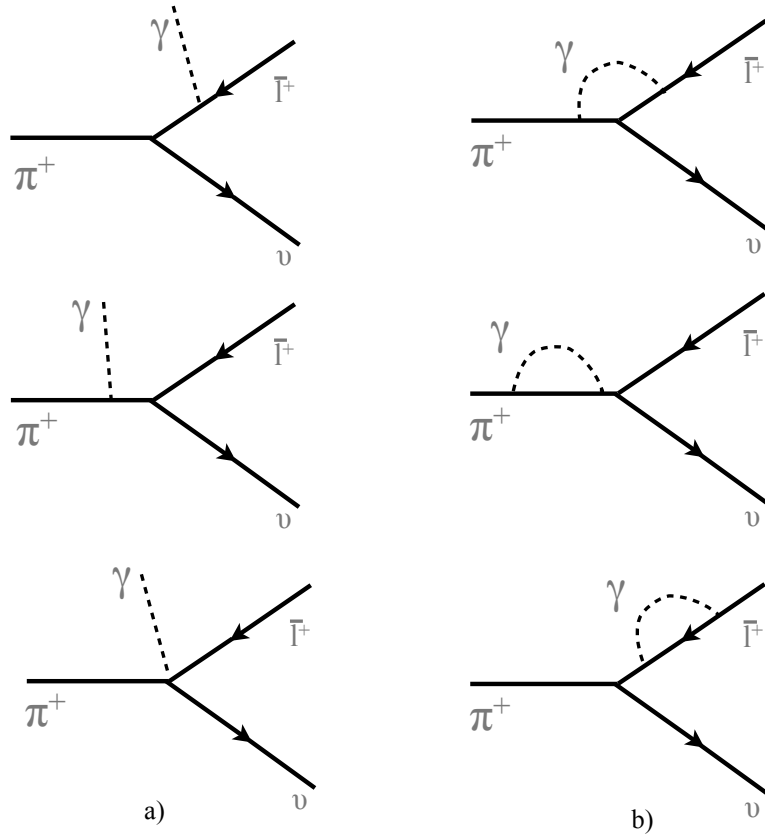


Figure 2.4: Feynman diagrams of radiative contributions to the branching ratio from: a) Inner Bremsstrahlung photons (IB γ). b) Emission and re-absorption of virtual photons (ER γ).

2.3. Radiative corrections

the infra-red divergences were equal and of opposite signs for $\text{IB}\gamma$ and $\text{ER}\gamma$ and therefore vanished in the sum. An ultra-violet cut-off Λ_{UV} also had to be introduced in the calculation of the contribution from $\text{ER}\gamma$. If Λ_{UV} is assumed to be equal for $\pi^+ \rightarrow e^+\nu_e$ and $\pi^+ \rightarrow \mu^+\nu_\mu$, then this divergence cancels out in the branching ratio. Finally, the branching ratio with the inclusion of $\text{IB}\gamma$ and $\text{ER}\gamma$ was found to be:

$$R^\pi = R_0^\pi \times (1 + \delta)(1 + \epsilon) \quad (2.22)$$

$$\text{with } \delta = -\frac{3\alpha}{\pi} \ln \frac{m_\mu}{m_e} \quad (2.23)$$

$$\text{and } \epsilon = -0.92 \frac{\alpha}{\pi} f \quad (2.24)$$

These calculations were subsequently checked and confirmed in the general framework of gauge theories, first by Goldman and Wilson [66] and then by Marciano and Sirlin [67] who expanded the total pion decay rate in a power series in m_l and $\ln m_l$ (with $l = e$ or μ) and proved that the dominant m_l dependent term (which therefore does not cancel in the branching ratio) has a coefficient which is not affected by the strong interaction. They first computed the contribution from $\text{ER}\gamma$ to the leading $\ln m_l$ term including the structure dependent $\text{ER}\gamma$ correction (its amplitude is labeled A_{SD-ER} in Fig.2.5). They found out that the $\text{ER}\gamma$ term is exactly cancelled by the contribution from the interference term A_{I-IB} between the structure dependent (A_{SD-IB}) and ordinary (A_{IB}) $\text{IB}\gamma$. After adding the contribution from ordinary $\text{IB}\gamma$ depicted in Fig.2.4 a) they obtained an expression for the dominant m_l dependent correction term to the branching ratio and showed that it is independent of strong interaction effects and can therefore be rigorously computed. Their computation agreed with Kinoshita's term in eq.2.23 that led to a correction of -3.929% to R_0^π [57].

Following the general parametrization of the hadronic effects in [69] corrections to R^π can be written as the following series of terms [57]:

$$R^\pi = R_0^\pi \times \left[1 + \frac{\alpha}{\pi} \left\{ F\left(\frac{m_e}{m_\pi}\right) - F\left(\frac{m_\mu}{m_\pi}\right) + \frac{m_\mu^2}{m_\rho^2} (c_2 \ln \frac{m_\rho^2}{m_\mu^2} + c_3) + c_4 \frac{m_\pi^6}{m_e^2 m_\rho^4} \right\} + c_5 \left(\frac{\alpha}{\pi} \ln \frac{m_\mu}{m_e} \right)^2 + \dots \right] \quad (2.25)$$

where $F(x)$ is a rather convoluted function that can be found in eq.7b of [69]. $m_\rho = 0.768$ GeV is the mass of the ρ particle chosen as a cut-off value

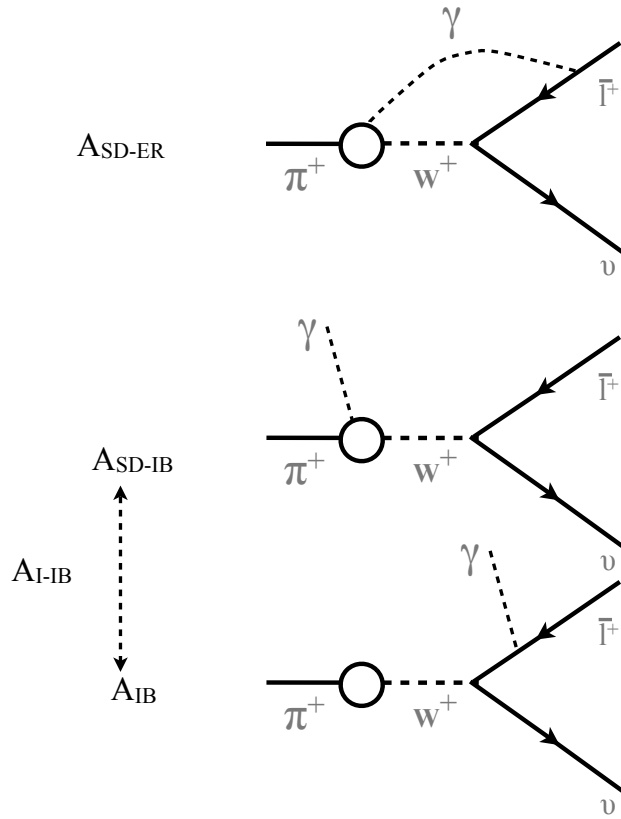


Figure 2.5: Additional Feynman diagrams which contribute to the leading order QED correction to the branching ratio. A_{SD-ER} represents the amplitude of the structure dependent virtual correction and A_{I-IB} is the amplitude of the interference between the structure dependent and structure independent Inner-Bremmstrahlung corrections [68].

2.3. Radiative corrections

at which the long and short distance parts of the radiative corrections are matched.

The term:

$$\frac{\alpha}{\pi} \left\{ F\left(\frac{m_e}{m_\pi}\right) - F\left(\frac{m_\mu}{m_\pi}\right) \right\} \quad (2.26)$$

corresponds to Kinoshita's and Marciano and Sirlin's dominant correction mentioned above which are the first order QED corrections to the decay of a pointlike pion.

There are three other corrections of order $\mathcal{O}(\alpha)$. The terms proportional to m_l^2 are only significant for the muon decay mode because of helicity suppression. The leading structure dependent virtual term (arising through the first diagram in Fig.2.5) is proportional to c_2 which was first calculated by Terent'ev [70] and later confirmed by Marciano and Sirlin in [69] to be:

$$c_2 = 3 + \frac{2}{3} \left(1 - \frac{7}{4}\gamma_1\right) \left(\frac{m_\rho^2}{4\pi^2 f_\pi^2}\right) \simeq 3.1 \quad (2.27)$$

where γ_1 ¹² is the ratio of the axial and vector form factors in radiative pion decay. The model dependent c_3 term has been recently calculated by Cirigliano and Rosel [71, 72] using Chiral Perturbation theory which provides an expansion of the correction amplitudes in terms of the lepton and meson masses and the electromagnetic coupling e . The authors made a full calculation of the electromagnetic corrections down to $\mathcal{O}(e^2 p^4)$ with the following chiral power counting:

$$R^\pi = R_0^\pi \times (1 + \Delta_{e^2 p^2} + \Delta_{e^2 p^4} + \Delta_{e^2 p^6} + \dots) \quad (2.28)$$

where the leading electromagnetic correction $\Delta_{e^2 p^2}$ corresponds to the pointlike pion approximation. The model dependent c_3 term is part of the $\Delta_{e^2 p^4}$ term and was calculated using a matching procedure. The c_3 term led to a small correction in the branching ratio of -0.004(11)% which however represents the leading uncertainty in the calculation. The result of their full calculation is summarized in Table 2.6.

Going back to eq.2.25, the last $\mathcal{O}(\alpha)$ term is the contribution from the pure structure dependent bremsstrahlung (A_{SD-IB} in Fig.2.5) which is unlike the other corrections, not helicity suppressed and therefore potentially large for the electronic decay. This term (which is $\mathcal{O}(e^2 p^6)$ in the chiral power counting) has been calculated to amount to a +0.073% correction¹³ to the branching ratio [72].

¹²The subscript is to avoid confusion with the photon.

¹³This calculation also relies on γ_1 mentioned above since both the vector and axial currents contribute to this amplitude.

2.4. Beyond the standard model

The next contributions are of order $\mathcal{O}(\alpha^2)$. The dominating correction is proportional to $(\ln(m_\mu/m_e))^2$ in analogy with the dominating correction of the order $\mathcal{O}(\alpha)$. This term (named Δ_{LL} in Table 2.6) was calculated in [21] to give a 0.054(10)% correction to the branching ratio.

Table 2.6: Summary of the electroweak corrections to R_0^π

Power counting	Corrections (%) from [72]
$\Delta_{e^2p^2}$	-3.929
$\Delta_{e^2p^4}$	0.053 ± 0.011
$\Delta_{e^2p^6}$	0.073
Δ_{LL}	0.054^a

^a The original correction in [72] is 0.055% but because of a shift in the pion's mass, it has become 0.054% [57].

An additional estimated uncertainty of $\pm 0.01\%$ [57] from the uncalculated two loops $\mathcal{O}(\alpha^2 \ln \frac{m_\mu}{m_e})$ can be added to the uncertainty list.

After including all those radiative and structure dependant corrections to the raw branching ratio and adding their respective uncertainties in quadrature, one finds the following value for the branching ratio [57]:

$$R^\pi = 1.2352(2) \times 10^{-4} \quad (2.29)$$

which is in agreement with the result from Cirigliano and Rosell : $R^\pi = 1.2352(1) \times 10^{-4}$. The latter authors quote a smaller uncertainty because they did not include the uncertainty from the uncalculated two loops term in their result.

As already stated, such a level of precision in a hadronic decay is possible because the strong interaction dynamics cancel out in the branching ratio and the structure dependence appears only through electroweak corrections. A deviation from this very precise result would be a definite sign of new physics. Potential new physics that could affect this result will be the subject of the next section.

2.4 Beyond the standard model

As briefly shown in §2.1.3, the SM has so far proved very successful in explaining experimental results but it is an incomplete theory. Several theories

predict that the effects of new physics should be present at the TeV scale which is the energy scale being probed at the new Large Hadron Collider. However, new physics that could be revealed at high energies could also be observed by high precision low energy electroweak experiments, like the PIENU experiment, which offer a complementary approach to the high energy frontier of colliders. Indeed, the effect from weak scale new physics, if translated in terms of a deviation from the pion branching ratio, is expected to be in the range $\Delta R_{e/\mu}^\pi/R_{e/\mu}^\pi \sim 10^{-4} - 10^{-2}$ [72]. Eq.2.29 shows that the theoretical calculations within the SM framework for the pion branching ratio has been pushed to the 10^{-4} precision. The final precision of the PIENU experiment is expected to be at the 10^{-3} level which will enable to probe part of the expected new physics phase-space.

The possible manifestations of new physics in the pion branching ratio are manifold. We will briefly expose them in the following sections.

2.4.1 Neutrinos

Neutrinos in the Standard Model

Neutrinos are the most common particles in the universe (aside from the unknown dark matter). They are a “special species” in the SM since they are the only particles that interact solely through weak interaction. This property led to a very early decoupling (around 1s after the Big Bang, i.e. temperature ~ 1 MeV) from the universe thermal bath leaving the neutrinos as mere observers of the later evolution of the universe while leaving a profound impact on it [73]. They are also the only fermions in the SM to be massless, which means that they exist in a single helicity state (ν_L and $\bar{\nu}_R$). This specificity has however been shown to be incorrect. Indeed, neutrinos were observed [74–76] to oscillate between different generations which implies the existence of at least two finite neutrino masses. A consequence is that the mass and weak eigenstates are distinct and can be related by a 3×3 matrix (called the U_{PMNS} matrix), which should be unitary if there exist only three types of neutrinos. The parameters of this matrix have been (and are currently being) measured by solar, accelerator and nuclear power plants neutrino oscillation experiments. The matrix has three mixing angles and a phase that, if non-zero, would be a source of CP violation. The amplitude of the oscillations are proportional to the mixing angles and the frequency of the oscillations to the difference of mass squared. Therefore, oscillation experiments are not sensitive to the absolute scale of the neutrino masses. However from direct measurement (endpoint measurement

of the β electron [77] or rate of neutrinoless double beta decay [78, 79]) it is known that the neutrino masses are very small, probably of the order of meV. Moreover, from cosmological constraints provided by the precise WMAP data combined with photometric red-shift survey [80] the sum of all neutrino masses should be less than 0.28 eV. This leads to the following questions: “What is the mechanism responsible for neutrino’s masses?” and “What extension of the SM is necessary to include those masses”. The answer to those questions is strongly linked to the nature of neutrinos: are they Majorana (the same as their antiparticle) or Dirac particles? If Dirac particles, a singlet right-handed neutrino state could be included to the SM and the neutrino masses would be generated by the coupling to the “standard Higgs”. However a mechanism would be needed to explain the suppression of the neutrino’s Yukawa couplings. If the neutrinos are Majorana-type, the smallness of the observed masses of the three types of neutrinos could be explained by the see-saw mechanism. The neutrino masses would be inversely proportional to right handed neutrino masses which would be similar to the scale where lepton number non-conservation occurs (the existence of Majorana neutrinos requires the violation of this SM conserved number): $m_{\nu_R} \sim m_{GUT} \sim 10^{14} - 10^{15}$ GeV.

In any case, extensions of the SM to include new flavour structures is required to account for neutrino oscillations. The next paragraph will briefly describe the sensitivity of the PIENU experiment to the existence of heavier neutrino types.

Massive neutrinos in $\pi^+ \rightarrow e^+ \nu_e$ decays

The PIENU experiment can be sensitive to the existence of massive neutrinos in two ways; either through universality test (i.e. massive neutrinos would affect the branching ratio due to a change in the phase space and because the equality of the weak interaction couplings to muon and positron is violated by neutrino mixing angles) or through a direct peak search in the $\pi^+ \rightarrow e^+ \nu_e$ spectrum. This latter option will be discussed in more detail in Chapter 8. However we can note here that from kinematics the $\pi^+ \rightarrow e^+ \nu_e$ decay is sensitive to massive neutrinos in the limited mass range $0 \text{ MeV}/c^2$ - $130 \text{ MeV}/c^2$ which is many orders of magnitude lower than the GUT scale neutrino mentioned above. However, the existence of electroweak scale heavy Majorana neutrinos is being foreseen by many extensions of the SM [81, 82]. Gelmini *et al.* [83] pointed out that bounds from precision experiments on the mixing of MeV scale sterile neutrinos with active neutrinos are much more stringent than cosmological bounds in particular cosmological scenarios. In the light

of the recent MiniBooNE oscillation result which seems to be inconsistent with the assumption of three generations of neutrinos [84] we should also note that the measurement of the $\pi^+ \rightarrow e^+ \nu_e$ branching ratio can, as well, set limits on the parameters of the PMNS matrix for a fourth generation of neutrinos [85].

Massive neutrinos in $\mu^+ \rightarrow e^+ \nu_e \bar{\nu}_\mu$ decays

A recent paper [86] claims that the puzzles from LSND, KARMEN and MiniBooNE experiments could be explained by the existence of a massive sterile neutrino with a mass in the range 40 to 80 MeV which would be in the PIENU detectable range. A search for such events in the data already collected is underway.

2.4.2 New pseudo-scalar interactions

If we go back to eq.2.8, the term $\langle 0 | V - A | \pi \rangle$ can in theory be replaced by $\langle 0 | \mathcal{O} | \pi \rangle$ where \mathcal{O} can be a scalar (S), pseudo-scalar (P), vector (V) or axial-vector (A) term. However, since the matrix element connects the pseudo-scalar pion to the scalar vacuum, there can only be A or P terms. A general relation for the pseudo-scalar current term would be [87]:

$$\langle 0 | \bar{u} \gamma^5 d | \pi \rangle = i\sqrt{2} f_{\pi_P} = i\sqrt{2} \frac{f_\pi m_\pi^2}{m_u + m_d} \quad (2.30)$$

with the pseudo-scalar four-fermi contact operator being:

$$\mathcal{L}_P = -i \frac{\rho}{2\Lambda^2} \left[\bar{l}(1 - \gamma^5) \nu_l \right] \left[\bar{u} \gamma^5 d \right] \quad (2.31)$$

where ρ is the pseudo-scalar coupling constant and Λ the mass scale of the new pseudo-scalar mediator. Using eq.2.30 we get the pseudo-scalar matrix element:

$$\mathcal{M}_P = \rho \frac{f_{\pi_P}}{\sqrt{2}\Lambda^2} \left[\bar{l}(1 - \gamma^5) \nu_l \right] \quad (2.32)$$

The overall matrix element would be the coherent sum of the new pseudo-scalar and the ‘‘familiar’’ axial term of eq.2.12. The largest contribution would come from the interference between those two terms which is proportional to $1/\Lambda^2$. Ignoring small contributions from $\pi \rightarrow \mu \nu_\mu$ decay in the presence of pseudo-scalar interactions and assuming a coupling similar to the weak coupling, the deviation of the new branching ratio from the SM

prediction can be parameterized as:

$$1 - \frac{R^{Exp}}{R^{SM}} \sim \pm \frac{\sqrt{2\pi}}{G} \frac{1}{\Lambda^2} \frac{m_\pi^2}{m_e(m_d + m_u)} \sim \left(\frac{1TeV}{\Lambda_{eP}}\right)^2 \times 10^3 \quad (2.33)$$

Considering the planned PIENU precision of 0.1%, the experiment could be potentially sensitive to pseudo-scalar mass scales Λ of up to 1000 TeV which is well beyond the reach of colliders. Of course, the energy probed is directly dependent on the couplings and on the actual mechanism that produces the pseudo-scalar current. We can consider several mediators of pseudo-scalar interactions [88]:

- Leptoquarks
- loop diagrams involving SUSY particles
- charged Higgs bosons

Leptoquarks

Leptoquarks (LQ) are hypothetical particles carrying both baryon and lepton number. They are natural in extensions of the SM that consider the similarities between leptons and quarks (see the discussion in §2.1.3) like the Pati-Salam model and grand unification theories based on SU(5) or SO(10) as well as some R-parity violation SUSY and technicolour models [89].

Leptoquark can be considered to couple to both left- and right-handed leptons (quarks) simultaneously. Such LQ states are called non-chiral while LQs which couple only to left- or right-handed quarks are called chiral leptoquarks. The current bound on non-chirally coupled LQs imposed by the $\pi^+ \rightarrow e^+ \nu_e$ decay is very strong. The bound on the mass (M_{LQ}^2) and the couplings (g_R and g_L) of the leptoquarks is indeed: $M_{LQ}^2/g_L g_R \geq (100TeV)^2$ [90]. Even if chiral coupling is required, pion decay can potentially still bring stringent constraints. For example, for scalar leptoquarks in a singlet representation, if one assumes a coupling similar to the strong coupling, the bound from the pion branching ratio is $M_{LQ}/g \geq 12$ TeV [91]. A complete listing of the bounds on scalar and vector leptoquark representations from the pion branching ratio can be found in [92]. In comparison, the latest results from the ATLAS and CMS experiments set a limit on first generation scalar leptoquarks masses of $M_{LQ} \sim 600$ GeV¹⁴ [93, 94].

¹⁴At the LHC, leptoquarks would be predominantly pair-produced with a cross section that depends on the strong coupling constant but is nearly independent of the leptoquark

SUSY particles

The contributions from R-parity conserving processes to the pion branching ratio tend either to be too small to be visible at the expected experimental uncertainties [95] or require “unnaturally” large splitting between the masses of the left-handed sleptons [96] making the pion branching ratio a non-favoured probe of the supersymmetric spectrum. However corrections from R-parity-violating (RPV) processes with violation of lepton number conservation ($\Delta L = 1$) would arise at the tree level and could therefore be detectable with the current foreseen precision or, if not detected, interesting new bounds for those processes could be achieved. Contribution to R_π from RPY interactions can be written as [96]:

$$\frac{\Delta R_\pi^{RPV}}{R_\pi^{SM}} = 2(\Delta'_{11k} - \Delta'_{21k}) \quad (2.34)$$

$$\Delta'_{i1k}(\tilde{f}) = \frac{\lambda'_{i1k}}{4\sqrt{2}Gm_{\tilde{f}}^2} \quad i = 1, 2 \quad (2.35)$$

where λ'_{11k} and λ'_{21k} are the coefficients of the RPY interaction for respectively the decay to an electron and the muonic decay. $m_{\tilde{f}}$ is the mass of the exchanged sfermion (\tilde{f}_k) and G is the Fermi constant. The values of λ'_{ijk} are constrained by existing electroweak precision experiments. The authors of [96] performed a fit on the result of those experiments and extracted the bounds on the $\Delta'_{1jk}(\tilde{f})$ shown in Fig.2.6. From this plot we can see that the current bound on those parameters, especially $\Delta'_{21jk}(\tilde{f})$ are not strong and can be substantially improved by the PIENU experiment. Indeed, with the foreseen PIENU experiment precision, a ΔR_π^{RPV} with a 5σ deviation from zero could be detected [96]. The detection of RPY interactions would have profound implications on neutrino physics and cosmology as it would induce Majorana mass terms for the neutrino [98] and would disfavour the lightest SUSY particle as a good dark matter candidate¹⁵.

couplings. This cross section depends on the mass of the leptoquark and has been calculated at the next-to-leading-order in QCD. Therefore, direct limits on leptoquark masses can be obtained.

¹⁵Although RPY means that the lightest SUSY particle would decay, it does not directly imply that it cannot be a candidate for dark matter since the coupling for the decay to SM particles could be very weak.

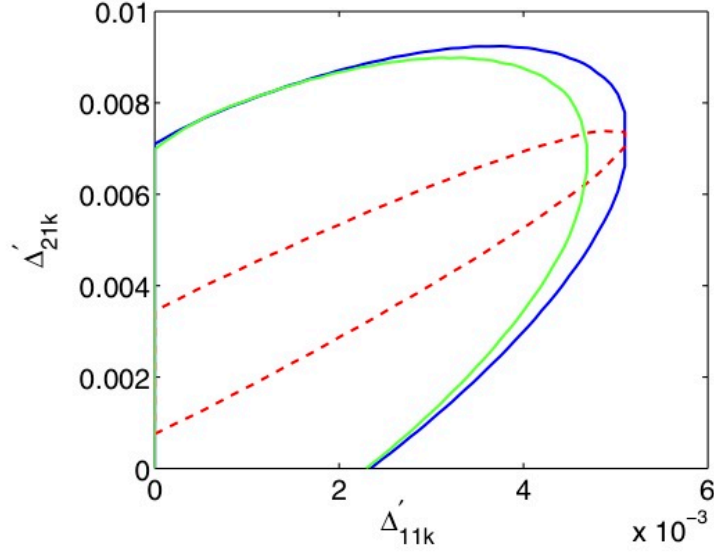


Figure 2.6: Present 95% C.L. constraints on RPV parameters Δ'_{11k} and Δ'_{21k} that enter R_π obtained from a fit to precision electroweak observables [96]. The dark blue (dark gray) contour shows the current constraints on those parameters (interior is allowed region). The dashed red (gray) shows the contour adding the future expected experimental precision (0.1%) from the PIENU experiment, assuming the same central value. The light green (light gray) curve indicates prospective impact of a future measurement of the proton weak charge at Jefferson Lab [97].

Charged Higgs

If we consider a charged Higgs boson with coupling $g/2\sqrt{2}\lambda_{ud}$ to the pseudoscalar current and $g/2\sqrt{2}\lambda_{l\nu}$ to the leptonic current $\bar{l}(1 - \gamma^5)\nu_l$, we can parametrize a deviation from the experimentally measured branching ratio in terms of those new λ_{ud} and $\lambda_{l\nu}$ couplings [57]:

$$1 - \frac{R^{Exp}}{R^{SM}} = \frac{2m_\pi^2}{m_e(m_u + m_d)} \frac{m_W^2}{m_{H^\pm}} \lambda_{ud} \left(\lambda_{e\nu} - \frac{m_e}{m_\mu} \lambda_{\mu\nu} \right) \quad (2.36)$$

If we suppose lepton universality for those couplings (as for the SM Higgs), i.e. $\lambda_{e\nu}/\lambda_{\mu\nu} = m_e/m_\mu$, the term inside the bracket in eq.2.36 vanishes and therefore no constraints to this model can be provided by the pion branching ratio. However, such a chiral relationship is not required. If we assume couplings at the loop level ($\lambda_{e\nu} \sim \lambda_{\mu\nu} \sim \lambda_{ud} \sim \alpha/\pi$), a measurement of the pion branching ratio at the 0.1% level would reach $M_{H^\pm} \sim 400$ GeV [57].

2.4.3 New scalar interactions

As already discussed, the branching ratio is in principle insensitive to additional scalar currents. However, the pion can decay through induced pseudoscalar interactions generated from the electroweak renormalization (i.e. loop effects) of the scalar couplings. For high mass scales (above 200 GeV) the indirect constraint on scalar currents from the pion branching ratio can be orders of magnitude better than direct searches in β decays [87].

2.4.4 Conclusions

We have seen that the measurement of the pion branching ratio at the 0.1% level precision can put interesting new bounds on a number of BSM scenarios which include new non-chiral scalar interactions. If we go back to the important open questions listed in §2.1.3, we can see that PIENU could shed some light on the first two items. Indeed, the origin of ν mass or possibly the nature of dark matter can be constrained by the search for sterile and massive neutrinos on the $\pi^+ \rightarrow e^+\nu_e$ spectrum. Some parameter space of the Supersymmetric model designed in particular to provide answers to the problem of the Higgs stabilization, can be probed by a precise measurement of the pion branching ratio. A detection of R-Parity-Violating interactions would also bring new insights on the nature of dark matter and the neutrino's mass.

Chapter 3

Description of the Experiment

And now for something completely different

Monty Python

In this chapter, the beamline, the experimental apparatus and the data acquisition system will be described.

3.1 The M13 beamline

The TRIUMF cyclotron delivers a 500 MeV proton beam with an intensity of about $120 \mu\text{A}$. The proton bunches of about 4 ns width hit the *BL1A-T1* production target located in the Meson Hall every 43 ns. The resulting positively charged pion beam is directed to the M13 area where the PIENU experiment is located. The M13 beamline is a low energy (0-130 MeV/c) muon and pion beamline [99]. It was modified to fulfill the requirements of the PIENU experiment which needed a background in beam particles about 100 times lower than what the M13 beamline was providing. Especially, because the PIENU detector is facing the beam, positrons (1/4 of the rate of pions) in the beam could mimic real decay positrons and increase the detector rates, trigger rates and the background in the $\pi^+ \rightarrow e^+ \nu_e$ spectrum. The layout of the M13 beam channel as well as the extension built to suppress the positron contamination in the pion beam is shown in Fig.3.1. Fig.3.2 and Fig.3.3 show pictures of the M13 area before and after the beamline extension installation.

The beamline takes off from the primary proton beam (labeled *BL1A* in Fig.3.1) at an angle of 135° from the 1-cm thick Beryllium production target (*BL1A-T1*). Prior to the extension, the beamline consisted of 2 dipole magnets (*B1* magnet: -60° and *B2* magnet¹⁶: $+60^\circ$) and a series of quadrupole

¹⁶To avoid confusion with the beam scintillator counters, italics are used for the beamline components.

3.1. The M13 beamline

magnets ($Q1-Q2$, $Q3-Q4-Q5$ and $Q6-Q7$) to collect pions and focus the beam [1]. $F1$, $F2$ and $F3$ indicate the 3 foci before the beamline extension. $F4$ is the last focus at the end of the extension which is the location of the PIENU target counter.

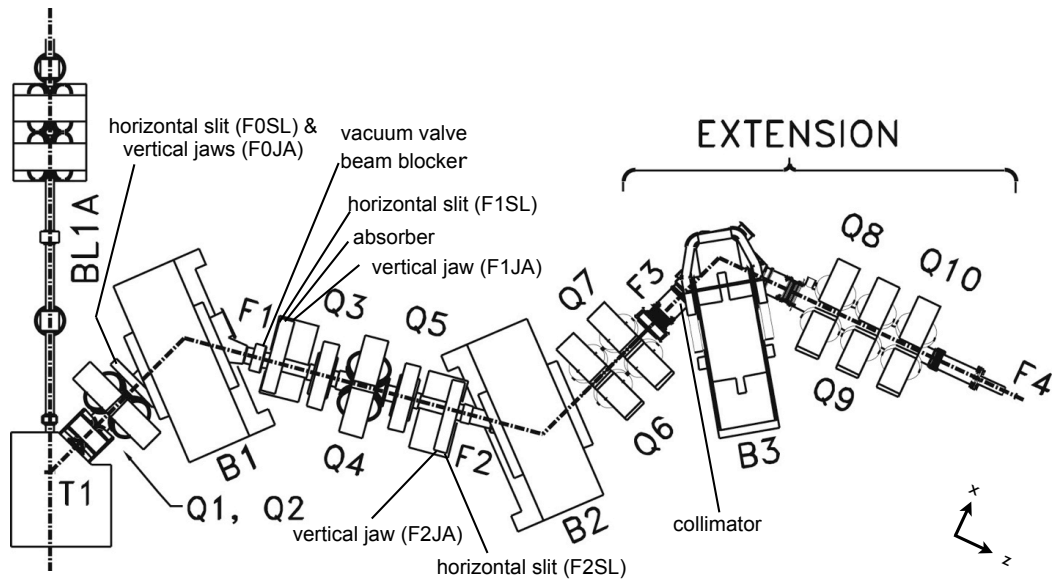


Figure 3.1: M13 beam channel with the extension built in 2008

Prior to the new beamline construction, tests were performed to determine the beam quality and its particle content. These tests were intended to verify the Monte Carlo calculations done with a beam transport program called REVMOC [100] used to design the beamline extension [101]. At $F3$, the NaI(Tl) calorimeter (described in §3.2.5) was placed to measure the energy of the particles and a plastic scintillator gave the energy and time information necessary to discriminate the particles with their time of flight (TOF). Fig.3.2 shows a picture of the test setup.

After traversing a degrader (1.45 mm thick Lucite absorber) placed near

3.1. The M13 beamline

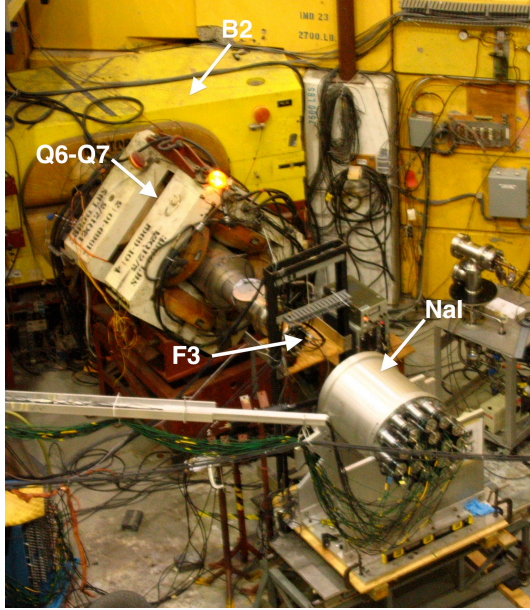


Figure 3.2: Test of the particle separation technique prior to the installation of the beamline extension.

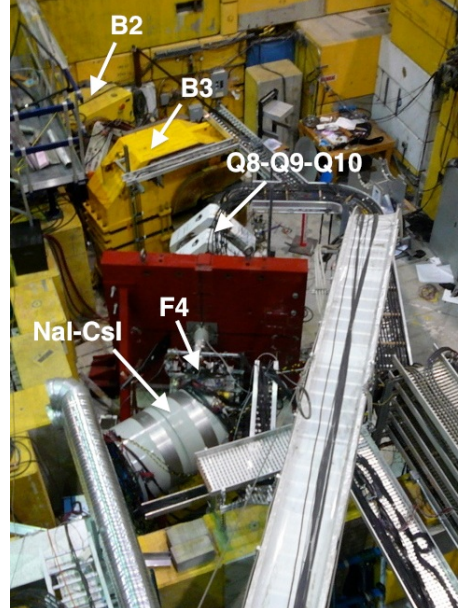


Figure 3.3: The experimental area after the beamline extension installation.

$F1$, the pions and positrons energy loss difference is large enough to obtain a clear particle separation at $F3$ as shown in Fig.3.4. A collimator (5 cm-thick lead bricks with a 3 cm square hole) can then be placed at this position to suppress the displaced positrons and redefine the pion image. After the collimator, the small momentum tail of the positron beam due to different energy loss processes results in the presence of some positrons at the pion spot. The contamination was however measured to be of the order of 0.5% at the location of the collimator (it is 2% at the location of the target counter due to pion decay-in-flight and collimation) which is almost a factor 100 smaller than without the absorber/collimator system.

After the collimator, the pion beam is directed toward the PIENU detector by a dipole magnet ($B3$ magnet: -70°) and refocused by a triplet of quadrupoles ($Q8-Q9-Q10$) placed after $B3$. A large 20 cm-thick steel wall isolates the location of the collimator from the detector, allowing better shielding from the γ -rays emitted by the stopped positrons in the collimator. The total length of the extension between $F3$ and $F4$ is 4.5 m (in comparison, the distance between $BL1A-T1$ and $F3$ is approximately 10 m)

which results in a pion intensity loss due to decays-in-flight.

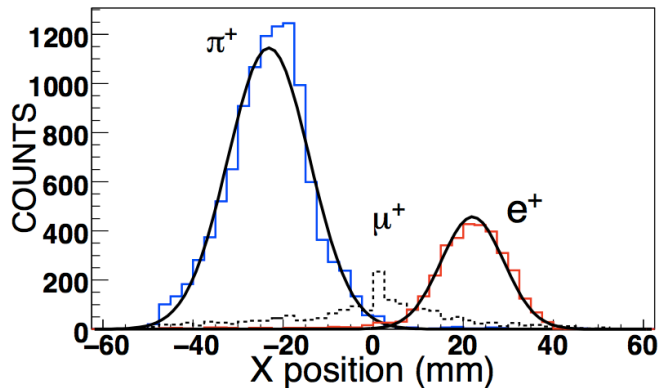


Figure 3.4: Pion, muon and positron position distributions transverse to the beam (see Fig.3.1 for coordinates) at $F3$. The solid lines are fitted Gaussian curves for pions and positrons.

3.1.1 Beamline momentum calibration

Due to the uncertainties in the dipole magnets' fringe field it is difficult to obtain an absolute beam momentum calibration. Usually, the endpoint of the positron energy spectrum from $\mu^+ \rightarrow e^+ \nu \bar{\nu}$ decay in the production target (Michel edge) and the energy peak of muons from $\pi^+ \rightarrow \mu^+ \nu$ decay at the surface of the production target (surface muons) are used to calibrate the beamline [102]. To obtain an additional calibration point we performed a measurement of $\pi^+ \rightarrow e^+ \nu_e$ decays in the production target ($BL1A-T1$) which gave a clear calibration peak at 69.8 MeV/c [1]. With those measurements we estimate the uncertainty of our beamline calibration to be around 1%.

The beam momentum bite is restricted to 1.5% FWHM using the $SL1$ slits which are located directly downstream of the $B1$ magnet. However, after the degrader the momentum bite is slightly worsened and a small dispersion of the beam is introduced which has a noticeable effect on the pion stopping distribution in the target.

Studies were performed to find the best combination of slit openings which minimized scattering and optimized the beam rate in our target.

Tuning of the quadrupoles upstream and downstream of $B3$ was done to

minimize the steering and place the beam close to the centre of our target detector. The control and monitoring of the beamline was done through EPICS [103].

3.1.2 Particle and magnetic background

The level of neutral (neutrons and γ rays) background in the experimental area was also measured to determine the location of additional shielding blocks. Simulation of the beamline with G4beamline software [104] was done to evaluate the effect of different slit materials as well as to determine the location of the shielding blocks¹⁷. Fig.3.5 shows a picture of the simulated beamline and the showers produced by the *SL1* slits. The location of the detector in the experimental area was chosen to minimize the level of neutrons emitted from the production target. The level of neutral particles hitting the detector and contributing to the neutral pileup is about five times smaller than for the E248 experiment.

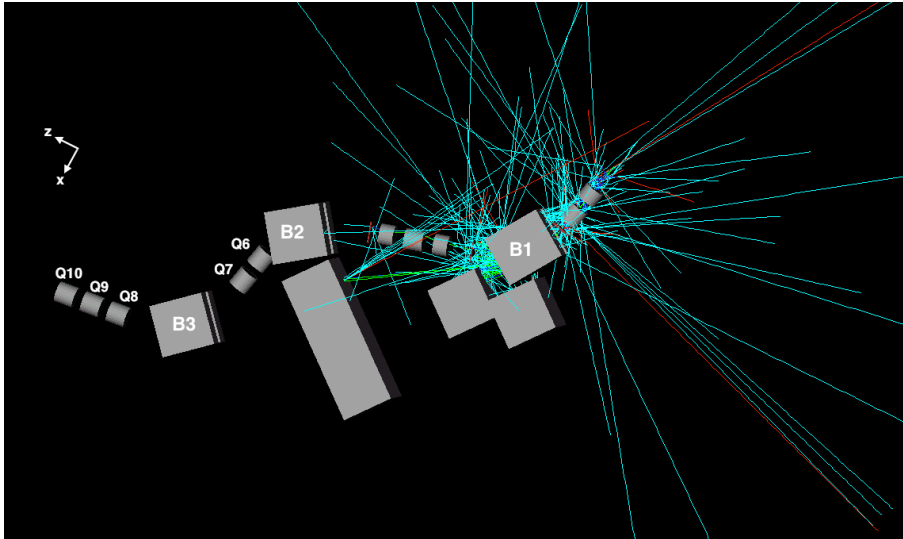


Figure 3.5: G4beamline simulation of the M13 beamline. The colored rays indicate the trajectories of the background particles produced in the beamline material.

¹⁷The red steel wall seen in Fig.3.3 was found to be necessary through these studies. It shields the detector apparatus from the showers caused by the stopped positrons in the collimator.

In order to measure the response function of the calorimeter¹⁸, the detector needs to be rotated around the beam axis and the vertical axis (Y axis in our reference frame). Since a PMT gain change with the rotation was observed in the E248 experiment, a measurement of the magnetic field in the experimental area and the effect of rotation on the PMT's gain was done and helped determine the appropriate magnetic shielding for every type of PMT used. The vertical component of the cyclotron fringe field was measured to be ~ 1.5 Gauss at the location of the detector. The horizontal components were smaller than 1 Gauss.

3.2 The detector

3.2.1 Overview

When exiting the beam pipe window the positively charged pions, with a momentum of 75 MeV/c, pass through a set of wire chamber planes that provide the beam profile. The beam is then degraded by two plastic scintillator counters, B1 and B2. Before stopping in the target, an 8 mm-thick plastic scintillator, the pions go through four planes of silicon-strip detectors. Another two planes of silicon-strip detectors are placed directly downstream of the target followed by a plastic scintillator counter (T1), an acceptance defining wire chamber (WC3) and another plastic scintillator counter (T2). T2 is covering almost the entire front surface of a large, 19 radiation-length-long crystal of NaI(Tl) which measures the energy of the decay positrons. Two rings of active material made of 97 crystals of pure CsI surround the NaI(Tl) crystal to contain the electromagnetic shower. A diagram of the experimental set-up is shown in Fig.3.6 and the physical dimensions of all the counters are presented in Table 3.1.

¹⁸This is important for the tail analysis, see §5.1

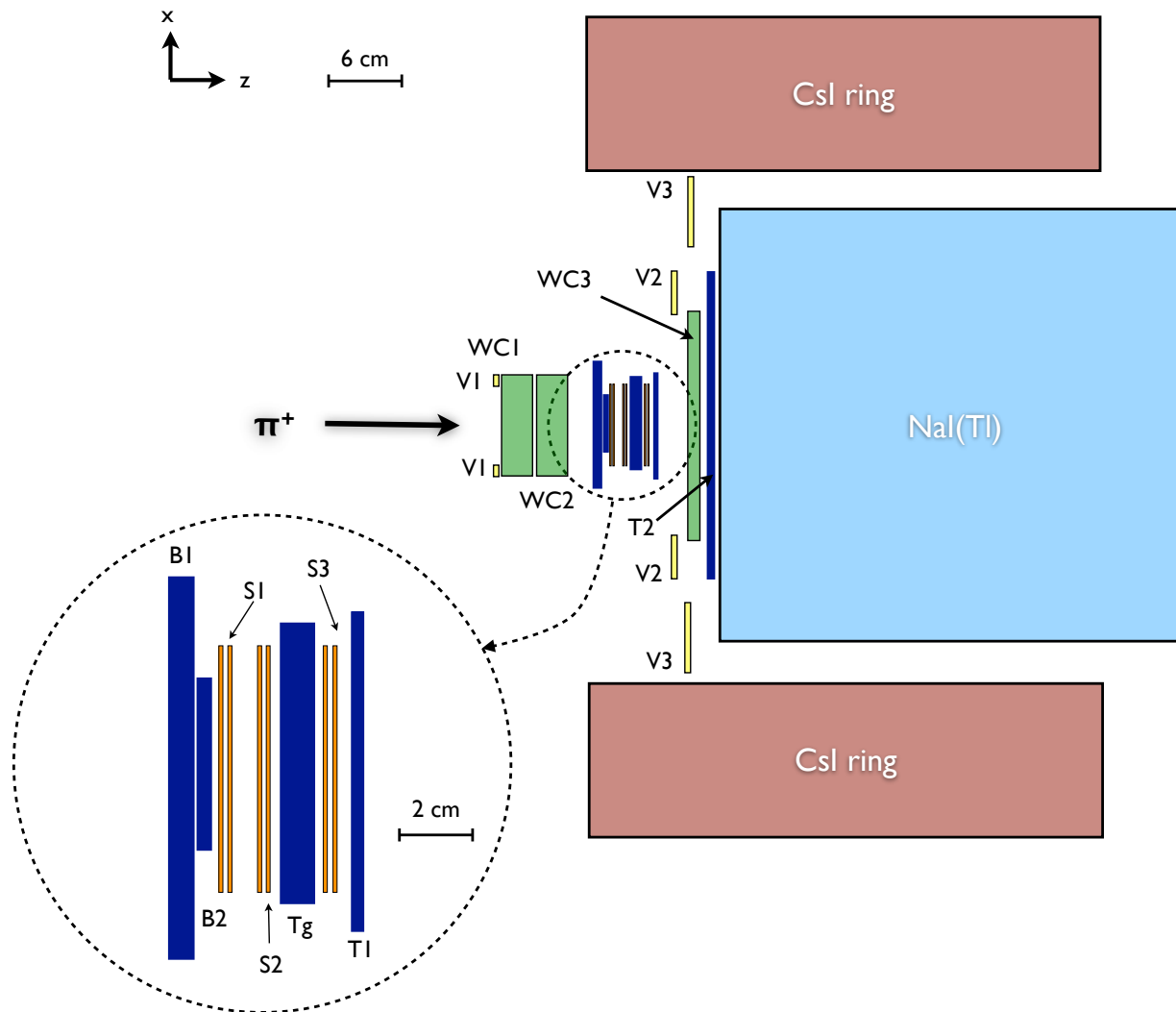


Figure 3.6: Schematic diagram of the experimental apparatus. See Table 3.1 and text below for the legend.

3.2. The detector

Table 3.1: Active sizes of the all the PIENU detectors. The numbers in parentheses represent the radii of round or annular counters.

Name	X(R-in) [mm]	Y(R-out) [mm]	Z/counter [mm]	rotation [°]	PMTs /counter
<i>Plastic Scintillators</i>					
B1	100	100	6.604	x	4
B2	45	45	3.07	x	4
target (Tg)	70	70	8.05	45	4
T1	80	80	3.04	45	4
T2	(0)	(171.45)	6.6	x	4
V1	(40)	(52)	3.175	x	1
V2	(107.95)	(150.65)	6.35	x	1
V3	(177.8)	(241.3)	6.35	x	1
<i>Wire Chambers</i>					
WC1 and WC2 ¹⁹	(0)	(96)	4.0	0,±120	x
WC3	(0)	(230.4)	4.0	0,±120	x
<i>Silicon Detector</i>					
S1, S2 and S3	61	61	0.285	x	x
<i>Scintillating Crystals</i>					
NaI	(0)	(480)	480	x	19
CsI ²⁰	85	90	250	x	1

3.2.2 Plastic scintillators

In Fig.3.6 the plastic scintillators are indicated in dark blue. They are all machined from Bicron BC-408 (polyvinyltolulene) scintillator. There are two square beam counters (B1 and B2) in front of the target which restrict the beam acceptance (B2 is smaller than the target), and define the pion timing. The energy deposited in those counters is used for particle identification. The target is followed by two telescope counters (T1 and T2). T1 defines the positron timing. The target and T1 counters are rotated with

¹⁹Sizes indicate the active area of a single plane. One chamber is made of three planes.

²⁰Sizes are for a single crystal. Since the CsI crystals have a complex shape, see Fig.3.15, x and y sizes are approximate. The complete CsI assembly is made of 97 crystals. The arrangement of these crystals is detailed in §3.2.6 and pictured in Fig.6.5.

3.2. The detector

respect to B1 and B2 counters by an angle of 45° around the beam axis. The T2 counter is a round acceptance-defining detector placed directly on the front face of the NaI(Tl) detector. After the target it is important to have a compact assembly to minimize the positron scattering. Since the T2 counter is sandwiched between the WC3 and the NaI(Tl), there was only a very limited space available for its read-out which is done by wavelength-shifting fibres.

There are also three veto counters (V1-V3) covering respectively the flanges of the WC1-2 assembly, WC3 and the NaI(Tl) crystal. All plastic scintillators (except the veto counters) are read with four PMTs. Table 3.2 shows the number and types of PMT used for each detector.

Table 3.2: Readout scheme of the plastic scintillators PMTs

PMT type	B1	B2	target	T1	T2	V1	V2	V3
H3178-51 1.5 in. Hamamatsu	4							
83112-511 1 in. Burle		4		4				
XP2262B 2 in. Photonis			4					
H3165-10 13 mm Hamamatsu					4		1	1
H3164-10 10.5 mm Hamamatsu						1		

3.2.3 Wire chambers

In Fig.3.6, the multi-wire proportional chambers are indicated in green. Each wire chamber consists of three wire planes which are rotated by an angle of 120° with respect to each other to form an X-U-V assembly. Fig.3.7 is a schematic cross-sectional drawing of a wire chamber plane. Each sensitive wire is connected to a multi-hit TDC channel (see §3.4.1) which records the time of the hit after pre-amplifiers and discriminators. The efficiency of every plane is higher than 99% for beam positrons. The chambers are filled with a CF_4 -Isobutane mixture (80% - 20%) at atmospheric pressure.

Beam wire chambers (WC1 & WC2)

The beam wire chambers are the first detectors seen by the beam. They are placed directly downstream of the 2 mil stainless steel vacuum window foil. WC1 and 2 (6 planes) are mounted together onto the beam pipe as seen on Fig.3.9. They provide position and angle information for the incoming pion

3.2. The detector

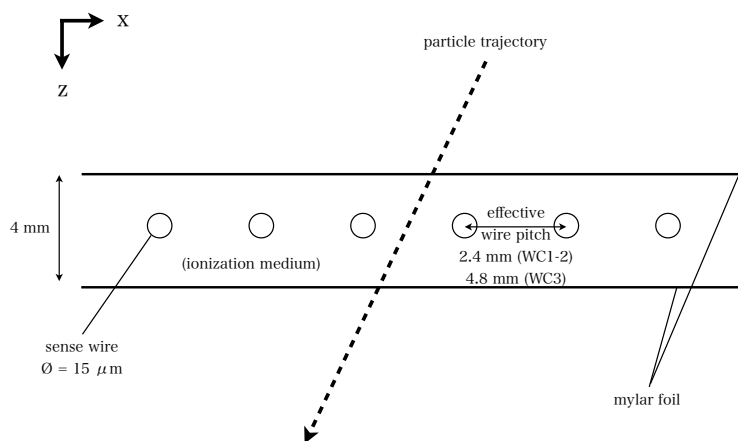


Figure 3.7: Schematic of a wire chamber plane.

beam (see §3.2.7 for a detailed description of the tracking detectors). Each wire plane has 120 wires grouped by three. Each group is connected to a read-out pad. The number of read-out channels is therefore 40 per plane and the effective wire read-out is 2.4 mm. The total active diameter of WC1 and WC2 is $\varnothing=10.6$ cm. Fig.3.8 shows a picture of a beam wire chamber plane with its preamplifier board.

Decay positron wire chamber (WC3)

The third wire chamber is part of the tracking devices for decay positrons. It is mounted on the flange of the NaI(Tl) crystal enclosure as seen in Fig.3.10. It measures the position of the decay positrons at the entrance of the calorimeter and defines the acceptance (see §3.2.7 for a detailed description of the tracking detectors). Each plane has 96 wires. However, wires are connected together by pairs on the same pad which reduces the number of channels to 48 with an effective read-out pitch of 4.8 mm. The active diameter of WC3 is $\varnothing=23.04$ cm.

3.2.4 Silicon detectors

In Fig.3.6 the silicon detectors are indicated in orange. There are three sets of silicon detectors (S1, S2 and S3). Each set consists of two identical

3.2. The detector

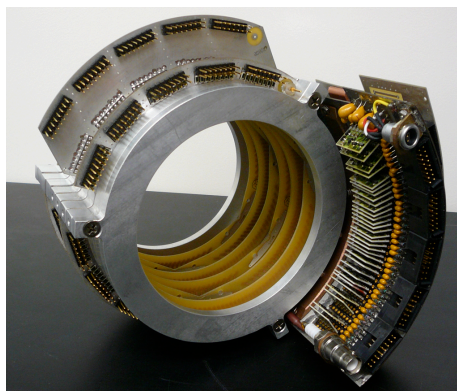


Figure 3.8: A beam wire chamber plane and its preamplifier board.

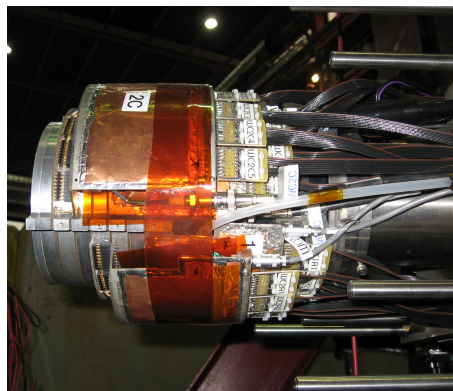


Figure 3.9: Wire Chamber 1 and 2 installed on the beam pipe.

hybrids fixed back to back with perpendicular orientation of the strips (to measure X and Y coordinates). S1 and S2 are both placed immediately upstream of the target while S3 is placed immediately downstream of it to provide the most accurate position and angle information in the target of the incoming pion and the outgoing positron respectively (see §3.2.7 for a detailed description of the tracking detectors). Fig.3.11 shows the first two silicon strip detectors (4 planes).

A plane of silicon detector has an active volume of $61 \text{ mm} \times 61 \text{ mm} \times 285 \mu\text{m}$. The Si sensor is a single sided AC-coupled micro-strip detector of the same type as the ones used in the ATLAS central tracker [105]. In the original design each strip has a pitch of $80 \mu\text{m}$ but since the required resolution for the PIENU experiment was of the order of $300 \mu\text{m}$ the design has been modified to bind four silicon strips to one read-out line. For further reduction of readout channels the lines are interconnected with capacitors and only every fourth line is connected to an amplifier as shown in Fig.3.12. A total of 48 channels per silicon plane (288 channels in total) are read out. The capacitive network forms a charge division line where the reconstruction of the ionization amplitude and position is made by proper weighting of the two or three channels that typically fire during an event.

In order to reduce the data size, a hardware threshold is set to suppress the channels which have no hit. Because of the noise level in these detectors, the threshold is set too high to be able to detect beam positrons in S1 and S2. However, S3 has a lower threshold to make sure that the detection efficiency for decay positrons is higher than 99%.

3.2. The detector

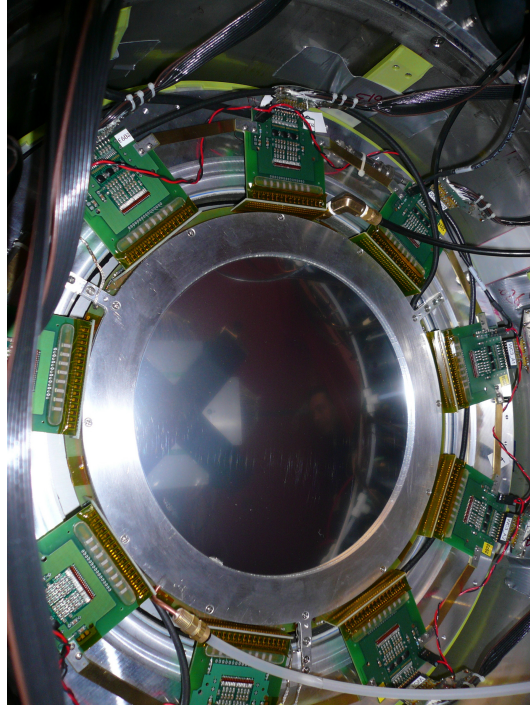


Figure 3.10: The WC3 mounted onto the flange of the NaI(Tl) crystal enclosure.

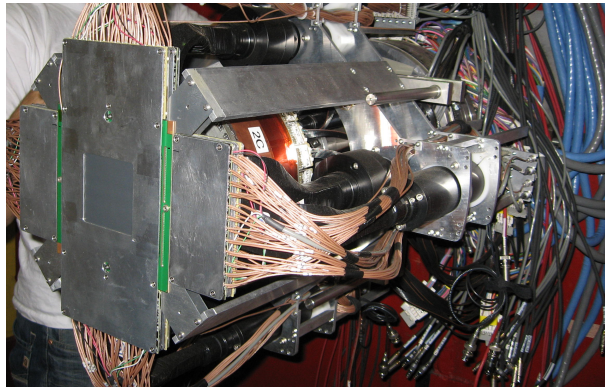


Figure 3.11: S1 and S2 assembly mounted on their support structure.

The signals of all channels are read out by 60 MHz ADCs, see §3.4.1.

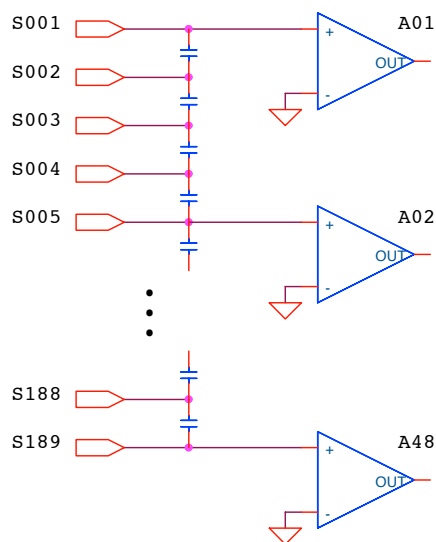


Figure 3.12: Schematic drawing of the silicon readout scheme.

3.2.5 NaI calorimeter

In Fig.3.6, the NaI(Tl) calorimeter is indicated in light blue. This detector is a single crystal of Thallium-doped NaI (in the rest of the thesis “NaI” will be used in place of “NaI(Tl)”) borrowed from BNL where it was used by the LEGS collaboration [106, 107].

The crystal is enclosed in a 3 mm thick²¹ aluminium enclosure which has 19 circular quartz windows at the rear end, Fig.3.13. Each window is viewed by a 3 inch diameter Hamamatsu R1911 PMT (with the exception of the centre PMT which is of type R1911-07) which is surrounded by a μ -metal shield to reduce the impact of the magnetic field on the PMT gain. The bases of the phototubes were modified to allow the last two dynodes to have a fixed voltage ($\sim \times 0.21$ and $\times 0.37$ of the high voltage applied to the resistor chain) instead of getting their voltage from the resistor chain. This modification

²¹the aluminium front face of the NaI is only 0.5 mm thick to minimize the amount of material on the positron path.

3.2. The detector

was needed to improve the performance at high count rates in the BNL experiment. This setup requires the use of 57 high voltage channels, instead of just 19 channels. Two tube (tube 2 and 4) bases have been restored to be powered with one high voltage unit and no difference was found in the gain between those and the modified bases at the typical count rates of the PIENU experiment.

The surface of the crystal is covered with a reflective material. An optical simulation was performed with the software Detect2000 [108] to study the dependence of the energy deposited in the crystal on the entrance location of the particle in the NaI. The results showed that the light emitted by the crystal is uniformly reflected [109]. Therefore, a similar amount of light is seen by every photo-tube independent of the entrance position of the ionizing particle in the front face of the NaI crystal. This was confirmed within 2% accuracy by bench tests using a positron source (^{22}Na) [110].



Figure 3.13: View of the NaI crystal from the back side on the test bench.



Figure 3.14: The NaI crystal surrounded by the 97 crystals of CsI arranged in two layers.

3.2.6 CsI calorimeter

In Fig.3.6 the CsI ring is indicated in red. On loan from BNL, this detector consists of 97 pure (undoped) CsI pentagonal crystals (Fig.3.15) of 25 cm in length (13.5 radiation length) and about 9 radiation length radially, arranged in two concentric layers around the NaI detector as can be seen on Fig.3.14.

3.2. The detector

Each of the two layers are divided²² in an upstream and downstream part, making a total of 4 rings [111]. The shapes and locations of the individual crystals was added in the MC as can be visualized in Fig.6.5. Each crystal is read out by a fine-meshed, 3 inch diameter Hamamatsu R5543 PMT [112] which was designed to operate in high magnetic fields²³. Before being brought to TRIUMF, the crystals and their PMTs were used in the endcap photon-veto detector in the E949 experiment at BNL. Each crystal has a built-in $\text{YAlO}_3:\text{Ce}^{245}\text{Am}$ source [113] which produces light pulses (~ 8 MeV) at a rate of ~ 50 Hz with wavelength and pulse width similar to the CsI scintillation to monitor the crystal's light output and the PMT's gain. Each crystal is also connected via a quartz fiber to the output of a Xe lamp pulser, which flashes twice a second during data taking [114]. This Xe lamp monitoring system traces the changes in the CsI PMT's gains only. Therefore, a comparison between the YAlO and Xe-lamp monitoring gives access to the evolution of the crystal's light collection efficiency. The stability of the Xe lamp was measured to be $\sim 1\%$.

Seven reference PMTs of the same types as the ones used for the calorimeter are enclosed in an incubator maintained at a constant temperature of 24.0°C and placed next to the location of the detector. The Xe-flash-lamp is also enclosed in an identical incubator but is maintained further away from the detector due to the noise its power supply induces in the counters. The Xe-lamp is connected to the reference PMTs through the same system as it is to the CsI crystals so that any changes in the Xe-lamp output can be traced back by the reference PMTs.

The CsI crystals are constantly flushed by dry Nitrogen gas from a liquid Nitrogen dewar to keep the humidity level as low as possible.

3.2.7 Detector assembly and performance

Fig.3.16 shows the CAD drawing of the complete PIENU detector assembly and a picture of the setup in the experimental area.

The PIENU detector is divided into two sub-detectors called PIENU-I and PIENU-II. PIENU-I consists of the beam assembly (beam WCs, B1, B2, S1 and S2), the target and part of the telescope assembly (namely S3 and T1). T2, WC3 and the crystals form the PIENU-II assembly. PIENU-II

²²Since there is an odd number of crystals, there are 46 crystals in the upstream part and 47 in the downstream part.

²³The components of the magnetic background in the M13 area are at maximum of 2 Gauss at the location of the detector. It is well within the operational specifications of those PMTs.

3.2. *The detector*

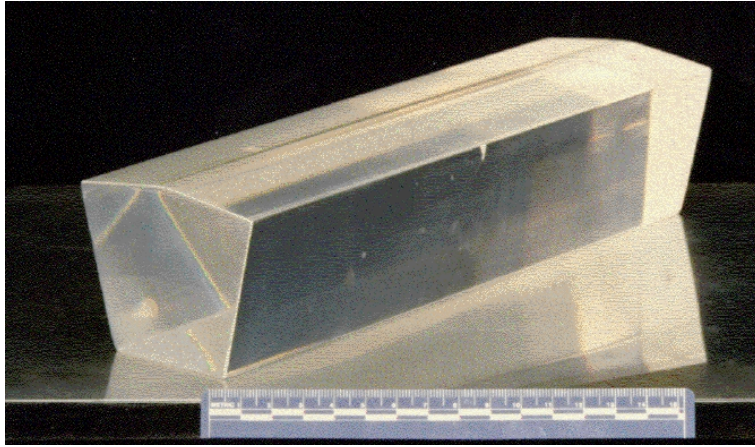


Figure 3.15: Picture of one of the CsI crystal.

is enclosed in a steel cylinder which forms the housing for the CsI crystals and also provides magnetic and radiation shielding. PIENU-II can be independently moved from PIENU-I.

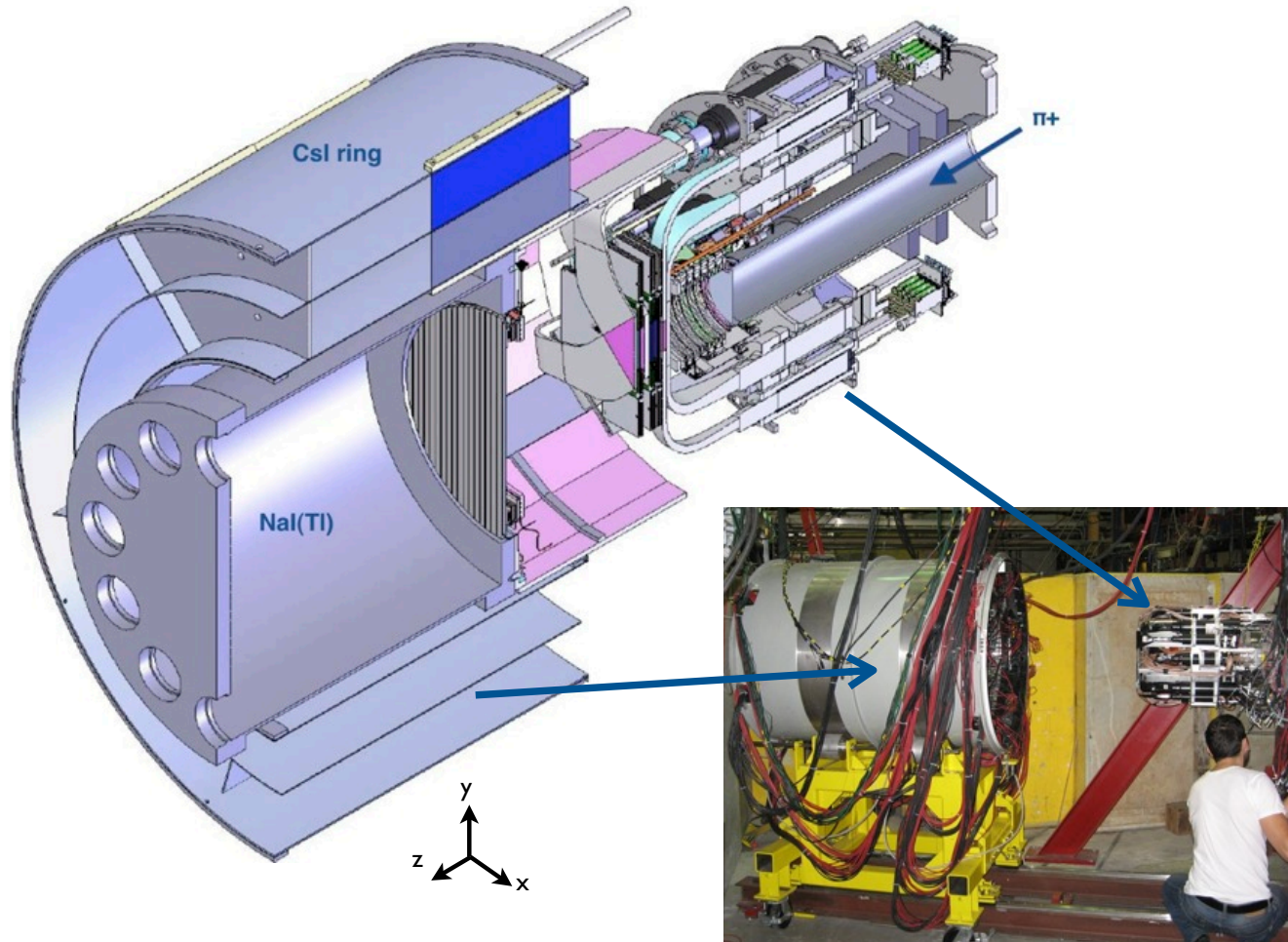


Figure 3.16: CAD drawing of the PIENU detector and picture of the detector setup (the physicist providing the scale).

Detector enclosure

During the 2009 data-taking run, temperature variations in the experimental hall noticeably affected the quality of the data taken. Not only the electronics but also the crystals' response were affected. To reduce the amplitude of this effect to a negligible level a temperature-controlled enclosure was built before the 2010 beam time period around the entire detector as seen in Fig.3.17. The temperature was maintained at 20°C with a fluctuation smaller than ± 0.5 °C over most of the running period, Fig.3.18.

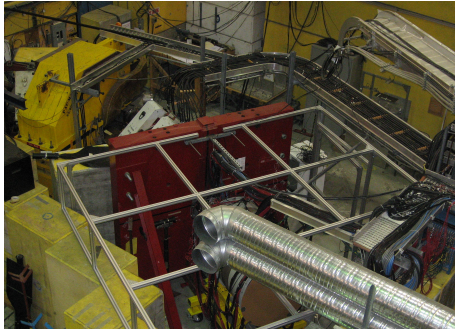


Figure 3.17: Picture of the PIENU detector inside the temperature-controlled enclosure.

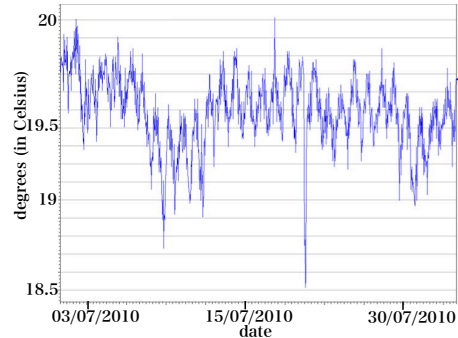


Figure 3.18: Temperature variation in the span of a month inside the detector area.

Special assembly

PIENU-II is mounted on a supporting structure on wheels as can be seen on the picture of Fig.3.16. The wheels are guided by rails to ensure that the position of PIENU-II with respect to PIENU-I does not change. However, for special runs which require the PIENU-II detector to be detached from PIENU-I and rotated, the rails are removed.

These special runs are dedicated to the measurement of the response function of the PIENU-II detector to beam positrons. This information gives access to the lineshape and is important for the determination of the $\pi^+ \rightarrow e^+ \nu_e$ low energy tail as discussed in §5.1. Fig.3.19 shows a schematic of the detector assembly for these special positron runs during which part of the PIENU-I detector was removed so as to enable the PIENU-II detector to be rotated axially (φ) as well as vertically (θ).

3.2. The detector

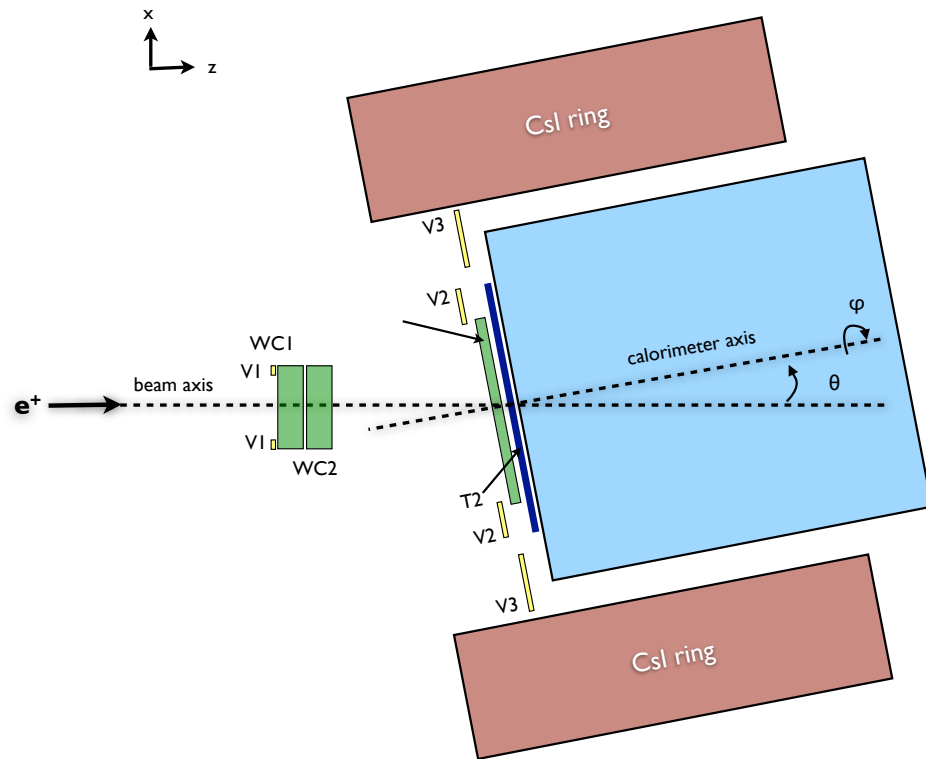


Figure 3.19: Schematic drawing of the detector setup for special positron runs.

Resolution of the calorimeter assembly

The PIENU NaI crystal is a high resolution calorimeter. Deconvoluting the beam momentum bite of 0.5%, the resolution of the 70 MeV positron peak is approximately 2.2% (FWHM), see Fig.3.20. With this resolution, we

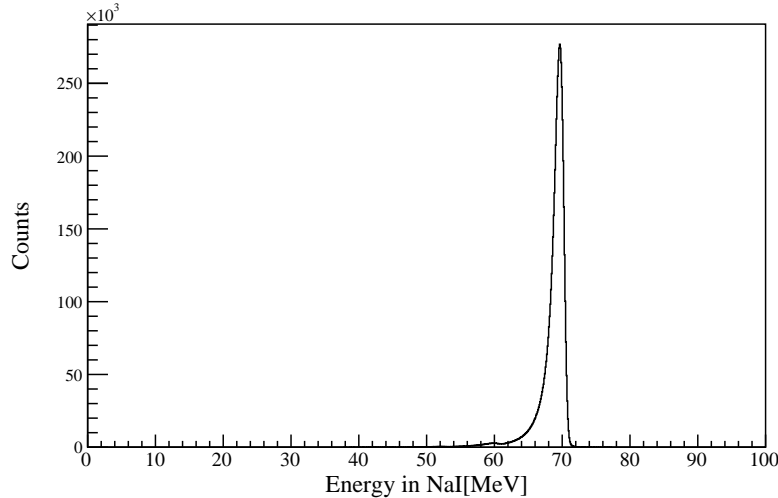


Figure 3.20: Beam positron spectrum in the NaI with positrons entering the crystal at its centre. The full peak resolution (including beam momentum spread) is 2.7% (FWHM).

have been able to identify structures, see Fig.3.21, at 61 and 53 MeV in the crystal's lineshape measured with a positron beam, that were not observed in the E248 and other experiments using NaI crystals [2]. Many studies were carried out to understand the presence of these peaks which excluded the beamline or the beam composition as the source of the observed structures. Eventually, these peaks were identified as lost energy due to neutron escape from the crystal. Indeed, photons produced by the shower induced in the NaI crystal by beam positrons can interact and be captured by a nucleus in the crystal. From a Monte Carlo simulation including hadronic interactions, it was observed that a photon captured by an ^{127}I nucleus in the crystal is followed by the emission of neutrons in 94% of the cases. If the neutron is not reabsorbed, its binding and kinetic energy (E_{1n}) is lost and is responsible for the peak at 61 MeV ($70 - E_{1n}$ MeV). The origin of the second peak in the spectrum is due to emission and escape of two neutrons. The neutrons

3.2. The detector

can come from a single nucleus or from two separate ones (due to two photo-absorptions in the same shower). Both cases contribute to the second peak which starts at an energy consistent with either the energy threshold of two neutron emission or twice the single neutron separation energy E_{1n} . Fig.3.21 shows the energy deposited by the beam positrons in the NaI as seen in the data and the Monte-Carlo with and without hadronic interactions. The agreement between MC and data is not perfect. The neutrons contributing to the lower energy peaks typically encounter 20 elastic scatterings in the NaI crystal before escaping. A small error in the simulation of neutron scatterings in the crystal could be amplified due to the high number of interactions and contribute to the discrepancy seen in Fig.3.21. However, the precise understanding of the impact of those photo-nuclear reactions on the shape and amount of the low energy tail is important and will be dealt with in §5.1.4.

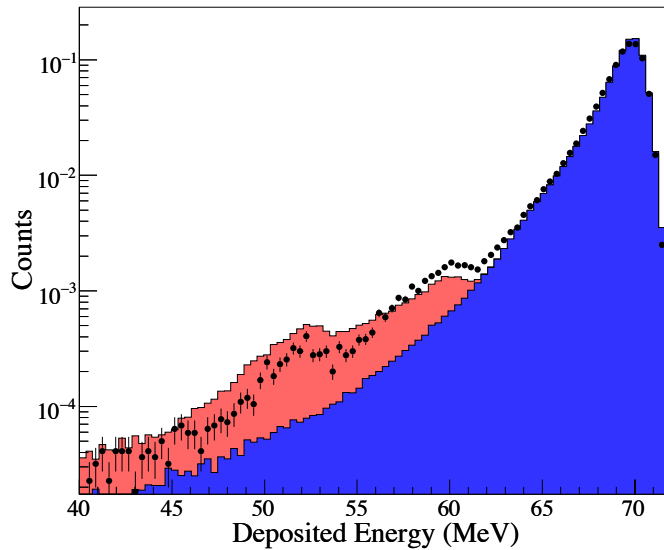


Figure 3.21: Beam positron energy in the NaI crystal. Comparison between data (filled circles with error bars) and simulation. The simulation was performed with (red/light shaded) and without (blue/dark shaded) hadronic reaction contributions. The histograms are normalized to the same area.

The CsI crystals have a resolution of about 10% (FWHM) at 70 MeV which

is five times worse than the NaI. The CsI crystals are used to detect shower leakages and see typically a few percent of the energy deposited by the decay electrons therefore the impact of their resolution on the overall resolution is limited.

Tracking and Suppression of Decay-in-Flight capabilities

As mentioned in §1.2.2 good tracking capabilities are important to be able to cleanse the $\pi^+ \rightarrow e^+ \nu_e$ spectrum from misidentified $\pi^+ \rightarrow \mu^+ \rightarrow e^+$ events due to decays in flight.

In the following a track is defined as a straight portion of a particle trajectory. The PIENU tracking system consists of three trackers²⁴: the beam wire chambers (Tr1), the first two silicon detectors (Tr2), and S3 and WC3 (Tr3). Tr1 provides 6 position measurements, Tr2 provides only four while Tr3 contains 5 position measurements. All trackers are schematically represented in Fig.3.22. Tr3 is used to track the decay positrons and determine whether or not they entered into the acceptance region of the NaI crystal. Tr1 and Tr2 are the two trackers used to identify pion decays-in-flight which happened after the last plane of WC2 and the first plane of S1.

Pions can decay-in-flight in or upstream²⁵ of the target. The muon from pion decay can also decay-in-flight. And, of course, a combination of those is possible. However since the probability of such an event is close to the product of the pion decay-in-flight and muon decay-in-flight probability, it is very small and negligible at our level of precision.

To summarize, the following $\pi^+ \rightarrow \mu^+ \rightarrow e^+$ decays can occur:

1. π^+ decay-in-flight upstream of the target and μ^+ decay at rest (PDIF up. - MDAR)
2. π^+ decay-in-flight in the target and μ^+ decay at rest (PDIF it. - MDAR)
3. π^+ decay at rest and μ^+ decay-in-flight in the target (PDAR- MDIF)

²⁴We call here “tracker” a system that can provide the position and angle information of a track in three dimensions.

²⁵By “upstream of the target” we mean: between the last plane of WC2 and the first plane of S1. Although, S1, S2 and the target form a rather compact assembly there is a portion of decays-in-flight happening between the first plane of S1 and the middle of the target. These cannot be removed using tracking information and therefore cannot be distinguished, as far as tracking is concerned, from the PDIF in the target. In this section they will be counted as PDIF in the target (PID it). There is an extra handle to help suppress those latter type of PDIF which will be used in §8.2.1.

3.2. The detector

4. π^+ and μ^+ decay-in-flight (PDIF-MDIF)

Table 3.3 indicates the proportions of each types of decay-in-flight to the “normal” decay-at-rest for $\pi^+ \rightarrow \mu^+ \rightarrow e^+$ and $\pi^+ \rightarrow e^+ \nu_e$ decays.

Table 3.3: Approximate proportions of decays in flight events to decay-at-rest events from Monte Carlo calculations.

Type of decay	DIF/DAR (in %)
$\pi^+ \rightarrow \mu^+ \rightarrow e^+$ decays	
PDIF up. - MDAR	0.6
PDIF it. - MDAR	0.6
PDAR - MDIF	8×10^{-4}
PDIF - MDIF	Prompt in time. Neglected.
$\pi^+ \rightarrow e^+ \nu_e$ decays	
PDIF	Prompt in time. Neglected.

The PIENU tracking system can only detect one of the two most frequent DIF event which is the PDIF up. - MDAR. Indeed, as can be seen in Fig.3.22, if the pion decay-in-flight between the beam wire chambers and the silicon trackers, a non-zero θ angle (called the kink angle) between Tr1 and Tr2 will be detected. Fig.3.23 shows the θ distribution for PDAR events and PDIF events obtained with Monte Carlo.

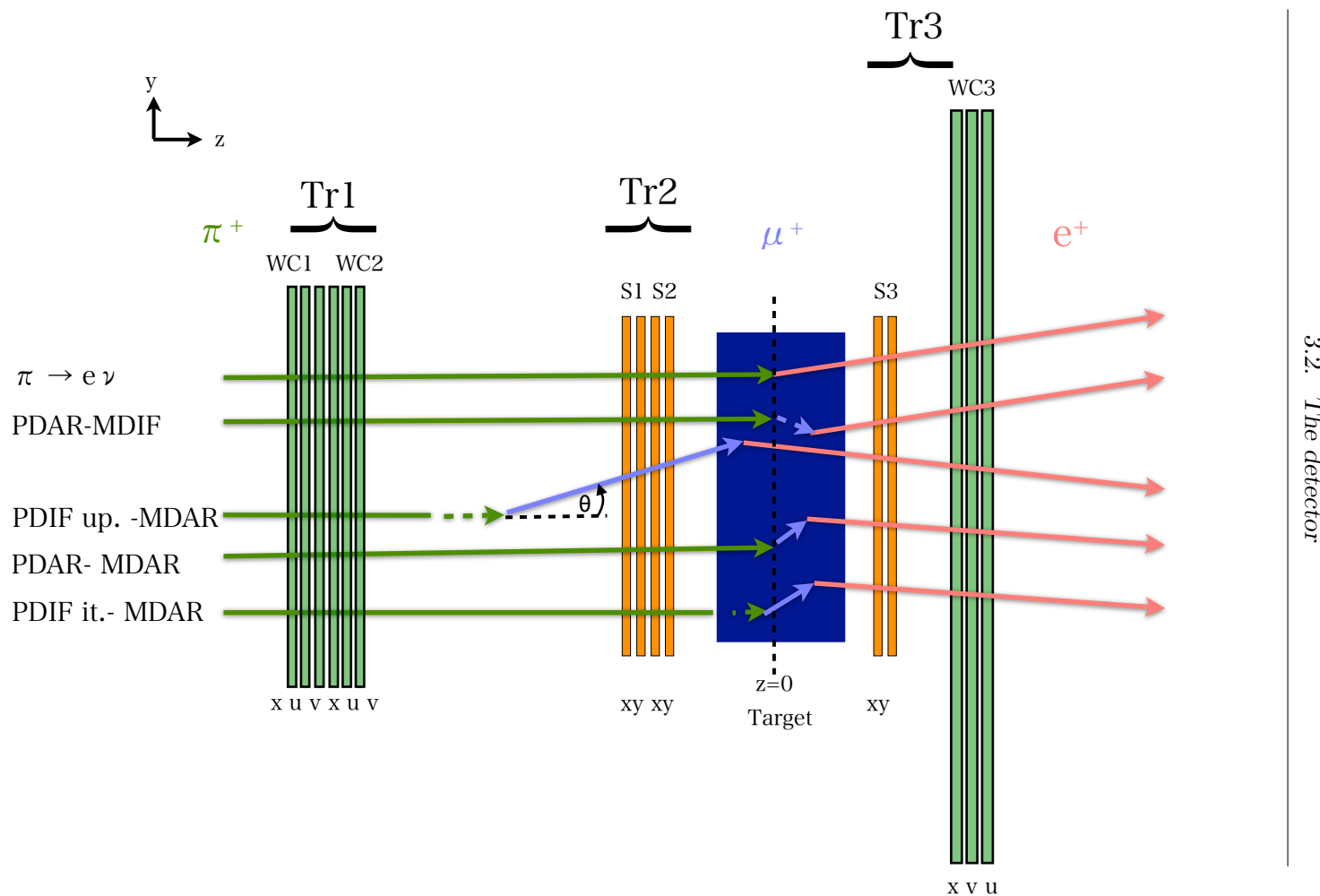


Figure 3.22: Schematic drawing of the tracking devices and the different decay-in-flight backgrounds (the sizes are not to scale). “u” orientation of a WC plane corresponds to a rotation of $+60^\circ$ while “v”= -60° .

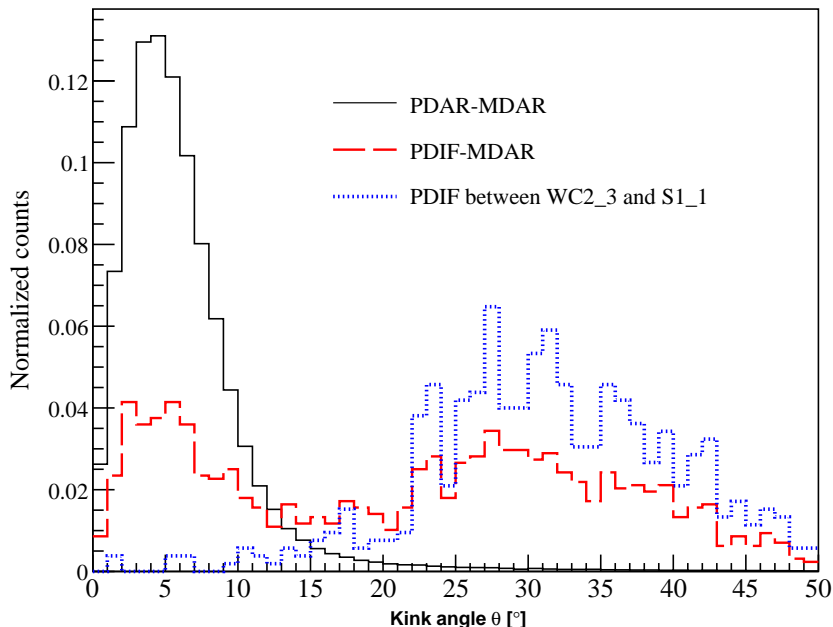


Figure 3.23: Simulation of the kink angle θ for different pion decay modes.

3.3 The trigger

The trigger logic was built mostly with NIM modules.

At first, pions and a small number of beam muons (used for the calibration of some detectors, see §4.3) are selected using energy deposit information in B1. Identification of a pion is done by requiring the coincidence of the beam counters: B1, B2 and target. A coincidence of T1 and T2 counters defines the decay-positron signal. A coincidence of pion and positron signals within a time window of -300 ns to 500 ns with respect to the pion stop is the basis of the main trigger logic, see Fig.3.24. We will call such coincidence “PIE”. Since $\pi^+ \rightarrow \mu^+ \rightarrow e^+$ decays happen much more often than $\pi^+ \rightarrow e^+\nu_e$ decays, a *Prescale* trigger selects only 1/16 of PIE events. Meanwhile, the $\pi^+ \rightarrow e^+\nu_e$ events are enhanced by the *Early* and *TIGC* triggers. The *Early trigger* selects decays which happen between 4 ns²⁶ and 40 ns after the pion

²⁶This time range selection excludes the prompt events.

3.3. The trigger

stop. Due to the short pion lifetime, more than 70% of the $\pi^+ \rightarrow e^+\nu_e$ events happen within this time range. The *TIGC trigger* selects events which deposit a high energy in the calorimeters (CsI and NaI). The energy threshold is set few MeVs below the Michel edge (around 46 MeV). Almost all the $\pi^+ \rightarrow e^+\nu_e$ events (with the exclusion of the tail events which extend below the Michel spectrum) are selected by this trigger²⁷. §3.4 explains in more detail how the energy sum is done by the TIGC module.

A simplified diagram of the trigger logic is shown in Fig.3.24. The three triggers mentioned above constitute the “physics triggers” but there are a number of additional triggers for data quality checks and calibration purposes:

- The Cosmic trigger: cosmic-ray events, mostly high energy cosmic muons, are selected by requiring a high energy deposit in the CsI outer layer or the coincidence of inner and outer layers. A prescaling factor of 16 is applied to reduce the rate of this trigger. These events are used for CsI calibration. The calibration technique will be explained in detail in §4.3.3.
- The Xe lamp trigger: as explained in §3.2.6 a Xe lamp provides flashes to all the CsI crystals. The lamp is triggered by a pulse generator twice per second.
- The Beam positron trigger: beam positrons are pre-scaled by a factor of 32. This trigger is used for plastic scintillators and NaI calibration (see §4.3.3).

The detailed trigger diagram is available in Appendix A.1. During a normal run all of these 6 triggers are turned on and several of them can be issued at the same time. The rates of the triggers are shown in Table 3.4. The total pion stop rate in the target is ~ 50 kHz.

The trigger signal issued by any of the six triggers mentioned above is then latched by the positron (t_{e^+}) and the pion (t_{π^+}) timings. These latched signals trigger the acquisition of the data. t_{e^+} is used to trigger the data acquisition by the VME modules (VF48 and VT48) while t_{π^+} triggers the COPPERs data acquisition. The different data acquisition modules are described in the next section.

²⁷ $\sim 0.6\%$ of $\pi^+ \rightarrow e^+\nu_e$ events are not recorded by those 2 triggers combined but they can be restored from the prescale trigger information.

3.4. The data acquisition system

Table 3.4: Rate of each trigger.

	Rate [Hz]
Pion stop in target	5×10^4
<i>Physics Triggers</i>	
Early trigger	160
TIGC trigger	170
Prescale trigger	240
<i>Other Triggers</i>	
Cosmics trigger	15
Beam Positron trigger	5
Xe lamp trigger	2
Total Trigger	600

3.4 The data acquisition system

3.4.1 The electronics

COPPER

All the scintillating counter's PMTs are read out by a 500-MHz waveform digitizer (FADC). This FADC system is based on the COPPER (The COmmon Pipelined Platform for Electronics Readout) platform [115]. The detailed characteristics of the COPPER system have been described in [116] but we will summarize the important characteristics here.

COPPER was developed by KEK for the Belle experiment at JPARC. One COPPER board has four frontend modules called "Finesse". Each Finesse can receive two analog input signals. Therefore each COPPER board can receive a total of 8 signals to digitize. The PIENU experiment is equipped with 4 COPPER boards to digitize the signals coming from the 23 PMTs reading out the plastic scintillators and a few other additional signals.

On each Finesse card, two 250-MHz FADC devices are driven in alternating phases in order to obtain 500-MHz sampling. The gains of these two synchronized FADCs are monitored and adjusted on a run-by-run basis using beam particle signals to be able to correctly sample the signal at 500 MHz. Fig.3.25 shows the digitized waveform from a PMT obtained with COPPER.

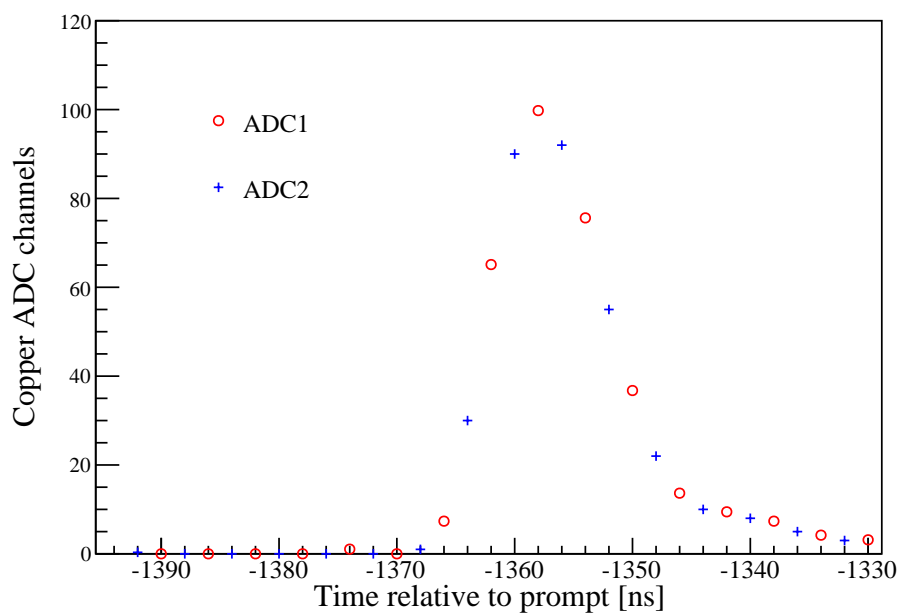


Figure 3.25: A waveform digitized by COPPER. The red circles and blue crosses show the digitization by each of the two 250 MHz ADCs which together produce a 500 MHz waveform.

3.4. The data acquisition system

The time window of the signals recorded by COPPER covers $\sim 8\mu\text{s}$ ($1.35\mu\text{s}$ after and $7.75\mu\text{s}$ before the trigger timing) to be able to detect pile up particles. Data below a certain threshold is suppressed to reduce the data bandwidth. However, no data suppression is applied for a given region around detected peaks to be able to record the ADC baselines (pedestals).

VF48

The VF48 is a 60 MHz FADC single width VME 6-U module which was designed at the University of Montréal in 2004 [117]. It has a resolution of 10 bits and a dynamic range of ± 250 mV. All the NaI and the CsI PMT signals as well as all the silicon channels are read out by this type of module. This makes a total of 404 channels (NaI: 19, CsI: 97, Silicon: 288) read out by 10 VF48 modules (each VF48 module reading out 48 channels). All VF48 modules are fed with the same 20-MHz clock signal provided by the TIGC module, see §3.4.1. This clock signal is multiplied internally in the VF48 to reach 60-MHz sampling. To ensure that the trigger always arrives in the middle of the clock, a synchronization logic is implemented as part of the trigger logic which latches the trigger to the TIGC clock before it goes to the VF48 (see the label “Synchro” in Appendix A.1).

Due to the large number of channels, it was necessary to have the possibility of suppressing (i.e. not reading-out) the channels which did not contain any useful information. Indeed, for a typical event, the energy deposited is recorded in 1 to 2 channels out of the 48 in the Silicon planes and only in 2 to 3 CsI channels out of the 97. All the other channels contain only noise. The implementation of the suppression in the VF48 is rather simple: if two subsequent samples in time have a pulse height difference higher than a given threshold the full waveform is recorded; otherwise no data is recorded for this channel. With the exception of the NaI signals which are always recorded, all channels are suppressed in this way. For the CsI channels the data suppression threshold is set at 5 mV while it is 4 mV for S1 and S2 and 3 mV for S3.

The number of samples recorded by the VF48 is different for each detector: 40 (666 ns), 40 (1333 ns)²⁸ and 70 (1162 ns) samples are recorded for the CsI, NaI and Silicon channels respectively.

²⁸Because the NaI signal is slow the sampling in the VF48 is done at a rate of 30 Hz instead of 60 Hz for the other detectors.

TIGC

TIGC (Tigress Collector) is a VME-based module built and developed by the University of Montréal and TRIUMF for the TIGRESS experiment at TRIUMF [118]. This module enables a summing on-the-fly of the VF48 signals before the read-out. Every 250 ns, the highest samples of the waveforms of all CsI and BINA channels are sent to the TIGC which sums them²⁹ and compares the result to a predefined threshold. This threshold is set to be ~ 4 MeV below the Michel edge. If the threshold is passed, TIGC generates a signal called “*TIGC*” in Fig.3.24 which, if in coincidence with a PIE signal, will start the read-out of the event.

In the PIENU setup the TIGC module also provides the clock to all the VF48 which enables a synchronization of the modules.

VT48

Each of the sensitive wires of the three Wire Chambers and all the logic signals issued by the PMT’s signals after discrimination and some trigger logic signals are read out by multi-hit TDC modules called VT48. This single width VME 6-U module [119] was designed at TRIUMF in 2006 for the KOPIO experiment [120]. The AMT3 chip [121] which was developed for reading out ATLAS muon detector channels is used as a TDC chip on the VT48. This device has a 25-MHz on-board clock which is internally multiplied to achieve 0.625 ns resolution. All VT48s, however, are fed with an external 25-MHz clock to ensure the synchronization of all modules.

One board can read out 48 channels for up to 20 μ s. To optimize the dead-time, only one channel is read out for 20 μ s to detect long-lifetime background originating from the beam while the rest of the channels read out 8.0 μ s before the trigger signal³⁰. However, because of the delay induced by the TIGC decision, the trigger signal arrives in those latter channels at the middle of the VT48 recording window meaning that signals up to 4.0 μ s before and after the trigger signals are read out by the VT48. In total, 11 VT48 modules are used in the experiment.

²⁹The NaI channels and CsI channels have different gains applied to take into account their different Energy/Voltage ratio.

³⁰As will be discussed in §4.7, because the linearity of those modules is not good enough, the data recorded by the VT48 will not be used for the time spectrum analysis. Instead, the information collected by the COPPER modules will be analyzed. However, the VT48s also record trigger logic signals which are of importance for the analysis.

3.4.2 The slow controls

The slow control system records a number of quantities at regular time intervals, typically minutes, to control the data taking conditions. Table 3.5 shows a summary of the main slow control information available.

Table 3.5: Summarized list of slow controls.

Slow control name	Variable
LRS	High voltage of NaI, CsI, scintillators PMTs and Silicon
Postamps	WC postamps thresholds and status
GASDVM	WC gas
M13DVM	WC high-voltage and currents
NMR	Beam magnets NMR
EPICS	Beam magnets current
M13DVM	Beam magnets temperature
M13DVM	Beam magnets voltage
ScalerN	Scalers
Temperature	Temperature of electronic racks and detectors
μ Beam	NMR regulator status
QOD	Online variables based on data
Runlog	Log of the data taking conditions

3.4.3 MIDAS

The PIENU data acquisition system consists of 3 VME crates (2 VMEs host the VF48 and VT48 modules while the third VME mostly runs slow control modules and modules used by the COPPER system) controlled by VME master modules and 4 COPPER boards with a processor on each board. Each processor is running the associated frontend programs to transfer the data to a host computer.

Collection of the data is done by the MIDAS data acquisition system which incorporates an integrated slow control system with a fast on-line database (ODB) and a history system [122]. The MIDAS server computer can be controlled via a web interface. All the information and errors from each frontend are issued on the web page and several programs checking the quality of the data online are connected to MIDAS during data taking.

3.5 History and future of the experiment

The history of the experiment is briefly summarized in Table 3.6. This thesis work covered the detector tests and installation, the setup of the trigger and data acquisition system as well as a significant part of the data taking and its analysis. At the time of writing, at least another year of data taking is foreseen.

Table 3.6: History and future of the PIENU experiment. The greyed area indicates the extent in time of this thesis's work. The numbers in parentheses are an estimate of the number of $\pi^+ \rightarrow e^+\nu_e$ events recorded.

Year	Month	Events
2005	Dec.	Proposal approved by TRIUMF
2006		Detector design and test
2007		Detector construction and beam tests in M9
2008	May	Beam test in M13
2008	Oct.	M13 beam channel extension completed
2008	Oct.-Nov.	Test in M13 with most of the detectors
2009	May	PIENU detector completed
2009	May-Sep.	Run-I (1M)
2009	Oct.-Dec.	Run-II (0.5M)
2010	March	Temperature controlled enclosure completed
2010	Apr.-Sep.	Run-III (4M)
2010	Oct.-Dec.	Run-IV (2M)
2011	Aug.	Systematic studies with beam
2011	Sept-Oct.	Lineshape measurements
2011	Nov.	Run-V (2M)
Future Plan		
2012	Apr.-Dec.	Run VI

Chapter 4

Time Spectrum Analysis

4.1 Overview

This thesis deals with the highest quality data taken to date. The set of selected data ranges from run 49669 to run 52003 (November 2010). This data set contains a total of 1908 good runs which amounts to 586×10^6 events (after the good run selection procedure and before addition of prescaled events). The total raw data size is 3.4 TB.

The raw data are decoded with a program called “proot” which extracts information from the ADC waveforms and TDC hits and stores them in a ROOT [123] tree³¹. Each tree contains over 1500 branches and yield a data size of around 1.3 GB per tree. The trees are then processed with an analysis package which was initially written [124] for the TWIST [125] experiment at TRIUMF and later adapted for PIENU. The outputs of the analysis package are in the form of ROOT histograms.

The first part of this chapter will briefly describe the passage from raw data to trees. In §4.4, the event selection common to the time spectrum and tail correction analyses are developed and from §4.5 the analysis specific to the “raw branching ratio” estimation is described.

4.2 Variable extraction

4.2.1 From VT48

The VT48 records hits in a window from $-3.6 \mu\text{s}$ to $+4.4 \mu\text{s}$ around the prompt which is defined by a “simultaneous” hit in B1 and T1 counters. For Wire Chambers, the hit provides the spatial position information. Based on the Silicon (read out by VF48, see §4.2.3) and Wire Chamber channels

³¹A ROOT tree enables to store information on an event-by-event basis in a structured way. Branches and leaves correspond to different levels of the structure. For example, a tracker would be a branch and the number of tracks recorded by this tracker for a particular event would be stored in a leaf of this branch.

that fired a track is reconstructed. In case of multiple hits (for WCs) or clusters (for Silicon), tracks are constructed with all possible combinations of hits. Information on each track is recorded in the tree [126]. If two adjacent WC wires are fired the track is assumed to have passed in between the two wires giving a factor of two improvement in the resolution. For each reconstructed track, the χ^2 , number of degrees of freedom, residuals and position information are stored.

4.2.2 From COPPER waveform

All hits happening between $-6.4 \mu\text{s}$ prior and $1.35 \mu\text{s}$ after the prompt are recorded by COPPER. Hits are identified by a hit finding algorithm that determines the highest sample before a drop. The time of the highest sample (t_{hit}), the pulse height (PH) and the charge deposited are recorded for each hit. The charge (Q) of each hit is obtained by integrating the pulse between -20 and $+20$ ns around the peak. Fig.4.1 illustrates this procedure. Another charge variable with an extended integration gate is also recorded (Qw: $t_{hit} - 20 < t < t_{hit} + 80$ ns). Several other charge variables at a fixed time (referred to as t_f) with respect to the trigger (corresponding to the pion time, see Fig.3.24) are also calculated. Those are Qf ($t_f - 20 < t < t_f + 20$ ns), Qfw ($t_f - 20 < t < t_f + 80$ ns) and Qfww ($t_f - 20 < t < t_f + 600$ ns). An integration of the full COPPER gate is also recorded (Qfull). For B1, T1 and Tg, a fit of the hit corresponding to the trigger is performed as described in §4.5.1 and §5.1.1. The amplitude, time and χ^2 of each pulse fit is recorded in the tree. The time region $-6.4 \mu\text{s} < t < -2.15 \mu\text{s}$ before the prompt is defined as the “Pre” region. Q, Qw, PH and the time of each hit in this specific region are also stored in the tree with a specific “Pre” flag. Finally, information on potential errors affecting single events are recorded in the tree (e.g. number of samples read out by each channel).

4.2.3 From VF48 waveform

Unlike COPPER, the VF48 only reads out a limited time range, typically $1 \mu\text{s}$ (see §3.4.1 for details) around the hit that generated the positron trigger. Hits are identified by a hit finding algorithm and the charge (Q: $t_{hit} - 5 < t < t_{hit} + 5$ samples³²), pulse height and time are recorded for each hit. Information on the charge deposited before (Qpre: $t_{hit} - 15 < t < t_{hit} - 5$ samples) and after (Qpos: $t_{hit} + 5 < t < t_{hit} + 15$ samples) the pulse is also stored in

³²For simplicity, we now refer to samples as opposed to ns because the NaI VF48 has a different sampling rate.

4.2. Variable extraction

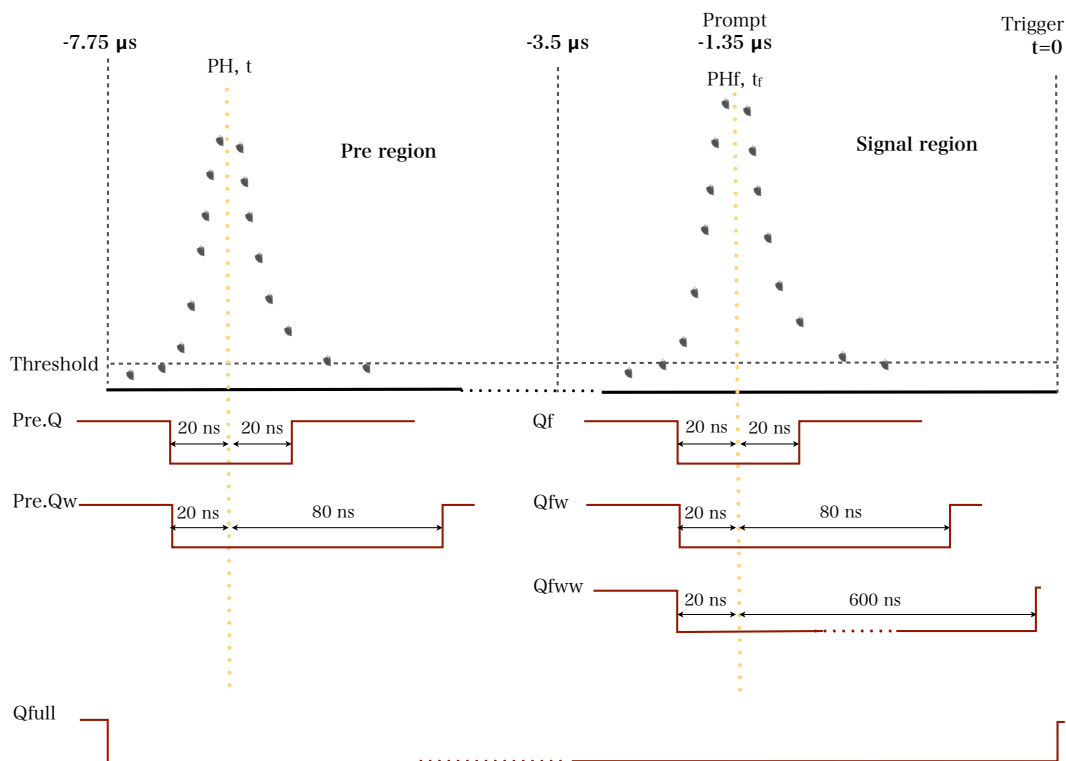


Figure 4.1: Schematic drawing of the variables extraction from a waveform readout by COPPER. In this example two hits were recorded: the hit at prompt time which generated the trigger and a pileup hit earlier.

4.3. Calibration

the tree as well as the charge deposited in extended gates Qw ($t_{hit} - 10 < t < t_{hit} + 10$ samples) and Qww ($t_{hit} - 10 < t < t_{hit} + 25$ samples). The latter variable is particularly useful for the NaI pulses which are very broad. Similarly to COPPER, charge variables at a fixed time (corresponding to positron time) are also recorded. Those include Qf ($t_f - 5 < t < t_f + 5$ samples), Qfw ($t_f - 10 < t < t_f + 10$ samples), Qfpos ($t_f + 5 < t < t_f + 15$ samples), Qfpre ($t_f - 5 < t < t_f$ samples), Qwwf ($t_f - 10 < t < t_f + 25$ samples). For every event the hit corresponding to the trigger is fitted for each NaI tube. Amplitude, time, χ^2 and the value of the fitted pedestal are recorded in the tree. The extraction of the charge deposited and the position of the hit in the silicon is more complex due to the charge division circuit. Hits on adjacent strips are clustered. For each cluster, the two strips in which the highest charge (Q: $t_{hit} - 128 < t < t_{hit} + 128$ ns) was deposited are tagged (they will be called “high-strips” in the rest of this thesis). Fig.4.2 shows the charge deposited in the two high-strips (“left” and “right” indicate their respective position). Events are clustered in bands which are representative of their positions with respect to the high-strips. The ratio of the amplitudes in the two high-strips are compared to estimate the position of the hit with a resolution of $\sim 95 \mu\text{m}$ ³³. The time of the hit is the average of the time recorded in the high-strips weighted by their respective charge. The number and size (corresponding to the number of strips hit) of clusters are also recorded.

The charge variables extracted from COPPER and VF48 are used to construct calibrated energy variables which are also stored in the tree. The section below details how the calibrated variables are constructed.

4.3 Calibration

4.3.1 ADC and pedestal calibration

As mentioned in §3.4.1 COPPER ADC have to be calibrated before waveform reconstruction. Each ADC gain factor is calculated based on the height of a physical pulse. The pedestal of each ADC is recorded in the tree for a cross-check.

In every run and for each ADC channel (COPPER and VF48) the pedestal is calculated based on the mean of the distribution of the first three samples

³³This resolution is reached if at least two strips are fired. It corresponds to the resolution on the readout strip ($1.28\text{mm}/\sqrt{12}$) divided by four. If only one strip is hit, the resolution is $1.28\text{mm}/\sqrt{12}=0.37$ mm.

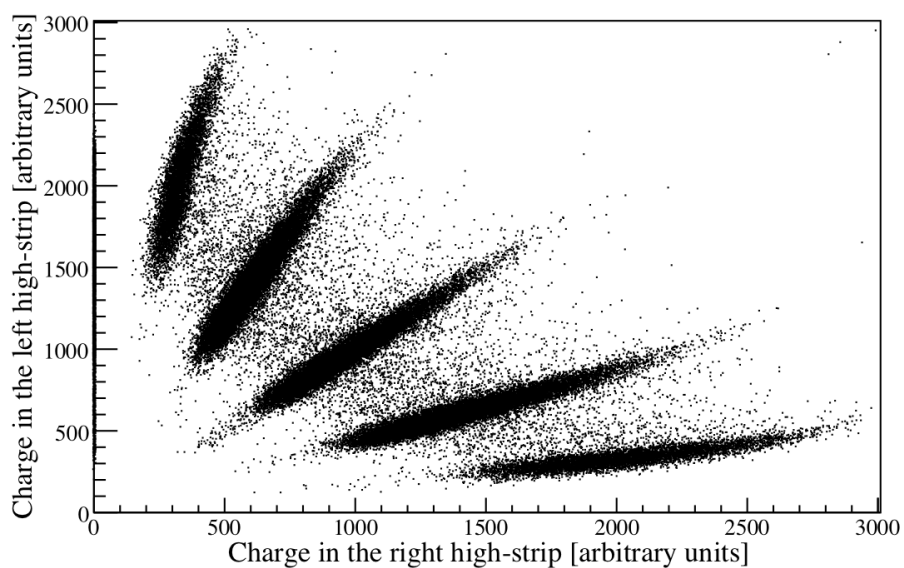


Figure 4.2: Charge deposited in the left “high-strip” versus the right “high-strip” (see text). The events in which only one strip fired appear as no charge in the right strip. Those events represent about 9% of the total number of events.

of the waveforms. This has the advantage over an event-by-event pedestal estimation to be insensitive to pileup. For the NaI and CsI pulses a flag is recorded in the tree in the case of a sudden change in the pedestal affecting three consecutive events. The pedestal is subtracted from the waveforms before the extraction of charge and PH variables.

4.3.2 Gain stabilization

Scintillators

For all counters read out by PMTs (except CsI which is the subject of the next paragraph) the charge deposited by beam particles is used for gain calibration. The beam positron (for the NaI), beam pion (for B1 and B2) and beam muon (for the target and T1) peaks are monitored every run. An automatic gain calibration is made based on the fluctuation of those peaks positions compared to a reference run. Due to the strong position dependence of T2, the gain calibration of its PMTs is done with decay positrons from the $\pi^+ \rightarrow \mu^+ \rightarrow e^+$ decay chain selecting their entrance position with a cut on WC3.

CsI

Each CsI PMT is connected to a Xe lamp through a quartz fiber. The pulse height of the Xe lamp signal in each PMT is compared run by run to a reference run in order to adjust for the PMTs gain fluctuation³⁴. Cosmic signals are used to trace the changes in CsI properties, see §4.3.3. The Xe reference run has to be regenerated every 20 runs due to the energy calibration procedure (see §4.3.3 for details).

Silicon

A calibration pulser is connected to the amplifier of all silicon channels. Every run, the charge recorded by each silicon detector is multiplied with the ratio of the calibration pulse signal of this run to the calibration pulse signal from a reference run. There is, therefore, for every run, a gain factor for every silicon strip (288 in total). This calibration procedure only corrects gain changes in the amplification electronics. It is not sensitive to changes in the silicon properties. The charge to energy ratio in the silicon itself is

³⁴The YAIO signal (see §3.2.6) could potentially be used to trace the change in the CsI light transmission. However, in order to see the signal from those radioactive sources a self trigger should have been implemented for each crystal.

expected to change because of temperature fluctuations, voltage fluctuations or degradation in the silicon due to radiation damage. Voltages and temperatures in the area are recorded for every run, see §3.4.2 so that the causes of the silicon properties changes, if any, could be at least partially identified and corrected for in offline analysis.

4.3.3 Energy calibration

Plastic scintillators

The energy calibration is based on the amount of energy deposited by a minimum ionizing particle (beam positrons) traversing a known amount of scintillator (Polyvinyltolulene). It has been calculated using the PDG value and checked with a MC simulation in which Birk’s correction [127] was applied.

Silicon

The energy calibration is based on the amount of energy deposited in the “high-strips” by a minimum ionizing particle traversing a silicon wafer. As for other detectors, this energy calibration factor has been calculated from PDG data and checked against MC predictions.

CsI calibration

Each CsI crystal is energy calibrated using cosmic rays. A cosmic trigger is set in parallel to the physics trigger (see §3.3) enabling a new cosmic calibration every 20 runs³⁵. The cosmic peak in each crystal is associated with the energy deposit predicted by a simulated cosmic shower using the CRY package [128]. This package is used to generate correlated cosmic-ray particle showers at sea level and at the latitude and longitude coordinates of the PIENU experiment. Fig.4.3 illustrates the agreement between the cosmics simulation and the data. Although the peak positions vary up to 20% with the position of the crystal in the detector enclosure as shown in Fig.4.4, the peak position is well reproduced in MC.

In summary, every run, the charge deposited in each CsI crystal is multiplied by a factor f :

$$f = \frac{\text{Cosmic}_{MC}}{\text{Cosmic}_{data}} \frac{\text{Xe}_{ref}}{\text{Xe}} \quad (4.1)$$

³⁵20 runs were needed to collect enough cosmic events for a reliable calibration.

4.3. Calibration

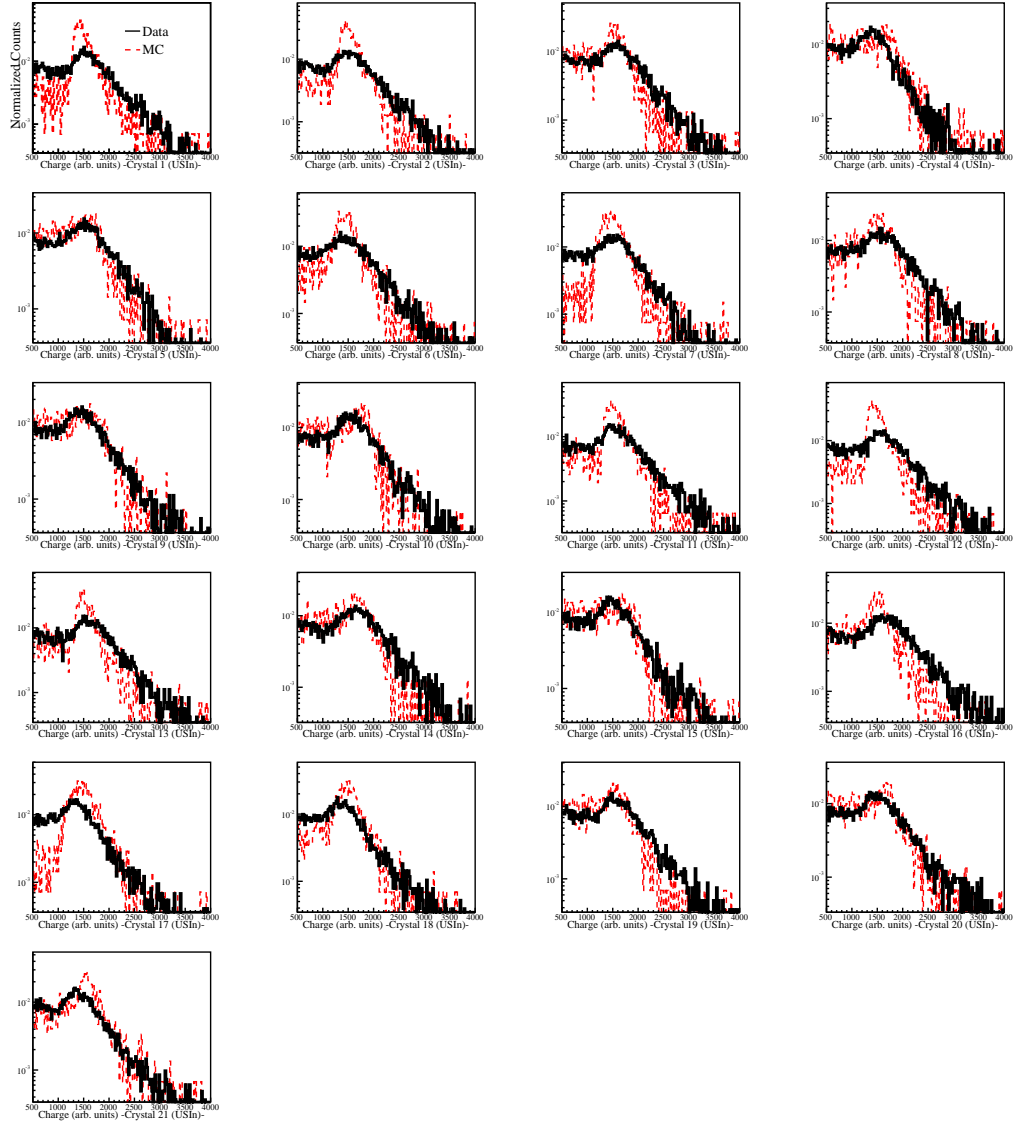


Figure 4.3: Comparison of the cosmic signal in each CsI crystal of the inner upstream part between data (black solid line) and MC (hatched red line). In this figure, the MC was not corrected for energy resolution.

4.3. Calibration

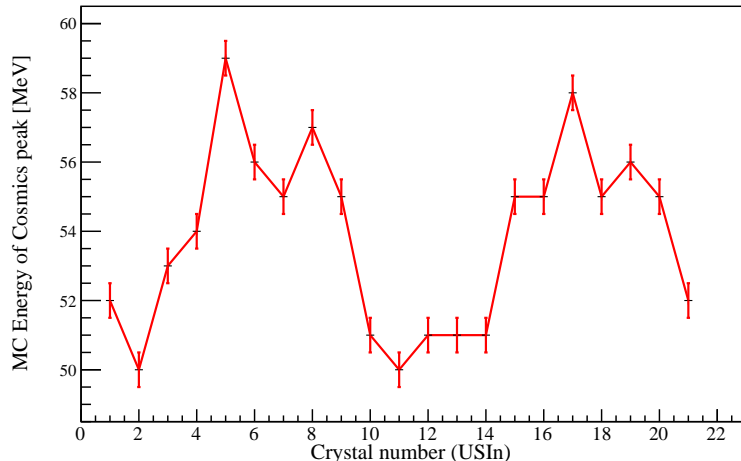


Figure 4.4: Variation of the cosmic peak energy with the CsI crystal position as obtained with the CRY cosmic simulation package. The error bars indicate the width of the cosmic distribution.

where Cosmic_{MC} is the predicted energy deposited in the crystal by MC. This factor was calculated once for the entire run range. Cosmic_{data} is the result of the fit of the cosmic distribution shown in Fig.4.3. Xe refers to the peak of the Xe lamp signal extracted every run as mentioned earlier, and Xe_{ref} is the same peak from a reference run. The reference run is renewed every 20 runs at the same time as the new cosmic calibration is obtained; this is done to avoid double counting of PMT's gain fluctuations. Indeed, the Xe signal only tests the stability of the PMT and is used to trace the change in the PMTs gain on a run-by-run basis. The cosmic signal also traces gain fluctuations in addition to changes in the crystal's light emission efficiency. Therefore, if the ratio of Xe signals, $\frac{\text{Xe}_{ref}}{\text{Xe}}$, is not set to 1 when the new Cosmic_{data} value is available, the potential PMT gain fluctuation would be accounted for twice. With this method, the PMT's gain fluctuations are corrected for on a run by run basis while the crystal's property changes are corrected every 20 runs. The ratio of Xe to Cosmics is very stable for the range of runs used in this analysis showing that there is no change in the crystal's properties over this run period.

NaI calibration

The energy calibration in the NaI is based on the total energy deposited in the downstream part of the detector by $\pi^+ \rightarrow e^+\nu_e$ events. The total energy should be equal to 70.3 MeV³⁶. In order to measure the full energy deposited by decay positrons the energies recorded by S3, T1, T2 (~ 2.5 MeV) are added together. The mean energy deposited in the target (~ 1 MeV) and the front face of the NaI is obtained from MC. The addition of all those is used to set the energy calibration for the NaI. The NaI calibration thus obtained was checked against the MC. The alignment of all physical pulses ($\pi^+ \rightarrow e^+\nu_e$ peak, beam muons, beam positrons and Michel edge) was also confirmed. For reference, Fig.4.5 shows the sum of the energy deposited in the downstream material³⁷ (including the aluminium front face of the NaI crystal in which positrons deposit an average of 0.22 MeV) by $\pi^+ \rightarrow e^+\nu_e$ positrons in MC. The structures seen in this spectrum are detailed below.

- I. 70.3 MeV is recorded which corresponds to the full kinetic energy of the positron plus twice the positron mass (corresponding to the mass of the positron and of the electron from the annihilation). Since the energy deposited in the Mylar foils is not added, these events correspond to positrons which have not hit WC3.
- II. The positrons go through WC3. The 50 keV deposited in the Mylar foil is missing.
- III. One 511 keV γ from an annihilation escapes the assembly.
- IV. Two 511 keV γ 's escape the assembly.

4.4 Event selection

Before the event-by-event selection, an automatic run selection was done to eliminate corrupted runs.

³⁶The positron kinetic energy amounts to 69.3 MeV to which is added the 511 keV rest mass of the positron and 511 keV rest mass of the electron with which the positron annihilates.

³⁷only the energy deposited in the Mylar foils of WC3, typically 50 keV, was not added.

4.4. Event selection

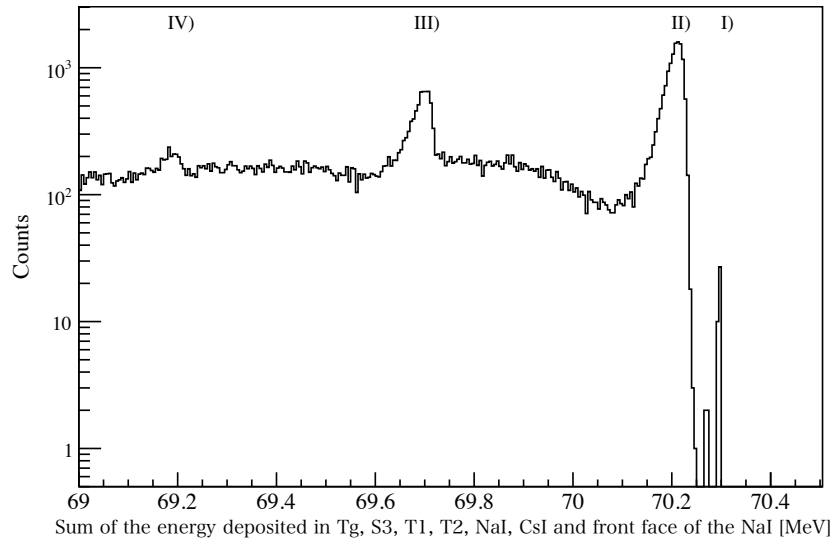


Figure 4.5: Sum of the energy deposited in the downstream material from MC.

4.4.1 Quality of data

DAQ errors

The runs with DAQ-related errors (no trigger received by one of the DAQ system, header or trailer not correct, etc.) are removed from the run selection. In total, 146 runs are affected by COPPER-related errors, 78 by VF48 and 125 by VT48. Since multiple types of DAQ errors appear per run, this DAQ selection only removes a total of 179 runs out of the initial 2334 runs. Since most of those runs are short, this run selection does not have a large impact on the data sample size.

Other run selection

Muon runs are taken for 8 hours every week (see §4.7 for details); those runs are removed from the nominal run selection. Runs much longer than usual indicate a major change in the beam rate (beam off during the run, beam intensity drop, maintenance runs) and are discarded. Runs with a prescale factor different from 16 indicate a non-nominal trigger setting (for special data or tests) and are also discarded.

Close to 200 histograms were generated every run and verified to make the

4.4. Event selection

data selection and identify possible problems. Fig.4.6 shows an example of the stability information provided by a set of such histograms. The left plot represents the average number of hits in S3_X as a function of run number. The dotted red lines show the 2.5σ around the average value indicated in a solid green line. Runs for which variables are clearly different from the average are removed. In general, the data selection is based exclusively on variables corresponding to detectors upstream of the target. The stabilities of downstream variables are also examined for indication of problems. An example of a problem detected by this procedure is illustrated in the right plot of Fig.4.6. This plot shows a clear jump in the average stopping point

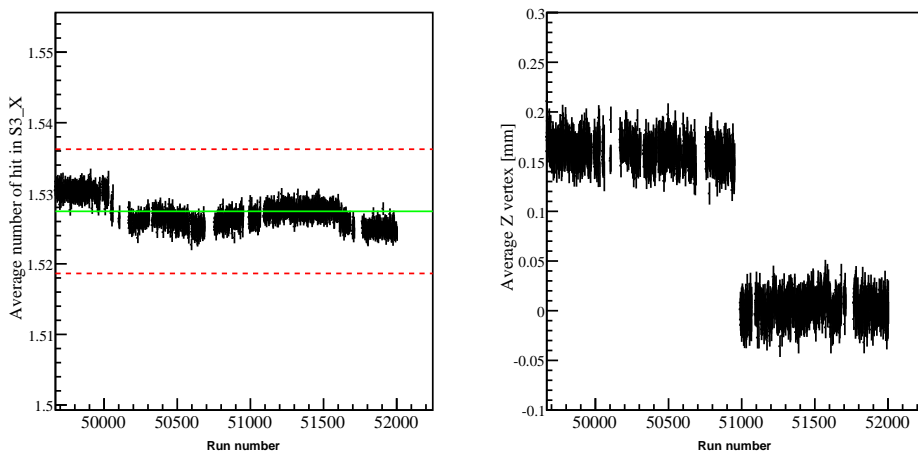


Figure 4.6: **Left:** Average number of hits in S3_X as a function of run number. **Right:** Average z vertex as a function of run number. Those plots span the entire data range used in this analysis. The four ranges of runs missing correspond to the special muons runs taken weekly, see §4.7.

of pions in the target³⁸ which happened at the middle of data taking. This was due to a wrong position of *F1SL* slit which defines the momentum distribution of the beam, see Fig.3.1. The nominal z-vertex position during 2010 data taking was $-0.80\mu\text{m}$ from the center of the target. The displacement in the z-vertex induced by this wrong setting is circa $+180\mu\text{m}$, which

³⁸The z vertex is the z coordinate of the point of minimum distance between tracks entering the target and tracks exiting it.

4.4. Event selection

corresponds to a momentum change of $\Delta p = +0.3\%$ ³⁹. The z-vertex stability plot also enabled the detection of a 3 mm change in PIENU-II detector position during the summer 2010 data taking.

A total of 426 runs (which amounts to $\sim 18\%$ of the total number of runs) are removed based on the criteria discussed in this section. The next section will describe the event selection.

4.4.2 Pion selection

The selection of pions is based on energy loss in B1 and B2 and time-of-flight (TOF) measured in B1 with respect to the primary proton beam burst. Fig.4.7 shows the energy deposited in B1 versus the TOF modulo the cyclotron radio frequency ($f \sim 23.1$ MHz \rightarrow T ~ 43.3 ns). The firing of a “physics trigger” (TIGC, Early or Prescale) is also required and all events for which a calibration trigger (cosmic, beam positrons, Xe lamp) fired are excluded.

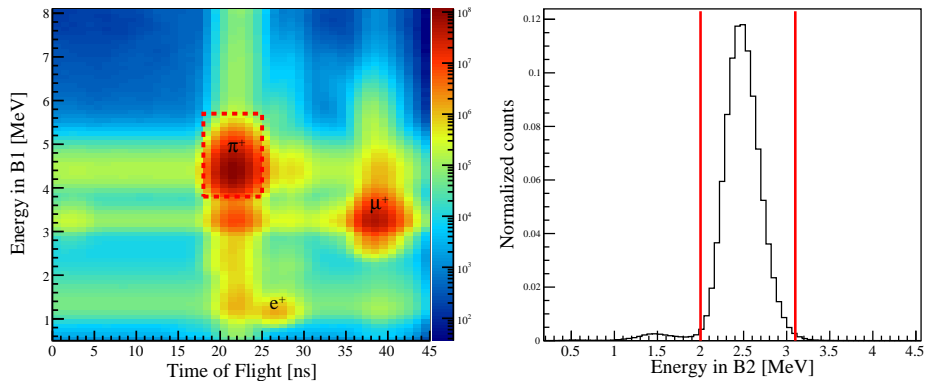


Figure 4.7: **Left:** Energy deposited in B1 versus the Time of flight. The spectrum has been slightly smoothed for better visualization. The red hatched box indicates the selected events. Events which have the same TOF as pions but lower energy deposit in B1 correspond to PDIF events before B1. **Right:** Energy deposited in B2 after B1/TOF cut. The red lines indicate the cut value.

³⁹As will be seen in §5.2.1 this change in momentum has a negligible effect on the acceptance correction. The energy calibration is however adjusted to take into account the change in energy of the beam particles used for calibration.

4.4. Event selection

A cut⁴⁰ on the beam profile in WC1 and WC2, Fig.4.8, is also done to remove particles (mostly positrons and muons) which had peculiar trajectories in the beamline. This cut also minimizes the tail of the pion momentum distribution. Additionally, events in which a hit is recorded in the V1 counter (which covers the frame of WC1) are removed. Using track reconstruction based on WC1 and WC2, a cut on the position of pion stop at the center of the target is made to exclude pion events stopping close to the edge of the target.

After this selection, the pulse in B1 which is synchronized with the trigger time (t_π) is associated with the pion event time.

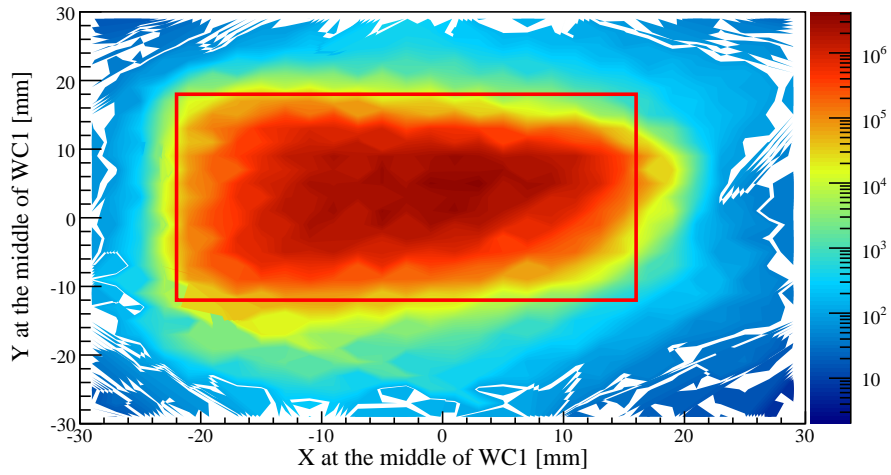


Figure 4.8: Contour plot of the beam profile at the centre of WC1. The red box indicates the boundaries of the cut (a similar cut is made on the beam profile at the centre of WC2).

4.4.3 Decay positron selection

A minimal number of cuts are applied on the decay positron information in order to minimize potential biases on the branching ratio.

1. A low energy cut is applied on T1 counter ($E_{T1} > 0.3$ MeV) to remove events which produced a trigger by hitting T1 light guides.

⁴⁰A cut is a selection applied to the data.

2. Pion interactions with nuclei of the target lead to the emission of protons. In the NaI, those protons have a very broad energy distribution spanning energies from a few MeV to above 100 MeV. Protons deposit a large amount of energy in the downstream counters which is anti-correlated with the total energy deposited in the NaI. They therefore appear as a band in the plot of the energy loss in the downstream counters⁴¹ as a function of the energy deposited in NaI, Fig.4.9. This cut mostly removes events which have prompt timing. Only 0.008% of events removed by this cut lie outside the prompt. The energy dependence of this cut can therefore be neglected.
3. Events in which at least one T1 pulse is in coincidence with the pion time are rejected. This cut removes muons from PDIF events which stop in T1 counter. Those events can decay and produce a trigger if the decay positron hit the T2 counter within 200 ns after the muon stop in T1. Since, in this case, T2 and T1 triggers have different timings, the trigger time is defined by T2 instead of T1. This has the effect of changing the trigger gate time by up to 200 ns. Although the number of muons from PDIF that reach T1 counter is very small, the impact on the time spectrum was found to be large due to the distortion it creates in the early time region.

4.4.4 Background rejection

Events in which pile-up is present are removed by the following set of cuts. Unless otherwise specified, the cuts are applied on COPPER variables only.

Beam Pile-Up Cut

1. At least one of B1 channels is required to have only a single hit in the COPPER inspection window. This removes multiple pion events but avoids the elimination of the events due to a noisy channel.
2. The fit in all B1 channels is required to have a good χ^2 . This eliminates cases in which two pulses are very close to one another and therefore not detected as multiple hits by the hit finding algorithm.
3. Further removal of pile-up close to the trigger pulse is reached by the study of the ratio: Q/Q_w in all of B1 and B2 channels. Upper

⁴¹For better separation of signal and background, the minimum energy deposited in the downstream counters is used.

4.4. Event selection

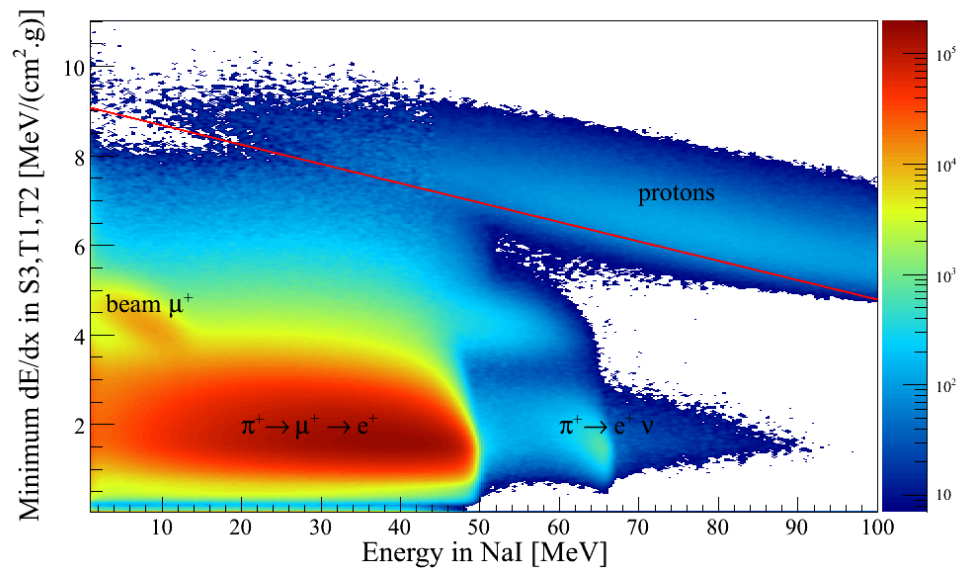


Figure 4.9: Scatter plot of the minimum energy deposited in the downstream counters (S3, T1, T2) as a function of the energy deposited in the NaI. The amplitude of this distribution is plotted on a logarithmic scale. The red line indicates the cut value.

and lower boundaries on this ratio are used to remove pile-up events. Events in which two pions arrive at the same time are removed by the previously mentioned TOF/B1 cut.

4. No hit in the “Pre” region ($-6.4 \sim -2.15 \mu\text{s}$ before the prompt) for all B1, B2 and Tg counters is required.
5. An additional pileup cut for beam muons hitting B1 up to $15 \mu\text{s}$ before the prompt is made (using a special VT48 channel with a longer inspection window). Those beam muons reach the NaI and can decay in the inspection window for decay positrons. In this case, the energy they deposit in the calorimeters is added to the one of the decay positron creating a pile-up event in the calorimeter which is not detectable by the scintillator counters. This cut also reduces by a factor 2 the level of “old muons”⁴² in the target originating from both beam muons and pions stopped in the target.

“Decay” Pile-Up Cut

1. Events which have a hit in V2 and V3 counters earlier or later than the positron time ($t < t_{e^+} - 20 \text{ ns}$ or $t > t_{e^+} + 20 \text{ ns}$) are rejected. This cut eliminates pile-up events due to charged particles hitting the flanges of the NaI and WC3 but retains shower leakage and Bhabha-scattering (positron-electron scattering) events. In the latter case, the scattered electron could generate a hit in the veto counters.
2. Events which have a hit in the “Pre” region in any of T1 or T2 channels read out by COPPER are removed.

Neutral Pile-Up Cut

“Neutral” pile-up refers to events that are not detected by the plastic scintillators but deposit energy in the calorimeters. Those can be neutral or charged particles.

Neutral particles (neutrons and γ -rays) emitted from the production target (BL1A-T1) and other sources in the beamline can reach the calorimeters. Their time distribution is mainly constant.

⁴²“Old muons” are muons coming from the beam or from a beam pion decay that hit the upstream scintillator counters without being recorded by the data acquisition system. Their decays in the direction of the downstream trigger counters around the time of a pion trigger create backgrounds to the measurement of the branching ratio.

4.4. Event selection

Neutral pile-up can also arise from γ particles emitted either during radiative decays or annihilations. In order to avoid removing radiative or annihilation components which could introduce an energy dependence, no neutral pile-up cut is applied in the calorimeters. However, due to the finite integration window in CsI and NaI, a time dependence for the detection of “neutral” pile-up is introduced. This is particularly important in the case of old muon pile-up in the “high-energy” time region and for $\pi^+ \rightarrow \mu^+ \nu_\mu \gamma$ followed by $\mu^+ \rightarrow e^+ \nu_e \bar{\nu}_\mu$ decays for which the γ and e^+ have different timings. Those two backgrounds will be discussed in §4.5.3.

Charged particles (π^+ , μ^+) coming earlier than our detection gate and stopping near the NaI and CsI also contribute to the “neutral” pile-up. Their decay around the trigger time adds energy in the calorimeters. As mentioned in the previous point, this type of neutral pile-up is reduced by a time cut on B1 read-out by an extended window. However, this special VT48 channel only records hits with muon energy deposit in B1. A pile-up component from early beam pions stopping in the target and decaying around the trigger time into the CsI and NaI is found to be large⁴³; its amplitude is of the order of 1% of $\pi^+ \rightarrow e^+ \nu_e$ events. To reduce this component by an order a magnitude, a cut on the number of hits recorded by T1 counter is implemented: events which have more than one hit in all of T1 channels are removed.

4.4.5 Acceptance cut

Because of the geometrical arrangement and shapes of the downstream counters as well as the width of the beam stopping distribution in the target, a radial acceptance cut in WC3 has to be made in order to insure that the decay positrons hit all the downstream counters (see §5.3.1). A tight acceptance cut also reduces the tail correction. Due to the small solid angle at small radii, a tight acceptance cut also leads to a large loss of data. Considering those arguments, the optimal radial cut was found to be $R=60$ mm for this set of data. The radial distribution in the middle of WC3 (using track reconstruction) is shown in Fig.4.10 together with the acceptance cut. It is important to note that no requirements are made on the number of tracks in the downstream tracker in order to keep Bhabha scattering events. In case of multiple tracks, the track with the best χ^2 is used to define the

⁴³This component cannot be removed by a cut on the number of hits in the target since it has a large bias on the branching ratio.

4.4. Event selection

acceptance. If one tracking plane has no signal (because of inefficiency) and multiple tracks are found, no χ^2 ordering of the tracks can be done. In this case, an arbitrary track would be chosen for the $\sim 0.4\%$ of the events that fall in this category. To allow the selection of the best possible track for those events, the target is added as a tracking device. The position of the hit in the target is assumed to be at the centre of the target and the error on the position is taken as half the target size. This implementation does not have any effect on the radial distribution for “normal” tracks where no plane is missing and enables the discrimination of very improbable tracks when one plane is missing using χ^2 information.

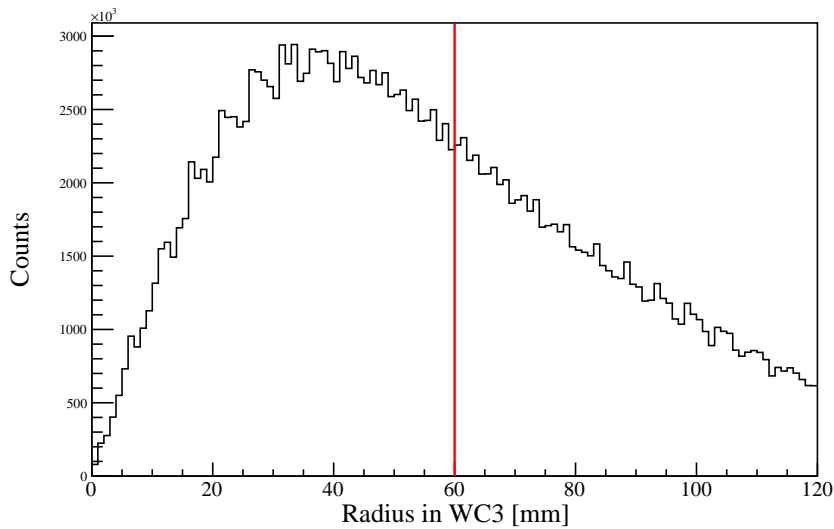


Figure 4.10: Radial distribution of events at the middle of WC3. The red line indicates the acceptance cut. The spikiness of the distribution is due to the resolution of the downstream tracker which is dominated by the WC3 wire pitch.

4.4.6 Summary of all selection cuts

The selection cuts remove $\sim 75\%$ of the events. The two major rejective cuts are the pion selection cuts and beam pile-up cuts. The combination of those rejects $\sim 60\%$ of the initial events. After all pile-up cuts, the acceptance cut rejects another $\sim 40\%$ of the events. Fig.4.11 shows a summary of the

fraction of events removed by each cut.

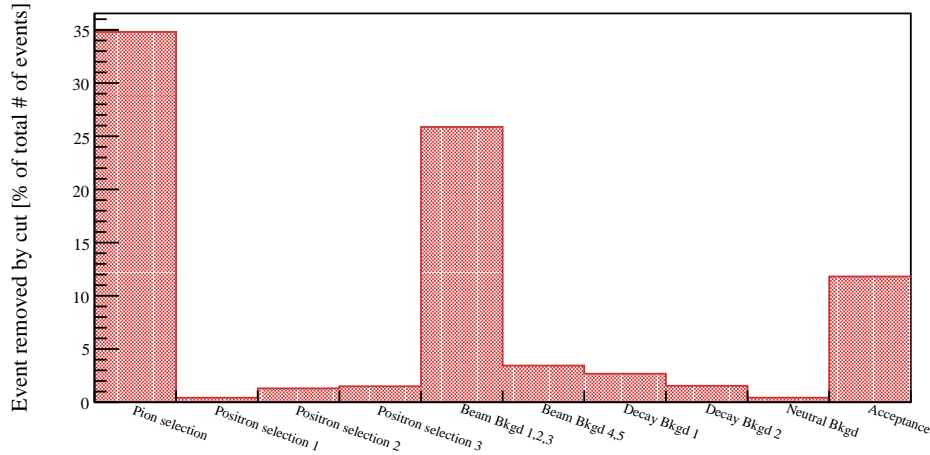


Figure 4.11: Summary of the fraction of events removed by each cut. The x-axis labels refer to the numbering in each sections.

After all selection cuts, the shape of the background to $\pi^+ \rightarrow e^+ \nu_e$ events in the “high-energy” region ($E_{NaI+Csl} > 50$ MeV) is consistent with the expected shape obtained from late muon decay events as shown in Fig.4.12.

4.5 Timing fit: extraction of the raw branching ratio

4.5.1 Pulse shape fitting

Every event, the pulses with the pion and positron timings are fitted in each PMT of B1 and T1 counters respectively. The fit template is obtained from a spline interpolation of the average PMT pulse shape [129, 130]. Fig.4.13 shows the average pulse shape in B1 and Fig.4.14 is an example of a pulse fitted with the template. The arithmetic mean of the four PMT times is taken as the counter time. The time resolution on the difference of T1 and B1 time thus obtained is 270 ps.

4.5. Timing fit: extraction of the raw branching ratio

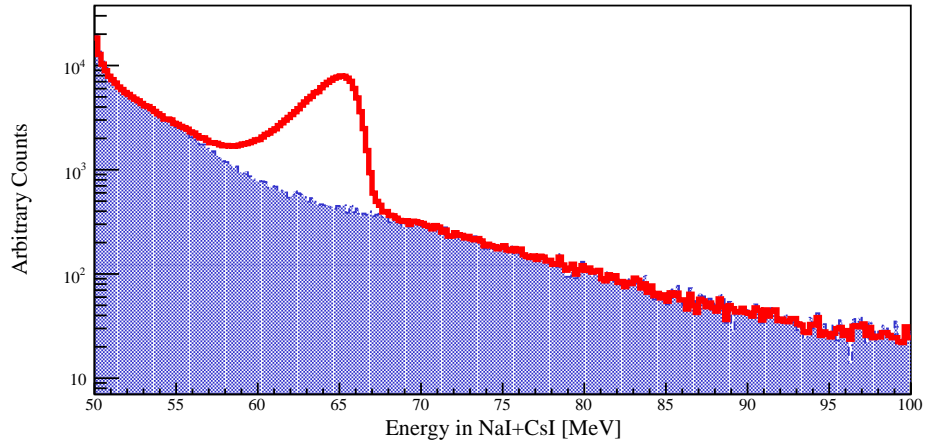


Figure 4.12: Comparison of all events with energies larger than 50 MeV in the calorimeters ($E_{NaI+CsI} > 50$ MeV) with late muon decay events ($t_{T1} - t_{B1} > 300$ ns). The red thick line shows the distributions of events for which $E_{NaI+CsI} > 50$ MeV, the shaded spectrum is the distribution of late decay events. The two spectra are normalized to the total number of events in the energy region $E_{NaI+CsI} > 75$ MeV.

4.5. Timing fit: extraction of the raw branching ratio

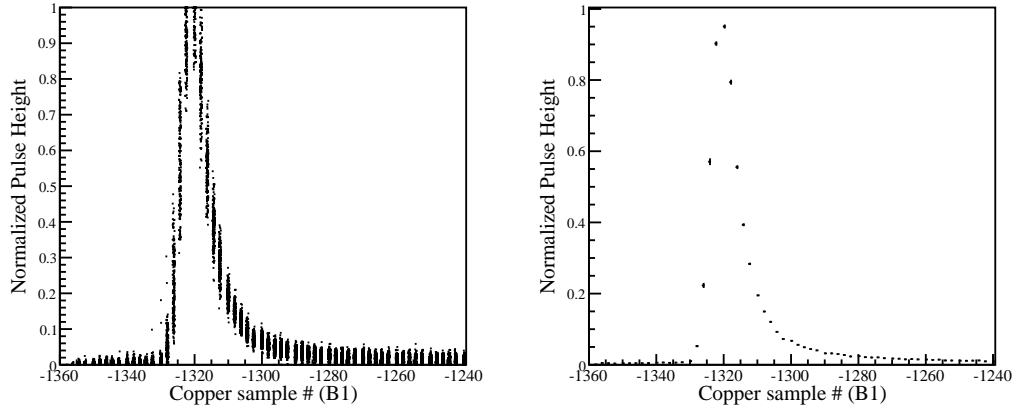


Figure 4.13: **Left:** Two dimensional histogram of the distribution of pulse height versus time for events in B1 which generated the trigger. **Right:** The average of the left histogram. This is the discrete template on which the spline interpolation is done, see Fig.4.14.

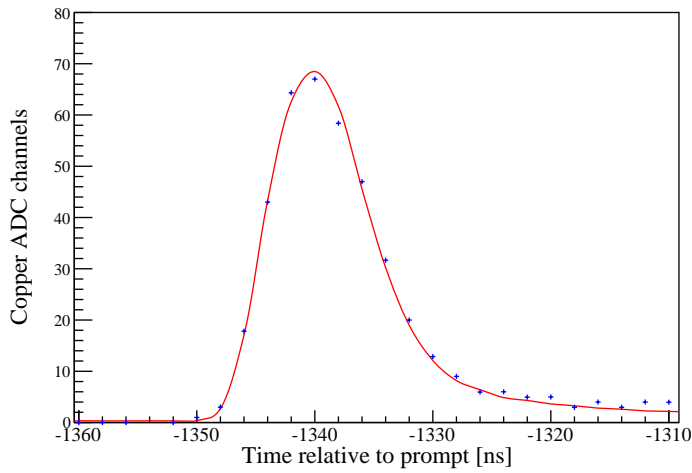


Figure 4.14: COPER 500 MHz waveform fitted with a template formed by a spline interpolation of the discrete template shown in the right plot of Fig.4.13.

4.5.2 Construction of the time spectra

Only events which passed the blinding procedure described in §1.3 are selected to produce the histograms used for the time spectrum fit thus blinding the result on the raw branching ratio.

Events are separated in “high-energy” ($E_{NaI+CsI} > 50$ MeV), and “low-energy” ($E_{NaI+CsI} \leq 50$ MeV) regions. The high-energy and low-energy regions are associated with $\pi^+ \rightarrow e^+ \nu_e$ and $\pi^+ \rightarrow \mu^+ \rightarrow e^+$ decays respectively. Events in the high-energy region are required to have fired the *TIGC* trigger. Events in the low-energy region are triggered by the *Early* trigger (in the early time window) and the *Prescale* trigger. Outside the boundaries of the early time region, the prescaled events are added 16 times to the spectrum and errors on each time bins are inflated accordingly. Fig.4.15 shows the thus obtained high and low-energy time spectra in which events in the time region $t_0 - 6 < t < t_0 + 4$ (where t_0 is the time of pion stop) are removed.

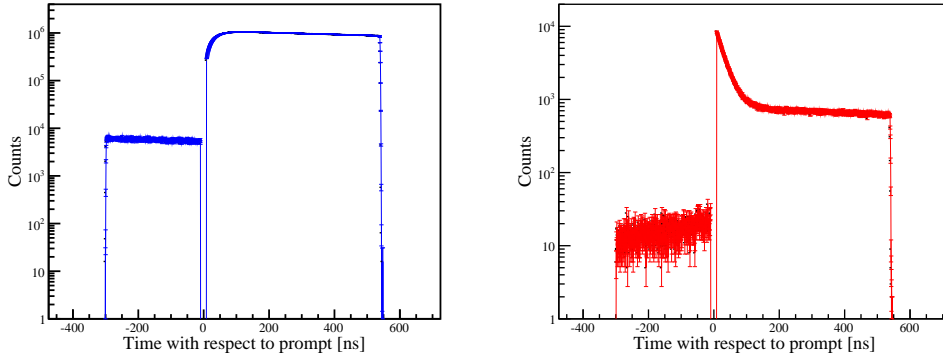


Figure 4.15: **Left:** “low-energy” time spectrum on a logarithmic scale. **Right:** “high-energy” time spectrum on a logarithmic scale. In both spectra the prompt events have been removed. See text for details on the construction of these spectra.

4.5.3 The fit

The spectra shown in Fig.4.15 are fitted in the following time regions:

- Prior to the prompt ($t < 0$): -290 to -15 ns
- After the prompt ($t > 0$): 4 to 510 ns

which avoids the time close to the prompt region where distortions could be present. The region $t < 0$ reflects the level of background in the region $t > 0$. Before detailing the fit functions used, we will briefly describe the different backgrounds present in each spectrum.

Time spectrum for $E_{NaI+CsI} \leq 50$ MeV

- I. For $t < 0$, the spectrum is dominated by the decay of so-called “old-muons” coming from the beam (or decay of beam pions) which stopped in the target or surrounding materials. Since this background comes from the beam, it is replenished every 43 ns and should contribute as a flat component to the time spectrum. However, the rejection of any event with an additional hit in a fixed inspection window extended to $6.4 \mu\text{s}$ prior to the prompt means that no further supplies of beam particles can add to the background after this time. The remaining background therefore follows an exponential decay with the muon lifetime. The probability of a decay from an “old-muon” originating from beam pions stopped in the target remaining after this pile-up cut is of the order of 0.8% which is consistent with the observed amplitude in Fig.4.15.
- II. In the $t > 0$ region:
 - (1) The spectrum is dominated by PDAR-MDAR events. A negligible portion of $\pi^+ \rightarrow e^+ \nu_e$ tail and MDIF which both decay with the pion lifetime can be ignored in the $\pi^+ \rightarrow \mu^+ \rightarrow e^+$ fit.
 - (2) A non negligible fraction, of the order of 1.2%, of PDIF-MDAR is present in the spectrum. This background starts at $t=0$ and decays with the muon lifetime.
 - (3) The background component coming from old muons identified in the $t < 0$ region is also contaminating the $t > 0$ region.

Time spectrum for $E_{NaI+CsI} > 50$ MeV

- III. In the $t < 0$ region:
 - (1) The spectrum is dominated by an “old-muon” background with an additional pile-up that causes the event to pass the cut-off energy. In this case, the pile-up event consists mostly of the actual $\pi^+ \rightarrow \mu^+ \rightarrow e^+$ decay which happens after the prompt generated by the incoming pion. The time spectrum of this “old-muon”

4.5. Timing fit: extraction of the raw branching ratio

background should be proportional to $e^{\frac{-t}{\tau_\mu}}$ where τ_μ is the muon lifetime. However, the amplitude of this background rises as the time of the positron hit approaches the prompt. This can be explained by the large (close to 1 μ s) integration window of the NaI pulse. Indeed, as the decay time of the “old-muon” approaches the prompt, the probability that the energy deposited in the NaI by the “real” pion decay happening after the prompt is added to that of the positron from the “old-muon” decay increases. This component was suppressed by an order of magnitude by a pile-up cut in T1 counter. The amplitude of the remaining pile-up source is of the order of 0.1% of $\pi^+ \rightarrow e^+\nu_e$ events and comes from decay positrons at high angles which miss the T1 counter but hit the NaI.

- (2) An additional component to this background appears at $t \sim -80$ ns when the energy deposited in the CsI by a positron from a “real” pion decay starts to be added to the energy deposited in the NaI and CsI by the positron from the “old-muon” decay.
- (3) Another background comes from $\mu^+ \rightarrow e^+\nu_e\bar{\nu}_\mu$ decays depositing more than 50 MeV in the calorimeters. The source of this background is multiple:
 - Because of the poor CsI resolution and the finite NaI resolution, $\pi^+ \rightarrow \mu^+ \rightarrow e^+$ events leak into the high energy region.
 - The source attached to the CsI adds ~ 8 MeV to the energy deposited by positrons from $\mu^+ \rightarrow e^+\nu_e\bar{\nu}_\mu$ decay and contributes to $\mu^+ \rightarrow e^+\nu_e\bar{\nu}_\mu$ events passing the energy threshold⁴⁴. Since the CsI source pileup is random in time, this component follows an exponential decrease with the muon lifetime.
- (4) Finally, muon radiative decays can deposit more than 50 MeV if the energy of the γ is recorded in the calorimeters. This component also follows an exponential decrease with the muon lifetime.

IV. In the $t > 0$ region:

- (1) $\pi^+ \rightarrow e^+\nu_e$ events manifest themselves in the time spectrum as an exponential decay with the pion lifetime. PDAR-MDIF events

⁴⁴The source present on each CsI crystal (with a total rate of 5 kHz) contribute to a large source of background if all energies recorded by the CsI crystals are added to the NaI. To reduce this component only energies which were deposited in the CsI in a short time window around the positron trigger (using the Qf variable) were added to the NaI.

contaminate this distribution. A correction detailed in §4.9 is applied to take into account this background.

- (2) A background from $\pi^+ \rightarrow \mu^+ \rightarrow e^+$ events is present. The source of this background is the same as developed in item III.(3) but the time spectrum is characteristic of $\pi^+ \rightarrow \mu^+ \rightarrow e^+$ decays (labelled $\mathcal{E}_{\pi \rightarrow \mu \rightarrow e}(t)$ in the next section).
- (3) Muon radiative decays also contribute to the background as mentioned in item III.(4). Considering the branching ratio for $\mu^+ \rightarrow e^+ \nu_e \bar{\nu}_\mu \gamma$ of 0.158 (with a cut-off energy of $E_\gamma > 0.5$ MeV), a MC simulation showed that 0.06% of generated $\mu^+ \rightarrow e^+ \nu_e \bar{\nu}_\mu \gamma$ events passed the cut-off energy of 50 MeV therefore contaminating the “high-energy” region. Thus, $\mu^+ \rightarrow e^+ \nu_e \bar{\nu}_\mu \gamma$ events constitute about 20% of the total amount of background in the “high-energy” region which has a time spectrum characteristic of $\pi^+ \rightarrow \mu^+ \rightarrow e^+$ events.
- (4) Similarly, pion radiative decay ($\pi^+ \rightarrow \mu^+ \nu_\mu \gamma$, with a branching ratio of 2×10^{-4} , see Table 2.4) followed by a muon decay can contribute to the high energy background contaminating the $\pi^+ \rightarrow e^+ \nu_e$ spectrum if the energy of the γ is recorded in the calorimeters. Since, in contrast to $\mu^+ \rightarrow e^+ \nu_e \bar{\nu}_\mu \gamma$ decays, the γ direction is independent of the e^+ direction, the probability of detecting high energy γ 's and therefore passing the energy cut-off is enhanced. If recorded in the calorimeter, the radiative γ will look like a pre-pileup event since it carries the time of the pion decay instead of the muon decay. Due to the long NaI pulse, the effect of such a pre-pileup in the $E_{NaI+CsI} > 50$ MeV region can persist long after the pion decay time.
- (5) The background component coming from an “old-muon” firing the T1-T2 trigger plus a $\pi^+ \rightarrow \mu^+ \rightarrow e^+$ pileup depositing energy in the NaI/CsI without hitting T1 counter also contaminates the $t > 0$ region.
- (6) The background component coming from a single “old-muon” passing the energy threshold persists at $t > 0$ as well.

The fit functions

As explained above, the “high-” and “low-energy” regions share common components. Both time spectra are therefore fitted simultaneously with the

4.5. Timing fit: extraction of the raw branching ratio

following functions:

$$\text{PIMUE}(t) = \mathcal{H}(t) \left[a(1-r)\mathcal{E}_{\pi \rightarrow \mu \rightarrow e}(t) \right] + b\mathcal{E}_{\mu \rightarrow e\bar{\nu}_\mu\nu_e}(t) \quad (4.2)$$

$$\begin{aligned} \text{PIENU}(t) = a\mathcal{H}(t) \left[Br \left\{ \mathcal{E}_{\pi \rightarrow e\nu_e}(t) + e\mathcal{G}_1(t) + f\mathcal{G}_2(t) \right\} + r\mathcal{E}_{\pi \rightarrow \mu \rightarrow e}(t) \right] \\ + c\mathcal{F}_1(t) + d\mathcal{F}_2(t) + b'\mathcal{E}_{\mu \rightarrow e\bar{\nu}_\mu\nu_e}(t) \quad (4.3) \end{aligned}$$

where the $\mathcal{E}(t)$ functions represent normalized exponential decay functions (τ_π and τ_μ are respectively the pion and muon lifetimes):

$$\mathcal{E}_{\pi \rightarrow \mu \rightarrow e}(t) = \frac{\exp(-\frac{t}{\tau_\mu}) - \exp(-\frac{t}{\tau_\pi})}{\tau_\mu - \tau_\pi} \quad (\text{refers to II.(1), IV.(2), (3)}) \quad (4.4)$$

$$\mathcal{E}_{\mu \rightarrow e\bar{\nu}_\mu\nu_e}(t) = \frac{\exp(-\frac{t}{\tau_\mu})}{\tau_\mu} \quad (\text{refers to I., II. (3)}) \quad (4.5)$$

$$\mathcal{E}_{\pi \rightarrow e\nu_e}(t) = \frac{\exp(-\frac{t}{\tau_\pi})}{\tau_\pi} \quad (\text{refers to IV.(1)}) \quad (4.6)$$

and $\mathcal{H}(t)$ is the Heaviside step function ($\mathcal{H}(t > 0) = 1$, $\mathcal{H}(t < 0) = 0$) and $t = t' - t_0$ where t'^{45} is the measured time and t_0 the pion stop time.

In Eq.4.2 and 4.3, parameters a and $a \cdot r$ represent the number of $\pi^+ \rightarrow \mu^+ \rightarrow e^+$ events in the $E_{NaI+CsI} \leq 50$ MeV and $E_{NaI+CsI} > 50$ MeV region respectively while b (see item I. and II.(3)) and b' (see item III.(3),(4) and IV.(6)) are the number of old-muon events in the $E_{NaI+CsI} \leq 50$ MeV region and $E_{NaI+CsI} > 50$ MeV region respectively. Br is the raw branching ratio, c and d are respectively the amplitudes of the NaI and CsI component originating from the “old-muon” plus pile-up background (items III.(1) and (2)). Finally, e and f are the amplitudes in the “high-energy” region of $\pi^+ \rightarrow \mu^+ \nu_\mu \gamma$ events hitting the NaI and CsI respectively (items IV.(4)).

The integrated area of the functions $\mathcal{F}_{1,2}(t)$ and $\mathcal{G}_{1,2}(t)$ are normalized to unity. $\mathcal{F}_{1,2}(t)$ model the “old-muon” plus $\pi^+ \rightarrow \mu^+ \rightarrow e^+$ pileup in the “high-energy” time spectrum (see items III.(1), (2) and IV.(5)). The shape of this background is obtained from a simulation in which the pulse shapes of the NaI and CsI and the energy and time distributions of $\pi^+ \rightarrow \mu^+ \rightarrow e^+$ and $\mu^+ \rightarrow e^+ \nu_e \bar{\nu}_\mu$ decays are provided. Fig.4.16 shows the time distributions of the events for which the positron from $\pi^+ \rightarrow \mu^+ \rightarrow e^+$ decay hit the

⁴⁵All time histograms presented in this document use t' . The offset to the pion stop time is $t_0 \sim 1.7$ ns.

4.5. Timing fit: extraction of the raw branching ratio

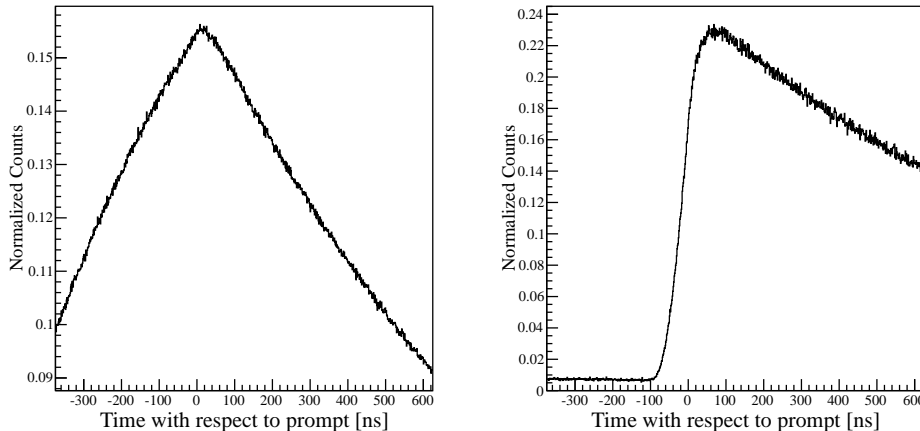


Figure 4.16: Simulation of the time distribution of “old-muon” with a $\pi^+ \rightarrow \mu^+ \rightarrow e^+$ pileup (see text for details). NaI (\mathcal{F}_1 , left plot) and CsI (\mathcal{F}_2 , right plot) shapes are added to the time spectrum fit. The amplitude of NaI and CsI components are left free in the fit.

NaI (\mathcal{F}_1) or CsI (\mathcal{F}_2). The shapes of those two components are constrained in the fit but the amplitudes are left free. The amplitudes of both NaI and CsI components turn out to be approximately 1 to 3 which is consistent with the ratio of acceptances for CsI and NaI (with the exclusion of the area covered by T1).

The functions $\mathcal{G}_{1,2}(t)$ model the background in the “high-energy” region from pion radiative decay (see item IV.(4)). The time spectra of this background originating from energy deposited by γ in CsI and NaI are obtained separately by a simulation which took into account the pulse shape of both calorimeters and the time distribution of pion and muon decay. Fig.4.17 shows the result of the simulation. A MC simulation of $\pi^+ \rightarrow \mu^+ \nu_\mu \gamma$ events which takes into account the PIENU detector geometry reveals that 2.3% and 1.8% of generated $\pi^+ \rightarrow \mu^+ \nu_\mu \gamma$ events (independently of the muon decay time and with a branching ratio of 1) hit the NaI and CsI calorimeter respectively and pass the 50 MeV threshold. These numbers modulated by the effect of the pulse shape and the branching ratio for the $\pi^+ \rightarrow \mu^+ \nu_\mu \gamma$ decay indicate that γ from $\pi^+ \rightarrow \mu^+ \nu_\mu \gamma$ decay hitting the NaI (CsI) and contaminating the “high-energy” region represent 0.5 (0.17)% of $\pi^+ \rightarrow e^+ \nu_e$ events. Those amplitudes are fixed in the fit. The error on the estimation of

4.5. Timing fit: extraction of the raw branching ratio

the components mainly comes from the uncertainty on the energy calibration and resolution of the calorimeters in the MC. A conservative 20% error on the estimation is assigned. The amplitude of both NaI and CsI components are varied in the fit within this error, the effect on the branching ratio value is smaller than 0.02%.

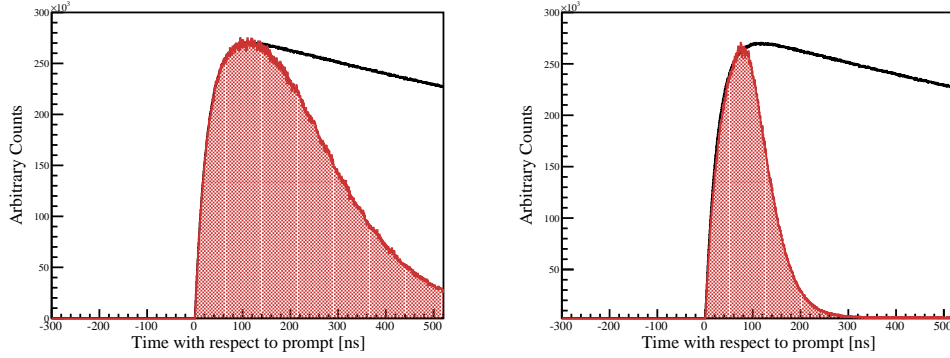


Figure 4.17: Time spectrum of $\pi^+ \rightarrow \mu^+ \nu_\mu \gamma$ background in the $E_{NaI+CsI} > 50$ MeV region. The right and left figures show the time distributions of $\pi^+ \rightarrow \mu^+ \nu_\mu \gamma$ events (shaded area) when the NaI and CsI pulse shapes respectively are taken into account. Both spectra are superimposed to the nominal $\pi^+ \rightarrow \mu^+ \rightarrow e^+$ time spectrum.

The parameter b' is left free in the nominal fit. However, because of correlations between the shapes of $\mathcal{E}_{\mu \rightarrow e \bar{\nu}_\mu \nu_e}$ and $\mathcal{F}_{1,2}$ functions, the error on this parameter extracted from the fit is large. In principle, the amplitude of this component is known since it is related to the $\pi^+ \rightarrow \mu^+ \rightarrow e^+$ background in the “high-energy” region and to the “old-muon” background in the “low-energy” region. The relation between those backgrounds follows the following simple equation:

$$b' \sim \frac{b}{a} \times a \cdot r = b \times r \quad (4.7)$$

Using the corresponding values reported in Table 4.1 we find:

$$b' \sim 8.9 \times 10^3 \quad (4.8)$$

Fixing b' to this value or setting it to zero has no effect on the branching ratio and only results in a small increase in the χ^2 .

4.5. Timing fit: extraction of the raw branching ratio

The PDIF component (see item II.(2)) is not explicitly included in the fit but the inclusion of a component decaying with the muon lifetime to the fit is mathematically equivalent to leaving t_0 free. As a cross-check, t_0 is fixed to the value extracted from muon runs (see §4.10 for details) and the amplitude of the $\mathcal{E}_{\mu \rightarrow e \bar{\nu}_\mu \nu_e}(t)$ component is left free to deviate from the amplitude constrained by the $t < 0$ region. An increase by a factor 1.9 in the amplitude of $\mathcal{E}_{\mu \rightarrow e \bar{\nu}_\mu \nu_e}(t)$ in the $t > 0$ region is found (with a negligible impact on the branching ratio) which is consistent with the estimated amount of PDIF. Fig.4.18 and Fig.4.19 show the “high-” and “low-energy” time spectra together with the fitted functions and their residuals for the time regions after the prompt ($t > 0$) and before the prompt ($t < 0$) respectively. The associated individual χ^2 and the number of degrees of freedom are indicated on each plot. The individual χ^2 are only indicative since the fit is performed on all spectra at once with a combined χ^2 . The total χ^2/DOF (DOF=1245) is 1.134. The result of the fit is reported in Table 4.1. The total number of $\pi^+ \rightarrow e^+ \nu_e$ events is slightly higher than 2.5×10^5 which is about two times higher than the E248 experiment. The statistical error on the blinded raw branching ratio is:

$$\sigma_{stat} = 2.41 \times 10^{-7} \tag{4.9}$$

Table 4.1: Result of the time spectrum fit. Parameters with a * are normalized to the total number of $\pi^+ \rightarrow e^+ \nu_e$ events and were fixed in the fit.

Parameter	Value \pm Error
a	$(2.1815 \pm 0.0003) \times 10^9$
r	$(8.36 \pm 0.02) \times 10^{-4}$
t_0	1.576 ± 0.006 [ns]
b	$(9.880 \pm 0.003) \times 10^7$
b'	$(0.06 \pm 7.63) \times 10^2$
Br	█ $\pm 2.41 \times 10^{-7}$
c	$(1.81 \pm 0.03) \times 10^4$
d	$(7.74 \pm 1.44) \times 10^3$
e^*	$(5.00 \pm 0) \times 10^{-3}$
f^*	$(1.70 \pm 0) \times 10^{-3}$

4.5. Timing fit: extraction of the raw branching ratio

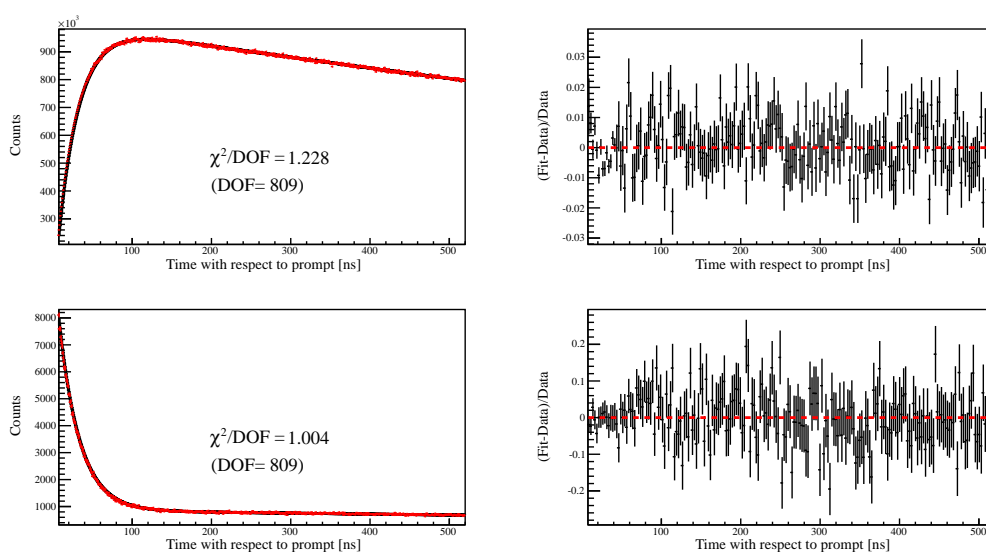


Figure 4.18: **Top:** “low-energy” time spectrum for $t > 0$ (red) superimposed to the fit function (black) described in the text. The residuals of the fit are shown in the right figure. **Bottom:** “high-energy” time spectrum for $t > 0$ (red) superimposed to the fit function (black) described in the text. The residuals of the fit are shown in the right figure.

4.5. Timing fit: extraction of the raw branching ratio

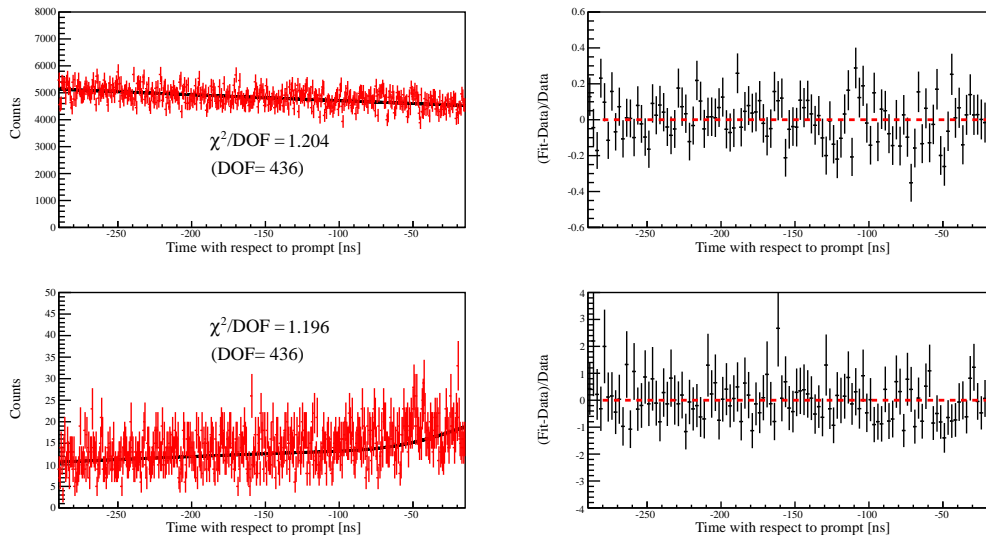


Figure 4.19: **Top:** “low-energy” time spectrum for $t < 0$ (red) superimposed to the fit function (black) described in the text. The residuals of the fit are shown in the right figure. **Bottom:** “high-energy” time spectrum for $t < 0$ (red) superimposed to the fit function (black) described in the text. The residuals of the fit are shown in the right figure.

4.6 Systematics checks

A series of checks is done on the fit stability to evaluate the level of systematic uncertainty.

- The fitting ranges are varied to evaluate the time dependence of the fit.
- The effect of resolution is studied by varying the fit range close to the prompt.
- A background amplitude is fixed while the others are left free.
- An additional flat component or a faster decaying component ($\tau_\mu/2$) is added to the fit to evaluate the impact of non-accounted for backgrounds on the branching ratio.
- The impact of freeing the lifetimes (τ_π and τ_μ) on the branching ratio is studied. The effect of the uncertainty of the pion lifetime ($\pm 5 \times 10^{-3}$ ns [22]) on the branching ratio is assessed by fixing the lifetime to the central value plus the error. The effect on the branching ratio can be fully neglected.
- Finally, the binning of the time histograms is varied.

Table 4.2 gives the details of the fluctuations of the branching ratio with each systematic test.

The Fourier transforms of the residuals of the $\pi^+ \rightarrow e^+ \nu_e$ and $\pi^+ \rightarrow \mu^+ \rightarrow e^+$ time fit is studied. No beam periodicity is found. To confirm that no contamination from beam positrons is present in the “high-energy” spectrum, a component with the beam periodicity (see Fig.4.20) is introduced in the fit. The effect on the branching ratio is negligible.

Overall the entire set of stability and systematic checks, the value of the branching ratio is consistent with statistical fluctuations. Therefore no additional systematic error is added.

However, to take into account the value of the χ^2 which may represent systematic uncertainties, the statistical error is inflated by $\sqrt{\chi^2/DOF} = \sqrt{1.134}$. Assuming statistical and systematic errors are independent, a systematic error of 0.0010×10^{-4} is extracted by subtracting the statistical uncertainty from the total uncertainty.

4.6. Systematics checks

Table 4.2: List of systematic checks on the time spectrum fit. \mathcal{A} and \mathcal{B} denote “low-energy” and “high-energy” time spectrum respectively. Numbers in the column labeled “variation in the branching ratio” refer to the subtraction of the nominal branching ratio to the branching ratio obtained under the different listed conditions. The change in the fitting ranges is done on a single time boundary at once. Only the boundary which is different from the nominal is indicated.

Checks	Variation in B.R [$\times 10^{-7}$]	Stat. Error [$\times 10^{-7}$]
Nominal	/	2.41
Fitting range		
t<400 in \mathcal{A} and \mathcal{B}	-0.14	2.43
t<300 in \mathcal{A} and \mathcal{B}	-0.99	2.46
t<-20 in \mathcal{A} and \mathcal{B}	0.13	2.42
-270 <t in \mathcal{A} and \mathcal{B}	-0.02	2.41
t<300 in \mathcal{A} only	-0.13	2.42
t<300 in \mathcal{B} only	-0.86	2.45
Free parameter		
τ_μ	0.01	3.05
τ_π	1.47	2.46
e	-0.4	2.41
f	-0.27	2.41
Binning		
$\times 2$	0.95	2.41
Resolution		
1 ns closer to prompt	0.30	2.34
1 ns further away from prompt	-0.31	2.45
Additional Background		
flat background in \mathcal{A} and \mathcal{B}	0.10	2.42
$\tau/2$ background in \mathcal{A}	0.19	2.41

4.6. Systematics checks

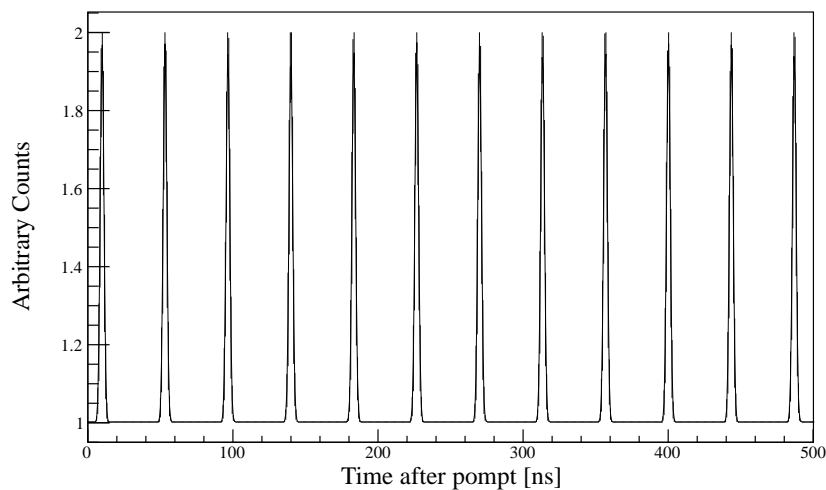


Figure 4.20: Time distribution of beam positrons approximated by a sum of gaussian peaks separated by the cyclotron RF period. This distribution is used in the time fit to estimate the remaining beam positron contamination. The phase and amplitude of this component are left free in the fit.

4.7. Linearity

The statistical and systematic errors are added in quadrature to give the following error on the blinded raw branching ratio:

$$\sigma_{raw_{br}} = 0.0026 \times 10^{-4} \quad (4.10)$$

4.7 Linearity

Non-linearities in the time measurement systems or noise in the electronics due to tiny cross-talks through the cables and NIM bins⁴⁶ can lead to distortions in the time spectrum. Earlier investigations on the time recorded by the VT48 modules showed large non-linearities with frequency multiples of the TDC clock. COPPER is chosen instead as the time measuring device. Pulse fitting on COPPER waveforms also provides three times better time resolution than the VT48. To measure and quantify any remaining non-linearities, special muon runs are taken every week. For these runs, the momentum of the beamline is changed to stop “cloud” muons (muons originating from pion decay near the production target) in the middle of the target. B1 and T1 time would correspond to the incoming muon and outgoing decay positron respectively. This method of measuring the non-linearities from physical beam pulses has the advantage of simulating the same path in the trigger electronics with similar pulse heights in the counters as taken by nominal data.

Over 43 M muon events were accumulated between June and November 2011 (Table C.1 in Appendix C lists the runs used). The time spectrum obtained is very well fit with an exponential as can be seen on Fig.4.21. No traces of non-linearities are detected⁴⁷.

⁴⁶The respective locations of the trigger NIM modules associated with pion and decay positron were chosen to minimize this effect.

⁴⁷One can note that the slope of the exponential is about 1% slower than the muon lifetime table value. This may be caused by a slow muon depolarization (cloud muons are about 40% polarized) in the target material. If after the fast depolarization, a remaining 50% of muons follow an exponential depolarization with a lifetime of $\sim 10 \mu\text{s}$, an enhancement of the lifetime by $\sim 1\%$ could be observed. No measurements of the time dependence of depolarization in plastic scintillator at low field could be found in the literature. However, a review paper [131] on muon spin relaxation in conducting polymers contains a model that is consistent with early measurements of residual polarization in scintillator at zero field [132, 133] and expectations for the time dependence. For zero field, the model predicts a rapid depolarization to about 50% of the initial value, followed by an exponential depolarization with a time constant of $\sim 10 \mu\text{s}$. This would result in an apparent enhancement of the muon lifetime by $\sim 1\%$, as we observe. A special trigger was built in 2011 to measure the yield difference between forward and backward positrons from muon decay. The change in the yield asymmetry with time would be an indication

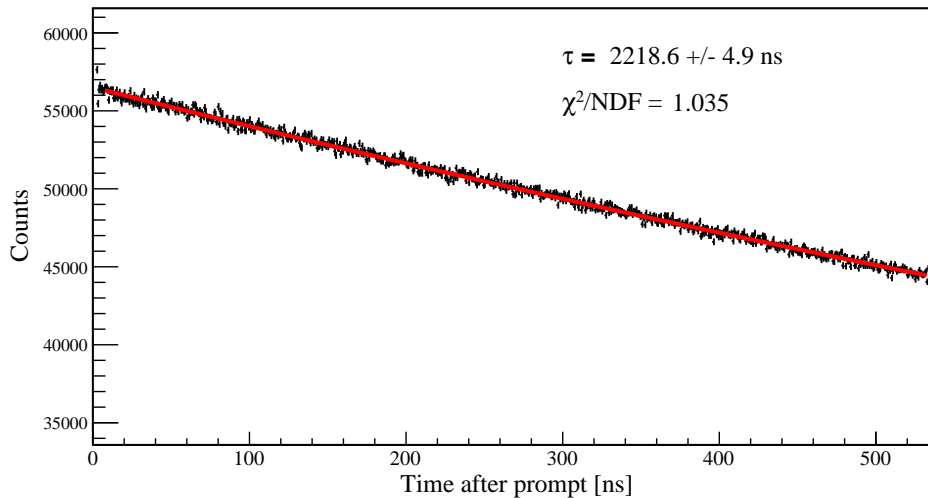


Figure 4.21: Time spectrum for muon runs fitted with an exponential function.

4.8 Effects of trigger inefficiencies

Inefficiencies of the downstream trigger counters could distort the time spectrum if they were time dependent. Inefficiencies of both T1 and T2 are therefore measured using special runs during which these counters are consecutively excluded from the trigger. Fig.4.22 shows the efficiency of the T2 counter as a function of the time (measured by T1) after the prompt. The slope is consistent with zero. Negligible time dependence of inefficiency is observed. The inefficiency of T1 counter is measured to be smaller than 0.01% with no time dependence.

of depolarization. The analysis of the data is underway. However, we should note that the effect of muon depolarization in the measurement of the branching ratio is expected to be small. It can only be seen due to the small difference in the acceptance for positrons coming from forward and backward muons in the $\pi^+ \rightarrow \mu^+ \rightarrow e^+$ decay chain. The effect on the lifetime of muons from $\pi^+ \rightarrow \mu^+ \nu_\mu$ decay is estimated to be smaller than 0.1%.

4.9. Muon decay-in-flight correction

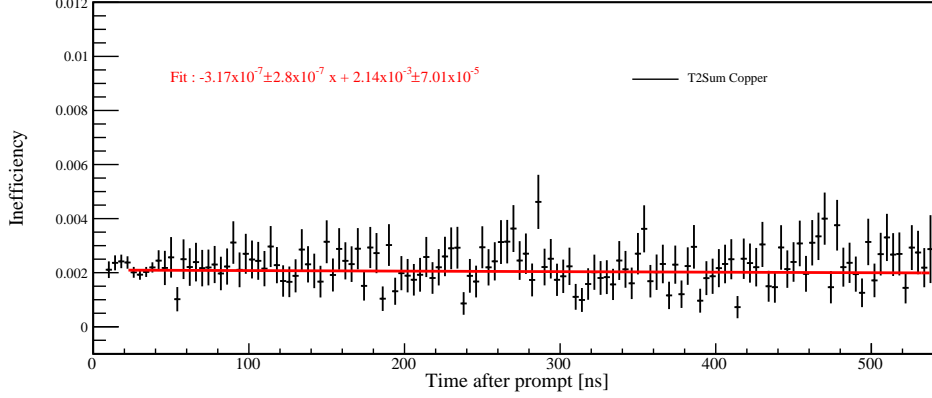


Figure 4.22: T2 inefficiency as a function of time. The solid red line shows the best fit to the data.

4.9 Muon decay-in-flight correction

Pion decay-at-rest followed by muon decay-in-flight events (PDAR-MDIF) cannot be distinguished from $\pi^+ \rightarrow e^+ \nu_e$ events since they have similar time spectra. Fig.4.23 shows the decay time of muons for PDAR-MDIF events with respect to the pion decay time obtained from MC. The energy spectrum (recorded by CsI and NaI) of the decay positron from PDAR-MDIF together with PDAR-MDAR events is shown in Fig.4.24. The positrons which have an energy greater than 50 MeV will be falsely counted as $\pi^+ \rightarrow e^+ \nu_e$ events in the time fit. The probability (p) of muon decay in flight can be approximated by:

$$p \sim 1 - \exp \frac{-\tau_{\mu_{DIF}}/\gamma}{\tau_{\mu}} \sim 8 \times 10^{-6} \quad (4.11)$$

where $\gamma = 1/\sqrt{1 - v^2/c^2} = 1.039$ for the muon kinetic energy of $K_{\mu}=4.1$ MeV, $\tau_{\mu_{DIF}}$ is the time the muon travels before it stops ($\tau_{\mu_{DIF}} = 18$ ps) and τ_{μ} the muon lifetime. The value of p was confirmed by MC.

From a MC simulation of MDIF, the proportion of positrons from MDIF that have an energy higher than the Michel end point indicated with a dotted black line in Fig.4.24 is $f_{MDIF}=2.99 \pm 0.20\%$. This results in 2.36×10^{-7} of $\pi^+ \rightarrow \mu^+ \rightarrow e^+$ decays being incorrectly counted as $\pi^+ \rightarrow e^+ \nu_e$ decays. The error assigned to f_{MDIF} comes from the agreement in the energy calibration between MC and data and on the error on the MDIF shape and

4.9. Muon decay-in-flight correction

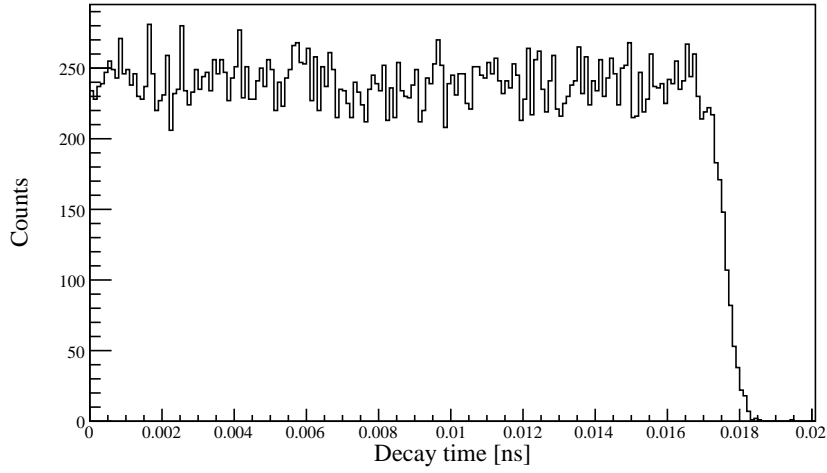


Figure 4.23: Decay time of muons with respect to the pion decay time for PDAR-MDIF events.

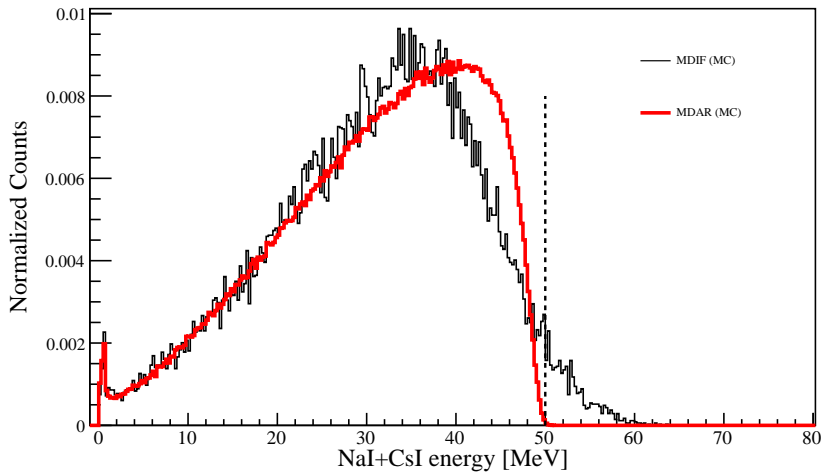


Figure 4.24: Positron spectra from muon decay at rest (red thick line) and muon decay in flight (black thin line) from MC.

4.10. Energy dependence of t_0

amplitude (which relates to the probability of MDIF calculated above) in the MC. The agreement between MC and data in the energy calibration is better than 0.1 MeV. This translates into an error on f_{MDIF} of 0.08%. The uncertainty on the shape of MDIF is deduced from the difference in the Michel spectrum shape between MC and data. In an energy range of 5 MeV to 46 MeV with a 0.4 MeV step, the highest discrepancy in the number of events between MC and data was of the order of 6%. Conservatively, a 6% error on f_{MDIF} is taken as the error contribution from the energy spectrum shape of positrons originating from MDIF. This gives an additional error of 0.18% on f_{MDIF} . The total error is therefore:

$$\sigma_{MDIF} = \sqrt{0.0008^2 + 0.0018^2} = 0.0020 \quad (4.12)$$

To obtain the correction on the branching ratio, f_{MDIF} is multiplied by the probability of MDIF. It leads to a multiplicative correction to the branching ratio of:

$$C_{MDIF} = 0.9976 \pm 0.00016 \quad (4.13)$$

4.10 Energy dependence of t_0

An energy dependence in t_0 (the prompt time) could be induced due to time-walk (pulse height dependence of the measured time) in T1 counter. Small signals have a slightly slower rise time, therefore reaching the discriminator threshold later. However, since fitted waveforms are used to determine the time of the event, and since there is only a very small energy-loss dependence on the total energy deposited in the thin plastic scintillators, this effect should be very small. The amplitude of the time-walk was estimated using muon runs (the same runs as used for the linearity measurement). For muon runs, t_0 is clearly defined (within the time resolution) as the time of the muon stop. The edge of the distribution is fitted with a step-function folded with a gaussian resolution and the evolution of t_0 is studied as a function of the positron energy as shown in Fig.4.25 . The difference in t_0 for $\pi^+ \rightarrow e^+\nu_e$ and $\pi^+ \rightarrow \mu^+ \rightarrow e^+$ events is found to be:

$$\Delta t_0 = 17 \pm 14 \text{ (stat.)} \pm 10 \text{ (syst.) ps} \quad (4.14)$$

This translates in a correction on the branching ratio of:

$$C_{t_0} = 0.9993 \pm 0.0007 \quad (4.15)$$

4.10. Energy dependence of t_0

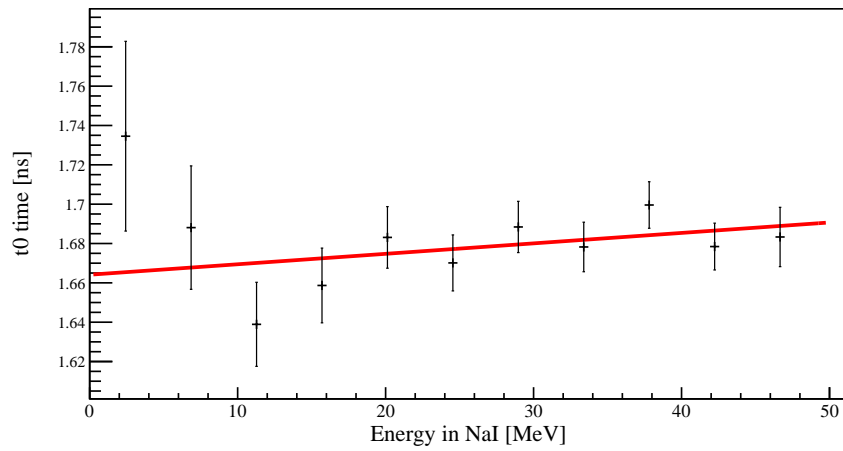


Figure 4.25: Variation of t_0 as a function of the energy deposited in the NaI.

Chapter 5

Corrections and Systematics

5.1 Tail correction

The main correction to the branching ratio comes from the low energy $\pi^+ \rightarrow e^+\nu_e$ tail buried under the $\pi^+ \rightarrow \mu^+ \rightarrow e^+$ spectrum. The $\pi^+ \rightarrow e^+\nu_e$ low energy tail arises from the response function of the calorimeter system (NaI+CsI) due to leakage of low energy photons from the sides and ends of the calorimeter and from radiative decays. The tail correction being relatively large, relying on MC simulation alone for its estimation is not satisfactory. Therefore an empirical determination of the tail is sought. A measurement of the calorimeter lineshape with beam positrons with similar energies as $\pi^+ \rightarrow e^+\nu_e$ positrons could give an estimate of the low energy tail. However, because of the momentum distribution of beam positrons and additional low energy components due to scattering in the beamline, the lineshape measurement only gives access to an upper-limit on the tail fraction. A lower-limit on the tail is obtained by suppressing the $\pi^+ \rightarrow \mu^+ \rightarrow e^+$ decay in order to get an estimate of the $\pi^+ \rightarrow e^+\nu_e$ low energy tail buried under the remaining $\pi^+ \rightarrow \mu^+ \rightarrow e^+$ background. The combination of upper and lower limits gives access to the tail fraction.

5.1.1 Suppressed spectrum

A $\pi^+ \rightarrow e^+\nu_e$ energy spectrum with a small contamination of $\pi^+ \rightarrow \mu^+ \rightarrow e^+$ decays (“suppressed spectrum”) is obtained by applying a set of cuts that preferentially removes $\pi^+ \rightarrow \mu^+ \rightarrow e^+$ decays.

Basic cuts

The same pion selection and background rejection cuts presented from §4.4.2 to §4.4.6 are applied to the data. A first suppression of the $\pi^+ \rightarrow \mu^+ \rightarrow e^+$ background can be obtained with an early time cut: $7 < t < 33$ ns with respect to the prompt which takes advantage of the slower decaying muon.

5.1. Tail correction

The muon from $\pi^+ \rightarrow \mu^+ \nu_\mu$ decay also leaves 4.1 MeV⁴⁸ in the target. Therefore the “Total energy” (the sum of the energy deposited in B1, B2, S1, S2 and Tg) can be used to obtain another suppression factor. The Total Energy cut, $15.7 < E_{tot} < 16.8$ MeV, is shown in Fig.5.1. Since this cut is applied after the time cut, the energy of both incoming and outgoing particles in the target are contained within the selected time window. The Total Energy integrated over ~ 100 ns therefore contains the full energy deposited in the target.

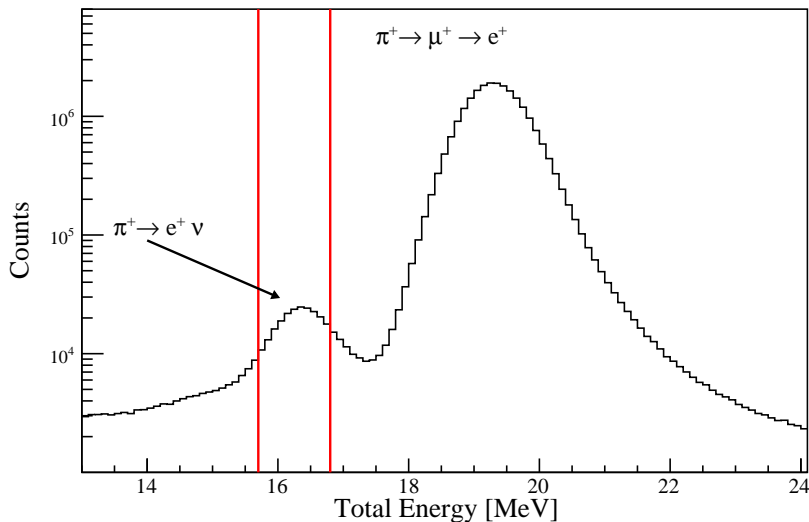


Figure 5.1: Sum of energies deposited in B1, B2, S1, S2 and Tg after the time cut. The vertical red lines show the cut limits that select $\pi^+ \rightarrow e^+ \nu_e$ events.

Another set of $\pi^+ \rightarrow \mu^+ \rightarrow e^+$ suppression cuts is also applied. The cuts are described in the following paragraphs.

Tracking Cut

The main background after the Total Energy cut comes from pion decays-in-flight before the target. Those events leave an energy similar to $\pi^+ \rightarrow e^+ \nu_e$

⁴⁸Because of saturation in the target, the $\pi^+ \rightarrow \mu^+ \rightarrow e^+$ and $\pi^+ \rightarrow e^+ \nu_e$ peaks are only separated by 3 MeV in the data.

events in the target. Fig.3.22 in §3.2.7 shows the different decay-in-flight backgrounds and the tracking detector arrangement. PDIF that happens between the two upstream trackers (Tr1 and Tr2) can be identified and rejected as shown by MC simulation (see Fig.3.23). The tracking package [126] used for the track reconstruction identifies all hits in each tracking plane and fits a track to all possible hit combinations⁴⁹. The different tracks are then ordered by increasing χ^2 . The second tracker however consists only of four planes which is the minimum amount of information needed to define a track. Therefore, all reconstructed tracks in Tr2 are equally probable. To avoid position bias, from a noisy strip for example, only events which have a single track in Tr2 are selected (which represents more than 99% of the events). For Tr1 the track with the best χ^2 is used. Fig.5.2 shows the angle between the track reconstructed in Tr1 and Tr2 for $\pi^+ \rightarrow e^+\nu_e$ and $\pi^+ \rightarrow \mu^+ \rightarrow e^+$ events selected through their energy deposit in the NaI, together with the kink cut position chosen to optimize the signal to noise ratio (S/\sqrt{N}).

S3 Energy Cut

The tracking cut can only suppress PDIF happening before the upstream silicon planes. About 1/2 of the PDIF remain after this cut. An additional suppression of this background can be obtained with a cut in the energy deposited in S3. Muons from PDIF get an extra boost and although they must traverse more material upstream of the target they tend to leak outside of the target into S3. MC simulation showed that about 30% of muons from PDIF after S1 traverse the target. If muons leak into S3, they deposit more energy than the decay positron and can therefore be suppressed. Fig.5.3 shows the energy deposited in S3 as a function of the Total Energy and the energy deposited in the second plane of S3 versus its first plane. The left plot clearly shows two high energy bands in S3 which leak into the $\pi^+ \rightarrow e^+\nu_e$ Total Energy region. One can also see that the lower energy band ($1.3 < E_{S3} < 1.7$ MeV) tends to have more Total Energy. These are PDIF events which happen the farthest away from the target and stop in the first plane of S3. Those events are concentrated in the bottom orange dotted box in the right plot of Fig.5.3. Similarly, the events in the top dotted box in the right figure correspond to the events in the higher energy band in the left figure. Those are muons having enough energy to traverse both S3 planes. The bands (indicated with the black arrows) connecting

⁴⁹Due to the charge division scheme, see §3.2.4, the position of a hit in the silicon planes has to be reconstructed from the charge deposit pattern.

5.1. Tail correction

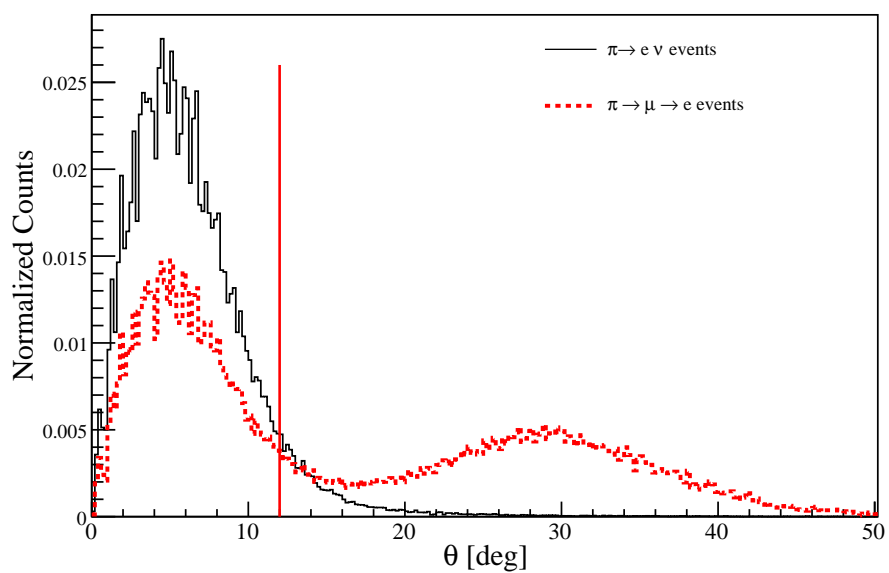


Figure 5.2: Kink angle for $\pi^+ \rightarrow e^+ \nu_e$ events ($E_{NaI} > 55$ MeV) and $\pi^+ \rightarrow \mu^+ \rightarrow e^+$ ($E_{NaI} < 30$ MeV) events. The vertical red line indicates the position of the cut.

the two boxes in the right figure are events leaking from the first plane to the second plane of S3. The events going from the bottom to the top tend to have lower kink angle and decay closer to the target. Those bands should actually be a single band. The separation is due to the different amount of energy seen by the silicon planes depending of the number of strips hit. Because of the threshold on the silicon detectors, the energy recorded by silicon grows with the number of strips hit (and read out). Finally, because of saturation in the silicon planes, the peaks from muons stopping in the plane and muons going through are merged. The S3 cut position is shown as a red curve in the right plot of Fig.5.3. It is a “soft” cut to minimize the suppression of Bhabha-scattered events which are roughly concentrated in the green ellipse. This cut has been reproduced in MC and shows that less than 2% of Bhabha-scattered events are suppressed by this cut. The events accepted by this cut include the events for which no energy was recorded in S3. Indeed, in 2009, it was noticed that a cross-talk that was associated with the pion time affected the pedestal level of S3 making it inefficient as a function of the decay time (since there is data suppression on the silicon detector, events which were missed because of pedestal fluctuation could not be recovered). This cross-talk was reduced to a very small level for 2010 data-taking but to prevent possible systematics, no low energy cut is made on S3.

Pulse Shape Cut

For every event, the target waveform recorded by COPPER is consecutively fitted with a 2-pulse (which fits the pion and positron waveforms in the case of a $\pi^+ \rightarrow e^+ \nu_e$ decay) and 3-pulse (which fits the pion, muon and positron waveforms in the case of a $\pi^+ \rightarrow \mu^+ \rightarrow e^+$ decay) function. The template for the pulses are obtained in the same way as for B1 and T1 fits (see §4.5.1). In the 2-pulse fit, the timing of the first and the second pulses are determined by B1 and T1 timings respectively. For the 3-pulse fit, the result from the 2 pulse fit is first subtracted from the waveform. The highest peak after subtraction is associated with the muon and is taken as an input parameter for the muon PH in the 3-pulse fit. Fig.5.4 shows an example of a target waveform with the 2-pulse and 3-pulse fit results. The timing of the highest peak is also used as an input parameter for the muon time in the 3-pulse fit. This procedure helps constraining the time of the muon pulse. For early pion decay, the 2-pulse and 3-pulse fits tend to give similar results for $\pi^+ \rightarrow \mu^+ \rightarrow e^+$ events. The χ^2 discrimination is therefore only effective for pion decays happening ~ 10 ns after the pion stop. For later

5.1. Tail correction

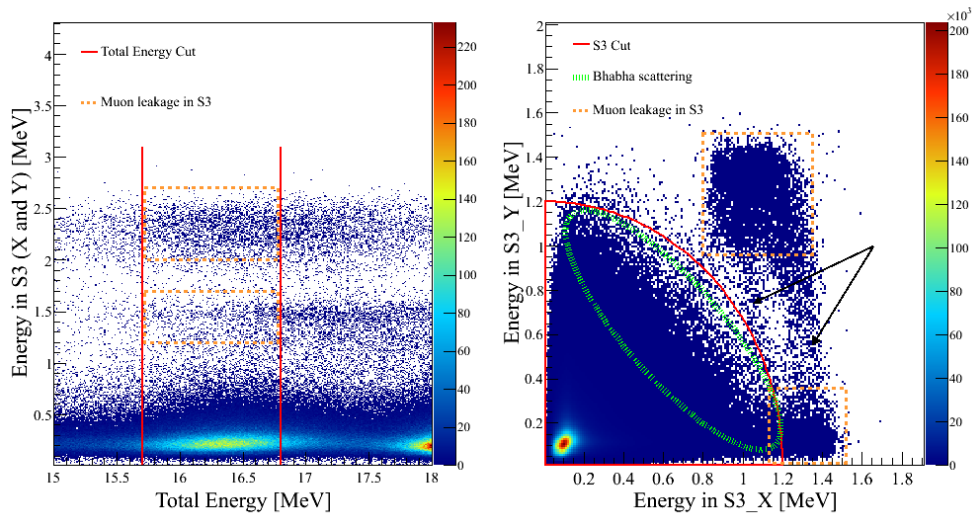


Figure 5.3: **Left:** Energy deposited in S3 as a function of the energy deposited in the upstream detectors (Total Energy). The red vertical lines indicate the position of the Total Energy cut. The orange dotted boxes indicate the region where muons (from PDIF) which leaked downstream of the target are concentrated. **Right:** Energy deposited in the second plane of S3 (S3_Y) versus its first plane (S3_X). The red curve indicates the cut position. See associated text for detailed explanation.

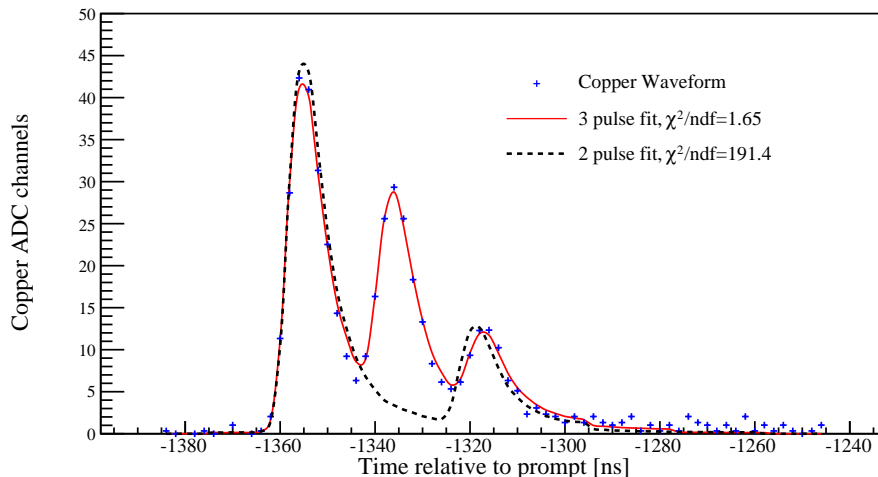


Figure 5.4: Comparison of 3-pulse fit and 2-pulse fit on an early (the pion minus the positron time is smaller than 40 ns) $\pi^+ \rightarrow \mu^+ \rightarrow e^+$ event in the target.

decays, a comparison between the 2-pulse and 3-pulse fit χ^2 helps reduce the remaining $\pi^+ \rightarrow \mu^+ \rightarrow e^+$ background. Fig.5.5 shows the Total Energy as a function of the difference in the 2-pulse and 3-pulse fit χ^2 (before the Total Energy and Early time cut are applied) together with the cut value (vertical red line).

Summary

The summary of all cuts and their effects on the NaI+CsI⁵⁰ spectrum is listed in Table 5.1. The signal efficiency has been estimated with a sample of $\pi^+ \rightarrow e^+ \nu_e$ events selected with the energy deposited in the NaI ($E_{NaI} > 55$ MeV). Fig.5.6 shows the NaI+CsI energy spectrum after each cut.

5.1.2 Lower limit estimation

The suppressed spectrum obtained after the cuts described above can serve to extract a lower limit on the tail in the following way (Fig.5.7 illustrates

⁵⁰Energy in the NaI is calculated based on the Qwwf variable while Qf is used for the CsI since it is a much faster scintillator.

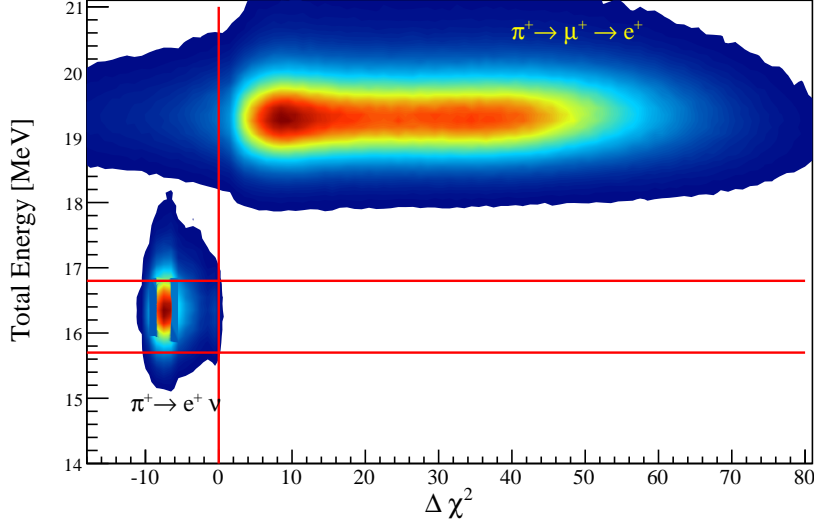


Figure 5.5: Contour plot of the Total Energy as a function of $\Delta\chi^2 = \chi_{2\text{-pulse}}^2 - \chi_{3\text{-pulse}}^2$ for $\pi^+ \rightarrow e^+ \nu_e$ ($E_{NaI} > 55$ MeV) and $\pi^+ \rightarrow \mu^+ \rightarrow e^+$ (amplitude of the muon in the 3-pulse fit is larger than 0) events. The red horizontal lines show the Total Energy cut. The vertical red line gives the value of the pulse shape cut. This figure shows events before any suppression cuts.

Table 5.1: Summary of the suppressed spectrum cuts. The low energy fraction represents the integral of events below 50 MeV divided by the integral of the full energy spectrum. The signal efficiencies are non-cumulative which means that they are representative of the efficiency of each cut while the low energy fraction is cumulative. The * indicates potentially energy-dependent cuts.

Cuts	Low energy fraction [%]	Signal efficiency [%]
Time	99.0	82.85
Total Energy *	30.7	76.80
Kink	18.4	93.14
S3 *	17.7	99.99
Pulse Shape *	16.7	99.46

5.1. Tail correction

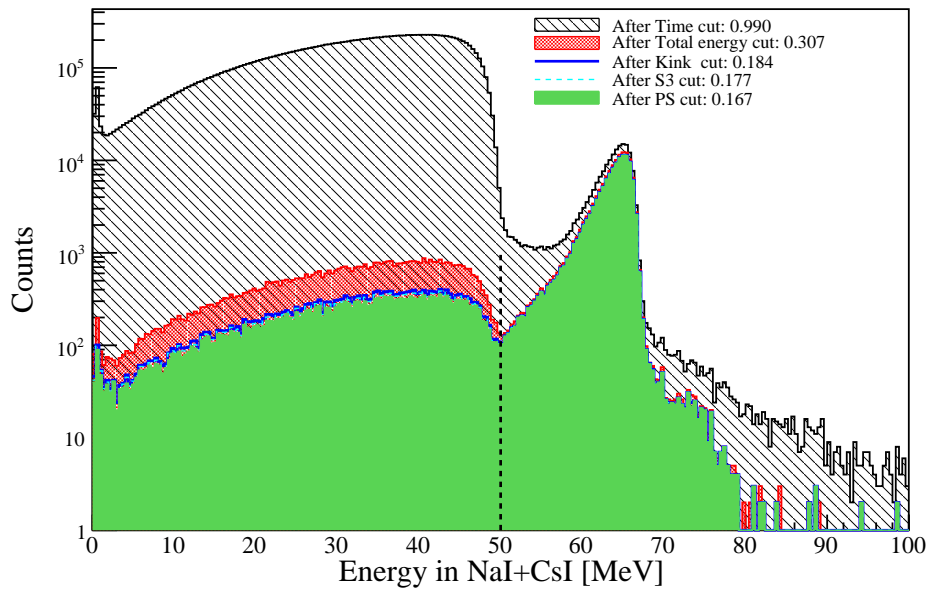


Figure 5.6: Evolution of NaI+CsI energy spectrum after each suppression cut. The legend indicates the fraction of low energy events after each cut (see Table 5.1). The dotted vertical line indicates the energy boundary below which events contribute to the “low energy” part.

5.1. Tail correction

the method). The counts in the suppressed spectrum are summed from zero energy to an energy i (less than 50 MeV, the edge of the Michel spectrum as recorded by the calorimeters). This sum is called $a[i]$. If we assume that all those events are coming from the remaining unsuppressed $\pi^+ \rightarrow \mu^+ \rightarrow e^+$ background in the spectrum, we can calculate, based on the $\mu^+ \rightarrow e^+ \nu_e \bar{\nu}_\mu$ spectrum shape obtained by a selection of late ($t > 100$ ns) decays, the fraction of the total number of events that $a[i]$ should represent. This ratio is obtained by summing the counts in $\pi^+ \rightarrow \mu^+ \rightarrow e^+$ spectrum from zero energy to the same energy i to obtain $b[i]$. $b[i]$ is then divided by the total number of events (B) in the $\pi^+ \rightarrow \mu^+ \rightarrow e^+$ spectrum (from 0 to 50 MeV). $a[i]$ divided by this ratio gives the total number of events (from 0 MeV to 50 MeV) that should be present in the suppressed spectrum from $\pi^+ \rightarrow \mu^+ \rightarrow e^+$ decays. If we subtract this number from the actual total number of events counted in the suppressed spectrum (this number is called A), we get the estimated lower limit on the tail ($Ll[i]$). Eq.5.1 summarizes this procedure.

$$Ll[i] = A - a[i] \frac{B}{b[i]} \quad (5.1)$$

This procedure is repeated at different energies. For low energies, the assumption that there is no tail in the suppressed spectrum is good but the statistical significance of the limit is poor. The higher the energy, the better the statistics but the worse the assumption. The lower limit at different radial cuts⁵¹ is shown in Fig.5.16 together with the upper limit obtained from the lineshape measurement described in §5.1.3 and following sections. We should note that to obtain this lower limit we assumed that the remaining background in the spectrum has the same shape as the one that was subtracted. This is correct for PDIF and PDAR⁵² events but is not correct for PDAR-MDIF. This will lead to a correction to the tail that will be detailed in §5.1.5.

5.1.3 Lineshape measurement

The lineshape measurement consists of data taken with a collimated positron beam at a momentum of 70 MeV/c, hitting the center of the NaI crystal with different entrance angles. These data give access to the response function

⁵¹The same radial cut is applied to the event sample from which the $\mu^+ \rightarrow e^+ \nu_e \bar{\nu}_\mu$ spectrum shape is extracted.

⁵²Muons from PDIF events which pass the Total Energy cut stop on average around 300 μm from the center of the target. There is therefore a negligible difference in the energy lost by positrons in the target from PDIF and PDAR events.

5.1. Tail correction

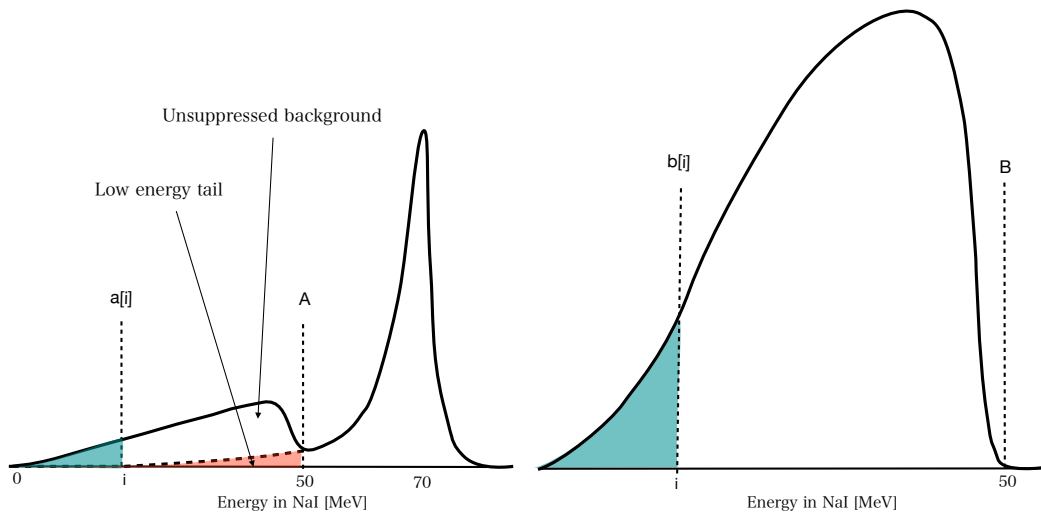


Figure 5.7: Illustration of the lower limit estimation technique using the suppressed spectrum. The shape of $\pi^+ \rightarrow \mu^+ \rightarrow e^+$ events in the calorimeters is obtained by selecting late ($t > 100$ ns) muon decays.

5.1. Tail correction

of the calorimeter at different angles which simulates the entrance angle of the $\pi^+ \rightarrow e^+\nu_e$ positrons. If the radiative decay spectrum is added and a correction made for the absence of the target, T1 and S3 counters, the tail produced by positrons from $\pi^+ \rightarrow e^+\nu_e$ decay should be correctly obtained from those measurements. However, due to the beam momentum dispersion and additional tail caused by scattering in the beamline, the spectrum obtained with beam positrons is broader than the $\pi^+ \rightarrow e^+\nu_e$ spectrum. Therefore, the lineshape measurement provides an upper limit for the $\pi^+ \rightarrow e^+\nu_e$ low energy tail.

A series of measurements was taken at the end of the 2009 beamtime for the NaI lineshape⁵³. Table 5.2 gives a summary of the data taken. The angles referred to are shown in Fig.3.19. Due to spatial constraints at that

Table 5.2: List of special positron runs taken in 2009. The * indicates the runs taken with an additional 1/4 inch-thick scintillator in front of the NaI.

Date	run number range	θ angle	φ angle	
2009/11/30	26827-26955	0	90	
2009/11/28	26383-26397	15	90	
2009/11/28	26398-26410	15	90	*
2009/11/27	26301-26312	27	90	
2009/11/27	26314-26383	27	90	*
2009/11/27	26245-26257	35	90	
2009/11/27	26258-26282	35	90	*
2009/11/30	26762-26785	40	90	
2009/11/30	26786-26812	40	90	*
2009/11/28	26410-26433	-18	90	*
2009/11/28	26434-26455	-30	90	*
2009/11/28	26456-26481	-36	90	*
2009/11/28	26482-26568	-43	90	*

time, the maximum angle that could be reached is $\theta = -43^\circ$ whereas the acceptance cut on $\pi^+ \rightarrow e^+\nu_e$ events made in this analysis reach angles up to 47° .

⁵³At the time of the lineshape measurements, the calibration of the CsI detector was not done (too few cosmic events were collected) and the HV settings changed between the 2009 and 2010 runs. So, it is not possible to obtain the CsI lineshape using those data.

5.1. Tail correction

The measurements were taken to estimate the effect of the entrance angle of the positron from $\pi^+ \rightarrow e^+\nu_e$ decay on the low energy tail. Indeed, the higher the entrance angle, the larger the shower leakage and therefore the larger the tail. However, the $\pi^+ \rightarrow e^+\nu_e$ positrons entering the crystal with an angle also enter the crystal off-center. Since the lineshape data were all taken on-center, the measurements tend to underestimate the tail fraction⁵⁴. To take this effect into account, the catalogue of all entrance angles for the lineshape data is compared with the $\pi^+ \rightarrow e^+\nu_e$ positron entrance angle and position in the crystal. For tracks hitting the center of the crystal at an angle smaller than 27° ⁵⁵ which correspond to tracks pointing toward the back face of the crystal (as opposed to the sides), the tracks with the same distance from the edge of the crystal measured at the back are considered to have the same lineshape. For higher angles, the tracks with the same distance traveled in the crystal are taken to have the same effect on the tail. Fig.5.8 illustrates this procedure. The effect of the tracks entering at angles between the measured ones (e.g.: between 0 and 10° etc.) is interpolated. This procedure is tested with MC and shows that the ratio of the tail fractions between the off-center measurement and its associated on-center measurement averaged over all angles up to 40° is 1 ± 0.02 . After this matching procedure, those angles were weighted according to the corresponding $\pi^+ \rightarrow e^+\nu_e$ acceptance. Since lineshape data were taken without the PIENU-I detector (see Fig.3.19) the energy deposited by the $\pi^+ \rightarrow e^+\nu_e$ positrons in the downstream counters (half of the target, S3 and T1) needs to be subtracted from the lineshape. The energy distributions in those counters are obtained from MC and sampled on an event-by-event basis and subtracted from the lineshape. Finally the radiative decay spectrum generated by MC is added⁵⁶. Fig.5.9 shows the obtained lineshape spectrum compared with the suppressed spectrum for two different radial cuts in WC3. The bottom plots show the ratio of the number of events in the suppressed spectrum and the lineshape within a 1 MeV region. This illustrates the level of agreement reached at different energies. The lineshape and the suppressed spectrum can only be compared down to ~ 55 MeV, below which the $\pi^+ \rightarrow \mu^+ \rightarrow e^+$ background left in the suppressed spectrum dominates. For higher energies, the agreement is very good showing that this procedure worked. We should also note

⁵⁴For the 2011 beamtime a technique was developed to rotate the crystal around the target to be able to measure the same off-center angles with beam positrons as with $\pi^+ \rightarrow e^+\nu_e$ decays.

⁵⁵ 27° corresponds to the track pointing to the back corner of the crystal.

⁵⁶See §6.3 for the details of the radiative decay simulation in the MC.

5.1. Tail correction

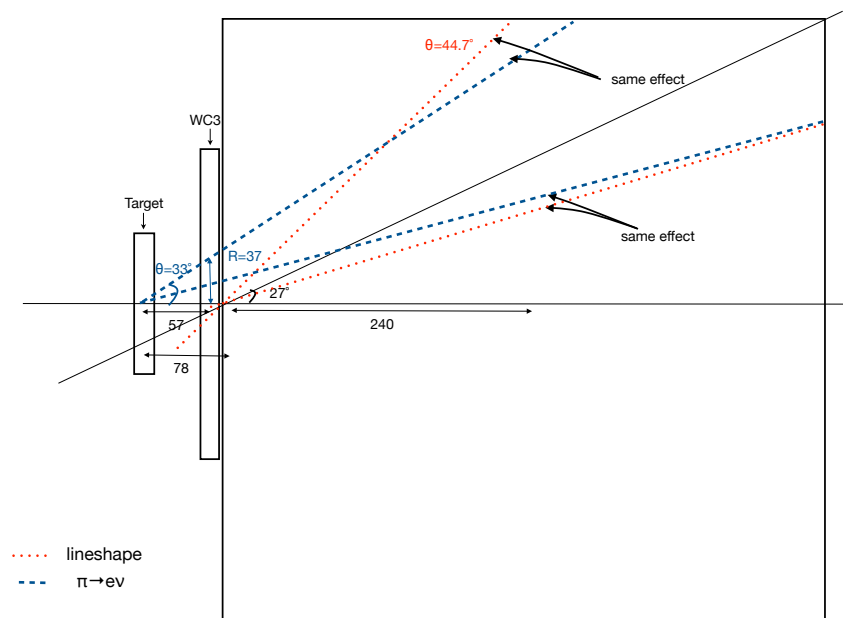


Figure 5.8: Illustration of the matching procedure which associates off-center ($\pi^+ \rightarrow e^+\nu_e$) tracks with on-center (lineshape) ones. The off-center and on-center tracks which have similar contributions to the tail fraction are labelled “same effect”. See text for details.

that the lineshape data should have a slightly broader spectrum due to the contribution from the beam. This is what is observed in Fig.5.9. Unless otherwise stated, “data lineshape” will from now on refer to the lineshape obtained with the matching procedure described above.

Unfortunately the data lineshape only reaches an angle of 43° and the CsI lineshape is not included. This means that this data cannot be used directly to estimate the upper limit on the tail. However it will serve as an input to the MC simulation. The most challenging part for the MC is to reproduce the peaks arising from neutron escape from the crystal (see §3.2.7). In Fig.5.9, the first peak⁵⁷ can be clearly seen. The difference between the number of events in the data lineshape and $\pi^+ \rightarrow e^+\nu_e$ spectrum over the lineshape at the location of this first peak⁵⁸ is around $5\pm 2\%$ as shown in the bottom plots of Fig.5.9. The data lineshape can therefore serve as a check of the MC simulation of the lineshape up to angles of 43° and down to very low energies which cannot be achieved by the suppressed spectrum due to the background which is dominant below 50 MeV. The next section will deal with obtaining the lineshape from the MC simulation.

5.1.4 Upper limit estimation from Monte Carlo

Addition of Photo-nuclear effects in the MC

As already discussed in §3.2.7, the “raw” MC with hadronic reactions turned on did not accurately reproduce the photo-nuclear peak amplitudes. Two different physics packages were tried: the standard hadronic physics lists (QGSP_BERT) and a very similar list containing better description of neutrons (QGSP_BERT_HP, HP stands for “High Precision Neutron Tracking”). The two gave different peak amplitudes but neither of them agreed with the data at the level required. Those lists are based on the interpolation of experimentally determined neutron cross-sections with a sample of nuclei. The neutrons contributing to the peaks in our spectrum typically encounter 20 elastic scatterings in the NaI crystal before escaping. A small error in the interpolation can have a sizeable effect over 20 scatterings. Since the MC simulation has to reproduce the lineshape data accurately in order to be used for the upper-limit estimation, the peaks were extracted from the data and input into the MC. This procedure is described below:

⁵⁷Throughout this section, we will call “the first peak” the peak at ca. 8 MeV below the main $\pi^+ \rightarrow e^+\nu_e$ peak.

⁵⁸The second peak is around 50 MeV which is in the region contaminated by background in the suppressed spectrum.

5.1. Tail correction

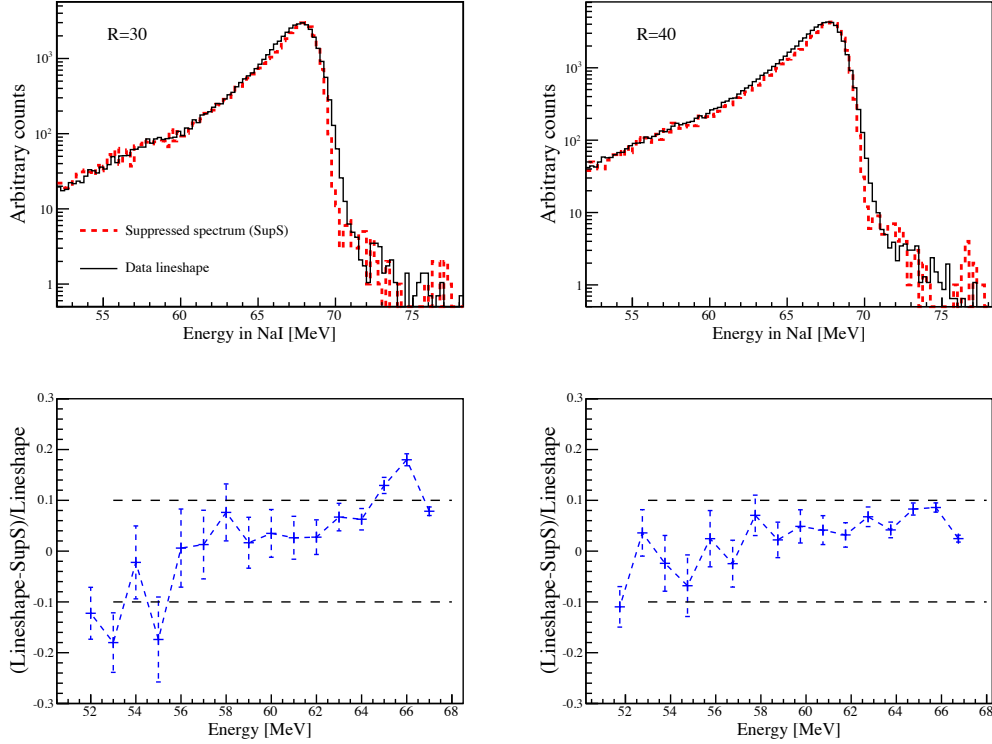


Figure 5.9: **Top:** Lineshape (with radiative corrections added and scintillator energies subtracted) obtained with data and compared to the $\pi^+ \rightarrow e^+\nu_e$ suppressed spectrum at two different radial cuts. The lineshape distribution is scaled to agree with the suppressed spectrum at the position of the peak. Discrepancy in the resolution of the peak is expected due on one hand to the additional scattering in the beamline for the data lineshape and on another hand to the Total Energy cut applied to the suppressed spectrum data. **Bottom:** Level of agreement of the lineshape data and the suppressed spectrum between 52 and 67 MeV. Each point represents the percentage difference between lineshape and suppressed spectrum in the number of events present in a 1 MeV energy region before the point. Since the lineshape spectrum is a construction of different statistical samples including interpolated spectra, the statistical errors are not representative. The error bars included in these plots are based on the suppressed spectrum statistics and are only indicative. The horizontal dotted lines indicate the 10% level agreement.

5.1. Tail correction

- A MC simulation with a positron beam hitting the center of the NaI crystal (without PIENU-I detector) is generated without hadronic interactions (only electro-magnetic interactions contribute to the MC spectrum. The only part of the QGSP_BERT physics list used is: G4EMStandard). This distribution is subtracted from the lineshape data at $\theta = 0^\circ$. The spectrum obtained between 32 and 61 MeV contains the shape and the amplitude of the “neutron-escape” peaks at $\theta = 0^\circ$.
- This spectrum is added to the MC at each angle. The amplitude of the peaks is assumed to be independent of the angle (see discussion below on the validity of this assumption). At high entrance angles, positrons deposit more energy into T2, the main peak in the NaI is therefore shifted with angle. To take into account this shift, the peaks are always added at a fixed energy from the main peak at each angle.
- Although the amplitude is assumed to be independent of the entrance angle of the positron, the broadening of the peak is not. For each angle, the broadening of the main positron peak is compared bin by bin to the shape of the peak at $\theta = 0^\circ$. The same broadening ratio is applied to the three peaks⁵⁹. As the angle grows so does the width of the peaks which tend to leak into the lower energy peaks. To take this into account, the first peak (at $E \sim 60$ MeV) is first broadened. The part of its peak which is leaking under the second peak is subtracted from the latter one before its own broadening. The same procedure is repeated for all three peaks.

Fig.5.10 shows the comparison of the data and MC lineshapes at all measured angles. The agreement around the peak regions (shown by the arrows) is very good⁶⁰ demonstrating that this procedure works. For the 0° configuration, the fourth “neutron-escape” peak is also noticeable. This peak is not added to the MC since it has a negligible effect on the tail. We should also note that there is no implementation of pile-up in the MC simulation, which explains the lack of events above the main positron peak in the MC. Given the level of agreement between MC and data for energies below the main positron peak, the effect of the high energy background on the low energy tail fraction is estimated to be less than a few percent.

⁵⁹The three peaks correspond to 1, 2 and 3 neutron escapes from the crystal.

⁶⁰The agreement for the angle $\theta = 15^\circ$ is worse. This will be discussed in the next paragraph.

5.1. Tail correction

The main assumption of this procedure is that the amplitude of the “neutron-escape” peaks is the same at all angles (and also that the electromagnetic part of the MC is correctly simulated).

So far, we have only considered particles hitting the front face of the NaI at its center. $\pi^+ \rightarrow e^+\nu_e$ positrons hitting the front face off-center and at high angles might provide different contributions. Naively, one would think that at higher angles, the height of the photo-nuclear peak might decrease due to the smaller amount of material traversed by the shower photons (less material to interact with). On the other hand, due also to the smaller amount of material, the neutron reabsorption probability in the crystal would decrease which would lead to a relative increase of the peaks. On the left plot of Fig.5.11, the mean length of material traversed by the shower particles (e^\pm, γ) is shown as a function of the positron entrance radius (this is for e^+ emitted isotropically like $\pi^+ \rightarrow e^+\nu_e$ positrons). The crossing of the red lines indicates the mean value for our radial cut of R=60 mm. On the right plot of Fig.5.11, the amount of material traversed by the photon before absorption by a nucleus is shown. This indicates that most of the photo-nuclear events happen within a few radiation lengths from the surface of the crystal. Therefore the amount of material “seen” by the shower particles is typically the same at all considered angles.

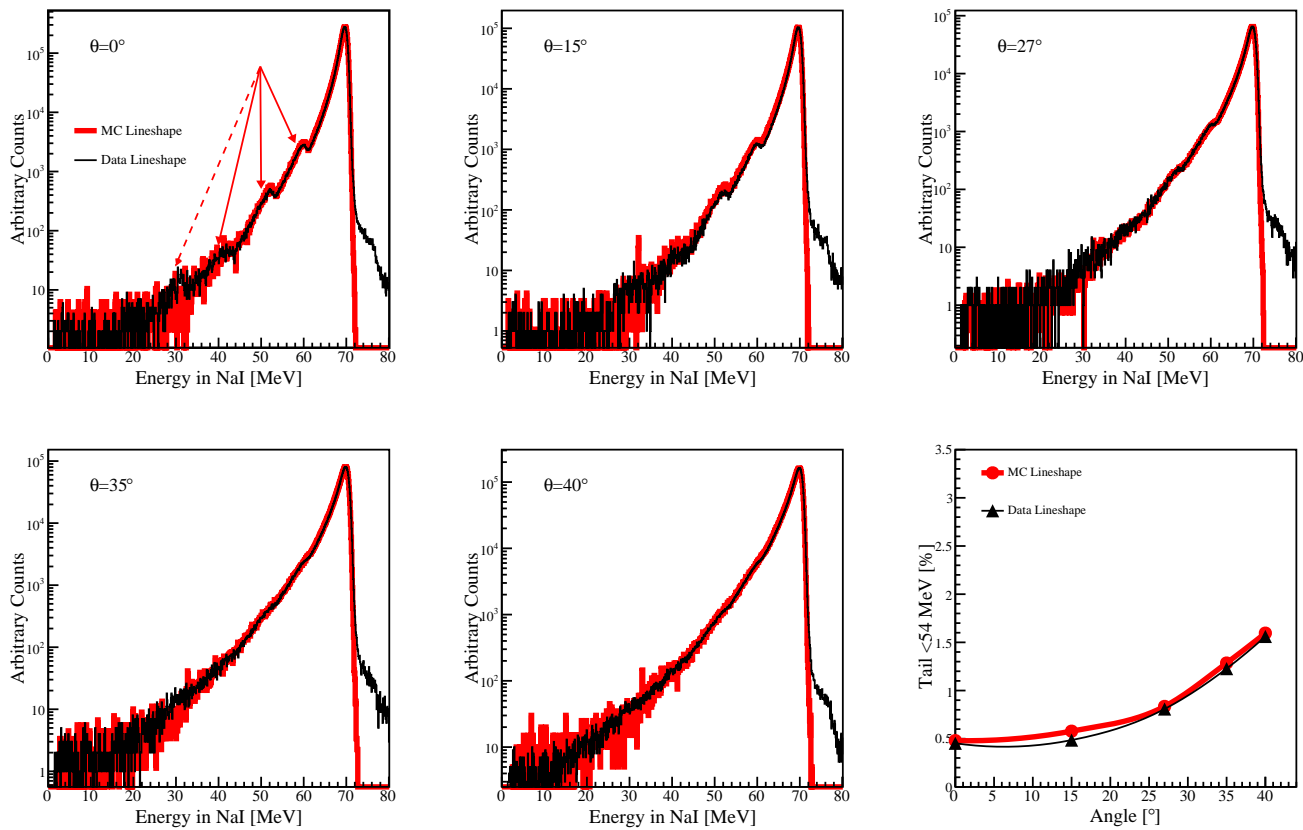


Figure 5.10: Comparison of the data (without matching procedure) and MC lineshapes with beam positrons hitting the center of the crystal at five different angles. The bottom right plot shows the tail fraction for both MC and data.

5.1. Tail correction

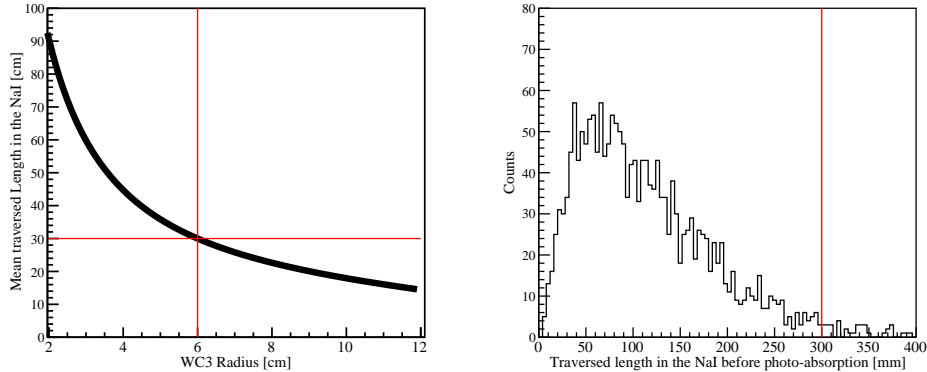


Figure 5.11: **Left:** The mean traversed length in the crystal as a function of the entrance radius measured by WC3. **Right:** Traversed length in the NaI before a photon is absorbed by a nucleus (MC).

Also, one should note that at higher angles the tail is dominated by shower leakages. This is illustrated by Fig.5.12. The contribution from photo-nuclear reactions stays the same but its relative importance on the tail decreases at high angles.

The next step for the validation of the procedure of adding the effect from neutron escape seen in the data into the MC is to produce a MC lineshape with positrons entering the NaI off- and on-center (which simulates $\pi^+ \rightarrow e^+ \nu_e$ positrons path length in the crystal) and compare it to the data lineshape obtained after the matching procedure. The peaks from neutron escape are implemented the same way in the off-center case as they were for the on-center case. The comparison between the isotropic MC and the data lineshape is shown in Fig.5.13 for three different radial cuts. The bottom plots show the level of agreement between the MC and data spectra. Since the peaks of the spectra are scaled to each other, the error bars are only indicative of the level of precision reached based on the MC statistics (since the data lineshape is a construction). For the two higher radii, the agreement is within 10% at every energy and better than 4% on the entire energy range. The vertical dotted lines in the bottom plots show the band in which 90% of the tail below 54 MeV is contained⁶¹. That shows that

⁶¹In this lineshape section, 54 MeV is used as a cutoff energy to compare the MC and data tail fractions. There is no direct relation with the nominal cut-off energy at 50 MeV used later in this chapter to determine the final tail fraction. If one takes into account

5.1. Tail correction

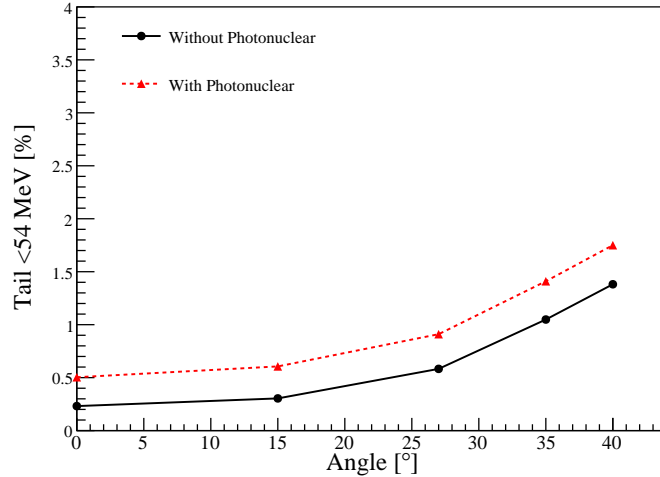


Figure 5.12: MC simulation of the increase of the tail fraction as a function of the beam positron angle hitting the center of the NaI crystal with or without photo-nuclear reactions.

energies below 42 MeV have very little effect on the tail. The R=20 mm spectra shows a higher discrepancy. This has not been understood to-date but it should be noted that the radial cuts are inclusive meaning that the cut at R=40 mm, for example, includes all smaller radii. This shows that the disagreement at R=20 mm has very little impact on the full lineshape due to the limited solid angle.

The discrepancy between MC and true data for angles close to 20° can also be seen in the direct comparison of the lineshape measurements (without the matching procedure described in §5.1.3) to a MC simulation of beam positrons. Fig.5.14 shows this comparison. The tail value at high angles is very sensitive to an error in the rotation angle. We estimate that the precision in the determination of the angle at which the crystal was rotated is of the order of 1°⁶². Fig.5.14 shows the 1° band from the MC simulation. All

the energy deposited in the downstream scintillators, a cut-off energy at 52 MeV for the lineshape would be closer to the nominal cut-off.

⁶²Measurement of the rotation angle was done with the help of plumb-bob attached to the NaI can. Displacement distances were measured on the floor of the experimental area with conventional rulers. A more sophisticated angle measurement method has been developed for the 2011 lineshape measurements.

5.1. Tail correction

lineshape measurements except the 15° point are within this 1° band which tends to exclude a measurement error⁶³ as the source of the discrepancy. Since this error has a very limited effect on the overall tail fraction determination, no further investigations have been carried out.

Finally, Fig.5.15 shows the tail value below 54 MeV obtained at different angles from MC and data lineshape. The agreement between those two is better than 4% at R=40 mm which is a satisfying agreement for the estimation of the upper limit from the MC lineshape.

⁶³An error in the angle measurement of $\sim 4^\circ$ would be necessary to explain the discrepancy.

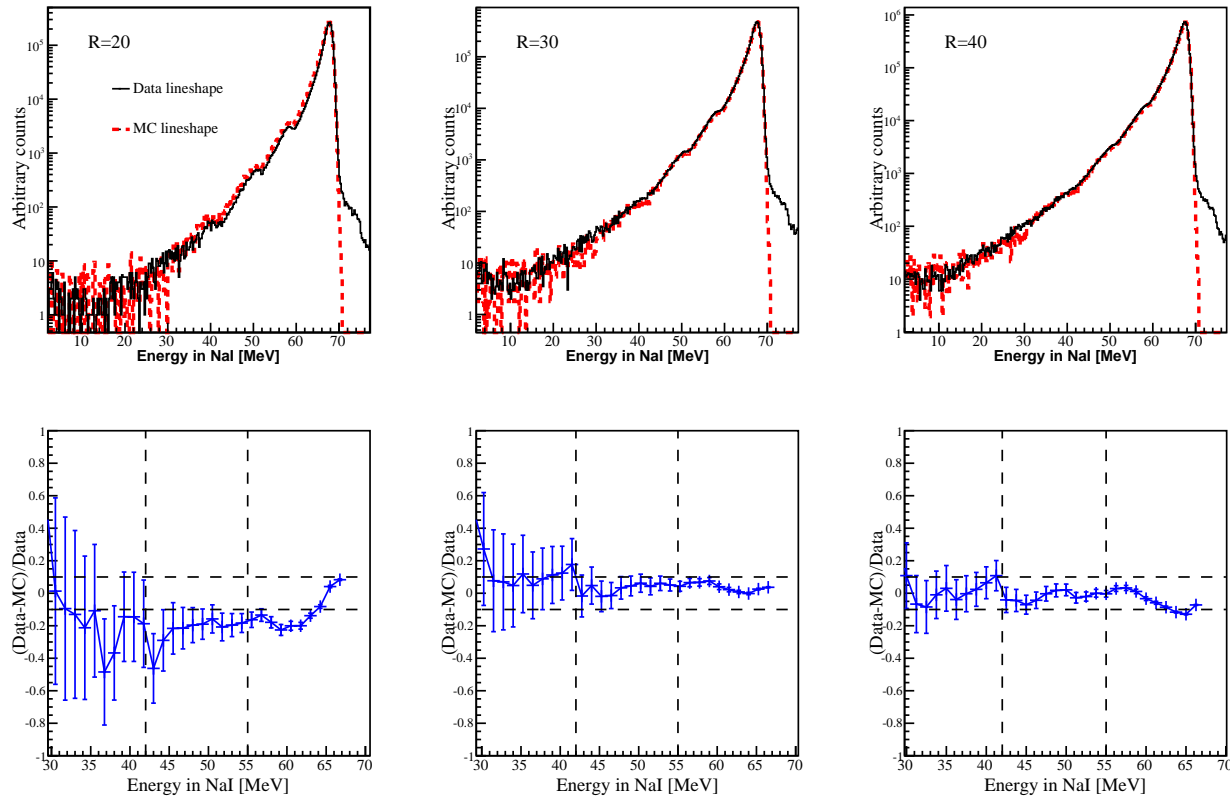


Figure 5.13: **Top:** MC and data lineshapes at three different radial cuts. **Bottom:** Level of agreement between MC and data. Each point represents the percentage difference between the data and MC lineshapes in the number of events present in a 1 MeV energy region before the point. The vertical dotted lines show the band in which 90% of the tail below 54 MeV is contained. The horizontal dotted lines indicate the 10% level agreement.

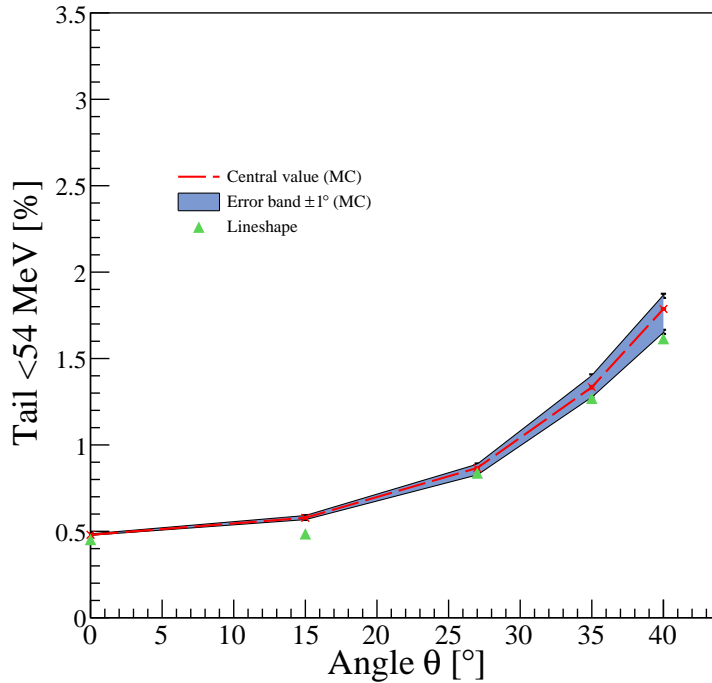


Figure 5.14: Comparison of the lineshape measurements with a MC simulation of beam positrons. The precision on the measurement of the NaI rotation angle is estimated to be 1° (blue band).

Estimation of the upper limit

On top of the procedure described above to include the effect of photo-nuclear reactions into the MC, other steps are involved to match the MC and data lineshapes in order to be able to determine the upper limit from the MC. For reference, the contribution from each step to the total tail is detailed in Table 5.3.

First, the real beam spatial distribution and energy spread are input into the MC. The generation of the beam distribution is detailed in §6.1.1. The resolution of the NaI is added to the MC based on the lineshape data. The positrons from the $\pi^+ \rightarrow e^+\nu_e$ decay have to traverse the downstream counters while the lineshape positrons were taken without the PIENU-I

5.1. Tail correction

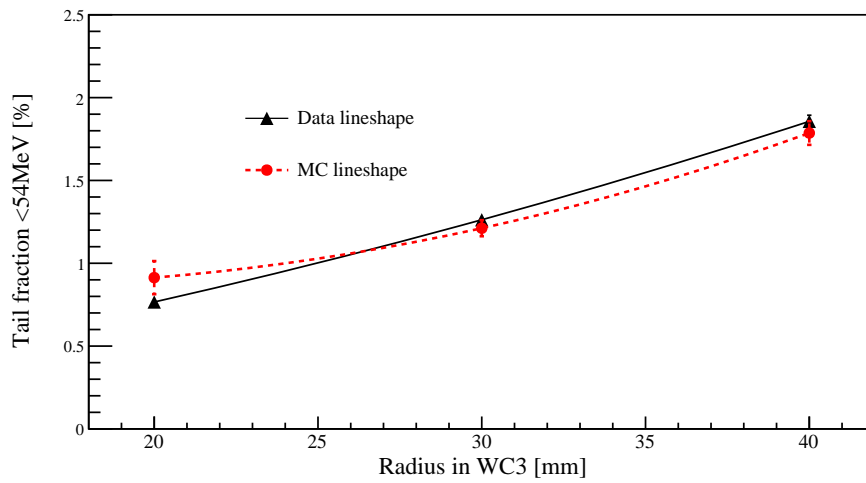


Figure 5.15: Tail fraction estimated from MC and data lineshapes. The error bars on the tail fraction extracted from the data lineshape represent the uncertainty on the matching procedure (as determined from MC). The error bars on the tail fraction from the MC lineshape represent the average difference in the tail fraction between MC and data for each angular measurement smaller than the acceptance cut (for example, at $R=30$, the average difference in the tail fractions between MC and data at $\theta = 0^\circ, 15^\circ$ and 27° is taken as the error on the tail).

5.1. Tail correction

detector. The energy deposited in the downstream counters by the positrons (obtained from data) is therefore subtracted from the MC lineshape. Finally, the radiative decay spectrum is added to the MC lineshape, see §6.3.

Table 5.3: List of the low energy tail components based on lineshape obtained with MC and data. For items 1 to 6, the tail below 52 MeV is considered while items 7 and 8 (after the subtraction of the energy deposited in the downstream counters) consider the tail below ~ 50 MeV.

Effects	Tail (NaI) at R=60 mm
1. Isotropic positron beam, 69.3 MeV	2.06%
2. Distribution in z taken from pion stopping distribution	2.01%
3. Addition of momentum spread ($\sigma = 0.44$ MeV)	2.13%
4. Addition of NaI resolution	2.24%
5. Addition of 0 degree “neutron-escape” peaks	2.48%
6. Smearing of “neutron-escape” peaks	2.85%
7. Addition of Tg, S3 and T1 energies	2.85%
8. Addition of Radiative decay	3.29%

The tail fraction is greatly increased if one does not add to the NaI energy the energy deposited in the CsI detector, e.g. at R=60 mm the tail is $\sim 3.3\%$ without the use of CsI. Before obtaining the MC lineshape with the CsI information added, the validity of the CsI simulation in the MC has to be confirmed. The same threshold as in the data is applied to the MC (2 MeV per crystal) and a Gaussian energy resolution of the form $\exp \frac{-x^2}{2(\sigma\sqrt{E})^2}$ with $\sigma = 0.2$ is applied to the distribution of each of the CsI rings to match the data distribution. The comparison for $\pi^+ \rightarrow e^+ \nu_e$ events in MC and data of the ratio of the number of events which pass the CsI threshold over the total number of events shows an agreement better than 3% (see §6.2.4). Finally, the upper limit is obtained by summing the counts in the MC lineshape up to an energy i and subtracting this number from $a[i]$ obtained from the suppressed spectrum (see Fig.5.7) before the multiplication by the ratio of the events estimated by the $\pi^+ \rightarrow \mu^+ \rightarrow e^+$ spectrum. If we call $c[i]$ the sum of the counts in the MC lineshape up to an energy i and $Ul[i]$ the upper limit value at this energy, an analogue of eq.5.1 is obtained (eq.5.2)

for the upper limit.

$$UL[i] = A - (a[i] - c[i]) \frac{B}{b[i]} \quad (5.2)$$

Since the lineshape has additional low energy components, an over-subtraction of the tail is done which leads to underestimating the background component. Thus, an upper limit on the tail is obtained. Fig.5.16 shows the upper limit on the tail fraction obtained from the MC lineshape together with the lower limit from the suppressed spectrum (see §5.1.2) obtained at two different radial cuts with and without the addition of CsI energy. The tail fractions are obtained by dividing the number of counts in the tail obtained by equation 5.1 and 5.2 by the number of counts in the spectrum above the 50 MeV cut-off. For low energies, since the $\pi^+ \rightarrow e^+ \nu_e$ tail component is small, the effect of underestimating the $\pi^+ \rightarrow \mu^+ \rightarrow e^+$ background on the upper-limit determination is small but the statistical uncertainty is large. The higher the energy, the worse is the estimation of the background which leads to the rise of the upper-limit with energies. Similarly, for the lower-limit, the assumption of no $\pi^+ \rightarrow e^+ \nu_e$ low energy tail is good at low energies but becomes worse as the integration to higher energies is done. This results in the downward-curved shape of the lower-limit. As per construction, the value of the lower limit hits zero at 50 MeV.

Results

From Fig.5.16, we see that the upper and lower limits constrain the value of the tail in a range of energies where statistical uncertainties are good enough and before the divergence of the limits. The upper limit is determined as the point (with the addition of the 1σ error) with the tightest constraint. Similarly, the lower limit is taken as the point (with the subtraction of the 1σ error) with the tightest constraint. The average of those two points (without the 1σ error) is used as an estimate of the tail fraction. This value is shown as a solid horizontal line in Fig.5.16.

The error on the tail fraction is a combination of statistical and systematic uncertainties. An estimate of the systematics is obtained by taking the standard deviation of the uniform distribution between the dashed lines in Fig.5.16. The statistical error is reflected by the error bars on the points at the lower and upper bounds. The largest error bar of those two bounds is taken as the statistical error estimate on the tail. The statistical and systematic uncertainties are summed in quadrature and indicated on each plot in Fig.5.16.

At R=60 mm with the addition of CsI energy, the $\pi^+ \rightarrow e^+ \nu_e$ tail fraction

5.1. Tail correction

obtained from the upper-lower limit technique and the associated systematic and statistical errors are:

$$\sigma_{UL}(\text{syst.}) = \frac{0.0032}{\sqrt{12}} = 0.00092 \quad (5.3)$$

$$\sigma_{UL}(\text{stat.}) = 0.00246 \quad (5.4)$$

$$f_{UL} = 0.97 \pm 0.26\% \quad (5.5)$$

The statistical error largely dominates the total error.

An independent estimate of the systematics on the upper limit can be obtained from the combination of the uncertainties in the procedure to obtain a MC lineshape. An error of 4% on the tail seen by the NaI is estimated after addition of the “neutron-escape” peaks to the NaI lineshape (this includes the 2% uncertainty on the tail from the matching procedure). An additional 3% error is estimated on the tail fraction seen by the CsI. Those contributions give an estimate of the total systematic error on the upper limit of 9.1×10^{-4} in agreement with the uncertainty extracted from the upper and lower limits.

Additional systematic errors arise from the uncertainties on the shape subtracted from the suppressed spectrum in order to obtain the upper and lower limits. This will be discussed in the next section.

We estimate that the systematics can be improved by at least a factor two with the new lineshape measurement made in 2011. Following the analysis of 2010 data, a new technique has been developed to rotate the calorimeter in order to get access to the lineshape for positrons hitting the crystal off-center. Moreover, information from the energy leaked in the CsI has also been recorded together with cosmic-ray events enabling a proper calibration of the CsI.

The statistical error can be improved with a larger $\pi^+ \rightarrow e^+\nu_e$ data set and more suppression of the low energy background. Because a larger suppression would affect the shape of the $\pi^+ \rightarrow e^+\nu_e$ spectrum, larger corrections would have to be made. An optimum would have to be found between the level of suppression and the number and amplitudes of the corrections.

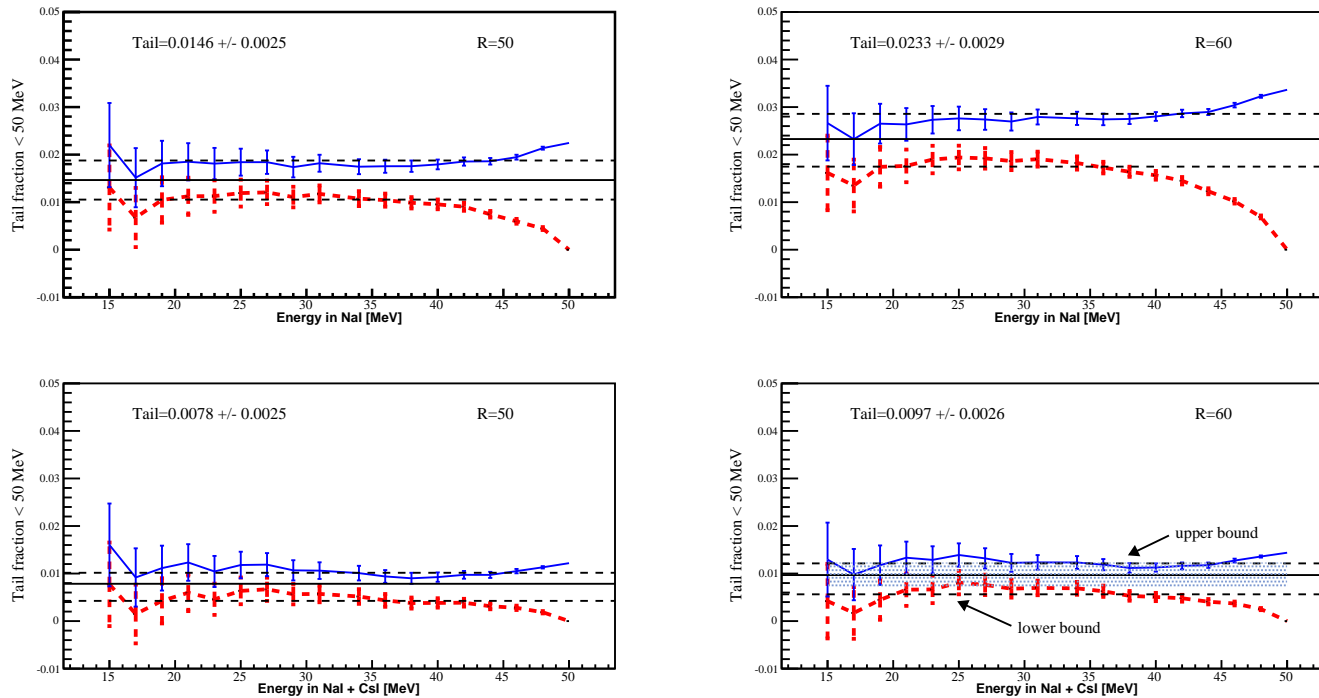


Figure 5.16: **Top:** Upper (thin blue solid line) and lower (thick red dotted line) limits on the tail at two different radial cuts (NaI only). **Bottom:** Upper and lower limit on the tail at two different radial cuts (NaI and CsI). The tail fraction and the error obtained (see text) are indicated on each figure. The dotted horizontal lines show the values of the upper and lower bounds. The solid horizontal lines indicate the tail fraction. To help visualizing the procedure explained in the text, the upper and lower bounds are indicated by arrows on the last figure and the 1σ error on the tail fraction is represented by the blue hatched area.

5.1.5 Corrections to the tail fraction

The cuts applied to obtain the suppressed spectrum for the lower and upper limits are not applied to the data used to obtain the raw branching ratio and could therefore create a bias. Table 5.1 indicates the cuts which are energy dependent and can potentially affect the $\pi^+ \rightarrow e^+\nu_e$ tail. A correction on the tail fraction has to be made for the events which are removed from the tail by those cuts. On top of the energy dependent correction, a correction has to be applied for MDIF events. Those two corrections are detailed in the following paragraphs.

Muon DIF correction

As mentioned in §4.9, the probability (p) of MDIF is 8×10^{-6} . Fig.4.24 showed the energy distribution in the calorimeters of MDIF events compared to MDAR. The Total Energy cut has a negligible impact on the shape of the MDIF spectrum in the calorimeters. Up to an energy of ~ 38 MeV, the shapes of MDAR and MDIF are similar. Since both the upper and lower limits are estimated by points below 38 MeV (see Fig.5.16), we can consider that the difference in the shapes of MDAR and MDIF does not affect the estimate of the tail. However, because MDIF events leak beyond the 50 MeV boundary, a correction on the tail fraction has to be made. Let's estimate the contribution of MDIF in the tail. A MC simulation shows that 22.7% (C_{Tg}) of MDIF remain after the Total Energy cut shown in Fig.5.17. All other suppressed spectrum cuts will have the same signal efficiency as $\pi^+ \rightarrow e^+\nu_e$ events (see Table 5.1). Taking the theoretical branching ratio $R = 1.24 \times 10^{-4}$ and the efficiency of the target cut on $\pi^+ \rightarrow e^+\nu_e$ events from Table 5.1, one finds the ratio (Q) of MDIF to $\pi^+ \rightarrow e^+\nu_e$ events:

$$Q = \frac{p \times C_{Tg}}{E_{Tg} \times R} = \frac{8.10^{-6} \times 0.227}{0.7680 \times 1.24 \cdot 10^{-4}} = 1.91 \times 10^{-2} \quad (5.6)$$

This corresponds to 11.44% (1.91/16.7%) of the low energy tail in the suppressed spectrum. Since the extrapolation to 50 MeV to obtain the upper and lower limits is done by integrating the full spectrum up to 50 MeV and 2.99% of the total number of MDIF are not contained within this energy range, an over-subtraction of the background by 0.0299×0.1144 is done. This would lead to a correction to the $\pi^+ \rightarrow e^+\nu_e$ tail of +0.0034.

The fraction of MDIF in the suppressed spectrum is confirmed with a simultaneous fit of both the energy recorded in the calorimeters and the time spectra for the events in the suppressed spectrum. Fig.5.18 shows the result of the fit. The energy spectrum of PDIF is obtained from data by

5.1. Tail correction

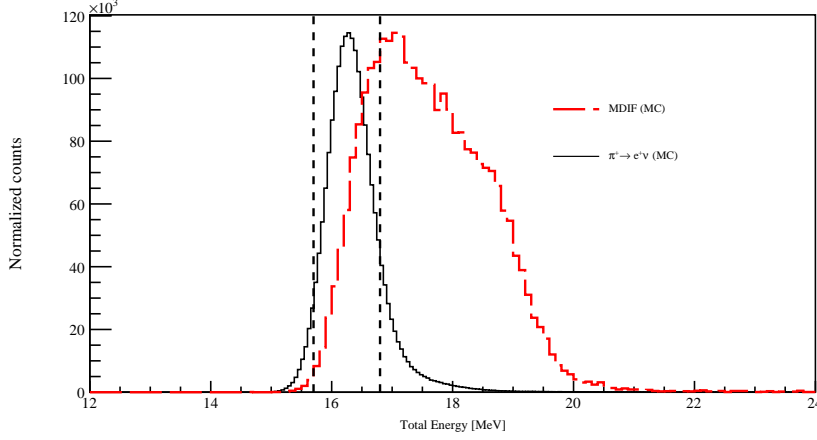


Figure 5.17: Total beam energy deposited by MDIF events compared to $\pi^+ \rightarrow e^+ \nu_e$ events.

selecting late muon decays while the shapes of MDIF and $\pi^+ \rightarrow e^+ \nu_e$ are obtained from MC. The fit range is 3 to 57 MeV in the energy spectrum and 10 to 35 ns⁶⁴ in the time spectrum. The combined χ^2 is indicated on the figure. The fit gives a contamination of MDIF in the low energy tail of $10.77 \pm 2.81\%$ which is in good agreement with the result of the calculation made above. MDIF is thus found to make up 1.8% ($(10.77 \times 16.7)\%$) of the suppressed spectrum which is in very good agreement with an independent analysis on data taken in 2009 dealing with a search for massive neutrinos in the suppressed spectrum. This analysis, detailed in chapter 8, found a contamination of the suppressed spectrum by MDIF of 1.7%. From §4.9, the error of the MDIF fraction above 50 MeV (f_{MDIF}) is estimated to be ± 0.002 . Therefore, the error on the fit (inflated by $\sqrt{\chi^2/NDF}$) summed in quadrature with the error on f_{MDIF} translates to an error of 9.0×10^{-4} on the $\pi^+ \rightarrow e^+ \nu_e$ tail correction from MDIF. Finally, the upper and lower limit tail fraction with MDIF correction gives a tail fraction ($f_{UL+MDIF}$) of:

$$f_{UL+MDIF} = 0.0097 + 0.0032 \pm \sqrt{0.0026^2 + 0.0009^2} = (1.29 \pm 0.28)\% \quad (5.7)$$

⁶⁴The region closer to the prompt cannot be fitted due to the distortions introduced in the Early region by the Pulse Shape cut.

5.1. Tail correction

The fit also gives a $\pi^+ \rightarrow e^+\nu_e$ tail fraction (f_f) of:

$$f_f = (6.66 \pm 0.1)\% \times 16.7\% = (1.11 \pm 0.02)\% \quad (5.8)$$

which is consistent with $f_{UL+MDIF}$ but provides an order of magnitude smaller error estimate due to the strong constraint on the shape of the $\pi^+ \rightarrow e^+\nu_e$ spectrum in the fit.

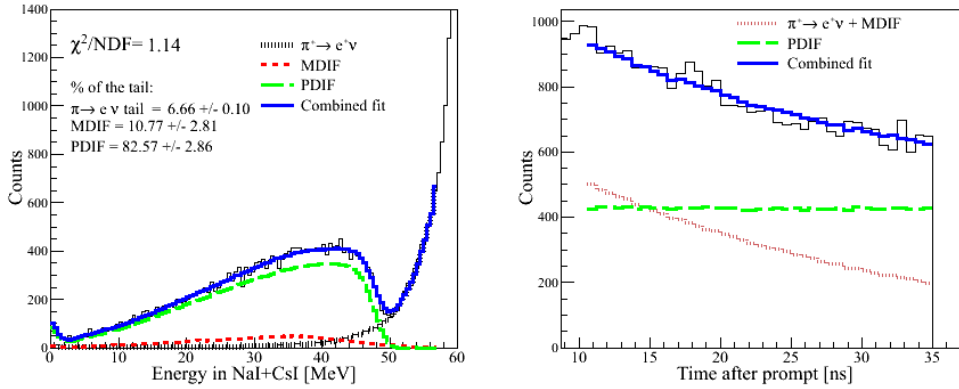


Figure 5.18: **Left:** Energy spectrum in the calorimeters and fit result. **Right:** Time spectrum and fitting functions for each component of the background.

Energy dependent correction

The only energy dependent cut which has a significant effect on the $\pi^+ \rightarrow e^+\nu_e$ spectrum, and could therefore affect the evaluation of the tail fraction, is the “Total Energy” cut. Indeed, the kink cut only uses information upstream of the target and the pulse shape and S3 cuts have a $\pi^+ \rightarrow e^+\nu_e$ efficiency close to 100%. The Time cut has no distorting effect.

The Total Energy cut suppresses both events which have lower and higher total energies. Bhabha-scattering events can produce higher energies in the target as shown in Fig.5.19. A large fraction of Bhabha-scattered events lie in the $\pi^+ \rightarrow e^+\nu_e$ tail which results in a positive correction to the tail fraction obtained so far. Also, lower energy positrons emitted together with a photon tend to deposit more energy in the target and would have been preferentially eliminated by the suppressed spectrum cuts. The correction for

5.1. Tail correction

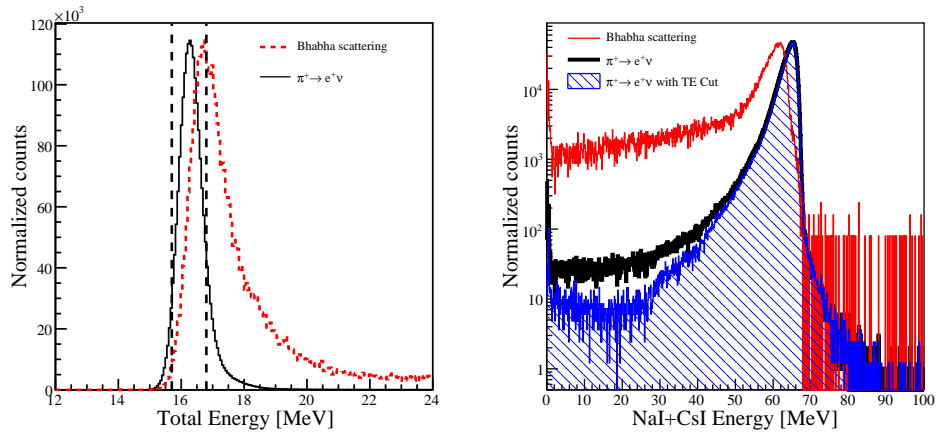


Figure 5.19: **Left:** Total Energy of Bhabha-scattering events compared to the full $\pi^+ \rightarrow e^+ \nu_e$ event distribution from MC. The distributions are scaled to the same peak amplitude. The black dotted vertical lines show the boundaries of the Total Energy cut. **Right:** Energy deposited in the calorimeter for Bhabha-scattering events compared to $\pi^+ \rightarrow e^+ \nu_e$ events and $\pi^+ \rightarrow e^+ \nu_e$ after Total Energy (TE) Cut from MC. All three distributions are scaled to the same peak amplitude.

5.1. Tail correction

this cut is obtained from MC and corresponds to an addition of +0.74% to the tail fraction. An estimate of the error on this correction can be obtained by comparing the correlation of the Total Energy with the energy deposited in the calorimeters obtained with MC and data. Fig.5.20 shows the average Total Energy versus the energy deposited in the calorimeters for early events with a small kink cut. The dependence (due to Bhabha-scattering and the Landau tail of $\pi^+ \rightarrow e^+ \nu_e$ events) shape is very well reproduced in the MC down to an energy of 60 MeV. Below this energy a small contamination in the suppressed spectrum from MDIF and $\pi^+ \rightarrow \mu^+ \rightarrow e^+$ events with an additional pileup have a large impact on the Total Energy. The blue band shows the uncertainty on the initial beam momentum. There is a smaller than 0.1 MeV discrepancy between MC and data for calorimeter energies above 60 MeV and therefore well within the uncertainty on the momentum. The 0.1 MeV discrepancy is taken as an error on the estimate of the energy dependent correction from MC. It translates into an error of $\pm 0.03\%$ on the MC correction.

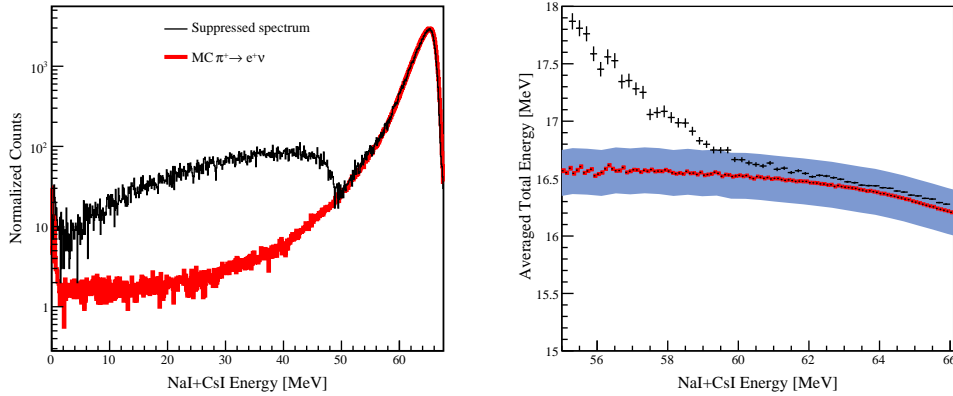


Figure 5.20: **Left:** Suppressed spectrum and $\pi^+ \rightarrow e^+ \nu_e$ spectrum obtained from MC. **Right:** Average Total Energy versus the energy deposited in the calorimeters for early events with a small kink cut for MC and data.

The MDIF and energy dependent corrections give a total tail fraction estimate of:

$$f_T = (2.03 \pm 0.28)\% \quad (5.9)$$

5.1.6 Tail estimation from Monte Carlo

The tail correction can also be directly obtained from a MC simulation of $\pi^+ \rightarrow e^+\nu_e$ decays with the addition of radiative decays (see §6.3 for details of the MC generation of radiative decays) and “neutron escape” peaks extracted from the data.

This gives a tail of $f_{MC} = (1.83 \pm 0.09)\%$ at R=60. The stated uncertainty is taken from the systematic error estimate on the MC lineshape used to obtain the upper-lower limit since many of the contributions to the simulation (“neutron-escape” peaks, energy resolutions, beam resolution etc) are identical. However this error is given as an order of magnitude estimate and does not reflect a thorough study of the possible systematics of the MC $\pi^+ \rightarrow e^+\nu_e$ simulation.

This tail correction obtained from MC is consistent with the tail obtained from the upper and lower limit method after correction for the Total Energy cut and MDIF contribution. Fig.5.21 shows a summary of the different tail corrections and the good level of agreement between the different tail determination techniques.

5.2 Acceptance correction

Energy dependent effects change the relative acceptance of low- and high-energy positron events. Those effects include multiple scattering, Bhabha-scattering, annihilation in flight and trigger losses.

- Multiple scattering denotes the many deflections of the positron due to the Coulomb force exerted by the nuclei. Those deflections result in events missing the trigger (called “out-scattered” events) counters while unperturbed they should have hit them. Similarly events which should not have triggered are deflected toward the trigger counters (“in-scattered” events). There is a small net difference between “in-scattered” and “out-scattered” events which is dependent on the specific geometry of the trigger counters. However, due to the energy dependence of the scattering cross-section, the net difference is slightly different for low (from $\mu^+ \rightarrow e^+\nu_e\bar{\nu}_\mu$ decays) and high (from $\pi^+ \rightarrow e^+\nu_e$ decays) energy positrons.
- Bhabha-scattering events in which two particles (a positron and an electron) are emitted from the target may lead to the rejection of the events. Since Bhabha-scattering cross-section is energy dependent, this process may have an effect on the acceptance.

5.2. Acceptance correction

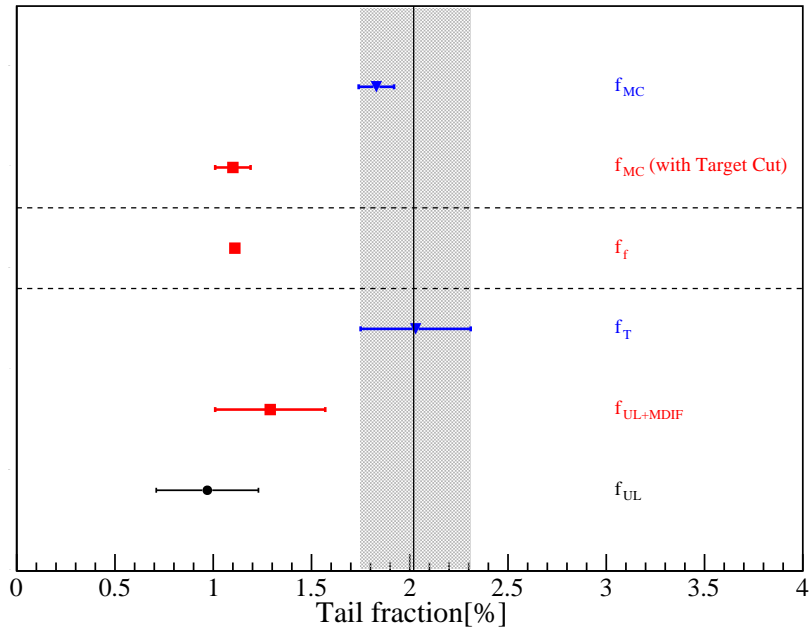


Figure 5.21: Summary of the evolution of the tail fraction with corrections. Identical colours (and marker styles) correspond to independent measurements of the same quantity. The blue triangles represent the tail fractions with all corrections included. The horizontal dotted lines separate independent tail fraction determination techniques. “ f_{MC} ” indicates the tail fraction obtained from a MC simulation of $\pi^+ \rightarrow e^+ \nu_e$ events with the addition of “neutron-escape” peaks and radiative decays. The same cuts as used for the branching ratio analysis are made. “ f_{MC} (with target cut)” is similar to “ f_{MC} ” but with the addition of the same target cut as made for the suppressed spectrum analysis. All other tail fractions are obtained from data (see text for details). The vertical solid line and the shaded area indicate the tail fraction and the error used as the correction to the raw branching ratio.

5.2. Acceptance correction

- Annihilation in flight can happen before the trigger counters or before sufficient energy has been deposited in the counters to pass the threshold leading to the loss of the event. Since annihilation is an energy dependent process, a correction has to be applied.
- Because the energy loss mechanism is energy dependent, low energy positrons from the $\mu^+ \rightarrow e^+\nu_e\bar{\nu}_\mu$ decay may stop and deposit their entire energy before reaching T1 or T2 counters. This leads to trigger losses and only affects low energy positrons.

The combination of those energy dependent effects leads to a correction on the branching ratio. This correction was calculated using MC and includes the cumulated effect on the acceptance of all processes mentioned above⁶⁵. Table 5.4 shows a MC estimate of the difference between $\pi^+ \rightarrow \mu^+ \rightarrow e^+$ and $\pi^+ \rightarrow e^+\nu_e$ events in the effective cross-sections of a few energy dependent processes.

Table 5.4: MC estimation of the proportion of a few energy dependent processes for $\pi^+ \rightarrow e^+\nu_e$ and $\pi^+ \rightarrow \mu^+ \rightarrow e^+$ events.

Processes	$\pi^+ \rightarrow e^+\nu_e$ [%]	$\pi^+ \rightarrow \mu^+ \rightarrow e^+$ [%]
Bhabha-scattering	2.298 ± 0.054	3.009 ± 0.054
Multiple scattering	0.013 ± 0.004	0.109 ± 0.010
Annihilation	0.027 ± 0.005	0.122 ± 0.011

5.2.1 Monte Carlo studies

An analysis of MC data was devised using the same cuts as used in the data analysis. The ratio of $\pi^+ \rightarrow e^+\nu_e$ and $\pi^+ \rightarrow \mu^+ \rightarrow e^+$ acceptances is obtained for an acceptance cut of R=60 mm (“nominal” acceptance cut). Sets of systematic studies are done to estimate the error on the acceptance correction. Each set requires to simulate 60M events. The description of each case studied is made below and summarized together with the results in Table 5.6. For comparison, Table 5.5 lists the expected uncertainties in the detector geometry. Fig.5.22, 5.23, 5.24, 5.25, 5.26 and 5.27 show the

⁶⁵We should also note that, due to the 1 mm traversed by the decay muons in the target, the acceptance is slightly different for positrons from $\pi^+ \rightarrow e^+\nu_e$ and $\mu^+ \rightarrow e^+\nu_e\bar{\nu}_\mu$ decays. This effect is also included in the acceptance correction.

5.2. Acceptance correction

ratio of $\pi^+ \rightarrow e^+\nu_e$ over $\pi^+ \rightarrow \mu^+ \rightarrow e^+$ acceptances as a function of the radial acceptance cut for each set of systematic studies.

- I. The influence of different pion stopping positions along the beam axis is studied. The nominal pion stop is at the middle of the target. An uncertainty in the pion stop position would lead to a different path length for the decay positrons affecting the energy dependent corrections. The stopping position is changed by varying the pion momentum in the MC. The effect of the different cases on the acceptance ratio is plotted in Fig.5.22. A stopping position 1 mm upstream of the nominal position has a slightly larger effect than 1 mm downstream, since it adds material to the positron path. Our knowledge of the position of the pion stop is on average better than 0.4 mm (see §5.2.3 for details). At our radial cut of 60 mm, an error of ± 0.4 mm on the pion stop distribution leads to an acceptance correction consistent with the nominal correction. This shows that the change in the momentum at the middle of the data taking (Fig.4.6) has no effect on the acceptance correction.

The width of the pion stopping distribution in the MC is $\sigma \sim 0.5$ mm due the momentum spread of the beam. This is consistent with a momentum bite of 0.5%. Our knowledge of the actual momentum bite is limited; but from lineshape measurements it is known to be smaller than 1%. If the momentum bite (Z_w in Fig.5.22) is increased to 1% in the MC, no significant change in the acceptance correction is observed.

- II. The displacement along the beam axis of the downstream tracking detectors is studied. S3 and WC3 are displaced while the reconstruction package assumes the nominal position. Fig.5.23 shows that displacements in both upstream and downstream directions have a very limited effect, of the order of 5×10^{-4} on the ratio of acceptances.
- III. The X and Y displacements of the downstream trackers are also studied, see Fig.5.24 and 5.25. X displacements in WC3 tend to have larger effects than Y displacements due to the fact that the X coordinate is well defined in WC3 (one plane is oriented along the X-axis). If WC3 is shifted toward positive values of X, the impact on the acceptance correction is larger than for negative shifts. This could be explained by the slight asymmetry of the beam which is shifted toward negative values of X (see Fig.6.1). A shift of WC3 in the opposite direction increases the discrepancy between the actual angle of the positron track and the reconstructed one. This has the effect of accepting larger

5.2. Acceptance correction

angles therefore bringing the correction down.

- IV. The effect of different downstream detector thicknesses is studied. T2 thickness has no effect on the acceptance since it is placed downstream of the WC3. T2 is therefore not included in the study. An increase in Tg and T1 counter thicknesses has the same effect as an earlier pion stop in the target: it increases the amount of material the positron has to traverse. The counter thicknesses are known with an accuracy better than 100 μm (see Table 5.5). A change in thicknesses within this range does not affect the correction significantly, see Fig.5.26. The scintillators are also wrapped in one layer of Aluminized Mylar[®] (polyester film) as well as one layer of Tedlar[®] (polyvinyl fluoride film), with respective thicknesses of 25 and 50 μm . The addition of those layers in the MC has a negligible effect on the acceptance correction.
- V. The effect of the trigger counter's threshold is also studied. In the data, the trigger threshold is estimated to be around 100 keV. An increase of up to 100 keV in both trigger detector threshold levels does not affect the correction at our radial cut within statistical uncertainties, see Fig.5.27.

Table 5.5: Estimation of the level of uncertainty in the detector positions based on multiple measurements.

Measured quantity	Measurement uncertainty [mm]
Z location of S3	0.100
Z location of WC3	2.000
Thickness of Tg	0.025
Thickness of T1	0.090
Thickness of S3	0.005
X/Y position of S3 *	0.005
X/Y position of WC3 *	0.200
Thickness of wrapping (Tg and T1)	0.015

* The uncertainties in those positions were not directly measured but estimated using track reconstruction with WC1.2 (see §6.1.2). This procedure was tested with MC and led to the stated uncertainties.

5.2. Acceptance correction

Table 5.6: List of systematics studies on the acceptance.

Case	Description	Ratio of acceptances at R=60 mm	Stat. Errors
π stop in Tg	[mm]		[%]
I.a)	z = 0.08 (nominal)	0.9994	0.04
I.b)	z =+1	0.9997	0.04
I.c)	z =-1	0.9993	0.04
I.d)	$\sigma=1\%$	0.9996	0.04
Displacement	[mm]		[%]
II.a)	z WC3 =+2	1.0000	0.04
II.b)	z WC3 =-2	0.9999	0.04
II.c)	z S3 =+0.2	0.9995	0.04
II.d)	z S3 =-0.2	0.9992	0.04
III.a)	x WC3 =+0.2	0.9988	0.04
III.b)	x WC3 =-0.2	0.9996	0.04
III.c)	y WC3 =+0.2	0.9997	0.04
III.d)	y WC3 =-0.2	0.9997	0.04
III.e)	x S3 =+0.02	0.9996	0.04
III.f)	x S3 =-0.02	0.9998	0.04
III.g)	y S3 =+0.02	1.0002	0.04
III.h)	y S3 =-0.02	0.9999	0.04
Thickness	[mm]		[%]
IV.a)	T1 z=+0.1	1.0003	0.04
IV.b)	T1 z =-0.1	1.0005	0.04
IV.c)	Tg z=+0.05	0.9999	0.04
IV.d)	Tg z =-0.05	0.9996	0.04
IV.e) Wrapping	T1 and Tg: +0.150	0.9999	0.04
Threshold	[KeV]		[%]
V.a)	T1 & T2 =+25	0.9994	0.04
V.b)	T1 & T2 = +100	0.9996	0.04

5.2. Acceptance correction

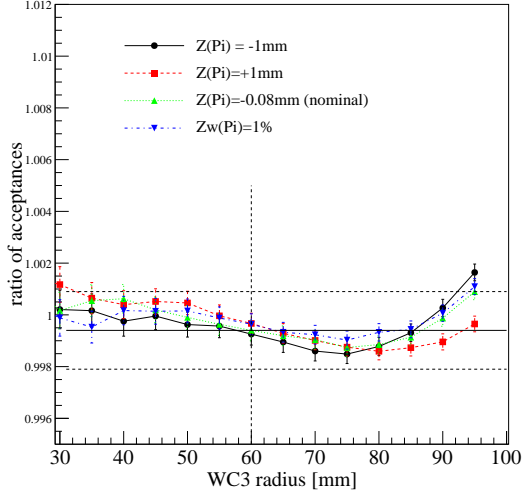


Figure 5.22: Effect on the acceptance of different pion stopping point along the beam axis.

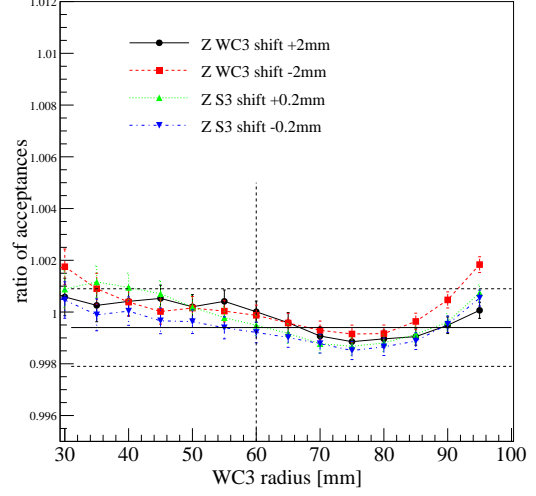


Figure 5.23: Effect on the acceptance of a shift of the tracking detectors along the beam axis.

5.2.2 Result

From Fig.5.22, we can see that for an acceptance cut at $R=60$ mm the multiplicative correction is very close to 1. An error estimation on this correction based on the set of systematic studies described above is not straight-forward due to the existence of correlations between the different sets. Considering the estimated level of uncertainty in the detector's positions shown in Table 5.5 and the result of the MC studies (Table 5.6), we can conclude that at a radial cut of 60 mm, an error in the position of the detector along the Z and Y directions has a very limited impact on the acceptance correction. The fluctuation in the acceptance correction from those shifts is smaller than 1×10^{-3} . Similarly, a change in momentum within our error estimate and changes in the downstream scintillator's thresholds are all, at $R=60$ mm, consistent with statistical fluctuations. The critical parameter seems to be the knowledge of the downstream detector thicknesses. Although all thickness cases are consistent with each other within statistical uncertainties, the knowledge of the counter thicknesses within $100 \mu\text{m}$ accuracy is limiting the acceptance correction determination. The effect of a change in thickness by $100 \mu\text{m}$ on the acceptance correction is of the order of 1.5×10^{-3} (including

5.2. Acceptance correction

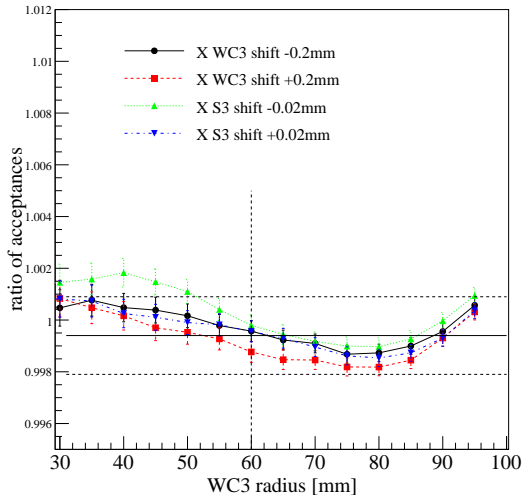


Figure 5.24: Effect on the acceptance of a shift of the tracking detectors along the x axis.

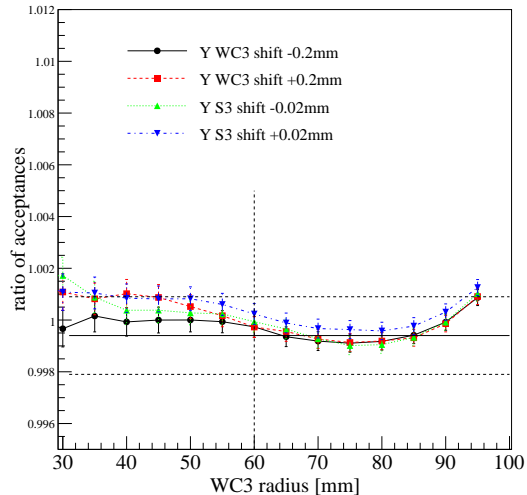


Figure 5.25: Effect on the acceptance of a shift of the tracking detectors along the y axis.

statistical uncertainties). This was chosen as the total uncertainty on the acceptance correction. This error band is represented by the horizontal lines on Fig.5.22, 5.23, 5.24, 5.25, 5.26 and 5.27. This is a rather conservative error estimate but given the level of statistics reached in this thesis, and since the acceptance correction in itself is very small, the error on the acceptance correction will have a limited impact on the overall uncertainty on the branching ratio.

To conclude, we can say that the acceptance correction is very small and certainly much smaller than the previous experiment at TRIUMF due mainly to the larger acceptance. With a careful study of the systematic error correlations and additional independent measurements on the position of the tracking devices, the error on the acceptance correction can be further improved and will not be a major source of error on the final branching ratio result.

5.2.3 Test of the Monte Carlo

To test the MC on the particular cases mentioned in the previous section, we have taken special sets of data. A more general confirmation of the validity

5.2. Acceptance correction

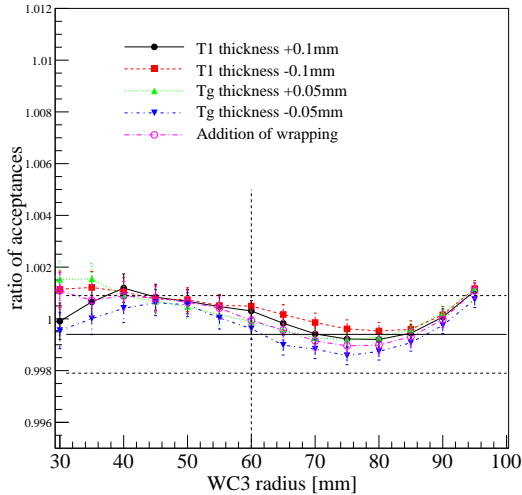


Figure 5.26: Effect on the acceptance of a change in the downstream plastic scintillators thicknesses.

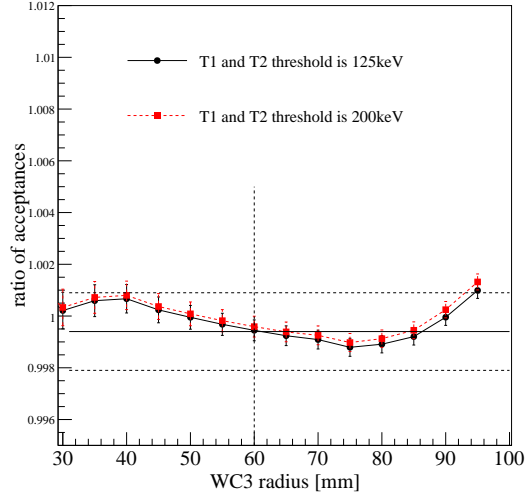


Figure 5.27: Effect on the acceptance of an increase in the threshold energy of the downstream trigger detectors.

of the PIENU simulation is described in Chapter 6.

Shift in PIENU II detector

Data were taken with the PIENU-II detector shifted by a known amount. Those shifts are propagated in the geometry file read out by the tracking package. The reconstruction of the z -vertex is shown to be insensitive to those shifts in the MC and in the data. This proves that the downstream tracking gives consistent results for different geometries for both MC and data.

Momentum scan

At the beginning of 2011 beamtime, a momentum scan was performed in order to verify the correctness of the z vertex reconstruction and estimate the error on the beam momentum. The comparison of the pion stop position in MC and data at different momenta gives an uncertainty on the momentum of 0.4%. At the nominal momentum, the difference in the z -vertex reconstruction between $\pi^+ \rightarrow e^+\nu_e$ events taken in 2010 and a MC simulation of $\pi^+ \rightarrow e^+\nu_e$ events is of the order of 80 μm . This difference can be due to

a slightly different geometrical arrangement of the detector⁶⁶ between 2010 and 2011. Conservatively it is entirely attributed to an error in the momentum. The sum of those two errors gives a total uncertainty of 0.6% on the beam momentum which translates in less than 0.4 mm uncertainty on the pion stop position.

5.3 Other systematics

5.3.1 Effect of tracking detector inefficiencies in the acceptance definition

A separate study is done to assess the effect of inefficiencies in the downstream tracking detectors on the definition of the acceptance. Indeed, if the definition of the acceptance is varying significantly with the detectors efficiencies, the acceptance correction would have to be modified.

Effect of WC3 inefficiency

WC3 inefficiencies are implemented in the MC based on the inefficiencies observed in the data. The average efficiency of each plane of WC3 for beam positrons is higher than 99.8%. The resulting acceptance change is shown in Fig.5.28. The change in acceptance is, within statistical errors, consistent with zero. The effect of the WC3 inefficiency can therefore be neglected.

Effect of S3 inefficiency

The same procedure is done with the S3 detector. The inefficiencies of S3 planes shown in Fig.5.29 are obtained before the WC3 acceptance cut. This is so as not to bias the sample by requiring a good track in the downstream detector. However, this tends to over-estimate the inefficiency since there are high angle positrons which hit T1 and T2 counters and hit WC3 outside of the nominal fiducial cut but miss S3. Fig.5.30 shows the distribution at the middle of WC3 of the events missed by S3_Y. Four sectors of high inefficiency outside the nominal fiducial cut (indicated by a red line) can clearly be seen and correspond to events which did not hit S3_Y due to the geometrical arrangement of T1 and S3 that are rotated by an angle of 45° with respect to each other (see Table 3.1). At our current level of statistics and systematics, an over-estimation of the effect of inefficiency

⁶⁶The detector was opened between 2010 and 2011 data taking and the momentum scan was taken without WC1.2.

5.3. Other systematics

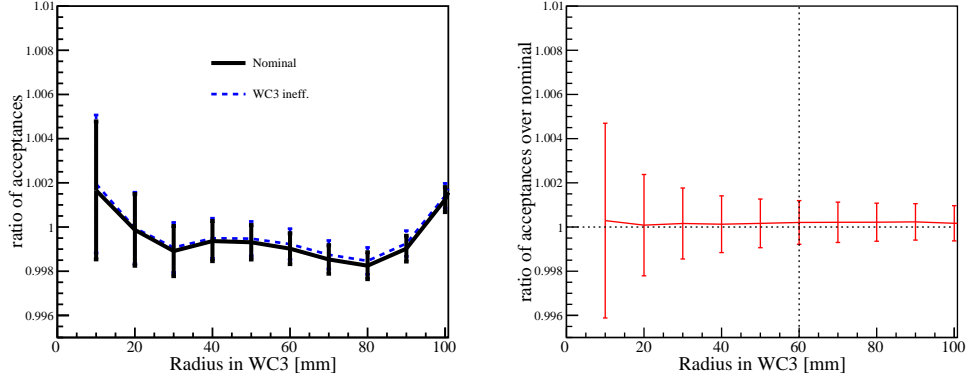


Figure 5.28: **Left:** ratio of $\pi^+ \rightarrow e^+ \nu_e$ over $\pi^+ \rightarrow \mu^+ \rightarrow e^+$ acceptances when no inefficiency is implemented (nominal) and when the inefficiency functions for all WC3 planes is implemented. **Right:** ratio of acceptances when WC3 inefficiency is simulated over nominal ratio of acceptances.

(which is in any case small) does not matter. Fig.5.31 shows the effect of the S3 inefficiencies on the acceptance. The change in acceptance is, within statistical errors, consistent with zero. The effect of the S3 inefficiency can therefore be neglected.

5.3.2 Effect of multiple hits in WC3

The radial cut in WC3 which defines the acceptance is based on the hits recorded in the downstream tracker detectors. In this analysis, the track which best fitted those hits is used to find the radial value at the center of WC3.2 plane. However, multiple hits in the downstream detectors arising from physical processes like Bhabha-scattering or delta rays blur the trajectory. The track with the best χ^2 might not always be the one corresponding to the track which triggers. Two extremes are used to test the effect on the acceptance correction: the acceptance is either defined by the track which gave the smallest radius in WC3 (called “Min R” in Fig.5.32) or by the one with the largest radius (“Max R” in Fig.5.32). Those acceptances are compared to the nominal acceptance based on the track which provides the best χ^2 . Again, within statistical error at our radial cut of 60 mm, the effect of misidentifying the correct track on the acceptance correction is found negligible.

5.3. Other systematics

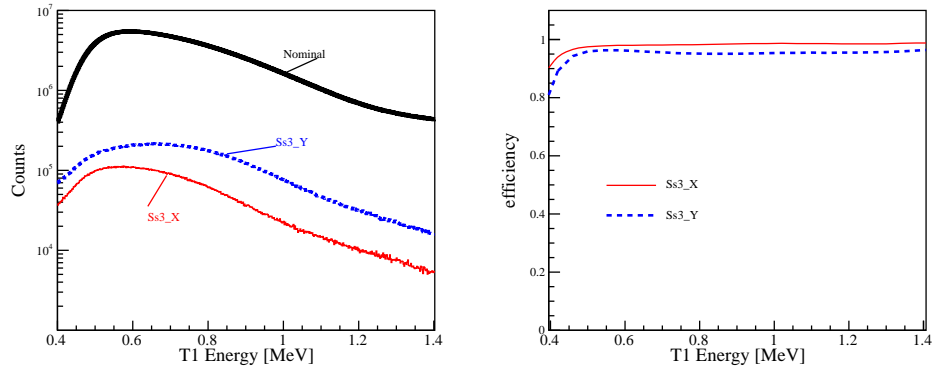


Figure 5.29: **Left:** Number of events that should have been detected by S3 (Nominal) and events missed by each plane as a function of T1 energy. **Right:** inefficiency function for each silicon plane as a function of T1 energy.

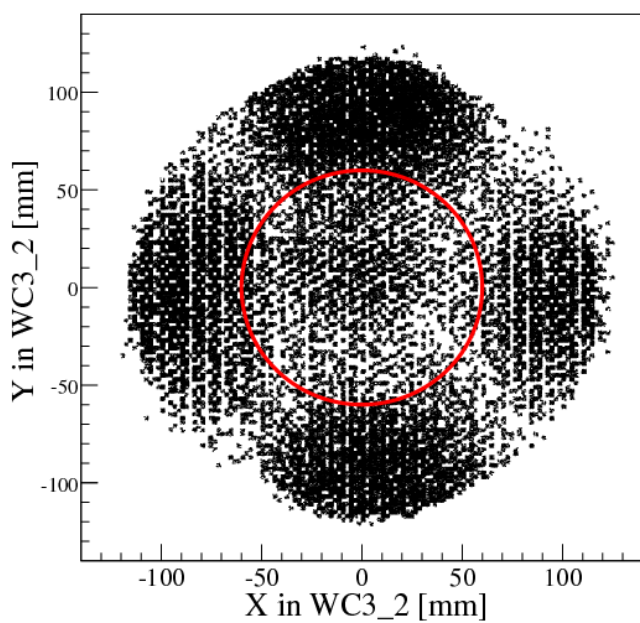


Figure 5.30: Distribution on the surface of WC3 of the events missed by S3_Y. The red circle indicates the fiducial cut used in this analysis. The four areas outside of the acceptance limits are the image of the corners of T1 counter which is rotated by 45° with respect to S3.

5.3. Other systematics

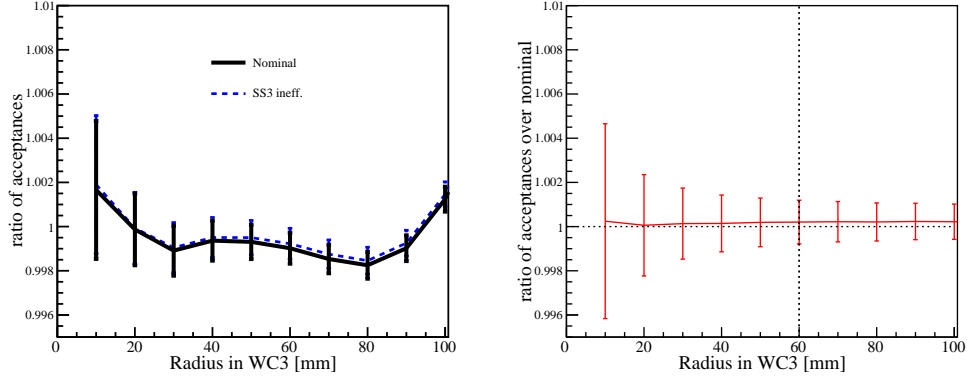


Figure 5.31: **Left:** ratio of $\pi^+ \rightarrow e^+\nu_e$ over $\pi^+ \rightarrow \mu^+ \rightarrow e^+$ acceptances when no inefficiency is implemented (nominal) and when the inefficiency functions for both S3 planes are implemented. **Right:** ratio of acceptances when S3 inefficiency is simulated over nominal ratio of acceptances.

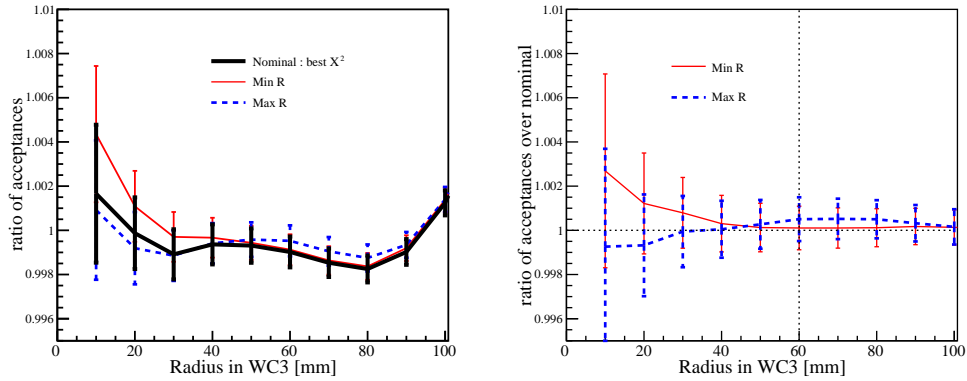


Figure 5.32: **Left:** ratio of $\pi^+ \rightarrow e^+\nu_e$ over $\pi^+ \rightarrow \mu^+ \rightarrow e^+$ acceptances when the WC3 radius is estimated from the track with the best χ^2 (nominal) and when it is estimated from the track with the minimum radius (Min R) or the maximum radius (Max R) in WC3. **Right:** ratio of acceptances with the maximal R or minimal R in WC3 to the nominal acceptance.

Chapter 6

Simulation

The PIENU experiment uses the GEANT4.9.3 (patch 2) package [134, 135] to simulate the particle interactions and the detector geometry. The effect of electronics and data digitization is not implemented in the MC. Since a number of corrections have been obtained from MC, it is fundamental to have an accurate MC simulation. This chapter describes the components of the MC specific to the PIENU experiment. An overview of the validation of the physics processes and the detector geometry is also presented.

6.1 Beam and tracking

6.1.1 Beam

The beam momentum and position distributions are generated by a beam transport program called REVMOC [100] from which predictions were tested against beam data prior to the installation of the beamline extension. A beam distribution based on data taken with the full detector in place is also built in the following way: the distributions of X and Y coordinates in the target and angles of the tracks along the X and Y axis are extracted from the data. The distribution of the sum of the energy deposited by pions in the upstream counters (B1, B2, S1&2 and circa 1/2 of the target⁶⁷) is formed from the calibrated data variables and scaled to match the mean of the momentum distribution obtained by REVMOC. The distribution of those 5 parameters are stored in a file. A 5×5 first order correlation matrix between the variables is built. Variables are sampled randomly from the data distributions and correlated according to the matrix discussed above. The transformed variables are used to generate the MC particles. The “data beam” thus obtained has the advantage of having a continuous distribution of rays while the REVMOC ray file had a small number of entries (ca 40,000) over which the MC has to loop. It is indeed observed that such a small repetition rate has an impact on the validity of the statistical errors. The beam

⁶⁷the energy deposited by pions in the target is based on the pulse shape fitting described in §5.1.1.

distribution based on data is used as input for the MC for all simulation analyses described in this thesis. Fig.6.1 shows the level of agreement between MC and data reached with this beam description.

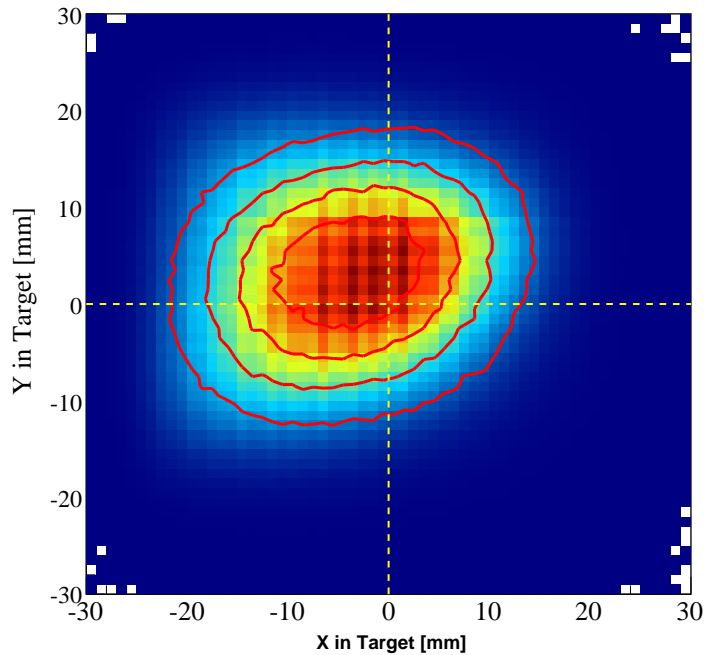


Figure 6.1: Comparison between data and MC of the pion beam distribution in the target. The coloured plot shows the distribution of the beam at the entrance of the target in the data as reconstructed with the tracking package while the red thick contours are those of the MC generated beam. The yellow dotted lines show the location of the centre of the target.

As can be seen in Fig.6.2, the vertex distribution is rather broad ($\sigma \sim 2$ mm). This is dominated by the reconstruction capability of our tracking detectors. The impact of the momentum bite on the width of the distribution is small. The “real” distribution of the pions in the target has a width of $\sigma \sim 0.5$ mm (for a momentum bite of $\sim 0.5\%$) as can be seen in Fig.6.2.

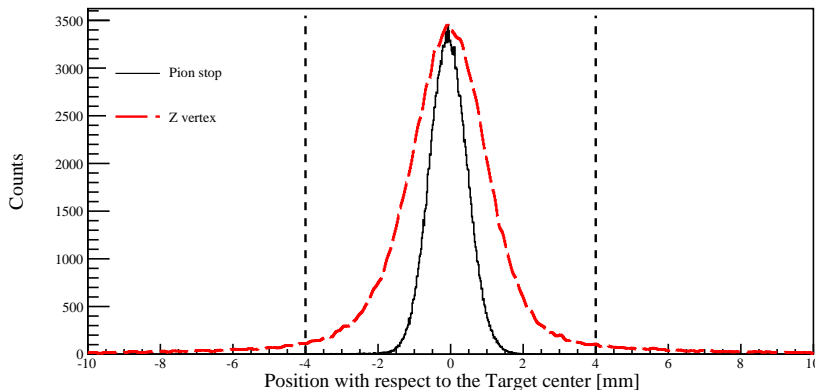


Figure 6.2: Z vertex reconstruction and “real” pion stop distribution in the target from MC. The black dashed vertical lines show the boundaries of the target.

6.1.2 Tracking performance

The X and Y positions of all tracking detectors have been verified using beam muons that traverse the entire PIENU assembly. The position of a track is reconstructed using WC1-2 information. For each tracking detector, the position determined by WC1-2 tracker is checked against the position measured by the detector along its sensitive axis. Fig.6.3 gives the distribution of the difference between the reconstructed and measured positions for S1_Y detector (the first tracking detector after WC1-2). The mean is centred on zero with a precision of the order of a μm which shows the accuracy with which the placement of the detector is known for the input into the MC. The distributions for all tracking detectors are given in Fig.B.1. Using this technique, the stability of the detector’s positions could also be checked as a function of time. Fig.6.4 shows a plot of the WC3_3 position stability along its sensitive axis over a period of seven months.

6.2 Detector geometry

The geometry of all detectors has been input into the MC. Dead materials (which are materials that are not read out) around the detectors are also coded and interactions with them are simulated. Surface mounted electronics are not coded. The electronics is typically placed far away from the

6.2. Detector geometry

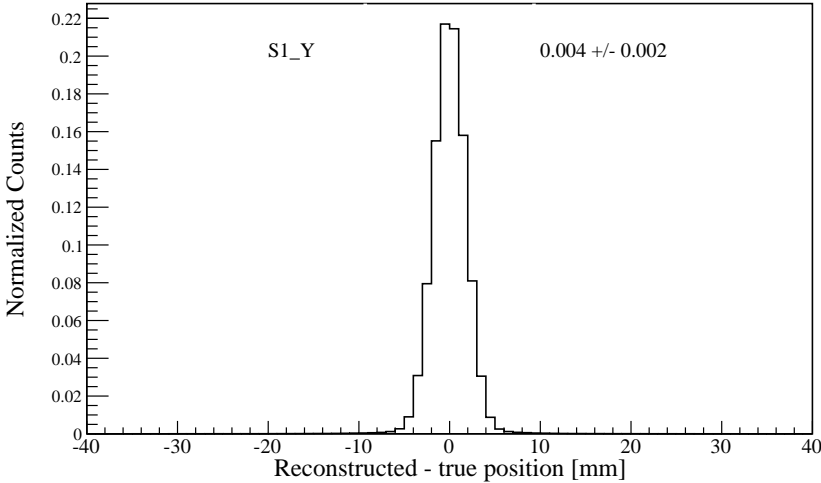


Figure 6.3: Difference between reconstructed and true position in S1_Y.

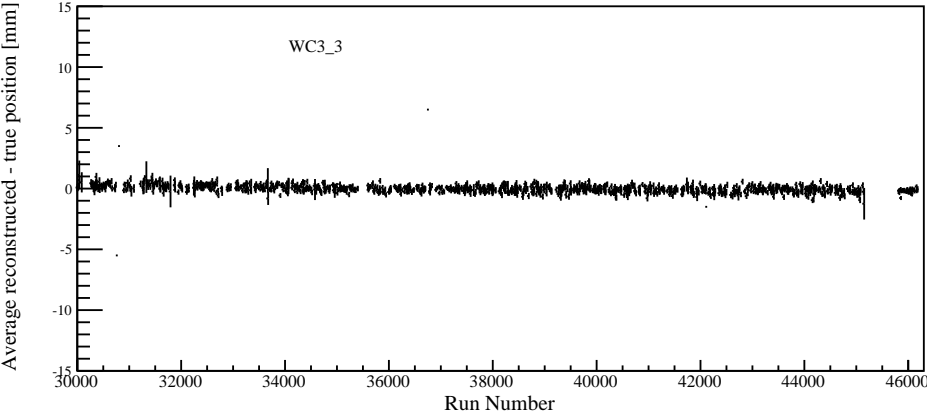


Figure 6.4: Stability of the difference between reconstructed and true position in WC3.3.

sensitive detector and should therefore have no effect on selected events.

6.2.1 Plastic scintillators

Light guides, support structure, PMTs and wrapping around the plastic scintillators are not added in the nominal MC. However, the effect of the addition of wrapping is tested and reported in §5.2. The impact of scattering on the support structure and light guides is believed to be negligible

6.2.2 Silicon

The ceramic frame is coded as dead material and the sizes of sensitive strips are input for tracking reconstruction purposes.

6.2.3 Wire chambers

The Wire Chambers are simulated as volumes filled with gas and separated by Mylar foils. The anode wires are not coded (the $15\mu\text{m}$ wires have a negligible impact on scattering); instead volume cells around the wires are delineated and a hit within this volume is associated with the corresponding wire for track reconstruction purposes. The postamplifier boards are coded as dead material.

6.2.4 CsI

The complex CsI geometry is fully coded as can be seen in Fig.6.5. The steel support structure as well as the gap spacers between the crystals is coded. Because of data suppression in the CsI, energies below a certain threshold are not recorded. In the data, this energy threshold is found to be 2 MeV. The same threshold is applied in the MC after addition of the resolution. The resolution of the CsI is matched for each of the four cylinders to that of the data. Fig.6.6 illustrates the agreement between data and MC after the energy threshold and resolution are implemented. The effect of signal attenuation in the crystals which could lead to a position dependence is not taken into account. Although the effect of the position on the energy recorded by the CsI crystal is measured to be smaller than 2%, for a further improvement in the agreement between MC and the data, this effect could be added to the MC. The difference observed in Fig.6.6 between MC and data for energies between 5 and 15 MeV is due on one hand to the presence of $\pi^+ \rightarrow \mu^+ \rightarrow e^+$ background in the data and on the other hand to a pileup in CsI induced by the source attached to each crystal (see §3.2.6).

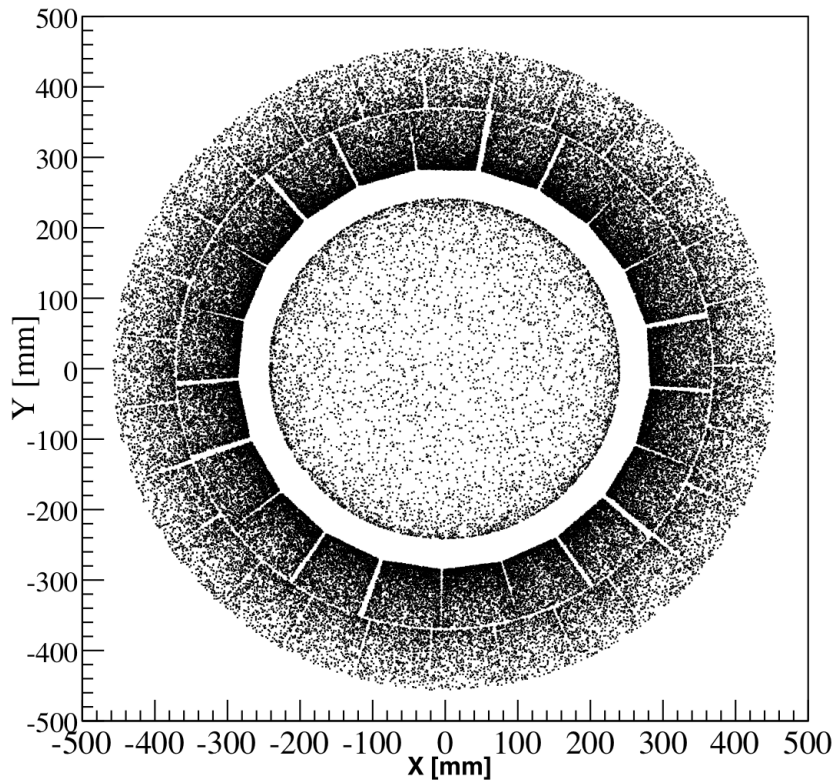


Figure 6.5: NaI and CsI front geometry in the MC (each point represents a hit recorded in the MC). The white gaps indicate that no sensitive detector is present.

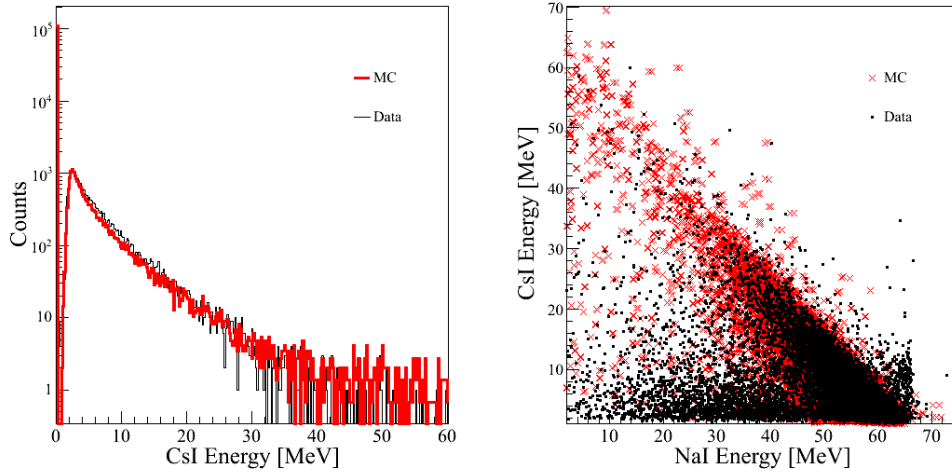


Figure 6.6: **Left:** Comparison of the energy deposited by $\pi^+ \rightarrow e^+ \nu_e$ and $\pi^+ \rightarrow e^+ \nu_e \gamma$ events in CsI for MC and data (“data” corresponds to the suppressed spectrum. In the MC, $\pi^+ \rightarrow e^+ \nu_e$ events are simulated and the same Total Energy cut as in the data is applied). The spectra have been normalized to the first bin (corresponding to “no energy” deposited in the CsI). The ratio of the number of events in the first bin to the integral of the full spectrum agrees within 3% between MC and data. **Right:** Energy deposited in the CsI versus NaI. The data events which have a low energy deposit in NaI correspond mostly to unsuppressed $\pi^+ \rightarrow \mu^+ \rightarrow e^+$ events.

This γ -ray source deposits an energy of about 8 MeV in a crystal, which, in coincidence with a $\pi^+ \rightarrow e^+\nu_e$ event brings the bulk of the $\pi^+ \rightarrow e^+\nu_e$ events with typical 0-5 MeV recorded in the CsI to up to 13 MeV. This background can also be identified in the right plot of Fig.6.6. Because of statistics it is most apparent at the peak of the $\pi^+ \rightarrow e^+\nu_e$ distribution in the NaI (around 66 MeV). Those pileup events represent only 0.2% of the total events in the suppressed spectrum.

6.3 Radiative decays in $\pi^+ \rightarrow e^+\nu_e$

The $\pi^+ \rightarrow e^+\nu_e \gamma$ decay width is calculated with a photon cut-off energy of 1 MeV. The calculation is checked with different photon cut-offs and angular restrictions against theoretical calculations [136, 137] and experimental measurements [138]. The following branching ratio is used for the MC simulation of $\pi^+ \rightarrow e^+\nu_e$ events⁶⁸:

$$R_{Rad} = \frac{\Gamma(\pi \rightarrow e\nu_e\gamma)}{\Gamma(\pi \rightarrow e\nu_e + \pi \rightarrow e\nu_e\gamma)} = 0.0621 \quad (6.1)$$

For the addition of the radiative decay to the MC lineshape, only radiative events which would have generated a trigger are considered. The branching ratio of triggered events is :

$$R_{Rad}^{trigger} = \frac{\Gamma(\pi \rightarrow e\nu_e\gamma)}{\Gamma(\pi \rightarrow e\nu_e + \pi \rightarrow e\nu_e\gamma)} = 0.0591 \quad (6.2)$$

The difference between $R_{Rad}^{trigger}$ and R_{Rad} is due to the higher fraction of low energy positrons (below ~ 2.5 MeV) that deposit their entire energy in the target and S3 counters and therefore do not trigger.

Fig.6.8 shows the energy distribution in the crystals for radiative events.

6.4 Energy loss processes

The simulated physics processes include energy loss in matter, multiple scattering and hard scattering such as bremsstrahlung emission and δ -ray production etc. None of these processes are modified from the GEANT4 package. The GEANT4 Physics List simulation engine used is : QGSP_BERT.

⁶⁸The number differs from the one reported in Table 2.4 since it is measured for a photon cut-off of 10 MeV and an angle between the photon and positron larger than 40° . The bremsstrahlung photons are mostly at low angles while the structure dependent photons to which the PSI experiment is most sensitive are emitted at high angles. Fig.6.7 shows the angle distribution between e^+ and γ .

6.4. Energy loss processes

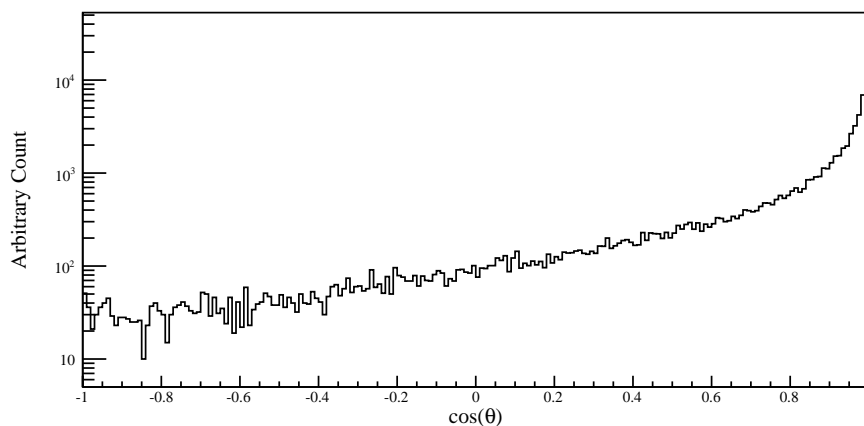


Figure 6.7: Angle between e^+ and γ for radiative events.

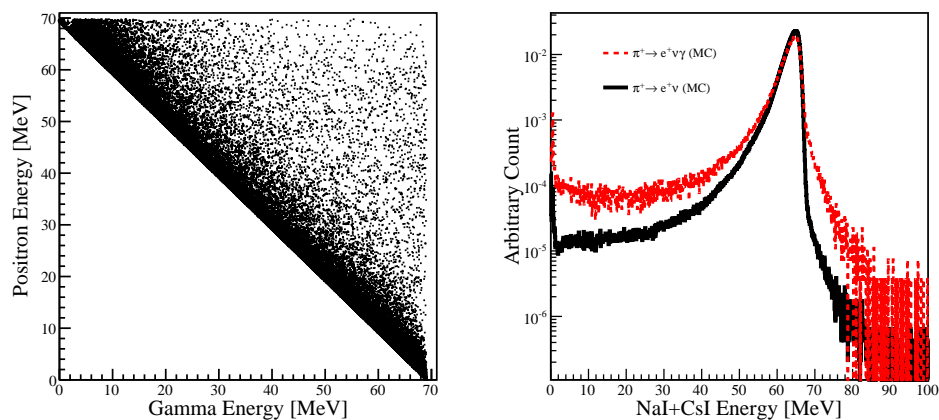


Figure 6.8: **Left:** Energy of photon versus positron for $\pi^+ \rightarrow e^+ \nu_e \gamma$ events in MC. **Right:** Energy deposited in NaI+CsI for $\pi^+ \rightarrow e^+ \nu_e$ and $\pi^+ \rightarrow e^+ \nu_e \gamma$ events in MC. The spectra are normalized to the same peak amplitude.

6.5. Muon decay-in-flight

For the lineshape simulation only the “G4EmStandard” part of the list is used. For all other MC analysis, all physics lists associated with QGSP_BERT are used.

The cut-off thresholds for electromagnetic processes that separate discrete from continuous handling of processes in GEANT4 are chosen as 1 mm and 0.1 mm for γ and e^+ , e^- respectively. An order of magnitude smaller thresholds on both γ and e^+ , e^- is tested and no significant impact on the acceptance correction is found (see Fig.6.9).

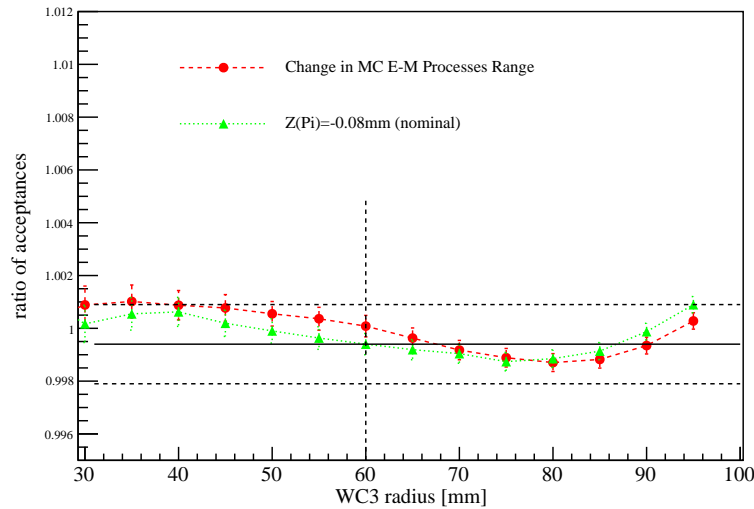


Figure 6.9: Acceptance as a function of WC3 radius for two different energy thresholds on electromagnetic processes in the MC. The dotted horizontal lines represent the 1σ error on the acceptance correction.

6.5 Muon decay-in-flight

Muon decay in flight in the target is a rare process due to the very brief time of flight of muons in the scintillator. The probability of such event compared to decay at rest is less than 0.001%. To be able to generate enough MC data, the muon lifetime is shortened to 100 ns to enhance the decay in flight component. Because the time distribution of the DIF events is flat as shown in Fig.4.23 and 100 ns remains large compared to 18 ps, this procedure did not affect the results of the simulation.

Chapter 7

Results

7.1 Corrections

Table 7.1 shows a summary of the corrections to the raw (and blinded) branching ratio together with the associated uncertainties. All uncertainties associated with the corrections are summed in quadrature to obtain the stated “Total correction” uncertainty. The theoretical branching ratio is used to calculate the total error on the experimental branching ratio.

Table 7.1: List of corrections to the branching ratio.

Process	Correction	Uncertainty		Section
		stat.	syst.	
“Raw” Branching ratio ($\times 10^{-4}$)	/	0.0024	0.0010	§4.5.3
t_0 energy dependence	$\times 0.9993$	/	0.0007	§4.10
Muon decay-in-flight	$\times 0.9976$	/	0.0002	§4.9
Low energy tail	$\times 1.0203$	0.0025	0.0013	§5.1.5
Acceptance correction	$\times 0.9994$	/	0.0015	§5.2
Total Correction	$\times 1.0165$	0.0025	0.0021	
Total Branching Ratio	/	0.0039	0.0028	

7.2 Systematic checks

The variation of the corrected branching ratio as a function of the acceptance cut and cut-off energy in the calorimeters is studied. Fig.7.1 and Fig.7.2 show the result of the study. The raw branching ratio is obtained from the time fit and the tail correction for each cut is extracted from MC. For the study of the cut-off energy variation, the correction for MDIF (obtained from MC) is added. The error bars on the raw branching ratio reflect the statistical errors only. Since the points are correlated, the error bars on the corrected branching ratios are only indicative. Any fluctuations of the corrected branching ratio are well within the statistical uncertainties.

7.2. Systematic checks

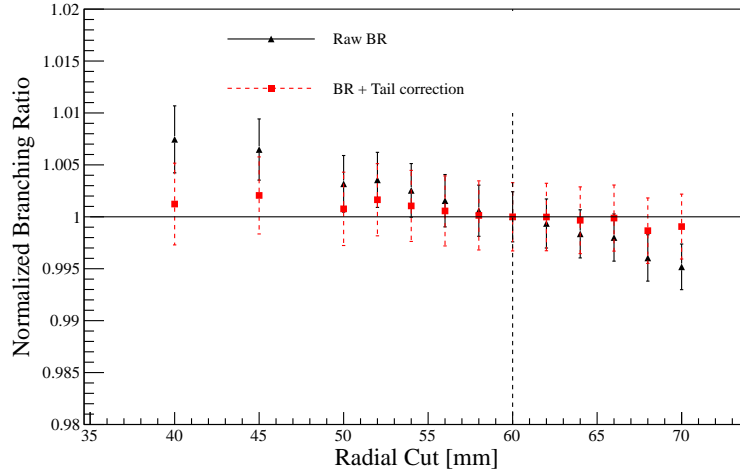


Figure 7.1: Effect of the acceptance cut. The branching ratios are normalized to the nominal value at $R=60$ mm indicated by a dotted vertical line.

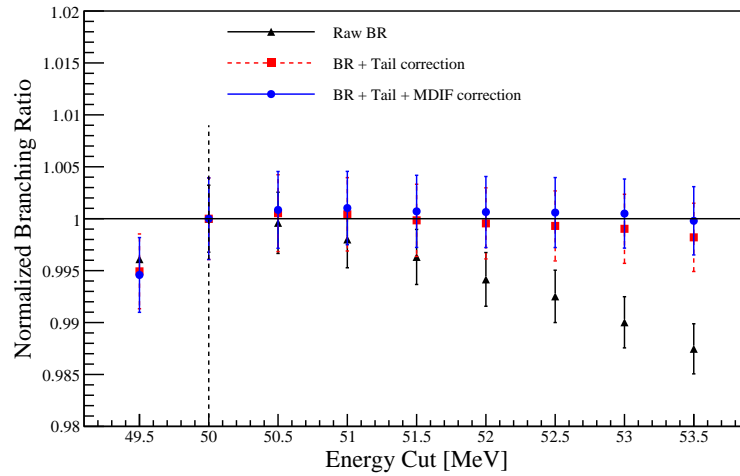


Figure 7.2: Effect of the cut-off energy. The branching ratios are normalized to the nominal value at $E=50$ MeV indicated by a dotted vertical line. For a low cut-off energy ($E=49.5$ MeV) the “high-energy” part is dominated by $\pi^+ \rightarrow \mu^+ \rightarrow e^+$ events.

Chapter 8

Neutrino Analysis

An analysis on massive neutrinos was performed by K. Yamada [116] on data acquired in the summer 2009. The analysis was subsequently refined and published in Physical Review D [3].

Because of several problems in the hardware, this portion of data would need several additional studies to be integrated in the branching ratio analysis, but it was appropriate for a massive neutrino search.

8.1 Brief introduction to the theory

Since the $\pi^+ \rightarrow e^+\nu_e$ decay is a two-body decay, the neutrino mass can be extracted from the energy of the positron with the simple equation:

$$m_\nu = \sqrt{m_{\pi^+}^2 + m_{e^+}^2 - 2m_{\pi^+}E_{e^+}} \quad (8.1)$$

where m_ν is the neutrino mass and E_{e^+} and m_{e^+} are respectively the positron energy and mass and m_{π^+} the pion mass. If the pion decays to a heavy neutrino instead of a “conventional neutrino”, this relation still holds and an extra peak at low energy would appear in the positron energy spectrum. Some models predict the mixing of massive sterile neutrinos with ordinary neutrinos and the mass eigenstates would be related to the weak eigenstates by a unitary matrix U:

$$\nu_l = \sum_{i=1}^{3+k} U_{li}\nu_i. \quad (8.2)$$

with the weak eigenstate indices $l = e, \mu, \tau, \chi_1, \chi_2 \dots \chi_k$

Since the peak of the $\pi^+ \rightarrow e^+\nu_e$ decay is around 70 MeV, an additional peak search in this spectrum is in principle sensitive to massive neutrinos in the mass range 0 MeV/c²-130 MeV/c². The ratio of the decay to massive and normal neutrinos $\Gamma(\pi \rightarrow e\nu_i)/\Gamma(\pi \rightarrow e\nu_e)$, is related to the mixing and phase space parameters by the following equations:

$$\frac{\Gamma(\pi \rightarrow e\nu_i)}{\Gamma(\pi \rightarrow e\nu_e)} = |U_{ei}|^2 \rho_e, \quad (8.3)$$

$$\rho_e = \frac{\sqrt{1 + \delta_e^2 + \delta_i^2 - 2(\delta_e + \delta_i + \delta_e \delta_i)(\delta_e + \delta_i - (\delta_e - \delta_i)^2)}}{\delta_e(1 - \delta_i)^2}, \quad (8.4)$$

$$\delta_e = \frac{m_{e^+}^2}{m_{\pi^+}^2} \quad (8.5)$$

$$\delta_i = \frac{m_{\nu_i}^2}{m_{\pi^+}^2}, \quad (8.6)$$

where ρ_e is a kinematic factor and m_{ν_i} the mass of a massive neutrino.

8.2 Brief description of the analysis

8.2.1 Selection cuts

A similar suppression technique to the one developed in §5.1.1 was used for this analysis. Pions were selected and pile-up rejected with a signal efficiency of about 40% and a fiducial cut in WC3 at 80 mm. Similarly to the suppressed spectrum analysis, a time cut, a Total Energy cut, a pulse-shape cut and a kink cut were used to select preferentially positrons from $\pi^+ \rightarrow e^+ \nu_e$ decays. Additional suppression of the $\pi^+ \rightarrow \mu^+ \rightarrow e^+$ background was obtained by using the reconstructed z-vertex information and the minimal distance between the downstream and upstream tracks at the vertex which helped suppress pion DIF events that were not suppressed by the kink cut. Those included PDIF events happening between the upstream silicon detectors and the target. Events with signal in the CsI (with a threshold around 6 MeV) were vetoed to reduce the low energy tail due to shower leakage from the NaI crystal (those last two cuts have a strong bias on the branching ratio and were therefore not used for the suppressed spectrum analysis).

The cuts were optimized by minimizing the S value :

$$S = \frac{\sqrt{N_{<54MeV}}}{N_{>54MeV}} \quad (8.7)$$

where $N_{<54MeV}$ and $N_{>54MeV}$ are respectively the number of events below and above 54 MeV in the positron energy spectrum in the NaI. After all cuts the remaining background below 54 MeV was 6.8% of the signal events (i.e. above 54 MeV) with $N_{>54MeV} = 4.8 \times 10^5$.

The improvement of the limits on the mixing parameters relies on a larger data set and a better suppression of the background below 54 MeV but also on a better resolution of the $\pi^+ \rightarrow e^+ \nu_e$ peak. Since the shower leakage increases with the radius in WC3, a better peak resolution is obtained with

tighter radial cuts. However, the S value starts worsening around a radial cut of 40 mm (corresponding to an angular cut of 35°). This cut was only applied to events with positron energies larger than 47 MeV for which the impact of the resolution is higher. The data were thus separated in two sets: for the energies below 47 MeV (corresponding to a neutrino mass larger than $80 \text{ MeV}/c^2$) no additional angular cut was done (we will call this set “No-cut”) while, for higher energies in the positron spectrum, an angular cut of 35° was applied. Fig.8.1 shows the positron energy spectrum in the NaI when no angular cut is applied and with a 35° angular cut together with the beam positron spectrum. The latter highlights the peaks arising from neutron escape after photo-absorption of a shower photon by iodide nuclei. The beam positron spectrum was subtracted from the $\pi^+ \rightarrow e^+ \nu_e$ spectrum to minimize the effect of the peaks on the fitting procedure described in the next section.

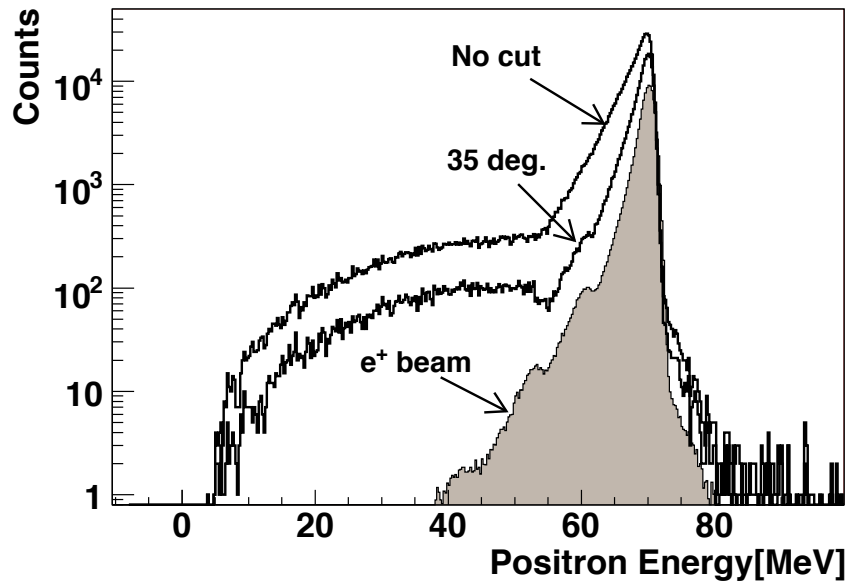


Figure 8.1: Positron spectra from $\pi^+ \rightarrow e^+ \nu_e$ decay with no angular cut (No-cut) and with a 35° angular cut together with the positron beam spectrum hitting the front face of the NaI crystal at 0° .

8.2.2 Fitting procedure

The positron spectrum obtained after the cuts described above was fitted with a 0.5 MeV step over an energy range between 10 and 60 MeV. The fit function was composed of different backgrounds and a possible peak. The position of the potential peak was fixed at every step. The spectrum was fitted between 9 and 50 MeV for the No-cut data and between 9 and 62 MeV for the 35° data.

The shapes of the two main backgrounds in the $\pi^+ \rightarrow e^+\nu_e$ spectrum, namely PDIF-MDAR and PDAR-MDIF, were extracted from the data. The shape of $\pi^+ \rightarrow \mu^+ \rightarrow e^+$ decays was obtained using a late time window cut. As shown in §4.9, the positron spectrum from PDAR-MDIF is different from the PDAR-MDAR due to the extra boost provided by the muon to the positron. The shape of the spectrum was calculated by applying a Lorentz transformation for muon kinetic energies between 3.3 and 4.1 MeV (the muons with lower kinetic energies were removed by the target cut). The effect of the muon polarization was also taken into account. The amplitudes of those two backgrounds were left free in the fit. An extra exponential background and a flat background were added to accommodate for slowly changing spectrum mismatch. The amplitudes and the attenuation (for the exponential) of those backgrounds were left free in the fit. Finally, the templates of the $\pi^+ \rightarrow e^+\nu_e$ peak at different energies were obtained from MC. The validity of the MC lineshapes were confirmed with positron data taken at various entrance angles into the NaI crystal and at different beam energies. Fig.8.2 shows the amplitudes of the the fitted peaks normalized to the main $\pi^+ \rightarrow e^+\nu_e$ peak. The amplitudes are consistent with zero as seen from Fig.8.2; no evidence of massive neutrinos was found. The χ^2/NDF of the fit without additional peak was 0.97 with the No-cut data and 1.00 with the 35° angular cut. The proportions of PDIF (and PDAR: those two backgrounds cannot be distinguished) and MDIF backgrounds were found to be respectively 2.8% and 1.7% of the $\pi^+ \rightarrow e^+\nu_e$ decay component.

8.3 Results

Using the Bayesian method, the amplitude of the potential peaks and the associated errors can be converted to upper limit on the ratio $\Gamma(\pi^+ \rightarrow e^+\nu_i)/\Gamma(\pi^+ \rightarrow e^+\nu_e)$ at each positron energy. Corrections for the energy dependence of the fiducial cut, CsI veto cut, Total Energy cut and the z-vertex cut had to be applied to those limits. Those corrections were estimated from MC over the entire energy range. The z-vertex cut had the largest energy

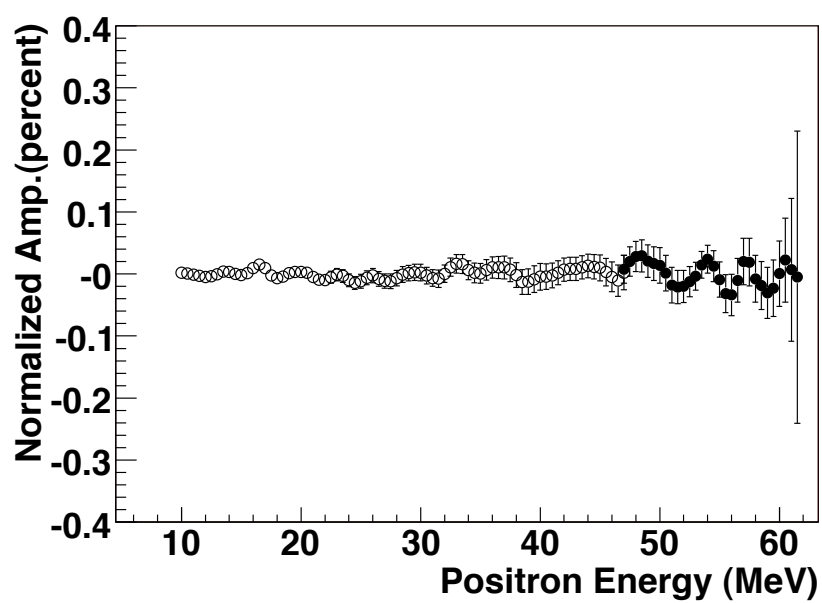


Figure 8.2: Normalized amplitude of the potential peaks in the $\pi^+ \rightarrow e^+ \nu_e$ spectrum obtained by the fit on the No-cut spectrum (open circles) and for the 35° spectrum (filled circles).

dependent effect. The combined relative acceptance for 10 MeV positrons compared to 70 MeV positron was 45% (35° data) and 42% (No-cut data). After correction, the upper limit on the massive neutrino branching ratio can be converted to upper limit on the mixing parameter $|U_{ei}|^2$ using eq.8.3. The upper limit can be expressed as a function of the neutrino mass using eq.8.1. In Fig.8.3 the results of this analysis together with the limits obtained by the previous experiment at TRIUMF [139] are shown. We can note that the limits obtained with this analysis reach a massive neutrino of 60 MeV (compared to 50 MeV for last experiment) because the subtraction process of the positron spectrum induced a bias below those masses.

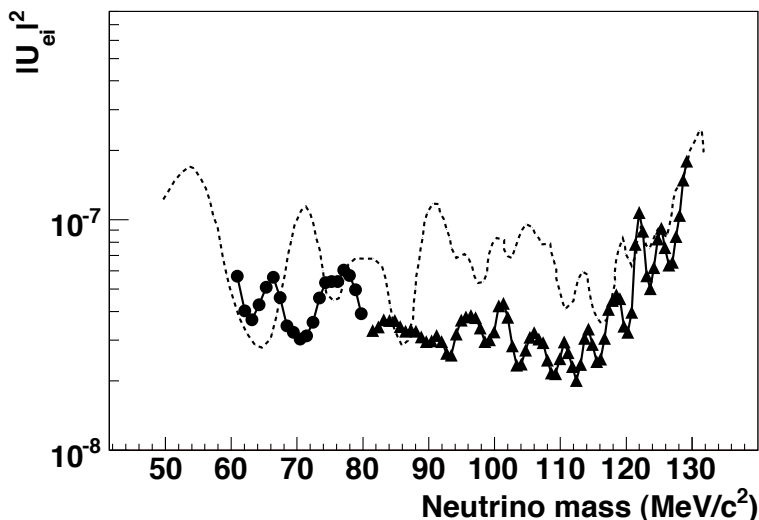


Figure 8.3: Combined 90% C.L. upper limits obtained from the 35° spectrum (circles) and No-cut spectrum (triangles) together with the previous limits (dashed lines) [139].

The low and high neutrino mass limits have been only marginally improved over the previous experiment. This could be explained by a different fitting procedure. In the last experiment, the shape of the normal $\pi^+ \rightarrow e^+\nu_e$ peak was determined from the suppressed spectrum and fixed in the fit. This procedure could have masked the presence of irregularities in the spectrum

8.3. Results

like the peaks from neutron escape after photo-nuclear reactions⁶⁹. Finally, an assumption for the scaling of the $\pi^+ \rightarrow e^+\nu_e$ peak shape at lower energies was assumed which is different from the procedure adopted here where the shape of the template was obtained from MC and verified with positron data.

⁶⁹Although it does not affect the bump-search procedure, it is worth noting that E248 experiment did not take into account the presence of muon decays in flight in the fit.

Chapter 9

Conclusions

One never notices what has been done; one can only see what remains to be done.

Marie Curie

9.1 Results

This work is the first example of a blind analysis on the measurement of $R^\pi = \frac{\Gamma(\pi^+ \rightarrow e^+ \nu_e + \pi^+ \rightarrow e^+ \nu_e \gamma)}{\Gamma(\pi^+ \rightarrow \mu^+ \nu_\mu + \pi^+ \rightarrow \mu^+ \nu_\mu \gamma)}$. No conclusions on the final value of the branching ratio can yet be drawn. However, the error estimate obtained after this analysis provides a factor 1.17 improvement over the E248 experiment and is dominated by statistical uncertainty. If normalized to the theoretical branching ratio, the total error is:

$$\sigma_{blind} = (0.0039 \text{ (stat.)} + 0.0028 \text{ (syst.)}) \times 10^{-4} = 0.0048 \times 10^{-4} \quad (9.1)$$

Added to the current PDG value [22] this result would reduce the error on the branching ratio by $\sim 25\%$. Fig.9.1 shows a break-down of the systematic and statistical contributions to the total error and a comparison with the E248 experiment.

9.2 Comments on the results

The main improvement over the E248 result is on the systematics related to the fit of the time spectra for which the systematic error has been reduced by a factor 2.3. With two times larger data set, a better time fit was obtained due to better time measurement devices and reduced electronic cross-talk. Additionally, a careful study of the background components and simulation

9.2. Comments on the results

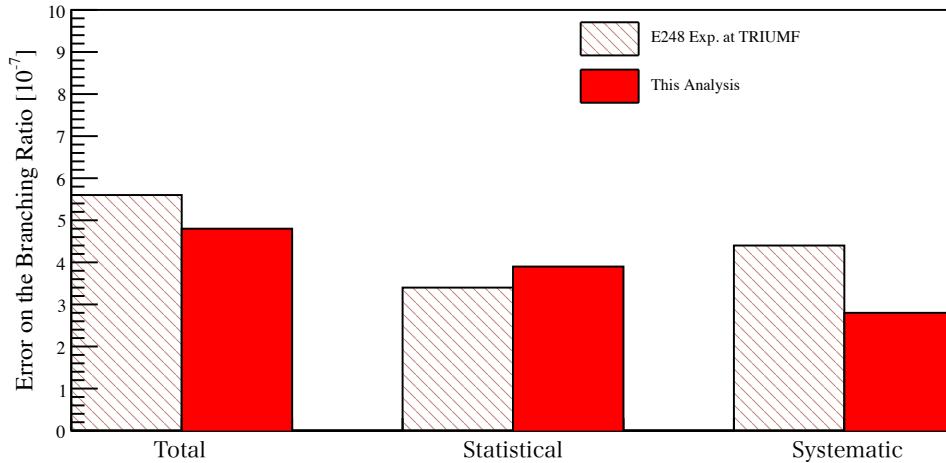


Figure 9.1: Summary of uncertainties and comparison with the E248 experiment.

of the effect of the calorimeter pulse shapes led to the inclusion of additional components to the fit which described the data well.

Another source of systematic error comes from the determination of the low energy tail. The measurement of the lineshape with a positron beam hitting the center of the NaI was not sufficient to correctly assess the lineshape of $\pi^+ \rightarrow e^+ \nu_e$ events. Indeed, due to the large acceptance, particles hitting the crystal on-center and off-center have different contributions to the low energy tail. This was considered during the lineshape measurements but too few events were accumulated for off-center points. The amplitude of this effect had to be estimated with a combination of Monte Carlo simulation and data. Moreover, “neutron-escape” peaks appearing in the lineshape due to photo-nuclear reactions in the NaI were discovered and contributed to an increase in the tail over previous estimation which tended to compensate for the gain from the improved calorimeter resolution. Despite these complications, a similar error on the tail fraction as the one obtained by the E248 experiment could be reached with a careful study of the MC and a 10% reduction in the pion decay-in-flight background contaminating the suppressed spectrum⁷⁰. An additional systematic uncertainty related to the tail determination comes from the inclusion of the energy spectrum of muon decay-in-flight events

⁷⁰We should note that the E248 result fully attributed the error on the tail to a systematic uncertainty.

which was not taken into account in the E248 experiment. Finally the energy-dependent acceptance correction is smaller due mainly to the larger acceptance.

9.3 Foreseen improvements

9.3.1 Statistical uncertainty

The statistical error will be reduced by at least a factor 3 with the addition of the remaining data taken in 2009, 2010 and 2011 added to the forecasted amount of data that will be recorded in 2012. Data taken in 2009 and in the summer of 2010 require additional analysis to optimize the use of the CsI information but should eventually contribute to reducing the statistical error.

Improvements on the $\pi^+ \rightarrow e^+ \nu_e$ efficiency could be reached with a more elaborate pileup rejection cut (beam pile-up cuts removed $\sim 30\%$ of the data in this analysis) which would for example allow pile-up particles within some time windows and use tracking to reconstruct their trajectories.

9.3.2 Time analysis

The systematics in the time fit might come from small remaining non-linearities in the time measurement devices and electronics. In this case, a larger data set would increase the fraction of systematic error with respect to statistical error. A larger data set of muon runs will be accumulated to be able to assess the non-linearities and correct for them. On the other hand, small distortions in the background shapes can also contribute to a larger χ^2 . This analysis showed that a large source of “old-muon” contamination comes from beam pions stopping and decaying in the target earlier than $6 \mu s$ before the triggered event. An additional TDC channel recording pion particles $15 \mu s$ before the trigger was implemented for the 2011 data taking. This should allow the suppression of “old-muon” contamination in the “high-energy” spectrum by almost an order of magnitude. For a further study of the shapes of the background in the “high-energy” spectrum, pile-up particles and pulse shapes of the calorimeters should be added to the GEANT4 simulation used by PIENU. Finally, improvements in the CsI calibration and the tagging of the additional energy coming from the source attached to the crystals (e.g. by only summing the energy in adjacent crystals) could significantly reduce the level of $\pi^+ \rightarrow \mu^+ \rightarrow e^+$ background in the “high-energy” time spectrum.

9.3.3 Tail analysis

After the result of this analysis, a new lineshape measurement technique was developed. Instead of measuring beam positrons at different angles hitting the center of the NaI, the crystal was rotated around the target to simulate $\pi^+ \rightarrow e^+\nu_e$ tracks. Furthermore, information from the energy leaked into the CsI was also recorded together with cosmic-ray events enabling a proper calibration of the CsI. Therefore, the dependence on the Monte-Carlo for the tail determination should be greatly reduced which should decrease the systematics on the tail correction.

Improvements to the suppressed spectrum are also envisioned. First, a larger data set would reduce the statistical error on the suppressed spectrum. A cut-off energy that minimizes the sum of the statistical errors on the raw branching ratio and on the tail correction should be chosen. Secondly, a larger suppression of the PDIF component will be reached due to a better $\pi^+ \rightarrow \mu^+ \rightarrow e^+$ rejection capability of the pulse shape cut. Indeed, because of a slightly too high threshold on the COPPER channel reading the target, 10% of the positron pulses in the target were not digitized⁷¹. The z-vertex cut and additional tracking cuts should help reduce the PDIF contamination if their effect on the $\pi^+ \rightarrow e^+\nu_e$ spectrum can be understood. Finally, the addition of beam pile-up to the MC would also help to better understand the effect of this background for the low energy tail. We should also note that a better PDIF suppression could have been reached with a tighter arrangement of the S1&2 and target detectors.

9.3.4 Acceptance correction

A better understanding of the detector geometry could constrain the level of the error on this correction. The uncertainty on the acceptance correction should only have a small impact on the total final error.

9.3.5 Massive neutrino analysis

The combination of 2009, 2010, 2011 and 2012 data should lead to an improvement in the massive neutrino limit. The inclusion of “neutron-escape” peaks in the Monte-Carlo developed for the tail analysis as well as a better lineshape measurement should lead to an improved understanding of the lineshape subtracted from the suppressed spectrum. A better limit on lower neutrinos masses could thus be potentially reached.

⁷¹Since the target information is not used for the raw branching ratio analysis, this fact had no impact on the analysis.

Bibliography

- [1] A.A.Aguilar-Arevalo *et al.* High purity Pion Beam at TRIUMF. *Nucl. Instrum. Methods Phys. Res., Sect. A*, 609:102–105, October 2009.
- [2] A. Aguilar-Arevalo *et al.* Study of a Large NaI(Tl) Crystal. *Nucl. Instrum. Meth.*, A621:188–191, 2010. [arXiv:1003.2235](https://arxiv.org/abs/1003.2235), [doi:10.1016/j.nima.2010.05.037](https://doi.org/10.1016/j.nima.2010.05.037).
- [3] PIENU Collaboration. Search for massive neutrinos in the decay $\pi^+ \rightarrow e^+\nu$. *Phys. Rev. D*, 84:052002, Sep 2011. Available from: <http://link.aps.org/doi/10.1103/PhysRevD.84.052002>, [doi:10.1103/PhysRevD.84.052002](https://doi.org/10.1103/PhysRevD.84.052002).
- [4] C. M. G. Lattes, H. Muirhead, G. P. S. Occhialini, C. F. Powell. Processes involving charged mesons. *Nature*, 159:694–697, 1933.
- [5] Official Website of the Nobel Prize. Available from: http://www.nobelprize.org/nobel_prizes/physics/laureates/1950/powell-b%io.html.
- [6] H.L. Anderson and C. Lattes. Search for the electronic decay of the positive pion. *Il Nuovo Cimento (1955-1965)*, 6:1356–1381, 1957.
- [7] S. Lokanathan and J. Steinberger. *Supl. Nuovo cimento*, 2:151, 1955.
- [8] E. C. G. Sudarshan and R. E. Marshak. Chirality invariance and the universal fermi interaction. *Phys. Rev.*, 109(5):1860–1862, Mar 1958. [doi:10.1103/PhysRev.109.1860.2](https://doi.org/10.1103/PhysRev.109.1860.2).
- [9] J. Mehra Clarendon. *The beat of a different drum: The life and science of Richard Feynman*. Press Oxford, 1994.
- [10] R. P. Feynman and M. Gell-Mann. Theory of the fermi interaction. *Phys. Rev.*, 109(1):193–198, Jan 1958. [doi:10.1103/PhysRev.109.193](https://doi.org/10.1103/PhysRev.109.193).

Bibliography

- [11] T. D. Lee and C. N. Yang. Question of parity conservation in weak interactions. *Phys. Rev.*, 104:254–258, Oct 1956. Available from: <http://link.aps.org/doi/10.1103/PhysRev.104.254>, doi:10.1103/PhysRev.104.254.
- [12] C. S. Wu, E. Ambler, R. W. Hayward, D. D. Hoppes and R. P. Hudson. Experimental test of parity conservation in beta decay. *Phys. Rev.*, 105(4):1413–1415, Feb 1957. doi:10.1103/PhysRev.105.1413.
- [13] T. Fazzini *et al.* Electron Decay of the Pion. *Phys. Rev. Lett.*, 1:247–249, 1958.
- [14] G. Impeduglia, R. Plano, A. Prodell, N. Samios, M. Schwartz, and J. Steinberger. β decay of the pion. *Phys. Rev. Lett.*, 1:249–251, Oct 1958. Available from: <http://link.aps.org/doi/10.1103/PhysRevLett.1.249>, doi:10.1103/PhysRevLett.1.249.
- [15] H.L. Anderson *et al.* Branching Ratio of the Electronic Mode of Positive Pion Decay. *Phys. Rev.*, 119:2050–2067, 1960.
- [16] E. Di Capua, R. Garland, L. Pondrom, and A. Strelzoff. Study of the decay $\pi \rightarrow e + \nu$. *Phys. Rev.*, 133(5B):B1333–B1340, Mar 1964. doi:10.1103/PhysRev.133.B1333.
- [17] Douglas Bryman and Charles Picciotto. Revised value for the $\pi \rightarrow e\nu$ branching ratio. *Phys. Rev.*, D11:1337, 1975. doi:10.1103/PhysRevD.11.1337.
- [18] D. A. Bryman, R. Dubois, J. A. MacDonald, T. Numao, B. Olaniyi, A. Olin, J.-M. Poutissou, and M. S. Dixit. Measurement of the $\pi \rightarrow e\nu$ branching ratio. *Phys. Rev. D*, 33(5):1211–1221, Mar 1986. doi:10.1103/PhysRevD.33.1211.
- [19] D. I. Britton, S. Ahmad, D. A. Bryman, R. A. Burnham, E. T. H. Clifford, P. Kitching, Y. Kuno, J. A. Macdonald, T. Numao, A. Olin, J.-M. Poutissou, and M. S. Dixit. Measurement of the $\pi^+ \rightarrow e^+\nu$ branching ratio. *Phys. Rev. Lett.*, 68:3000–3003, May 1992. Available from: <http://link.aps.org/doi/10.1103/PhysRevLett.68.3000>, doi:10.1103/PhysRevLett.68.3000.
- [20] G. Czapek, A. Federspiel, A. Flükiger, D. Frei, B. Hahn, C. Hug, E. Hugentobler, W. Krebs, U. Moser, D. Muster, E. Ramseyer, H. Scheidiger, P. Schlatter, G. Stucki, R. Abela, D. Renker, and

- E. Steiner. Branching ratio for the rare pion decay into positron and neutrino. *Phys. Rev. Lett.*, 70(1):17–20, Jan 1993. doi:10.1103/PhysRevLett.70.17.
- [21] W. J. Marciano. Proceedings of the Workshop on Future Directions in Nuclear and Particle Physics at Multi-GeV Hadron Beam Facilities.
- [22] K. Nakamura et al. (Particle Data Group). *J. Phys. G: Nucl. Part. Phys.*, 37(7a):075021, 2010. Available from: <http://stacks.iop.org/0954-3899/37/i=7A/a=075021>.
- [23] D. I. Britton, S. Ahmad, D. A. Bryman, R. A. Burnham, E. T. H. Clifford, P. Kitching, Y. Kuno, J. A. Macdonald, T. Numao, A. Olin, J-M. Poutissou, and M. S. Dixit. Measurement of the $\pi^+ \rightarrow e^+\nu$ branching ratio. *Phys. Rev. D*, 49(1):28–39, Jan 1994. doi:10.1103/PhysRevD.49.28.
- [24] Joshua R Klein and Aaron Roodman. Blind analysis in nuclear and particle physics. *Annual Review of Nuclear and Particle Science*, 55(1):141–163, 2005. Available from: <http://www.annualreviews.org/doi/abs/10.1146/annurev.nucl.55.090704.151521>, arXiv:<http://www.annualreviews.org/doi/pdf/10.1146/annurev.nucl.55.090704.151521>, doi:10.1146/annurev.nucl.55.090704.151521.
- [25] Joel G. Heinrich. Cdf/memo/statistics/public/6576 version 1 benefits of blind analysis techniques, 2003.
- [26] P F Harrison. Blind analysis. *Journal of Physics G: Nuclear and Particle Physics*, 28(10):2679, 2002. Available from: <http://stacks.iop.org/0954-3899/28/i=10/a=312>.
- [27] C. Malbrunot and M. Aoki. BLIND ANALYSIS SCENARIO for PIENU. Technical report, PIENU collaboration, TRIUMF, August 2010.
- [28] E. D. Bloom, D. H. Coward, H. DeStaebler, J. Drees, G. Miller, L. W. Mo, R. E. Taylor, M. Breidenbach, J. I. Friedman, G. C. Hartmann, and H. W. Kendall. High-energy inelastic $e - p$ scattering at 6° and 10° . *Phys. Rev. Lett.*, 23(16):930–934, Oct 1969. doi:10.1103/PhysRevLett.23.930.

Bibliography

- [29] M. Breidenbach, J. I. Friedman, H. W. Kendall, E. D. Bloom, D. H. Coward, H. DeStaebler, J. Drees, L. W. Mo, and R. E. Taylor. Observed behavior of highly inelastic electron-proton scattering. *Phys. Rev. Lett.*, 23(16):935–939, Oct 1969. doi:10.1103/PhysRevLett.23.935.
- [30] G Zweig. An SU_3 model for strong interaction symmetry and its breaking; Part II. (CERN-TH-412):80 p, Feb 1964.
- [31] Murray Gell-Mann. A Schematic Model of Baryons and Mesons. *Phys. Lett.*, 8:214–215, 1964. doi:10.1016/S0031-9163(64)92001-3.
- [32] Gerard't Hooft. Renormalization and gauge invariance. *Presented at the Yukawa Tomonaga Centennial Symposium - Progress in Modern Physics, Tokyo*, December 2006.
- [33] Gerhart Lüders. Proof of the TCP theorem. *Annals of Physics*, 2(1):1–15, 1957. Available from: <http://www.sciencedirect.com/science/article/B6WB1-4DF56HF-2K3/2/dd2a0e65800e426b9642f4d6826f4f77>, doi:DOI:10.1016/0003-4916(57)90032-5.
- [34] J.S. Bell. PhD thesis, Birmingham University thesis, 1954.
- [35] W. Pauli. *Niels Bohr and the Development of Physics*. edition McGraw-Hill, New York, 1995.
- [36] Makoto Kobayashi and Toshihide Maskawa. cp -violation in the renormalizable theory of weak interaction. *Progress of Theoretical Physics*, 49(2):652–657, 1973. Available from: <http://ptp.ipap.jp/link?PTP/49/652/>, doi:10.1143/PTP.49.652.
- [37] Nicola Cabibbo. Unitary symmetry and leptonic decays. *Phys. Rev. Lett.*, 10(12):531–533, Jun 1963. doi:10.1103/PhysRevLett.10.531.
- [38] Cliff Burgess and Guy Moore. *The Standard Model: A Primer*. Cambridge University Press, December 2006. Available from: <http://www.worldcat.org/isbn/0521860369>.
- [39] G. D. Coughlan, J. E. Dodd, and B. M. Gripaios. *The Ideas of Particle Physics: An Introduction for Scientists*. Cambridge University Press, 3 edition, August 2006.

Bibliography

- [40] Roe P. Byron. *Particle Physics at the new Millenium*. Springer Verlag, 1996.
- [41] Donald H. Perkins. *Introduction to High Energy Physics*. Cambridge University Press, April 2000. Available from: <http://www.worldcat.org/isbn/0521621968>.
- [42] Guido Altarelli and Martin W. Grunewald. Precision electroweak tests of the standard model. *Phys. Rept.*, 403-404:189–201, 2004. arXiv:hep-ph/0404165, doi:10.1016/j.physrep.2004.08.013.
- [43] R. Barate et al. Search for the standard model Higgs boson at LEP. *Phys. Lett.*, B565:61–75, 2003. arXiv:hep-ex/0306033, doi:10.1016/S0370-2693(03)00614-2.
- [44] Combination of CDF and D0 Results on the Mass of the Top Quark. 2009. arXiv:0903.2503.
- [45] Updated Combination of CDF and D0 Results for the Mass of the W Boson. 2009. arXiv:0908.1374.
- [46] G. Bernardi, M. Carena, and T. Junk. Higgs bosons: theory and searches. *Reviews of Particle Data Group: Hypothetical particles and Concepts*, 2010. Available from: http://pdg.lbl.gov/2008/reviews/higgs_s055.pdf.
- [47] The LEP Electroweak Group. <http://lepewwg.web.cern.ch/LEPEWWG>.
- [48] T. Aaltonen et al. Combined CDF and D0 Upper Limits on Standard Model Higgs Boson Production with up to 8.2 fb^{-1} of Data. 2011. arXiv:1103.3233.
- [49] Combined search for the Standard Model Higgs boson using up to 4.9 fb^{-1} of pp collision data at $\sqrt{s} = 7 \text{ TeV}$ with the ATLAS detector at the LHC. 2012. arXiv:1202.1408.
- [50] Serguei et al. Chatrchyan. Combined results of searches for the standard model Higgs boson in pp collisions at $\sqrt{s} = 7 \text{ TeV}$. 2012. arXiv:1202.1488.
- [51] G. Altarelli. Status of the Standard Model at the LHC Start. *Nuovo Cim.*, B123:257–269, 2008. arXiv:0804.4147, doi:10.1393/ncb/i2008-10519-5.

- [52] Riccardo Barbieri and Alessandro Strumia. The “LEP paradox”. 2000. [arXiv:hep-ph/0007265](https://arxiv.org/abs/hep-ph/0007265).
- [53] Nasa webpage on dark matter and the universe content. http://map.gsfc.nasa.gov/universe/uni_matter.html.
- [54] A D Sakharov. Violation of CP in variance, C asymmetry, and baryon asymmetry of the universe. *SOV PHYS USPEKHI*, 34 (5):392393, 1991.
- [55] Y. Abe et al. Indication for the disappearance of reactor electron antineutrinos in the Double Chooz experiment. 2011. [arXiv:1112.6353](https://arxiv.org/abs/1112.6353).
- [56] K. Abe et al. Indication of Electron Neutrino Appearance from an Accelerator-produced Off-axis Muon Neutrino Beam. *Phys.Rev.Lett.*, 107:041801, 2011. [arXiv:1106.2822](https://arxiv.org/abs/1106.2822), [doi:10.1103/PhysRevLett.107.041801](https://doi.org/10.1103/PhysRevLett.107.041801).
- [57] D. A. Bryman, W. J. Marciano, R. Tschirhart and T. Yamanaka. Rare kaon and pion decays: Incisive probes for new physics beyond the standard model. *Annual Review of Nuclear and Particle Science*, 2011. To be published.
- [58] A. Pich. Tau Physics: Theory Overview. *Nucl. Phys. Proc. Suppl.*, 181-182:300–305, 2008. [arXiv:{0806.2793}](https://arxiv.org/abs/0806.2793).
- [59] Alberto Lusiani. Measurements of $|V_{us}|$ and Searches for Violation of Lepton Universality and CPT in Tau Decays at BaBar. *PoS, ICHEP2010:251*, 2010. [arXiv:1012.3734](https://arxiv.org/abs/1012.3734).
- [60] C. Lazzeroni et al. Test of Lepton Flavour Universality in $K^+ \rightarrow l + \nu$ Decays. 2011. [arXiv:1101.4805](https://arxiv.org/abs/1101.4805).
- [61] Bernard Aubert et al. Measurements of Charged Current Lepton Universality and $|V_{us}|$ using Tau Lepton Decays to $e^- \bar{\nu}_e \nu_\tau$, $\mu^- \bar{\nu}_\mu \nu_\tau$, $\pi^- \nu_\tau$, and $K^- \nu_\tau$. *Phys. Rev. Lett.*, 105:051602, 2010. [arXiv:0912.0242](https://arxiv.org/abs/0912.0242).
- [62] Tatsu Takeuchi. Future constraints on and from lepton universality. *Journal of Physics: Conference Series*, 136(4):042045, 2008. Available from: <http://stacks.iop.org/1742-6596/136/i=4/a=042045>.
- [63] Michel Davier. Lepton Universality appeared in : The physics of leptons. Proceedings, 25th Summer Institute of Particle Physics, SSI’97,

- Stanford, USA, August 4-15, 1997. Proceedings of the 26th SLAC Summer Institute on Particle Physics: Gravity – From the Hubble Length to the Planck Length (SSI 98), Stanford, CA, 3-14 Aug 1998.
- [64] Toichiro Kinoshita. Radiative corrections to $\pi - e$ decay. *Phys. Rev. Lett.*, 2(11):477–480, Jun 1959. doi:10.1103/PhysRevLett.2.477.
- [65] S. M. Berman. Radiative corrections to pion beta decay. *Phys. Rev. Lett.*, 1(12):468–469, Dec 1958. doi:10.1103/PhysRevLett.1.468.
- [66] Terrence J. Goldman and Warren J. Wilson. Radiative corrections to muon-electron universality in a gauge theory of charged-pion decay. *Phys. Rev. D*, 14(9):2428–2430, Nov 1976. doi:10.1103/PhysRevD.14.2428.
- [67] W. J. Marciano and A. Sirlin. Theorem on π_{l2} decays and electron-muon universality. *Phys. Rev. Lett.*, 36(24):1425–1428, Jun 1976. doi:10.1103/PhysRevLett.36.1425.
- [68] D. A. Bryman and P. Depommier and C. Leroy. $\pi \rightarrow e\nu$, $\pi \rightarrow e\nu\gamma$ decays and related processes. *Physics Reports*, 88(3):151 – 205, 1982. Available from: <http://www.sciencedirect.com/science/article/B6TVP-46TY5JN-48/2/7a9613ca153d3d64cd5d26ddf49b1180>, doi:DOI:10.1016/0370-1573(82)90162-4.
- [69] William J. Marciano and A. Sirlin. Radiative corrections to π_{l2} decays. *Phys. Rev. Lett.*, 71(22):3629–3632, Nov 1993. doi:10.1103/PhysRevLett.71.3629.
- [70] M. V. Terent’ev. *Yad. Fiz.*, 18(870), 1973.
- [71] Vincenzo Cirigliano and Ignasi Rosell. Two-Loop Effective Theory Analysis of $\pi(K) \rightarrow e\nu_e[\gamma]$ Branching Ratios. *Phys. Rev. Lett.*, 99(23):231801, Dec 2007. doi:10.1103/PhysRevLett.99.231801.
- [72] Vincenzo Cirigliano and Ignasi Rosell. $\pi/K \rightarrow e\nu$ branching ratios to $O(e^2p^4)$ in Chiral Perturbation Theory. *JHEP*, 10:005, 2007. arXiv:0707.4464, doi:10.1088/1126-6708/2007/10/005.
- [73] Sergei Bashinsky and Uro š Seljak. Signatures of relativistic neutrinos in CMB anisotropy and matter clustering. *Phys. Rev. D*, 69(8):083002, Apr 2004. doi:10.1103/PhysRevD.69.083002.

- [74] Ashie, Y. et al. Evidence for an Oscillatory Signature in Atmospheric Neutrino Oscillations. *Phys. Rev. Lett.*, 93(10):101801, Sep 2004. doi: {10.1103/PhysRevLett.93.101801}.
- [75] B. Aharmim et al. Electron energy spectra, fluxes, and day-night asymmetries of ^8B solar neutrinos from measurements with NaCl dissolved in the heavy-water detector at the Sudbury Neutrino Observatory. *Phys. Rev. C*, 72(5):055502, Nov 2005. doi:10.1103/PhysRevC.72.055502.
- [76] K. Eguchi et al. First results from KamLAND: Evidence for reactor anti- neutrino disappearance. *Phys. Rev. Lett.*, 90:021802, 2003. arXiv:hep-ex/0212021, doi:10.1103/PhysRevLett.90.021802.
- [77] Thomas Thummler and for the KATRIN Collaboration. Introduction to direct neutrino mass measurements and KATRIN. 2010. arXiv:1012.2282.
- [78] C. E. Aalseth et al. The IGEX Ge^{76} Neutrinoless Double-Beta Decay Experiment: Prospects for Next Generation Experiments. *Phys. Rev.*, D65:092007, 2002. arXiv:hep-ex/0202026, doi:10.1103/PhysRevD.65.092007.
- [79] H. V. Klapdor-Kleingrothaus et al. Latest Results from the Heidelberg-Moscow Double Beta Decay Experiment. *Eur. Phys. J.*, A12:147–154, 2001. arXiv:hep-ph/0103062, doi:10.1007/s100500170022.
- [80] Shaun A. Thomas, Filipe B. Abdalla, and Ofer Lahav. Upper bound of 0.28 eV on neutrino masses from the largest photometric redshift survey. *Phys. Rev. Lett.*, 105(3):031301, Jul 2010. doi:10.1103/PhysRevLett.105.031301.
- [81] Takehiko Asaka, Shintaro Eijima, and Hiroyuki Ishida. Mixing of Active and Sterile Neutrinos. 2011. arXiv:1101.1382.
- [82] Anupama Atre, Tao Han, Silvia Pascoli, and Bin Zhang. The Search for Heavy Majorana Neutrinos. *JHEP*, 05:030, 2009. arXiv:0901.3589, doi:10.1088/1126-6708/2009/05/030.
- [83] Graciela Gelmini, Efunwande Osoba, Sergio Palomares-Ruiz, and Silvia Pascoli. MeV sterile neutrinos in low reheating temperature cosmological scenarios. *JCAP*, 0810:029, 2008. arXiv:0803.2735, doi:10.1088/1475-7516/2008/10/029.

-
- [84] A. A. Aguilar-Arevalo, C. E. Anderson, S. J. Brice, B. C. Brown, L. Bugel, J. M. Conrad, R. Dharmapalan, Z. Djurcic, B. T. Fleming, R. Ford, F. G. Garcia, G. T. Garvey, J. Mirabal, J. Grange, J. A. Green, R. Imlay, R. A. Johnson, G. Karagiorgi, T. Katori, T. Kobilarcik, S. K. Linden, W. C. Louis, K. B. M. Mahn, W. Marsh, C. Mauger, W. Metcalf, G. B. Mills, C. D. Moore, J. Mousseau, R. H. Nelson, V. Nguyen, P. Nienaber, J. A. Nowak, B. Osmanov, Z. Pavlovic, D. Perevalov, C. C. Polly, H. Ray, B. P. Roe, A. D. Russell, R. Schirato, M. H. Shaevitz, M. Sorel, J. Spitz, I. Stancu, R. J. Stefanski, R. Tayloe, M. Tzanov, R. G. Van de Water, M. O. Wascko, D. H. White, M. J. Wilking, G. P. Zeller, and E. D. Zimmerman. Event excess in the minibooNE search for $\bar{\nu}_\mu \rightarrow \bar{\nu}_e$ oscillations. *Phys. Rev. Lett.*, 105(18):181801, Oct 2010. doi:10.1103/PhysRevLett.105.181801.
- [85] H. Lacker and A. Menzel. Simultaneous Extraction of the Fermi constant and PMNS matrix elements in the presence of a fourth generation. *JHEP*, 07:006, 2010. arXiv:1003.4532, doi:10.1007/JHEP07(2010)006.
- [86] Sergei N. Gninenko. Resolution of puzzles from the LSND, KARMEN, and MiniBooNE experiments. *Phys. Rev.*, D83:015015, 2011. arXiv:1009.5536.
- [87] Bruce A. Campbell and David W. Maybury. Constraints on scalar couplings from $\pi^+ \rightarrow l^+ + \nu_l$. *Nucl. Phys.*, B709:419–439, 2005. arXiv:hep-ph/0303046, doi:10.1016/j.nuclphysb.2004.12.015.
- [88] O. Shanker. constraints on leptoquarks and supersymmetric particles. *Nuclear Physics B*, 204(3):375 – 386, 1982. Available from: <http://www.sciencedirect.com/science/article/B6TVC-471YVGM-1BM/2/ee44f89753090b75fc6b1a52f55fb98b>, doi: DOI:10.1016/0550-3213(82)90196-1.
- [89] S. Rolli and M. Tanabashi. Leptoquarks. *Reviews of Particle Data Group: Hypothetical particles and Concepts*, 2010. Available from: pdg.lbl.gov/2010/reviews/rpp2010-rev-leptoquark-quantum-numbers.pdf.
- [90] M. Hirsch, H. V. Klapdor-Kleingrothaus, and S. G. Kovalenko. New low-energy leptoquark interactions. *Physics Letters B*, 378(1-4):17 – 22, 1996. Available from: <http://www.sciencedirect.com/science/article/B6TVN-3VSR0KP-H/>

Bibliography

- 2/56684102f9f82c683e1245f2ce2ea9bf, doi:DOI:10.1016/0370-2693(96)00419-4.
- [91] Miriam Leurer. Comprehensive study of leptoquark bounds. *Phys. Rev. D*, 49(1):333–342, Jan 1994. doi:10.1103/PhysRevD.49.333.
- [92] Sacha Davidson, David Bailey, and Bruce A. Campbell. Model independent constraints on leptoquarks from rare processes. *Zeitschrift fr Physik C Particles and Fields*, 61:613–643, 1994. 10.1007/BF01552629. Available from: <http://dx.doi.org/10.1007/BF01552629>.
- [93] Search for first generation scalar leptoquarks in pp collisions at $\sqrt{s}=7$ TeV with the ATLAS detector. 2011. arXiv:1112.4828.
- [94] CMS Collaboration. Search for first generation scalar leptoquarks in the channel in pp collisions at. *Physics Letters B*, 703(3):246–266, 2011. Available from: <http://www.sciencedirect.com/science/article/pii/S0370269311009518>, doi:10.1016/j.physletb.2011.07.089.
- [95] A. Masiero, P. Paradisi, and R. Petronzio. Probing new physics through μe universality in $K \rightarrow l\nu$. *Phys. Rev.*, D74:011701, 2006. arXiv:hep-ph/0511289, doi:10.1103/PhysRevD.74.011701.
- [96] Michael J. Ramsey-Musolf, Shufang Su, and Sean Tulin. Pion Leptonic Decays and Supersymmetry. *Phys. Rev.*, D76:095017, 2007. arXiv:0705.0028, doi:10.1103/PhysRevD.76.095017.
- [97] R. Carlini, J.M. Finn, S.Kowalski, and S. Page, spokespersons. JLab Experiment E-02-020.
- [98] Ernest Ma. Neutrino masses and leptogenesis from R parity violation. 2000. arXiv:hep-ph/0008050.
- [99] J. Doornbos. M13 a new low energy pion channel at TRIUMF, Internal Design Report, 1978.
- [100] C. Kost and P. Reeve. TR-DN-82-28, 1982.
- [101] J. Doornbos. TN01 : Reduction of electron contamination in M13 with degrader-. Technical report, PIENU collaboration, TRIUMF, January 2006.

-
- [102] C.J. Oram, J.B. Warren, G.M. Marshall, and J. Doornbos. Commissioning of a new low energy π - μ at TRIUMF. *Nuclear Instruments and Methods*, 179(1):95 – 103, 1981. Available from: <http://www.sciencedirect.com/science/article/B73DN-473D9CG-CJ/2/c3623ef6898578bdd0590abf2c0f5777>, doi: DOI:10.1016/0029-554X(81)91166-6.
- [103] Martin R. Kraimer. EPICS Application Developers Guide, 1998. Available from: <http://www.aps.anl.gov/epics/base/R3-13.php>.
- [104] K B Beard, P Degtiarenko, and T J Roberts. G4 beamline program for radiation simulations. (JLAB-ACC-08-829):3 p, 2008.
- [105] Y. Unno. ATLAS silicon microstrip detector system (SCT). *Nuclear Instruments and Methods in Physics Research Section A: Accelerators, Spectrometers, Detectors and Associated Equipment*, 511(1-2):58 – 63, 2003. Proceedings of the 11th International Workshop on Vertex Detectors. Available from: <http://www.sciencedirect.com/science/article/B6TJM-48TM37W-4/2/684bf29d73d0103d7718120ccc799e3d>, doi:DOI:10.1016/S0168-9002(03)01751-0.
- [106] G. Blanpied, M. Blecher, A. Caracappa, C. Djalali, G. Giordano, K. Hicks, S. Hoblit, M. Khandaker, O. C. Kistner, A. Kuczewski, M. Lowry, M. Lucas, G. Matone, L. Miceli, B. Preedom, D. Rebreyend, A. M. Sandorfi, C. Schaerf, R. M. Sealock, H. Ströher, C. E. Thorn, S. T. Thornton, J. Tonnison, C. S. Whisnant, H. Zhang, and X. Zhao. $N \rightarrow \Delta$ Transition from Simultaneous Measurements of $p(\vec{\gamma}, \pi)$ and $p(\vec{\gamma}, \gamma)$. *Phys. Rev. Lett.*, 79(22):4337–4340, Dec 1997. doi:10.1103/PhysRevLett.79.4337.
- [107] V. Bellini, M. Capogni, A. Caracappa, L. Casano, A. D’Angelo, F. Ghio, B. Girolami, S. Hoblit, L. Hu, M. Khandaker, O. C. Kistner, L. Miceli, D. Moricciani, A. M. Sandorfi, C. Schaerf, and C. E. Thorn. Polarized Compton scattering from ${}^4\text{He}$ in the Δ region. *Phys. Rev. C*, 68(5):054607, Nov 2003. doi:10.1103/PhysRevC.68.054607.
- [108] Cayouette F., Moisan C., Zhang Nan, Thompson C. J. DETECT2000: An Improved Monte-Carlo Simulator for the Computer Aided Design of Photon Sensing Devices. *IEEE Transactions on Nuclear Science*, 49:624–628, 2002.

- [109] Chloe Malbrunot. Presentation: Bina optical simulation, April 2008. Available from: <https://pienu.triumf.ca/InternalDocuments/Meetings/TRIUMF/Regular%20Meetings/apr-15-2008/simulation-Bina.pdf/view?searchterm=Detect2000>.
- [110] Alexis A. Aguilar-Arevalo, Ahmed Hussein and Chloé Malbrunot. TN08 : Testing and Setting Up BINA Using Gamma Ray Calibration Sources. Technical report, PIENU collaboration, TRIUMF, May 2008.
- [111] Luca Doria. TN11 : Installation of the CsI Calorimeter for the PIENU experiment. Technical report, PIENU collaboration, TRIUMF, February 2009.
- [112] T. K. Komatsubara, T. Morimoto, K. Omata, S. Sugimoto, K. Tauchi, T. Inagaki, S. Kabe, M. Kobayashi, Y. Kuno, T. Sato, T. Shinkawa, Y. Yoshimura, I. H. Chiang, S. Kettell, K. K. Li, L. S. Littenberg, A. Yamashita, H. Suzuki, and S. Suzuki. Performance of fine-mesh photomultiplier tubes designed for an undoped-csi endcap photon detector. *Nuclear Instruments and Methods in Physics Research Section A: Accelerators, Spectrometers, Detectors and Associated Equipment*, 404(2-3):315 – 326, 1998. Available from: <http://www.sciencedirect.com/science/article/B6TJM-41FDHDB-G/2/991752e1295863553a80417ac3f8f893>, doi:DOI:10.1016/S0168-9002(97)01107-8.
- [113] Masaaki Kobayashi, Takao Shinkawa, Takahiro Sato, Shojiro Sugimoto, Michail V. Korzhik, Andrey A. Fyodorov, and Vasilij A. Kachanov. YAlO₃: Ce-Am light pulsers as a gain monitor for undoped CsI detectors in a magnetic field. *Nuclear Instruments and Methods in Physics Research Section A: Accelerators, Spectrometers, Detectors and Associated Equipment*, 337(2-3):355–361, 1 1994. Available from: <http://www.sciencedirect.com/science/article/B6TJM-473FRB0-2N4/2/21b282cb90c7601d8eb982dd9abcb54c>.
- [114] Alexis A. Aguilar-Arevalo. TN10 : Stand-Alone Setup and Testing of the Xe-Flash Tube Monitoring System. Technical report, PIENU collaboration, TRIUMF, October 2008.
- [115] Y. Igarashi, H. Fujii, T. Higuchi, M. Ikeno, E. Inoue, T. Murakami, Y. Nagasaka, M. Nakao, K. Nakayoshi, M. Saitoh, S. Shimazaki, S.Y. Suzuki, M. Tanaka, K. Tauchi, T. Uchida, and Y. Yasu. A common

Bibliography

- data acquisition system for high-intensity beam experiments. *IEEE Transactions on Nuclear Science*, 52(6):2866–2871, 2005.
- [116] K. Yamada. *Search for Massive Neutrinos in $\pi^+ \rightarrow e^+ \nu$ Decay*. PhD thesis, Osaka University, February 2010.
- [117] J.-P. Martin and P.-A. Amaudruz. A 48 channel pulse shape digitizer with dsp. *IEEE Transactions on Nuclear Science*, 53(3):715–719, 2006. doi:10.1109/TNS.2006.875049.
- [118] J.-P. Martin, C. Mercier, N. Starinski, C.J. Pearson, and P.-A. Amaudruz. The TIGRESS DAQ/Trigger System. *IEEE Transactions on Nuclear Science*, 55(1):84–90, 2008. doi:10.1109/TNS.2007.910853.
- [119] C. Ohlmann, TRIUMF, Vancouver, Canada. VT48 Rev.A, 48-Channel Time-to-Digital Module. User’s Manual, 2007.
- [120] KOPIO webpage. Available from: <http://www.bnl.gov/rsvp/KOPIO.htm>.
- [121] Y. Arai. AMT-3 -ATLAS Muon TDC version 3 & AMT-2- User’s Manual, February 2005.
- [122] S. Ritt and P. A. Amaudruz. The midas data acquisition system. Available from: midas@triumf.ca.
- [123] R. Brun and F. Rademakers. ROOT - An Object Oriented Data Analysis Framework. *Nucl. Inst. & Meth. in Phys. Res. A*, 389:81–86, 1997.
- [124] A. Hillaret, TRIUMF, Vancouver, Canada. Private communication, 2009.
- [125] TWIST experiment at TRIUMF. Available from: <http://twist.triumf.ca/~e614/experiment.html>.
- [126] D. Vavilov. Acces to Tracking Information in PIENU tree, 2010. Available from: https://pienu.triumf.ca/InternalDocuments/run-information/2009-run/ana%lysis/tracking/tracking_info_intree.pdf/view.
- [127] J. Birks. Theory and Practice of Scintillation Counting. *Proc. Phys. Soc.*, A64:874, 1951.

Bibliography

- [128] NADS. Cry simulation package for cosmics, May 2010. Available from: <http://nuclear.llnl.gov/simulation/>.
- [129] K. Yamada, M. Yoshida, Y. Igarashi, M. Aoki, K. Tauchi, M. Ikeno, Y. Takubo, A. Muroi, M. Tanaka, and Y. Kuno. Pion Decay-Mode Tagging in a Plastic Scintillator Using COPPER 500-MHz FADC. *IEEE Transactions on Nuclear Science*, 54(4):1222–1226, 2007.
- [130] L.Doria. Pulse Shape Fitting. Technical report, PIENU collaboration, TRIUMF, 2011.
- [131] F L Pratt. Muon spin relaxation as a probe of electron motion in conducting polymers. *Journal of Physics: Condensed Matter*, 16(40):S4779, 2004. Available from: <http://stacks.iop.org/0953-8984/16/i=40/a=019>.
- [132] R.L. Garwin T. Muller J.C. Sens A. Zichich G. Charpak, F.J.M. Farley. A New Limit to the Electric Dipole Moment of the Muon. *Nuovo Cim*, 22:1043–1050, 1961.
- [133] A. Buhler, T. Massam, Th. Muller, M. Schneegans, and A. Zichichi. Measurements of Muon Depolarization in Several Materials. *Nuovo Cim.*, 39:824–828, 1965. doi:10.1007/BF02734620.
- [134] J. Sulkimo *et al.* GEANT4 a simulation toolkit. *Nucl. Inst. & Meth. in Phys. Res. A*, 506:250–303, 2003.
- [135] J. Allison *et al.* GEANT4 developments and applications. *IEEE Transactions on Nuclear Science*, 53:270–278, 2006.
- [136] A. A. Poblaguev. Analysis of the $\pi \rightarrow e\nu\gamma$ experimental data. *Phys. Rev. D*, 68:054020, Sep 2003. Available from: <http://link.aps.org/doi/10.1103/PhysRevD.68.054020>, doi:10.1103/PhysRevD.68.054020.
- [137] Yu. M. Bystritsky, E. A. Kuraev, and E. P. Velicheva. Radiative corrections to radiative $\pi e2$ decay. *Phys. Rev. D*, 69:114004, Jun 2004. Available from: <http://link.aps.org/doi/10.1103/PhysRevD.69.114004>, doi:10.1103/PhysRevD.69.114004.
- [138] M. Bychkov, D. Počanić, B. A. VanDevender, V. A. Baranov, W. Bertl, Yu. M. Bystritsky, E. Frlež, V. A. Kalinnikov, N. V. Khomutov, A. S. Korenchenko, S. M. Korenchenko, M. Korolija, T. Kozłowski,

N. P. Kravchuk, N. A. Kuchinsky, W. Li, D. Mekterović, D. Mzhavia, S. Ritt, P. Robmann, O. A. Rondon-Aramayo, A. M. Rozhdestvensky, T. Sakhelashvili, S. Scheu, U. Straumann, I. Supek, Z. Tsamalaidze, A. van der Schaaf, E. P. Velicheva, V. P. Volnykh, Y. Wang, and H.-P. Wirtz. New precise measurement of the pion weak form factors in $\pi^+ \rightarrow e^+ \nu \gamma$ decay. *Phys. Rev. Lett.*, 103:051802, Jul 2009. Available from: <http://link.aps.org/doi/10.1103/PhysRevLett.103.051802>, doi:10.1103/PhysRevLett.103.051802.

- [139] D. I. Britton, S. Ahmad, D. A. Bryman, R. A. Burnham, E. T. H. Clifford, P. Kitching, Y. Kuno, J. A. Macdonald, T. Numao, A. Olin, J. M. Poutissou, and M. S. Dixit. Improved search for massive neutrinos in $\pi^+ \rightarrow e + \nu$ decay. *Phys. Rev. D*, 46(3):R885–R887, Aug 1992. doi:10.1103/PhysRevD.46.R885.

Appendix A

Full Trigger Diagram

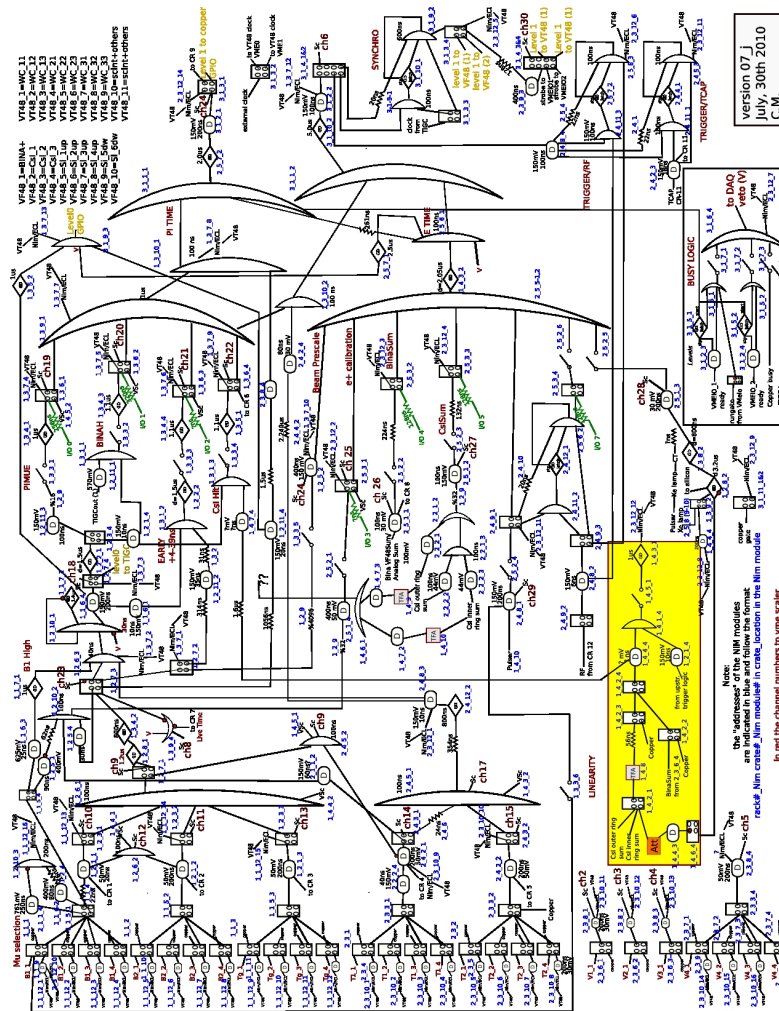


Figure A.1: The complete PIENU trigger diagram.

Appendix B

X and Y Position of Tracking Detectors

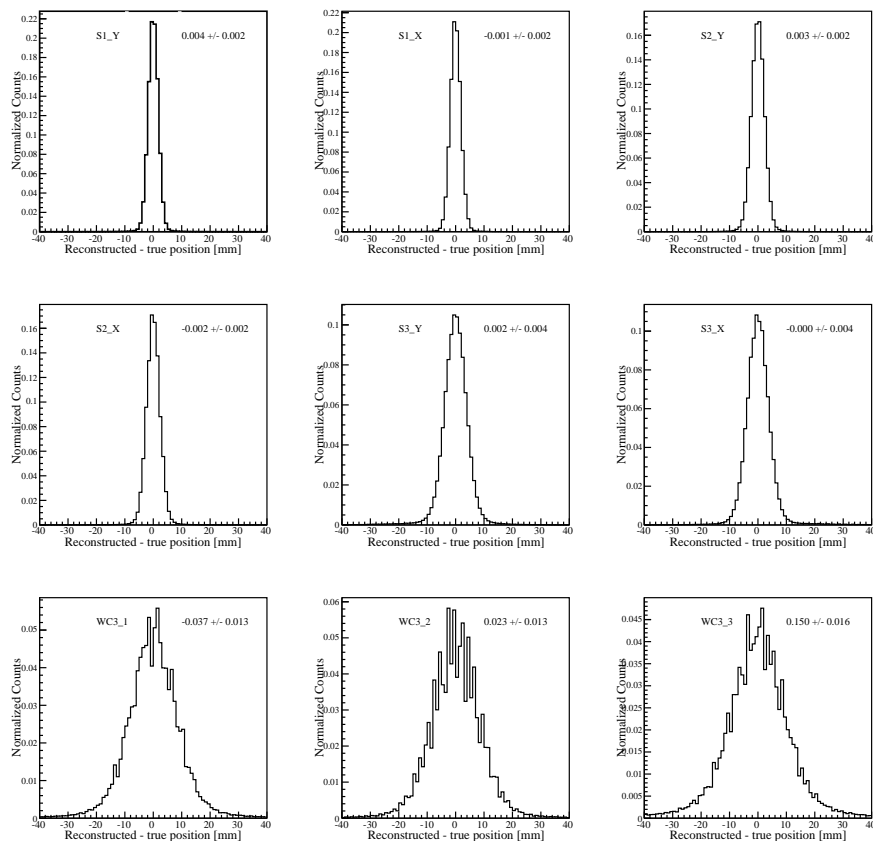


Figure B.1: Distribution of the difference between reconstructed tracks from WC1-2 detectors and hit position in all other tracking detectors using beam muons. The distribution width grows with the distance from WC1-2 due mainly to multiple scattering.

Appendix C

Muon Runs

Table C.1: List of muon runs taken in 2010.

Date	run number range
2010/06/10	35962 - 35990
2010/06/17	36750 - 36780
2010/06/24	37589 - 37625
2010/07/08	39526 - 39547
2010/07/15	40418 - 40449
2010/07/21	41223 - 41250
2010/07/30	42124 - 42141
2010/08/06	42524 - 42552
2010/08/20	44404 - 44429
2010/10/08	46753 - 46794
2010/10/22	48448 - 48479
2010/10/29	49367 - 49404
2010/11/05	50108 - 50153
2010/11/12	50953 - 50990
2010/11/19	51713 - 51764